



HAL
open science

Strong radiative shocks relevant for stellar environments : experimental study and numerical approach

Raj Laxmi Singh

► **To cite this version:**

Raj Laxmi Singh. Strong radiative shocks relevant for stellar environments : experimental study and numerical approach. Physics [physics]. Université Pierre et Marie Curie - Paris VI, 2017. English. NNT : 2017PA066092 . tel-01722700

HAL Id: tel-01722700

<https://theses.hal.science/tel-01722700>

Submitted on 5 Mar 2018

HAL is a multi-disciplinary open access archive for the deposit and dissemination of scientific research documents, whether they are published or not. The documents may come from teaching and research institutions in France or abroad, or from public or private research centers.

L'archive ouverte pluridisciplinaire **HAL**, est destinée au dépôt et à la diffusion de documents scientifiques de niveau recherche, publiés ou non, émanant des établissements d'enseignement et de recherche français ou étrangers, des laboratoires publics ou privés.



THESE DE DOCTORAT
SORBONNE UNIVERSITE - PIERRE ET MARIE CURIE

École doctorale “Physique en Ile-de-France”

Préparée

au Laboratoire de Physique des Plasmas
et au Laboratoire d’Étude du Rayonnement et de la Matière en
Astrophysique et Atmosphères

Présentée par

Raj Laxmi SINGH

Sujet de la thèse :

**Strong radiative shocks relevant for stellar environments:
experimental study and numerical approach**

Soutenance le 02 Mars 2017

à Université Pierre et Marie Curie, devant un jury composé de :

Mme FALK Katerina	Senior Scientist ELI Beamlines, Czech Republic	Rapporteur
Mme TURCK-CHIEZE Sylvaine	Directrice de Recherches honoraire du CEA	Rapporteur
M. GONZALEZ Matthias	Maître de conférences U. Denis Diderot	Examinateur
Mme RICONDA Caterina	Professeur UPMC	Examinateur
M. LAROUR Jean	Chargé de Recherche CNRS	Directeur de thèse
Mme STEHLÉ Chantal	Directrice de Recherche CNRS	(Invitée) Co-directrice de thèse



Except where otherwise noted, this work is licensed under
<http://creativecommons.org/licenses/by-nc-nd/3.0/>

ACKNOWLEDGEMENTS

First and foremost I would like pay my sincere gratitude to Dr. Jean Larour and Dr. Chantal Stehlé, my thesis supervisors, who have introduced me to the marvelous world of Laboratory Astrophysics. I would express my thanks for their continuous support during my PhD journey, for encouraging me to learn challenging things. Working under their guidance was a unique experience and a great joy. I am particularly grateful for their serenity and patience that helped me in developing my space and style in research. Coming all the way from India to a non-English speaking community had been presented by them to me like a second home through their benign love and affection.

I have imparted a significant time during my PhD for conducting experiments in PALS laser facility at Prague through LASERLAB access. Being newbie in such a large scale experimental facility has never been a problem for which I am thankful to all the team members for their help and guidance from Paris, PALS Prague and Imperial College, London. Special thanks to Dr. M. Kozlova, Dr. M. Krus, Dr. J. Nejd, Dr. J. Dostal and all other staff members at the PALS laser facility, and the target fabrication to Mr. P. Barrasso and team at the Observatoire de Paris, without whom none of these experiments could have been possible. Special acknowledgement to Dr. F. Suzuki Vidal, Mr. T. Clayson, P. Barroso and Dr. U. Chaulagain for sharing their insight and explanations during the experiments.

I especially appreciate the constructive help and comments of Dr. F. Suzuki Vidal, Dr. M. Kozlova, Dr. M. Cotel, Dr. R. Rodríguez and Dr. U. Chaulagain in the data analysis, article and thesis writing.

I am grateful to all the jury members of my PhD committee, Dr. Sylvaine Turck-Chieze, Dr. Kateřina Falk, Dr. Caterina Riconda, Dr. Matthias Gonzalez, Dr. Chantal Stehlé and Dr. Jean Larour, for taking time to attend my PhD defense. Thanking very much to Dr. Turck-Chieze and Dr. Falk for reviewing my thesis and providing valuable comments and feedback, which have surely improved my thesis.

I would like to express sincere thanks to the directors of LPP, Dr. P. Chabert, and of LERMA Dr. D. Lis, for allowing me to work on the thesis in such a fabulous university ambience. It would be unjust if I do not mention the administrative help received from Dr. D. Zahorski, former Project chief of Plas@Par as well as Dr. X. Fresquet, the present project chief of Plas@Par. I am grateful to Plas@Par Labex for funding my PhD studies in France.

Next, I would like to thank Dr. U. Chaulagain for helping me in Paris during my stay from the very first day. I am also grateful to Dr. L. de Sà, Dr. L. Ibgui, Dr. M Drouin, Dr. A. Stan, Mr. B. Khiar, Mr. L. Nicolas, Dr. J. Freundlich for their help and support during my stay in France.

My thanks is due to my friends for creating a homely atmosphere during my thesis in France. In particular, I would like to thank Dr. R. Mourya and Mr. A. Ranjan for their continuous support in the administrative formalities and others which helped me a lot to concentrate and speed up my thesis writing. I would also like to mention the names of my friends Miss T. Bhowmik, Miss V. Shaw and Dr. A. Gupta for their support.

Good company plays a very important role in the life. In this, I am particularly thankful to Dr. S. C. Tripathi, Dr. J. Pal, Dr. R. Kumar, Dr. M. Dave, Dr. A. Bharadwaj, Mr. K. Singh, Miss S. Mishra and Miss S. Pandey for helping me in keeping pace with research and daily life developments. I am indebted to my brother Dr. A. Awasthi for his sincere guidance, encouragement and cooperation during my entire doctoral study. Also, I would like to take this opportunity to thank my childhood friend Miss R. Yadav for her love and encouragement during my thesis.

Finally, last but not the least, I express my whole hearted gratitude to the support I received in the form of love and affection from my grandparents, parents, sisters, brothers and my other family members. This is something beyond acknowledgements. They were always with me and the encouragement I received from them will never fade away.

Raj Laxmi Singh

Strong radiative shocks relevant for stellar environments: experimental study and numerical approach

ABSTRACT

Strong shocks are present in various astrophysical phenomena. Such shocks are strongly influenced by the radiation through its coupling with hydrodynamics. Thus their topology and dynamics are quite complex. Generating such hypersonic shocks in the laboratory, with controlled conditions, is thus an adequate tool to study the influence of radiation and to compare them with numerical simulations. Such shocks can be generated by intense lasers and electromagnetic devices. The first part of this dissertation concerns the numerical and experimental study of the interaction of two counter propagating laser-driven shocks. The experiments, performed at the kJ PALS laser facility allowed to generate shocks with different speeds (~ 30 - 55 km/s and 10 - 25 km/s), in noble gases and low pressure (less than 1 bar). Several diagnostics were implemented: visible interferometry, time- and space-resolved visible spectroscopy, and time integrated XUV spectroscopy. Our experiment shows a strong interaction of one radiative precursor onto the second one. The physical parameters of the plasma were deduced from the diagnostics and compared with 1-D simulation results. The second part is devoted to the design of an experiment where the shock is generated electromagnetically. The optimization of this generator is presented and also the full experimental set up which allows studying shock ~ 30 km/s in noble gas at ~ 1 mbar.

Keywords: Radiative shock – hydrodynamics – laser-plasmas – visible and XUV spectroscopy
– numerical simulation – laboratory astrophysics –high energy density physics.

Chocs forts et radiatifs d'intérêt pour les environnements stellaires : étude expérimentale et approche numérique

RESUME

Les chocs forts sont présents dans des phénomènes astrophysiques variés. De tels chocs sont fortement influencés par le rayonnement par son couplage avec l'hydrodynamique. Par suite, leur topologie et leur dynamique sont assez complexes. Générer de tels chocs hypersoniques en laboratoire, dans des conditions contrôlées, est ainsi un outil pertinent pour étudier l'influence du rayonnement et pour comparer aux résultats des simulations numériques. Ces chocs sont générés par des lasers intenses et par des moyens électromagnétiques. La première partie du texte est consacré à l'étude numérique et expérimentale de l'interaction de deux chocs induits par laser se propageant en sens contraires. Les expériences ont été menées sur l'installation laser kJ PALS, qui permet de former deux chocs avec des vitesses propres différentes (~ 30 - 55 et 10 - 25 km/s respectivement) dans des gaz rares à pression faible (moins de 1 bar). Des diagnostics ont été installés : interférométrie visible, spectroscopie visible à résolution spatiale et temporelle, spectroscopie XUV intégrée en temps. Nos expériences montrent une forte interaction entre les deux précurseurs radiatifs. Les paramètres physiques du plasma ont été déduits de ces diagnostics et comparés aux résultats de simulations monodimensionnelles. La seconde partie est consacrée à la conception d'une expérience où le choc est généré de façon électromagnétique. L'optimisation de ce générateur est présentée ainsi que l'environnement expérimental permettant d'étudier des chocs jusqu'à 30 km/s dans des gaz rares peu denses (1 mbar).

Mots clés: chocs radiatifs; plasmas laser; hydrodynamique; spectroscopie visible et XUV; simulation numérique; astrophysique de laboratoire; physique à haute densité d'énergie.

Résumé long

En introduction (chapitre 1), les chocs radiatifs (CR) sont présentés dans de nombreux environnements astrophysiques, en particulier dans les étoiles. Ce sont des chocs forts, avec un nombre de Mach élevé ($M \gg 1$) et une très haute température, ce qui induit un rayonnement intense. Alors que l'observation de cette signature, avec une résolution spatiale, est très difficile en astrophysique, une approche innovante, celle dite des plasmas astrophysiques de laboratoire, fournit un puissant moyen d'étude des CR sur Terre. Depuis plus d'une décennie, ces chocs sont étudiés en laboratoire, principalement sur de grandes installations laser, dans les gaz rares et sous différentes géométries. L'interaction entre un laser et une feuille mince produit une forte ablation et par effet fusée accélère la feuille qui se propage dans le gaz à plusieurs dizaines de km/s. Pour des irradiations laser entre 10^{14} and 10^{15} W/cm², on enregistre des vitesses de chocs entre 40 et 150 km/s. En parallèle une description fine est permise par des simulations numériques.

Au début de ce travail, les expériences étaient concentrées sur des CR simples, alors que la situation astrophysique est celle d'un CR interagissant avec un milieu plus dense, donnant des chocs réfléchis et transmis. Des exemples représentatifs de ces phénomènes sont la propagation de restes de supernovae dans des nuages moléculaires denses, les chocs d'accrétion sur la photosphère des étoiles T-Tauri ou encore les chocs d'étrave à l'avant des jets stellaires. La collision (ou l'interaction) de deux CR est bien sûr un événement rare en astrophysique, mais un exemple est fourni par l'interaction de débris de la supernova DEM L316 (cf Fig. 1 de Williams et al. (1997)) même si l'hypothèse est contestée (Velarde et al. (2006)).

Il y a donc une forte motivation pour réaliser une expérience de laboratoire pour étudier la propagation et l'interaction de deux chocs face à face et interpréter les signatures observées. Cette approche constitue une grande part de mon travail. En complément aux expériences laser, j'ai étudié un générateur compact de puissance pulsée alimentant un canon à plasma coaxial pour créer des chocs d'intérêt astrophysique dans les gaz à basse pression. Les chocs ainsi créés sont de plus grande taille et peuvent être étudiés plus facilement (Kondo et al., 2008). Pour cette thèse, je me suis attachée à présenter les chocs radiatifs dans le contexte de l'astrophysique de laboratoire, en suivant ces deux approches.

Le deuxième chapitre traite de la physique des CR. Ils composent une classe de chocs supersoniques qui sont chauffés à haute température et sont par conséquent sources d'un rayonnement intense. En retour, ce rayonnement modifie la dynamique et la structure du choc, ce qui complexifie la description. Les CR se rencontrent dans des situations astrophysiques comme les chocs d'accrétion lors de la formation des protoétoiles (Stahler,

Palla, et Salpeter, 1986), l'explosion de supernovae et l'interaction de leur restes avec le milieu interstellaire dense (Chevalier, 1977), ou encore les chocs d'étrave en tête des jets stellaires (Hartigan et al., 2001). Les CR sont maintenant étudiés en laboratoire, ce qui permet de comparer les résultats aux modèles de la littérature et de vérifier la possibilité de les retrouver avec les simulations numériques disponibles (Bouquet et al. (2004); Leygnac et al. (2006)). L'étude expérimentale des CR est cruciale notamment pour comprendre les processus énergétiques au sein des plasmas astrophysiques. Dans le cas des gaz parfaits, le saut au niveau d'un choc est décrit par les équations de Rankine-Hugoniot, qui relient les quantités thermodynamiques de part et d'autre de la discontinuité. La solution monodimensionnelle d'un choc se propageant à la vitesse u_s dans un gaz au repos est usuellement décrite dans le repère lié au choc, et on distingue la région amont (ou pré-choc) à la vitesse $u_1 = -u_s$ et, en arrière du choc (région post-choc ou aval), la vitesse est u_2 selon la Fig. 2.1. Pour les chocs forts, où le nombre de Mach M est très grand devant 1, les sauts des quantités thermodynamiques d'un gaz parfait sont donnés par les éq. 2.1 à 2.4. Pour un gaz monoatomique, le rapport de compression est de 4 et la température de la zone post-choc est proportionnelle au carré de la vitesse du choc et à la masse atomique. La situation est plus complexe pour un gaz réel car une part de l'énergie cinétique sert à exciter et à ioniser le gaz du post choc. La température attendue est donc inférieure à celle du cas idéal ; en outre la pression est modifiée par l'ionisation (Michaut et al., 2004). Un nouveau jeu d'équations incorpore la charge effective Z des ions (éq. 2.5 à 2.8). Ces modèles ignorent le chauffage et le refroidissement radiatifs, alors que le rayonnement émis affecte la structure d'un choc fort. Cette description demande d'ajouter aux équations de conservation de la masse, quantité de mouvement et énergie, les contributions radiatives (flux, énergie et pression. Le cas est plus complexe et les équations d'hydrodynamique radiative ont été exprimées dans le repère du choc (Mihalas and Mihalas, 1999; Drake, 2006) selon les éq. 2.9 à 2.11.

Les contributions de la pression radiative et du champ de rayonnement sont importantes à très haute température (vitesse) mais déjà pour nos chocs le flux radiatif est dominant. Selon l'opacité, le rayonnement du choc peut être absorbé par la région pré-choc, induisant un chauffage loin en avant de la discontinuité. Egaleme nt, la zone choquée proche de la discontinuité est affectée par la compétition entre l'émission (refroidissement) et l'absorption (chauffage). Ainsi l'épaisseur optique locale (éq. 2.11) devient le paramètre pertinent. Comme on raisonne sur le flux radiatif moyenné en fréquence, c'est l'opacité de Rosseland qui est utilisée et on différencie les régimes optiquement épais et optiquement mince ce qui permet de classer les chocs radiatifs.

Notre intérêt s'est concentré sur les chocs présentant un précurseur radiatif. En laboratoire, une intensité laser au dessus de 10^{14} W/cm² le permet

et les installations sont rappelées dans le tableau 2.1. Il est aussi possible de lancer des chocs moins rapides, donc peu radiatifs ($\sim 10\text{-}30$ km/s) avec un piston électromagnétique.

Le chapitre 3 est consacré à l’analyse numérique des CR, en décrivant les processus physiques jouant un rôle dans ces systèmes physiques. De même que les observations, les expériences en laboratoire ne sont pas directement interprétables et la simulation numérique devient un outil précieux. Diverses approches numériques sont utilisées pour simuler les plasmas de laboratoire. On considère soit des grilles fixes, soit des grilles adaptables (Adaptive Mesh Refinement) pour maintenir une résolution suffisante sur chaque zone du plasma. Une autre approche utilise des grilles qui suivent le fluide dans son mouvement (modèle Lagrangien), donc sans passage de matière d’une cellule à la voisine. Les équations sont alors différentes (Orban et al., 2013).

Pour décrire les collisions de chocs, j’ai utilisé le code commercial HELIOS, un code Lagrangien mono-dimensionnel pouvant gérer le rayonnement et l’hydrodynamique (MacFarlane, Golovkin, et Woodru, 2006). Assez facile à prendre en main, il a le gros avantage de pouvoir simuler notre configuration, deux chocs de vitesses opposées lancés par deux lasers. HELIOS décrit les plasmas hors d’équilibre thermodynamique (hors ETL) grâce à un modèle collisionnel-radiatif (HELIOS-CR) de calcul des populations atomiques à chaque pas de simulation hydrodynamique. De fait, j’ai utilisé HELIOS dans une approximation ETL qui correspond aux conditions expérimentales (Rodriguez et al., 2011) et cela est discuté en détails.

Le code résout les équations fluides en introduisant les pressions des électrons, des ions et du rayonnement. Electrons et ions sont décrits par deux fluides en interaction de températures respectives T_e et T_i . La conduction thermique est gérée par celle des électrons à partir de la conductivité de Spitzer et le dépôt d’énergie laser par un modèle de Bremsstrahlung inverse. L’émission et l’absorption du rayonnement sont introduites dans l’équation d’énergie des électrons et dans celles du transport radiatif. Une méthode utilise un modèle de diffusion du rayonnement multi-groupes et à flux limité, où le flux radiatif est proportionnel au gradient de l’énergie radiative et inversement proportionnel à l’opacité de Rosseland, avec une pondération pour obtenir une bonne description du cas optiquement mince, selon Olson, Auer, et Hall (2000). Une seconde méthode utilise un schéma dépendant du temps à courte distance et multi-angles. Dans notre cas, où rayonnement et hydrodynamique sont fortement couplés et aussi en variation rapide, on utilise le modèle de diffusion et les opacités ETL multi-groupes de Planck et Rosseland.

En outre, notre version d’HELIOS utilise PROPACEOS (MacFarlane, Golovkin, et Woodru, 2006), une table d’équation d’état et d’opacité multi-groupes générée par le code, sans possibilité d’introduire une autre table. La

connaissance des conditions thermodynamiques est nécessaire pour la simulation du plasma dans nos cas : masse volumique entre 10^{-4} et 10^{-1} g/cm³, température entre 0 et 50 eV. Une évaluation précise par Rodriguez et al. (cf. Fig. 2 de Rodriguez et al., 2011) pour le Xénon, indique que les conditions thermodynamiques de nos CR correspondent au régime ETL. L'équation d'état relie pression, ionisation et énergie interne à la masse volumique et à la température. Notre version d'HELIOS pour plasma ETL utilise PROPACEOS, qui est peu documentée ; elle utilise le modèle de More et al. (1988) en régime de couplage fort (haute densité et basse température) et un modèle d'atome isolé pour un couplage faible. Des interpolations sont incluses pour passer au couplage fort (<http://www.prism-cs.com/Software/PROPACEOs>).

J'ai réalisé des simulations HELIOS 1D pour divers cas de CR, choc seul ou chocs en collision, qui sont décrites dans ce chapitre 3. Les CR se propageant dans le Xe à 0.1 bar et à 50 km/s sont caractérisés par un précurseur radiatif étendu. Une compression élevée (38) dans le post-choc est attribuée à l'ionisation du gaz et au refroidissement radiatif. Les températures du post-choc et du pré-choc, de part et d'autre du pic, sont identiques, signe d'un choc supercritique. Le rôle spectaculaire de l'opacité a été remarqué, mais, à considérer l'incertitude sur l'opacité du Xénon et le traitement 1D, j'ai décidé de ne pas chercher à raffiner la simulation en termes de nombre de groupes.

L'étude numérique permet de retrouver les caractéristiques de l'interaction de deux chocs opposés avec des vitesses respectives 50-50 km/s et 50-20 km/s. Dans tous les cas, la principale signature de l'interaction (donc avant la collision) est le recouvrement des précurseurs à t_0+8 ns pour 50-50 km/s et à t_0+15 ns pour 50-20 km/s. Ensuite, on assiste à une remontée régulière de la densité et de la température électroniques. L'instant de la collision voit une augmentation soudaine de la densité électronique (par un ordre de grandeur), qui atteint 6.6×10^{21} et 3×10^{21} cm⁻³ respectivement, alors que la température monte à 39 et 28 eV.

Dans le quatrième chapitre, je présente l'installation laser PALS puis la cellule d'interaction, son implantation et les diagnostics associés. Rappelons le principe expérimental. Quand une impulsion brève de lumière laser est focalisée sur une feuille mince, une part importante d'énergie est transférée et le chauffage du solide conduit à son ablation. Un plasma coronal, chaud et peu dense, est éjecté vers l'arrière et un choc vers l'avant se forme dans la feuille par effet fusée. Comme cette feuille limite le tube, le choc se transmet au gaz, la feuille agissant comme un piston. Des expériences ont été menées sur le Prague Asterix Laser System (PALS) au printemps 2015 (5 semaines: 20 avril - 22 mai) avec pour objectif la première étude de l'interaction puis de la collision de deux CR sous l'action de deux lasers au niveau de 10^{14} W/cm². Le Prague Asterix Laser System (PALS) repose

sur un laser à iode infrarouge (Asterix IV, Jungwirth et al., 2001). Après amplification, il délivre jusqu'à 1 kJ en 0,3 ns à la longueur d'onde fondamentale de 1315 nm. Des faisceaux auxiliaires sont disponibles à fréquence doublée ($\lambda = 657$ nm) ou triplée (438nm). PALS délivre deux tirs par heure à haute énergie, et dans de bonnes conditions d'homogénéité du faisceau. Pour nos expériences nous utilisons deux faisceaux. Le faisceau fondamental est divisé après le 4ème amplificateur en deux faisceaux d'énergie 60% et 40% (voir Fig. 4.2). Le plus puissant est injecté dans le 5^{me} amplificateur et sa fréquence est triplée. Ce faisceau à 438 nm est nommé MAIN. Le second faisceau est utilisé sans modification, donc à 1315 nm, et est nommé AUX. Le schéma de distribution est en Fig. 4.2 et les propriétés de MAIN and AUX laser sont rappelées dans le tableau 4.1.

PALS propose deux chambres à vide, sphérique et cylindrique respectivement : nous avons utilisé la chambre sphérique (Fig. 4.3). D'un diamètre de 100 cm, elle est accessible aux faisceaux MAIN et AUX par deux hublots de 80 cm et 50 cm. Des portes sont aménagées ainsi que de nombreux ports. A l'intérieur, la cellule et des diagnostics sont montés sur une table optique découplée mécaniquement de la chambre. Les cibles (Fig. 4.5) comprennent un petit tube long de 4 mm fermé à ses deux extrémités par des feuilles minces de parylène-N doré de 11 μm sur lesquelles les deux lasers sont focalisés au niveau de 10^{14} $\text{W}\cdot\text{cm}^{-2}$. Le tube est rempli du gaz dans lequel le choc se propagera à une vitesse attendue entre 30 et 60 km/s. Les feuilles minces assurent la conversion de l'énergie laser en énergie cinétique via l'ablation et la génération de choc. Des cellules spécifiques en dural massif permettent l'alignement et la mesure du diamètre du faisceau. Toutes les cellules sont réalisées par le Pôle instrumental de l'Observatoire de Paris.

Les cellules à gaz sont remplies in situ à une fraction de bar, avec Xe, Ar, Xe90/He10 et He, permettant ainsi de bien connaître le milieu où se propagent les chocs. Le système de remplissage (Fig. 4.10) permet de limiter l'écart de pression sur les fenêtres de la cellule et permet de suivre la pression jusqu'au moment du tir. C'est critique pour ne pas casser la fenêtre ultra fine de Si_3N_4 pour la spectroscopie XUV et pour gérer une fuite éventuelle.

Le réglage de la position et de la focalisation permet d'obtenir des taches laser centrées de diamètres 450 - 500 μm et 250 - 300 μm pour MAIN et AUX respectivement. Ce contrôle est répété chaque jour. Les impacts sont toujours suivis par des caméras X au keV, même si l'impact sur la feuille de parylène-N donne un signal X faible comparé à celui du tir sur Al.

Les diagnostics du plasma sont principalement l'interférométrie visible et la spectroscopie, XUV et visible. L'alignement est suivi par des caméras dans le visible. Pour l'interférométrie visible précisément, on doit prendre une image de référence (sans franges) de chaque cible (Fig. 4.17a). Le faisceau de référence de l'interféromètre Mach-Zehnder est bloqué et le faisceau sonde est utilisé seul. La fente est ensuite réduite à 200 μm pour ne sonder que la zone

centrale du tube, mais s'étendant le long de l'axe jusqu'aux pistons pour avoir une référence des positions initiales. Ensuite, en mode interférogramme, on crée un système de franges perpendiculaires à la fente, donc perpendiculaires à la direction de propagation du choc (cf Fig. 4.17b et Fig. 4.13). Le tube de choc est imagé sur la caméra avec un grandissement suffisant (5,4 mm) et il est possible d'assurer un balayage électronique de la fente sur le détecteur jusqu'à 200 ns. Un interférogramme dit streak permet ainsi de suivre l'impact des chocs sur les franges en fonction du temps.

L'émission XUV du plasma est enregistrée avec une intégration spatiale et temporelle sur un spectrographe à champ plan muni d'un réseau concave. Il est installé dans la partie haute de la chambre (cf Fig. 4.18) et enregistre l'émission XUV traversant la fenêtre de Si_3N_4 . Une spectroscopie visible, résolue en temps et en position longitudinale, a été installée (Fig. 4.19a) mais n'a pas encore pu être exploitée complètement.

Le chapitre 5 présente les résultats des deux diagnostics, surtout l'interférométrie qui a été complètement analysée. J'ai développé une procédure de dépouillement avec des outils numériques ad hoc de calcul et d'analyse d'image. Certes l'interférométrie ne permet pas de sonder des plasmas plus denses que la densité critique imposée par le laser ($4 \times 10^{21} \text{cm}^{-3}$ à 627 nm), et on constate que le post-choc est opaque. Au contraire, le rayonnement XUV est présent dans toute la structure et la spectroscopie XUV intégrée en temps et en espace permet d'explorer à la fois le post-choc et le précurseur. L'analyse des interférogrammes streak en visible part d'une évaluation de l'effet de l'indice de réfraction des électrons détaillée dans l'appendice A, mais qui se heurte assez vite à une perte de contraste et à une disparition des franges bien en dessous de la valeur de la densité critique déjà mentionnée. Les déphasages accessibles avec précision ne dépassent guère 2 ou 3 fois 2π . La recherche de maxima des franges est semi automatisée et permet d'arriver à une densité électronique moyennée sur les 600 μm de l'épaisseur du tube de choc. Le profil non plan du choc conduit à penser que la moyenne sous-estime d'un facteur 2, voire plus, la densité dans le précurseur. La disparition des franges est attribuée à la présence du front de choc. Par suite, les interférogrammes permettent de mesurer des vitesses de chocs de 30-55 et 10-30 km/s pour MAIN et AUX respectivement, ainsi que des densités électronique dans les précurseurs entre 10^{17} et 10^{19}cm^{-3} .

Nous avons ainsi démontré l'interaction entre deux précurseurs radiatifs dans Xe at 0.1 bar, pour deux chocs à 54 et 23 km/s. L'interaction est clairement caractérisée par l'augmentation de l'onde d'ionisation puis par la superposition des deux précurseurs à $t_0+20\text{ns}$. La collision est enregistrée à $t_0+47 \text{ns}$, un résultat retrouvé par la simulation.

Nous avons répété mais à plus haute pression, 0.2 bar, et trouvé des vitesses de $\sim 41 \text{km/s}$ pour MAIN et $\sim 18 \text{km/s}$ pour AUX. Cependant

nous n'avons pas de signature du précurseur radiatif pour AUX et le temps de collision n'a pas été accessible à l'enregistrement. Le précurseur côté MAIN n'est pas influencé par AUX jusqu'à la limite de t_0+48 ns (Fig. 5.9(b) et (c)). La simulation prédit un très faible précurseur côté AUX et une interaction des précurseurs à t_0+49 ns.

L'interférométrie transverse à 0.2 bar, avec des vitesses ~ 40 et 20 km/s indique que le précurseur côté MAIN a une extension latérale de ~ 600 μm contre 300 μm pour AUX. Le précurseur de MAIN est légèrement affecté près des parois alors que celui de AUX est fortement courbé. Les effets 2D sont donc prononcés pour AUX et faibles pour MAIN. En outre, pour le Xénon, nous disposons de la température et de la charge moyenne par le spectre XUV intégré (tir#48143, Xénon, 0.6 bar). On peut en conclure que la charge moyenne est au moins égale à 6 et qu'on a atteint une température de 15 eV.

Nos simulations donnent une description qualitative des CR en interaction, à la réserve près que nous introduisons dans HELIOS une fluence laser ajustée pour donner la bonne vitesse. Cependant, il est maintenant admis que les simulations 2D (avec les opacités correctes) décrivent bien les expériences (González, Audit, et Stehlé, 2009; Leygnac et al., 2006; Stehlé et al., 2010). A la même énergie laser, le calcul 2D conduit à diminuer la vitesse du choc, compare au calcul 1D, et aussi à une baisse de la densité électronique. Par exemple, pour un choc lancé à PALS par un laser à 1315 nm dans le Xénon à 0.3 bar avec une fluence de 85000 J/cm^2 , ARWEN 2D donne une vitesse de 44 km/s en accord avec l'expérience (Cotelo et al., 2015). La simulation 1D demanderait 30000 J/cm^2 pour obtenir la même vitesse.

De même la spectroscopie XUV intégrée à 0.6 bar, pour des vitesses réelles de ~ 39 et 18 km/s, indique que la température a atteint 15 eV et que la charge moyenne a atteint 6 ou 7, alors que la simulation 1D prédit 10-30 eV et 5-10 respectivement (Fig. 5.18). On peut en conclure qu'une étude détaillée basée sur des simulations 2D et un post-traitement du transfert de rayonnement sont nécessaires pour raffiner l'analyse. Pour les autres gaz rares (Ar, Kr), on a observé que, à énergie laser donnée, la vitesse de CR est une fonction décroissante de la masse volumique. Ceci confirme que, pour une densité et une vitesse, les effets radiatifs augmentent avec le numéro atomique. Pour le Krypton, on a observé un petit précurseur mais aucune interaction. Celle-ci ne serait possible qu'en augmentant nettement la vitesse, donc l'énergie du laser. Ceci a été rendu possible sur l'installation laser Orion (A.W.E., Aldermaston, G-B) où la collision de deux CR d'égale vitesse a été obtenue à ~ 80 km/s pour une fluence laser $\sim 6 \times 10^{14}$ W/cm^2 (Clayson et al., 2016; Suzuki-Vidal et al., 2016) pour une large gamme de gaz rares et des pressions entre 0.1 et 1 bar. Pour étudier à la fois les chocs et les précurseurs radiatifs, de nombreux diagnostics étaient installés: radi-

ographie X, imagerie optique en caméra à balayage de fente, interférométrie multi-vues et à balayage de fente. Bien que je n'aie pas pu participer aux campagnes, j'ai fait des simulations 1D pour interpréter les résultats. Cet aspect n'est pas décrit dans cette thèse mais a été publié très récemment (Clayson et al., 2017).

Après des chapitres consacrés aux chocs radiatifs générés par laser, le chapitre 6 décrit un moyen alternatif passant par la voie électrique à haute puissance. Les chiffres de la voie laser sont très élevés en fluence, plus de 10^{14} W/cm², mais représentent des énergies modérées dans l'impulsion (120 et 60 J pour MAIN et AUX au PALS). Or un système électrique devant délivrer 100 J reste modeste pour sa partie stockage. Les vitesses de 50 km/s seront probablement difficiles à atteindre mais on peut tabler sur un régime complémentaire des chocs radiatifs avec plus de 10 km/s si le rendement de conversion en énergie cinétique reste correct. D'où un nécessaire travail d'optimisation. Des vitesses jusqu'à 100 km/s avaient été mesurées très tôt dans des canons à plasma d'hydrogène à basse pression (Lee, 1969) mais ceci a été exploité ensuite pour d'autres finalités. La littérature ne mentionne qu'un cas de canon électromagnétique coaxial dédié aux chocs d'intérêt astrophysique (Kondo et al., 2006). Il est signalé que le lanceur électromagnétique produit des chocs plans de grande dimension transverse (1 ordre de grandeur par rapport à la voie laser) et donc plus faciles à investir (Kondo et al., 2008). Le principe de fonctionnement est le suivant : i) création d'un claquage haute tension initial, sur une surface diélectrique face à du gaz, ii) chauffage ohmique du plasma par le courant en croissance rapide, iii) accélération de la couche de plasma sous la pression magnétique auto-générée par le courant (dizaines de kA), iv) maintien (1 μ s) de la pression magnétique pour communiquer une impulsion importante. Des travaux sur le *Z-pinch* ou le *plasma focus* permettent de postuler des géométries convenables pour accélérer une masse de l'ordre de 10^{-5} 10^{-4} g.

Après avoir étudié le fonctionnement d'un circuit électrique rapide, j'ai listé les points forts et les points faibles en fonction des objectifs et j'ai proposé une géométrie coaxiale compacte. L'optimisation du canon à plasma a été faite en terme de vitesse maximale à la sortie avec comme seules contraintes une énergie stockée de 1 kJ, une dimension transverse de 4 mm et une dimension axiale d'un ordre plus grande. L'objectif était le choc fortement supersonique, 10-30 km/s à quelques mbar d'Ar ou de Xe. Un modèle simple (0D) a été comparé à un modèle 3D MHD par le code GORGON qui décrit bien les expériences de plasmas astrophysique par puissance pulsée (Ciardi et al., 2007).

La pression magnétique s'exprimant par $B^2/2\mu_0$ un courant supérieur à 100 kA apparaît nécessaire, et atteignable sur un générateur 1 kJ - 1 μ s compact de type R-L-C. Ensuite il a fallu monter un modèle de circuit déformable

comportant une section formée de la lame de plasma en mouvement, et qui prene en compte l'accrétion du gaz dans un modèle dit *snowplow* (Potter 1971). Des paramètres géométriques, comme la forme et les dimensions du canon, ont pu être optimisés pour donner une grande vitesse de sortie du plasma pour Ar et Xe et dans la gamme 0.1 - 10 mbar. Un canon a été construit et connecté à un générateur électrique pulsé existant. Des observations du mouvement du plasma par la dynamique du rayonnement radial donnent des vitesses cohérentes avec le modèle, avec la simulation 3D MHD et des nombres de Mach élevés, de 20 à 60. Ces travaux ont soutenu la conception d'un autre générateur pour obtenir des performances plus élevées, en vitesse de choc et en taux de répétition.

Contents

List of Figures

List of Tables

1	Introduction	1
1.1	General Context	1
1.2	Outline of Chapters	2
1.3	My contribution	3
2	Radiative shock waves	5
2.1	Rankine-Hugoniot(R-H) relations	6
2.1.1	Jump relations for a real gas	9
2.1.2	Effect of radiation on shock waves	11
2.1.3	Radiative hydrodynamics equations	13
2.2	Radiative shock regimes	15
2.2.1	Typical radiative shock waves with a precursor	16
2.3	Radiative shock waves experiments	16
2.3.1	Laser-driven shock experiments	18
2.3.2	Electromagnetically launched shock	21
3	1D Simulations	23
3.1	HELIOS	23
3.2	LTE approximation	24
3.2.1	Mean opacity	25
3.2.2	Equation of State	27
3.3	Single radiative shock waves	27
3.4	Interacting radiative shock waves	40
3.5	Summary	44
4	Experimental Setup	47
4.1	Prague Asterix Laser System (PALS) facility	48
4.2	Targets	49
4.2.1	Massive Targets	51
4.2.2	Gaseous Targets	51
4.2.3	Target holder	55

4.2.4	Target filling	56
4.3	Laser Focusing	57
4.3.1	Focal Lenses and Phase Zone Plates	57
4.3.2	Focusing of the MAIN and AUX laser beams	58
4.4	Diagnostics	59
4.4.1	Visible interferometry	61
4.4.2	XUV spectroscopy	65
4.4.3	Visible spectroscopy	67
4.5	Summary	68
5	Results and Interpretation	71
5.1	Visible interferometry	71
5.1.1	Longitudinal interferometry: shock speed and electron density	74
5.1.2	Transverse interferometry: lateral extension of the shock	91
5.2	XUV Spectroscopy	92
5.3	Simulations based on experimental results	93
5.4	Summary	97
6	Electromagnetically launched shock	101
6.1	Principles of operation of a high current generator	102
6.2	Principles of the run-down phase in a PFD	103
6.3	Proposed design for the plasma gun	104
6.4	Dynamic circuit modelling	106
6.5	3-D MHD simulations using GORGON code	111
6.6	Measurements	116
6.7	Summary	118
7	Conclusion	121
7.1	Conclusions	121
7.2	Perspectives	123
8	Thesis summary	127
	Appendices	141
A	Visible Interferometry	143
A.0.1	Refractive index of a plasma	143
A.0.2	Absorption of the laser beam	144
A.0.3	Principle of interferometry	145
A.0.4	Mach Zehnder Interferometer	146
B	Opacities and mean charge	149

List of Figures

- 2.1 Schematic diagram for a 1-D shock moving in the x direction. The speed of the shock front is u_s . In the frame of reference of the shock front, the pre-shock region has a relative speed $u_1 = -u_s$, density ρ_1 , total pressure P_1 , temperature T_1 , whereas these quantities are respectively u_2 , ρ_2 , P_2 and T_2 for the post-shock region. 6
- 2.2 Profiles of temperature ($T_e = T_i = T$) and mass density (ρ) at 10 ns for a shock propagating in Xenon at 0.1 bar ($\rho_1 = 5.7 \times 10^{-4}$ g/cm⁻³), with a speed of ~ 45 km/s. It is to note that the given pressure value are at 298 K. The simulation is performed with the HELIOS code, excluding the radiation effect, and for a polytropic gas ($\gamma=5/3$). The initial temperature of Xenon is set to 1 eV and with a negligible (10^{-5} W/m/K) thermal conductivity. The Mach number is then equal to 40. For this simulation, the shock is launched by a 100 μm thick Aluminium piston moving at the velocity of 33 km/s. The position $x=0$ corresponds to the position of the Xe/Al interface at time $t=0$ 8
- 2.3 Electron temperature (T_e), ion temperature (T_i) and mass density (ρ) profiles at 10 ns, derived from 1-D simulation for the case of ionisation (no radiation). The shock propagates in Xe gas at 0.1 bar ($\rho_1 = 5.7 \times 10^{-4}$ g/cm⁻³ by ~ 45 km/s). It is to note that the given pressure value is at 298 K. The simulation is performed with the HELIOS ($T_e \neq T_i$ case), using the PROPACEOS equation of state, without any radiation and with a negligible thermal conductivity (10^{-05} W/m/K). The initial temperature in Xenon is set to 1 eV and thus the Mach number is equal to 40. For this simulation, the shock is launched by a 100 μm thick Aluminium piston moving at the velocity of 38 km/s. The position $x=0$ corresponds to the position of the Xe/Al interface at time $t=0$ 10

2.4 Figure 14 & 17 of Michaut *et al.* (2004) (a): Compression ρ_2/ρ_1 (full circles, thin line), kT_2 in eV (inverted full triangles, thin line) in Argon (a)/ Xenon (b) for initial conditions kT_1 ($= 10$ eV for Ar and $= 0.1$ eV for Xe), $\rho_1 = 5 \times 10^{-4}$ g/cm³, versus shock speed in km/s, with (full markers, full lines) and without (empty markers, dashed lines) radiation. The ionization stage $\langle z \rangle_2$ is plotted with the diamond symbol. 12

2.5 Simulated electron temperature (T_e), ion temperature (T_i) and mass density (ρ) profiles at 10 ns of a radiative shock propagating with a 15 km/s (a: sub-critical) and 48 km/s (b: supercritical). The shock is propagating in Xenon at 0.1 bar ($\rho = 5.4 \times 10^{-4}$ g/cm⁻³, at 298 K). The initial temperature in Xenon is set to 1eV. The two Mach numbers are respectively equal to 13 and 43. The radiation and ionisation effects are included in the simulation which is performed for two different temperatures ($T_e \neq T_i$) and a negligible thermal conductivity (10^{-05} W/m/K). For this simulation, the shock is launched by a 100 μ m thick Aluminium piston moving at the speed of 12 km/s and 45 km/s for case (a) and (b) respectively. The position x=0 corresponds to the position of the Xe/Al interface at time t=0. 17

3.1 PROPACEOS Monochromatic opacity versus the photon energy in eV of Xenon at 10 eV and at two electron densities respectively equal to 10^{18} and 10^{20} cm⁻³. 26

3.2 Mass density and temperature (a), electron density and mean charge (b) at 10 ns for a radiative shock of speed ~ 47 km/s in Xenon at 0.1 bar. The vertical dotted black lines show the position of the interface between piston and backing Xenon gas. Zero at x-axis is the interface of piston and Xenon at time zero. Spitzer thermal conductivity has been used in the simulation. 29

3.3 Mean Rosseland opacity (in cm².g⁻¹) and opacity (cm⁻¹) at 10 ns for a radiative shock of speed ~ 47 km/s in Xenon at 0.1 bar. The vertical dotted black lines show the position of the interface between piston and backing Xenon gas. Zero at x-axis is the interface of piston and Xenon at time zero. Spitzer thermal conductivity has been used in the simulation. 30

3.4 (a): Mass density and temperature (b): electron density and mean charge at 10 ns for a radiative shock of speed ~ 47 km/s in Xenon at 0.1 bar. The vertical dotted black lines show the position of the interface between piston and backing Xenon gas. Zero at x-axis is the interface of piston and Xenon at time zero. A negligible constant thermal conductivity (10^{-12} W/m/K) have been used in the simulation for Xenon. 31

LIST OF FIGURES

3.5 (a): Electron density and electron temperature (b): Mass density and mean charge at 10 ns for a radiative shock of speed ~ 48 km/s in Xenon at 0.1 bar, for the case when the electron and ion temperature are different. The vertical dotted black lines show the position of the interface between piston and backing Xenon gas. Zero at x-axis corresponds to the position of the interface between the piston and Xenon at time zero. The Spitzer thermal conductivity has been used in this simulation. 32

3.6 (a): Mass density and electron temperature (b): electron density and mean charge at 10 ns for a radiative shock of speed ~ 45 km/s in Xenon at 0.1 bar, for the case when the electron and ion temperature are different. The vertical dotted black lines show the position of the interface between piston and backing Xenon gas. Zero at x-axis corresponds to the position of the interface between the piston and Xenon at time zero. In this simulation value of thermal conductivity (10^{-12} W/m/K) is negligible for Xenon. The peak value of ion temperature is found to be 405 eV whereas theoretically, this value is expected to be ~ 600 eV. It is possible to achieve the expected value by increasing the resolution of the simulation. 34

3.7 Electron temperature profiles for various numbers of frequency groups, $N = 1, 20, 50, 60, 70, 90$ and 100 35

3.8 (a): Electron temperature (a), mean charge (b) and mass density (c) for four (1, 10, 30 and 40) multipliers of the Xenon opacity at 10 ns. 36

3.9 Planck and Rosseland monochromatic opacity profiles T_e for $\rho = 1.5 \times 10^{-3}$ from PROPACEOS (I), BIGBART (II) and Rodriguez et al. (III). 38

3.10 Monochromatic Xenon opacity versus the photon energy in eV at $T = 15$ eV and for $\rho = 1.5 \times 10^{-3}$ g.cm $^{-3}$ for the PROPACEOS (a) and Rodríguez *et al.* (2015) (Fig. 16 of Rodríguez *et al.* (2015)) (b) models. 39

3.11 Electron density N_e (a) and electron temperature T_e (b) versus axial position (along a 0.4 cm long shock tube) at 3, 10, 20, 30 and 38 ns from HELIOS simulations (with opacity $\times 20$) for the cases of single shock of ~ 50 km/s (dotted line) and two identical counter-propagating shocks of ~ 50 km/s (solid lines). The vertical dotted lines show the position of the interface between piston and backing Xenon gas. 41

3.12 Variations of N_e (a) and T_e (b) versus axial position for the case of two identical counter-propagating shocks (of speeds ~ 50 km/s) at 3, 10, 20, 30, 35 and 40 ns as derived from HELIOS simulations. For these simulations, we have neglected the effect of radiation by keeping the Xe opacity equal to zero. The vertical dotted lines show the position of the interface between the piston and backing Xenon gas. 43

3.13 Variations of N_e (a) and T_e (b) with axial position for the case of two non-identical counter-propagating shocks (of speeds ~ 50 & 20 km/s) and two single shocks (dotted lines) of speeds ~ 50 & 20 km/s respectively at 3, 10, 30, 35 and 46 ns as derived from HELIOS simulations. The vertical dotted lines show the position of the interface between piston and backing Xenon gas (with opacity $\times 20$). 45

4.1 a: Spatial profile of the PALS Laser beam. b: Intensity profile of laser pulse $I(t)$ with time. 48

4.2 Energy distribution scheme for MAIN and AUX laser beams. . . 49

4.3 Snapshot of the spherical chamber showing the horizontal bread-board, and, on the right, the focusing MAIN lens. 50

4.4 Dimension drawing (a) and snapshot (b) of Aluminum massive (“mock”) target. 50

4.5 Values on the figures are in mm. (a): Vertical cross section view of the gaseous target. (b): Horizontal cross section view. 52

4.6 Picture of a the gaseous target on its base. 53

4.7 Schematic of the gaseous target. 53

4.8 Transmission of 100 nm thick Si_3N_4 membrane (CXRO database). 54

4.9 Snapshot of a target holder with one V-shield regarding the AUX laser, which will pass through the hole in this shield, marked in green in the Figure. The target, which faces the two diagnostics (tubes), and is located behind the V-shield, is thus not visible. . . 54

4.10 In-situ system for target filling and pressure monitoring. 56

4.11 Schematic of the keV camera. 59

4.12 (a): Sign convention for the respective positions of the lens and the target. (b): keV image of a MAIN impact on a massive target (lens position: $+1500 \mu\text{m}$). The spot size is $475 \pm 25 \mu\text{m}$. Pixel size for MAIN keV camera is $5.6 \mu\text{m}$. (c): keV image of an AUX impact (lens position: $-1500 \mu\text{m}$). The spot size is $\sim 280 \pm 20 \mu\text{m}$ on target. One pixel = $6.6 \mu\text{m}$ on AUX’s keV camera. 60

4.13 First interferometric setup. All the optical elements are 1 inch. For simplicity, the plasma slab is not reported in the probe beam. 61

4.14 Second interferometric setup. 63

4.15 Schematic of the Streak camera (from Hamamatsu notice). . . . 64

LIST OF FIGURES

4.16 Imaging setup of the Mach Zehnder Interferometer setup operating in the longitudinal mode. The channel of the target is fully illuminated by the probe beam. In this mode, the lens images the axis of symmetry of the two shock waves along the slit of the streak camera. 65

4.17 (a): Reference 2D image of a target, before the shot, recorded on the Streak camera. The positions of the two pistons closing the 4 mm long target are located at 800 and 4800 μm . The dark zones along them (between 800 to 1000, and 4600-4800 μm) corresponds to the glue. This glue is then visible through vertical black strips in the interferometric record. (b): Corresponding interferometric time-space record. 66

4.18 Typical ray tracing in a grazing incidence XUV spectrograph. The detector (GMCP or image plate) is installed tangentially to the Rowland circle. 67

4.19 (a): Setup of the XUV spectrometer in the spherical chamber; (b) Typical record between ~ 10 and 40 nm is shown in the bottom panel. 68

4.20 (a): Schematic of setup employed to record the time and space visible plasma emission. (b): A typical spectrogram. 69

5.1 Original record of shot #48055 (left), FFT of the original image (center) and the frequency filtered image (right). 73

5.2 A cropped section of the record from shot the #48055. The first five positions have been selected manually '+' signs (in red color) on each fringe. On this record, the distance between two unperturbed fringes is correspond to 15 pixels (i.e. 159 μm). . . . 73

5.3 (a): Representative points of the fringes as derived from the spline fitting of the 5 manually selected points (Fig. 5.2 (II)) on each fringe. (b): Positions of the fringes maxima along Y-axis for each fringe, derived by locating the points of maximum intensity in X-direction of the previous points obtained by spline fit. 75

5.4 Fringe maxima on the full image. 76

5.5 Imaging setup of the Mach Zehnder Interferometer operating in the longitudinal mode. The lens images the axis of symmetry of the two shock waves along the slit of the streak camera. 76

5.6 Interferometric image recorded for the shot #48055 in Xe at 0.1 bar. The shock speeds for the shocks driven by MAIN (from left side) and AUX (from right side) lasers are respectively equal to ~ 54 and 23 km/s. The time of laser arrival on the piston is at 146 ns. The positions of the Au-Xe interface on the record are respectively 950 ± 50 and 4950 ± 50 microns. 77

5.7 (a) MAIN shock speed (calculated by the *last fringe* method) versus the MAIN energy, for Xenon or Xe/He mixture at different pressures, with the error bars. (b) AUX shock speed versus AUX energy, also for Xenon or Xe/He mixture at different pressures. 79

5.8 MAIN shock speed (calculated by the *last fringe* method) versus the MAIN laser energy, for Xe (at 0.1 bar only), Ar, He and Kr at different pressures, with the error bars. 82

5.9 Left panel: interferometric records #48055 in Xe at 0.1 bar (a), #48132 in Xe+He at 0.2 bar (b) and #48138 in Xe+He at 0.2 bar (c). Right panel: electron density at 10, 20, 30 and 40 ns versus distance for these records. The positions of maxima have been identified on the records in the left panel. The time $t = 0$, corresponds to the time of laser arrival on the target and the position $x = 0$ corresponds to the interface between the piston (Au layer) and the gas. Its determination is precise within 100 microns. The distances between two unperturbed fringes for records #48055, #48132 and #48138 are 159, 244 and 244 μm respectively. The $\langle N_e \rangle$ uncertainty (± 2 pixels) is indicated by the error bar in the right panels. It corresponds respectively to $\pm 9 \times 10^{17}$, $\pm 6 \times 10^{17}$ and $\pm 6 \times 10^{17} \text{ cm}^{-3}$ for the figures (a), (b) and (c). The limit of detection (2 pixels) is presented by a dotted line on each figure. 85

5.10 (a): Interferometric record in Ar at 0.3 bar (#48079). The estimated speeds for MAIN and AUX are 49 ± 5 and 23 ± 3 km/s. (b): Same record, where the fringes maxima are marked by points. The bins definition is as follows: bin 0: $N_e \leq 1.1 \times 10^{18} \text{ cm}^{-3}$ (white), bin 1: $1.1 - 1.8 \times 10^{18} \text{ cm}^{-3}$ (yellow) and bin 2: $3.9 - 5.7 \times 10^{18} \text{ cm}^{-3}$ (red). The time $t = 0$, corresponds to the time of laser arrival on the target and the position $x = 0$ corresponds to the interface between the piston (Au layer) and the gas. Its determination is precise within 100 microns. 87

5.11 Results for temperature (a) and Rosseland opacity (b) obtained from HELIOS simulation at 10 ns for two counter-propagating shocks at ~ 50 and 18 km/s, for Xe (with opacity multiplier 1 and 20), Ar and Kr at $5.4 \times 10^{-4} \text{ g.cm}^{-3}$ initial mass density. A comparison Ar, Kr and Xe PROPACEOS opacity shown in APPENDIX B. 88

LIST OF FIGURES

5.12 (a): Raw interferometric record in Kr at 0.2 bar (shot #48146). The estimated speed for MAIN shock is 53 ± 2 km/s. The time $t = 0$, corresponds to the time of laser arrival on the target.(b): Same record shown in (a) maxima is marked by colored points. The bins definition is as follows: bin 0: $N_e \leq 1.1 \times 10^{18} \text{ cm}^{-3}$ (white), bin 1: $1.1 - 1.8 \times 10^{18} \text{ cm}^{-3}$ (yellow) and bin 2: $3.9 - 5.7 \times 10^{18} \text{ cm}^{-3}$ (red). The time $t = 0$, corresponds to the time of laser arrival on the target and the position $x = 0$ corresponds to the interface between the piston (Au layer) and the gas. Its determination is precise within 100 microns. 90

5.13 Schematics of the Mach Zehnder Interferometer setup to record transverse interferometric images. The lens allows to make, on the slit of the camera, the image of a section perpendicular to direction of shock propagation. 91

5.14 Transverse interferometric images for (a): shot#48111 (MAIN shock only). (b): shot#48130 (AUX shock only). The time is measured after an offset equal to 14 and 23 ns respectively after the time of the laser arrival on the target. The position 'zero' on the x-axis of each image corresponds to the base of the target. . . 92

5.15 Interferometric image for the shot#48143. The time $t = 0$, corresponds to the time of laser arrival on the target and the position $x = 0$ corresponds to the interface between the piston (Au layer) and the gas. Its determination is precise within 100 microns. . . 94

5.16 Raw (a) and corrected XUV spectrum (b) for the shot #48143. . . 95

5.17 Recorded electron density (shot #48055) together with the HELIOS results (with Xenon opacity $\times 20$) at different times in Xenon at 0.1 bar. 97

5.18 Time evolution of the mass density (a), electron temperature (b) and mean charge (c) at 56, 57, 58, 60, 64 and 65 ns within the shock tube derived from the HELIOS simulations (with Xenon opacity multiplier = 20), for two counter streaming shocks of ~ 39 and 18 km/s in Xenon at 0.6 bar. 98

6.1 (a): Sketch of the shock generator showing the pulsed electrical circuit, the set of coaxial conical electrodes with a constant radial gap and the plastic insulator, featured in grey, on which a planar surface discharge is initiated. The installation of three optical fibers allows looking radially at the plasma moving in the shock tube. (b): Schematics of the plasma dynamics inside the coaxial gun: in fast-pulse mode, the electrical current flows in the superficial layers of the two coaxial conical electrodes and through an annular plasma layer. The magnetic pressure P_{mag} pushes the discharge axially. 105

6.2 Exploded view of the plasma gun. 106

LIST OF FIGURES

6.3	Time dependence of the main parameters for Ar gas at 1 mbar according to the circuit model. (a): current (kA) and voltage (V), (b): accreted mass (kg) and rate of accretion (kg/s), (c): speed (m/s) and kinetic energy (J).	108
6.4	Plot of the different output parameters (normalized with respect to the peak values) obtained at the top of the inner electrode. For each group, upper panel represents the variation for Ar gas whereas lower panel is for Xe gas. Profiles of output parameters are given: (a) with cone angle (b) with accretion factor, (c) with gas pressure and (d) with damping resistance.	109
6.5	Example of mapping of the electron density from a 3-D MHD simulation (background gas Argon at 1 mbar) when the plasma sheath is : (left) at the exit of the plasma gun, (right) in free flight conditions (log scales for the false colors).	113
6.6	Time history of plasma merging and early free flight through the mapping of the electron density, electron temperature and average ionic charge, as given by a 3-D MHD simulation (background gas Argon at 1 mbar) (scales for the false colors).	114
6.7	Axial profiles, values taken in the shock tube along a line slightly off-axis at a distance of 1 mm, for mass density, ion temperature, ion density, average ion charge, magnetic field, electron temperature, electron density and average speed at 1500 ns (background gas Argon at 1 mbar). A mapping of $ B $ is given, with a dashed line indicating shock front position as well.	115
6.8	Experimental results : (a) time history of the passive optical records compared to the main current for Argon gas close to the reference pressure (b) time-integrated signal vs Ar pressure for the different fibers. (c) averaged speed vs Ar backing pressure.	117
7.1	Interferometric record obtained at 5.46 ns for a single radiative shock of speed ~ 100 km/s propagating in Xe+He gas at 0.6 bar driven by laser at 348 nm with energy 170 J. The different colors in (b) correspond to: yellow: $\leq N_e \leq 3.5 \times 10^{17}$ cm $^{-3}$; cyan: $3.7 - 7.4 \times 10^{17}$ cm $^{-3}$; blue: $7.4 - 1.5 \times 10^{18}$ cm $^{-3}$; green: $1.5 - 1.8 \times 10^{18}$ cm $^{-3}$; magenta: $1.8 - 2.2 \times 10^{18}$ cm $^{-3}$; red: $2.2 - 2.6 \times 10^{18}$ cm $^{-3}$; orange: 2.6×10^{18} cm $^{-3} - 1.8 \times 10^{19}$ cm $^{-3}$	124
A.1	Schematics of Mach Zehnder interferometer, with two mirrors, two 50% beam splitters and the detector. A plasma slab is placed in one of the two arms of the interferometer.	147
B.1	Rosseland and Planck opacity for three gases Xe, Kr and Ar at mass densities 5.1×10^{-4} g/cm 3 (a) and 1.6×10^{-3} g/cm 3 (b).	150

LIST OF FIGURES

B.2 Mean charge for three gases Xe, Kr and Ar at mass densities 1.6×10^{-3} g/cm³ (a) and 5.1×10^{-4} g/cm³ (b). 151

List of Tables

2.1	Summary of the radiative shocks experiments and outcomes in different laser installations. All the experiments are performed in Xe except Keiter <i>et al.</i> (2002) and Visco <i>et al.</i> (2012). In these two experiments, the first uses SiO ₂ * and the second uses Ar** as a shocked medium.	20
4.1	Nominal characteristics of MAIN and AUX laser beams.	49
4.2	Specifications of the MAIN and AUX focal lenses and the f- number (focal length/beam diameter) is given (see table 4.1 for the beam diameters).	57
4.3	Specifications of the two Phase Zone Plates.	58
4.4	Specifications of the two uEye keV cameras (1stVSION company).	59
4.5	Specifications of Andor CCD camera.	67
4.6	Specifications of the XUV grating.	67
5.1	Shock speeds estimated from the ‘last fringe’ method. ‘NA’ represents the entries which could not be deduced from the record. Further, entries in the bold font are discussed in detail in this chapter.	81
5.2	Atomic data and density at 0.1 bar (at room temperature) for He, Ar, Kr and Xe.	82
6.1	Input parameters, their standard values and range of variation.	110
6.2	Launching performance Ar/Xe.	111
6.3	Values of variables in various conditions: at rest (with seed electrons), inside the shock and inside post-shock region. A star * denotes the insulator surface.	112

Introduction

1.1 General Context

Radiative shocks (RS) are present in various astrophysical environments, especially in stars. They are then present in all the supersonic accretion/ejection processes during the stellar evolution, from the early phase of the protostellar collapse, up to the magnetosphere accretion on to the already formed T-Tauri stars, up to the late stage of the supernovae shocks.

Radiative shocks are strong shocks (i.e. Mach number, $M \gg 1$), which reach high temperatures and thus are the source of intense radiation. Although the observation of (i.e. spatially resolved) signatures of such shocks in the astrophysical environments is very difficult, an alternate approach, named laboratory plasma astrophysics provides a powerful tool to study them on the Earth.

These waves have been experimentally studied since more than a decade, mostly on large-scale laser facilities, in noble gases and with different targets geometries. The ablation process, generated by the interaction between the laser and a foil, induces a shock wave in the foil, which then propagates in the gas at a speed of several tens of km/s. Numerical simulations can describe these shocks with an improving precision. With laser intensities on target comprised between 10^{14} and 10^{15} W/cm², these experiments allowed to record shock speeds ranging between 40 and 150 km/s.

All previous experimental studies have been focused on the case of single radiative shocks. However, in astrophysical conditions, the radiative shock in general interacts with a denser medium, leading to the development of reflected and transmitted shocks. A few representative examples of such phenomena are the interaction of supernovae remnants with dense molecular clouds, the accretion shocks on the photosphere of T-Tauri stars and the bow shocks at the head of fast stellar jets. The collision (or the interaction) of two radiative shock waves is obviously a rare astrophysical event and the template case of the supernova remnants DEM L316 (see Fig. 1 of Williams *et al.* (1997)) is still the subject of debates (Velarde *et al.*, 2006). In this regard, the development of dedicated laboratory experiments to the study of propagation and interaction of counter-propagating shock waves is important as a tool to characterize such events through their specific signatures.

Complementary to laser experiments, compact pulsed power generators may drive an electromagnetic coaxial plasma gun to create astrophysical

relevant shocks in lower pressure noble gases, with a high availability and a rather modest capital cost. The electromagnetically driven shock waves may have larger scales than those by laser. Thus they can be analyzed rather easily with the adequate diagnostics (Kondo *et al.*, 2008).

In this thesis, I am presenting radiative shocks in the context of laboratory astrophysics, using two experimental approaches: laser-driven shocks and electromagnetically driven shocks.

1.2 Outline of Chapters

In the first chapter, the physics of radiative shocks wave will be summarized. I will discuss the Rankine-Hugoniot (RH) for the perfect gas and generalized RH equations for ionized gas. Further, the effects of radiation on the shock equations will be introduced and I will review the different regimes of the radiative shocks presenting a radiative precursor. Then, I will present a short historical review of laser and electromagnetically laboratory experiments on this topic. Finally, I will highlight the objectives of my work in this framework.

The chapter two is dedicated to the numerical analysis of radiative shock waves and of the main physical processes, which play a role in these complex processes. The simulations will be performed in 1D, using the commercial radiation hydrodynamic HELIOS code (MacFarlane, Golovkin, and Woodruff, 2006). After a description of the code and his possibilities, several simulations will be performed to analyze the effects of the two fluids (electrons and ions) approach, compared to the one fluid case (identical temperature for both), of the thermal conductivity and the multi-groups opacity description. Then, a brief overview of single and two counter-propagating radiative shocks will be presented.

Chapter three will start with a short overview of the Prague Asterix Laser System facility (PALS). It will be followed by the experimental setup including the two high energy beams and targets description. These paragraphs will be followed by the detail of the diagnostics.

The fourth chapter will be dedicated to the data analysis, the results and the interpretation of the experimental records. I will first describe the method I followed for the analysis of interferometric records. Subsequently, the results obtained from a few representative records for Xe, Ar and Kr will be discussed in details. Complementary 1D simulations, performed with initial conditions similar to that in the experiment will be shown and help to interpret the experimental results. Finally, the results of XUV spectroscopy diagnostics will be presented.

In the fifth chapter, I will present the calibration of a table top electromagnetic plasma generator, which is able to launch supersonic shocks up to ~ 40 km/s speed at static pressures of few mbar. The results of this cali-

bration will also be presented and a comparison with 3-D MHD simulations will be performed. The diagnostics, which have been implemented, will be presented to illustrate the model as well as preliminary records of the plasma speed.

The final chapter of the thesis is dedicated to the summary of this work, together with perspectives for the follow-up of these experiments.

1.3 My contribution

I joined Ph.D. on November 12, 2013, under the supervision of Dr. Jean Larour and Dr. Chantal Stehlé. My Ph.D. thesis is comprised of two parts: the first part of the work is to study the laser-driven shocks. The second part of my thesis is to study the electromagnetically launched strong shocks.

Concerning the laser-driven shocks, I have started to work on the analysis and interpretation of XUV images recorded previously during an experimental campaign conducted at the Prague Asterix Laser System (PALS) facility in 2011. This enabled me to estimate the local opacity by employing Abel inversion. Although, this work not presented in this thesis, it shed light on the basic understanding of radiative shock as seen in the experiments as well as the knowledge of experimental setups. Later in April - May 2015, I have participated in a five weeks experimental campaign on PALS laser facility in Prague, which was dedicated to the study of the spectroscopic and interferometric signatures of laser-produced shocks. Especially the experiment was designed to study the physics during the collision of counter-propagating shocks. In the preparation of this campaign, I became acquainted with the instruments and the targets to be used as well as prepared a master report containing all the crucial aspects of the experiment to be referred by all the participants during the experiments. During the campaign, we have performed around 55 shots corresponding to different gases (Xenon, Argon, Helium, and Krypton) at different pressure and used three types of diagnostics i.e. visible interferometry, visible spectroscopy, and XUV spectroscopy. In this experiment particularly, I was in charge of the target selection, its installation in the experimental chamber, gas filling, preparing logbook, recording of the visible spectroscopy data from the control room, quick data analysis for the spot size, shock speed from interferometry data etc. In addition, I have worked on spectroscopic and interferometric data analysis recorded during the experiment. Next, in order to interpret the experimental results, I have performed several 1D hydrodynamic simulations with varying input conditions. In parallel, I have also performed simulations for another experiment performed by my collaborators at ORION laser facility in the United Kingdom. However, I have not presented this work in this thesis. Based on the results obtained from my analysis of records obtained from the PALS experiments in 2015, grabbing the opportunity, we have planned

and participated to a complementary experimental campaign at PALS in September 2016. The analysis of data recorded during experiments is still under progress and forms the future scope of the thesis.

The second part of my thesis has been comprised of the study of shock launched through the electromagnetic generator setup. In this, I have worked on the optimization of the design of the electric generator in view of the required shock parameters. Moreover, I have derived various shock characteristics viz. radial discharge layer, namely speed, mass, acceleration etc. at the different positions of its propagation. In present, a upgraded electric generator with new diagnostics is ready to perform the new experiments.

Radiative shock waves

Contents

2.1	Rankine-Hugoniot(R-H) relations	6
2.1.1	Jump relations for a real gas	9
2.1.2	Effect of radiation on shock waves	11
2.1.3	Radiative hydrodynamics equations	13
2.2	Radiative shock regimes	15
2.2.1	Typical radiative shock waves with a precursor	16
2.3	Radiative shock waves experiments	16
2.3.1	Laser-driven shock experiments	18
2.3.2	Electromagnetically launched shock	21

Small-amplitude disturbances in a medium often take the form of linear waves. On the contrary, strong disturbances, generally produced by processes such as explosions, lightning, supersonic movements of bodies, powerful electric discharges etc., where the fluid properties change rapidly, generate nonlinear waves like shock waves. As a consequence of shock waves, the flow moves faster than the sound speed. A shock is characterized by a sudden increase in the density and velocity of the medium. The Mach number (M) is commonly used to characterize the strength of the shock. This number defined as the ratio of the shock speed to the speed of sound in the upstream medium in which the shock propagates.

Radiative shock waves are hypersonic shock waves, which are heated to high temperature and, as a consequence, become the source of intense radiation. This radiation, in turn, modifies the dynamics and structure of the shock itself, which makes its structure more complicated. Radiative shock waves occur in several astrophysical circumstances such as in the accretion shock of protostellar formation (Stahler, Palla, and Salpeter, 1986), the supernova explosion and the interaction of their remnants with the dense interstellar medium (Chevalier, 1977), the bow shocks at the head of stellar jets (Hartigan *et al.*, 2001).

Radiative shock waves can now be studied in the laboratory, which allows to compare the data with models existing in the literature and to check the ability of the numerical codes to reproduce them (see for instance Bouquet *et al.* (2004); Leygnac *et al.* (2006)). The experimental study of radiative

shock characteristics is crucial in understanding these various energetic processes occurring in the astrophysical plasmas. In this chapter, I will first present a short summary of the jump conditions (Rankine-Hugoniot relations) for the simple case of an ideal gas, which rely on the values of the thermodynamical quantities on both sides of the discontinuity. Next, I will present the role played by the ionisation and excitation of the gas and then the role played by the radiation energy and pressure. The description of the different regimes of radiative shocks, which depend on the opacity of medium and can be characterized by the presence or absence of a radiative precursor, will follow. Further, I will give a brief overview of the literature focusing on the generation of radiative shocks in the laboratory, and I will present the motivations and objectives of my work.

2.1 Rankine-Hugoniot(R-H) relations

Let us consider a one-dimensional shock propagating in a gas at rest with the speed u_s . In the frame associated with the shock front, the pre-shock (upstream) fluid velocity is then $u_1 = -u_s$, while, behind the shock (post-shock or downstream region), this velocity is u_2 , as shown in the Fig. 2.1.

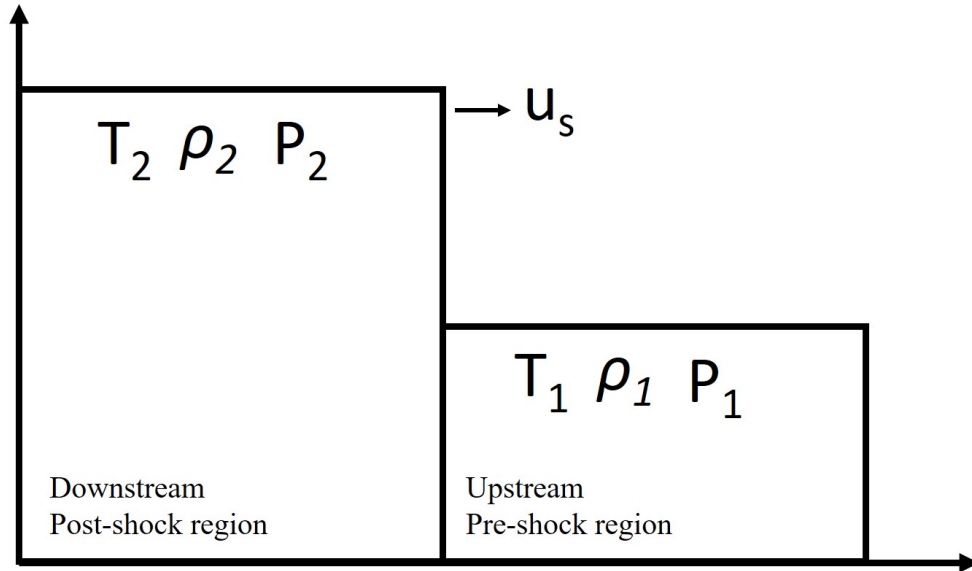


Figure 2.1: Schematic diagram for a 1-D shock moving in the x direction. The speed of the shock front is u_s . In the frame of reference of the shock front, the pre-shock region has a relative speed $u_1 = -u_s$, density ρ_1 , total pressure P_1 , temperature T_1 , whereas these quantities are respectively u_2 , ρ_2 , P_2 and T_2 for the post-shock region.

Assuming that a stationary state is reached, the conditions which determine the post-shock thermodynamical quantities are the well known Rankine-

Hugoniot equations (Macquorn Rankine, 1870; Hugoniot, 1887, 1889). Deduced from the Euler equations, these conservation equations for the mass, momentum, and energy are given by:

$$\rho_2 u_2 = \rho_1 u_1 \quad (2.1)$$

$$\rho_2 u_2^2 + P_2 = \rho_1 u_1^2 + P_1 \quad (2.2)$$

$$u_2 \left(\varepsilon_2 + \frac{P_2}{\rho_2} \right) + \frac{1}{2} u_2^3 = u_1 \left(\varepsilon_1 + \frac{P_1}{\rho_1} \right) + \frac{1}{2} u_1^3 \quad (2.3)$$

where, ε_1 and ε_2 are the specific internal energies (energy per unit mass) in the two (upstream and downstream) regions.

For an ideal gas of atomic mass $m = m_P A$ (m_P proton mass, A atomic number) and having an adiabatic index γ , the speed of sound is given by

$$C_s = \sqrt{\frac{\gamma P}{\rho}} = \sqrt{\frac{\gamma k_B T}{m}} \quad (2.4)$$

and the Mach number (M) of the shock is then,

$$M = \frac{u_1}{C_{s,1}} \quad (2.5)$$

Inserting these the aforementioned form of M and C_s in the equations 2.1, 2.2 and 2.3, we can derive the compression, pressure and temperature ratios for the system as follows,

$$\frac{\rho_2}{\rho_1} = \frac{u_1}{u_2} = \frac{M^2(\gamma + 1)}{2 + M^2(\gamma - 1)} \quad (2.6)$$

$$\frac{P_2}{P_1} = \frac{2M^2\gamma - (\gamma - 1)}{(\gamma + 1)} \quad (2.7)$$

$$\frac{T_2}{T_1} = \frac{P_2 \rho_1}{P_1 \rho_2} = \frac{(2M^2\gamma - (\gamma - 1))(2 + M^2(\gamma - 1))}{M^2(\gamma + 1)^2} \quad (2.8)$$

Considering the case of strong shocks, where M may be considered to be $\gg 1$, these equations become:

$$\frac{\rho_2}{\rho_1} = \frac{(\gamma + 1)}{(\gamma - 1)} \quad (2.9)$$

$$\frac{T_2}{T_1} = \frac{2M^2\gamma(\gamma - 1)}{(\gamma + 1)^2} \quad (2.10)$$

$$k_B T_2 = \frac{2(\gamma - 1)}{(\gamma + 1)^2} m u_s^2 \quad (2.11)$$

For mono-atomic gases, $\gamma = 5/3$, the compression ratio is estimated to be 4, and the post-shock temperature is

$$k_B T_2 = \frac{3}{16} m u_1^2 = \frac{3}{16} m_P A u_1^2 \quad (2.12)$$

Temperature is thus proportional to the square of the shock velocity and to the atomic mass. Therefore, to achieve a high temperature in the radiative shock experiment we often use high atomic number and mass gases. For Xenon, ($A=131.29$), the post-shock temperature is then equal to $T_2 = 0.257 u_1^2$ (eV, km/s), which, for instance, gives ~ 520 eV for a shock propagating at 45 km/s (see Fig. 2.2).

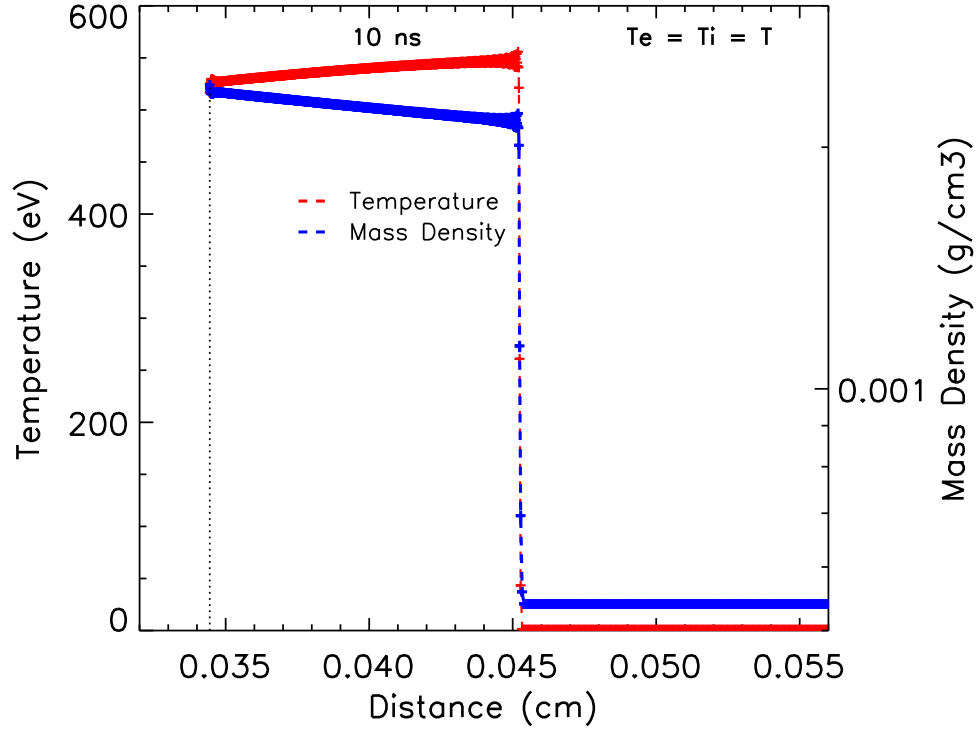


Figure 2.2: Profiles of temperature ($T_e = T_i = T$) and mass density (ρ) at 10 ns for a shock propagating in Xenon at 0.1 bar ($\rho_1 = 5.7 \times 10^{-4}$ g/cm $^{-3}$), with a speed of ~ 45 km/s. It is to note that the given pressure value are at 298 K. The simulation is performed with the HELIOS code, excluding the radiation effect, and for a polytropic gas ($\gamma=5/3$). The initial temperature of Xenon is set to 1 eV and with a negligible (10^{-5} W/m/K) thermal conductivity. The Mach number is then equal to 40. For this simulation, the shock is launched by a 100 μ m thick Aluminium piston moving at the velocity of 33 km/s. The position $x=0$ corresponds to the position of the Xe/Al interface at time $t=0$.

2.1.1 Jump relations for a real gas

In contrast to the discussion on ideal gas presented in the previous section, the case of a real gas is a little more complicated. It is to note that in this case, a part of the kinetic energy is used to excite and ionize the post-shock gas. As a result, its temperature is lower than that for the case of ideal gas. In addition, the pressure is also modified due to ionisation (Michaut *et al.*, 2004), as discussed below.

Let us now define j as the ionization stage of the atom (varying between 0 and z) and i to be the atomic state in this ionisation stage. We shall denote by \mathcal{P}_j & $\mathcal{P}_{j,i}$ the fractional ionization of the ion and the population of the atomic state i in the j th ionization stage, respectively. Then, the mean ionization stage (average charge) per atom can be written as,

$$\bar{z} = \sum_{j=0}^z j \mathcal{P}_j \quad (2.13)$$

and the excitation energy (including ionization) per atom and per unit of mass is

$$\epsilon_{\text{exc}} = \frac{\sum_{j=0}^z \sum_i \mathcal{P}_{j,i} E_{j,i}}{m_p A} \quad (2.14)$$

where $E_{j,i}$ is the energy of the ionisation stage j in the atomic stage i

Thus, the total pressure of gas can be written as,

$$P = P_i + P_e \quad (2.15)$$

where, P_i and P_e are the ionic and electronic pressures contributions.

Using the charge neutrality condition $N_e = \bar{z} N_i$, this gives:

$$P = N_i(1 + \bar{z}) k_B T = \rho \frac{k_B T}{m} (1 + \bar{z}) \quad (2.16)$$

The thermal pressure and enthalpy of the real gas are given by,

$$P_{th} = \rho \frac{(1 + \bar{z})}{m} k_B T \quad (2.17)$$

$$h = \frac{5}{2} \frac{(1 + \bar{z})}{m} k_B T + \epsilon_{\text{exc}} \quad (2.18)$$

Next, the speed of sound, including the effect of ionization with the average charge \bar{z} in the medium is now modified by ionisation:

$$C_s \simeq \sqrt{\frac{5}{3} \frac{\gamma(\bar{z} + 1) k_B T}{m}} \quad (2.19)$$

Thus, the continuity relations in the frame moving with the shock front become:

$$\rho_2 u_2 = \rho_1 u_1 \quad (2.20)$$

$$\rho_2 u_2^2 + \rho_2 \frac{k_B T_2}{m} (1 + \bar{z}_2) = \rho_1 u_1^2 + \rho_1 \frac{k_B T_1}{m} (1 + \bar{z}_1) \quad (2.21)$$

$$\rho_2 u_2 \left[\frac{5}{2} \frac{(1 + \bar{z}_2)}{m} k_B T_2 + \epsilon_{\text{exc}_2} + \frac{u_2^2}{2} \right] = \rho_1 u_1 \left[\frac{5}{2} \frac{(1 + \bar{z}_1)}{m} k_B T_1 + \epsilon_{\text{exc}_1} + \frac{u_1^2}{2} \right] \quad (2.22)$$

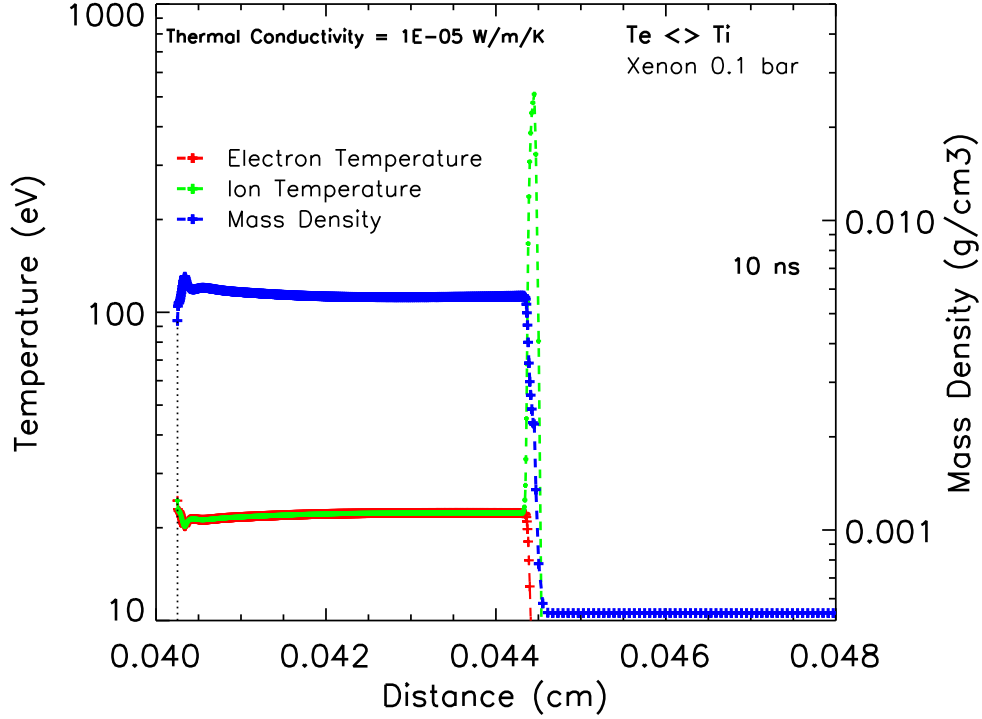


Figure 2.3: Electron temperature (T_e), ion temperature (T_i) and mass density (ρ) profiles at 10 ns, derived from 1-D simulation for the case of ionisation (no radiation). The shock propagates in Xe gas at 0.1 bar ($\rho_1 = 5.7 \times 10^{-4} \text{ g/cm}^3$ by $\sim 45 \text{ km/s}$). It is to note that the given pressure value is at 298 K. The simulation is performed with the HELIOS ($T_e \neq T_i$ case), using the PROPACEOS equation of state, without any radiation and with a negligible thermal conductivity (10^{-05} W/m/K). The initial temperature in Xenon is set to 1 eV and thus the Mach number is equal to 40. For this simulation, the shock is launched by a $100 \mu\text{m}$ thick Aluminium piston moving at the velocity of 38 km/s . The position $x=0$ corresponds to the position of the Xe/Al interface at time $t=0$.

Similar to the Fig. 2.2, however for the case of a real gas, the Fig. 2.3 shows the variation the electron and ion temperatures, as well as the mass density with the distance for a shock propagating in Xenon at $\sim 45 \text{ km/s}$. Now, the post-shock electron temperature peaks at 22 eV, which is much smaller than the maximum temperature of the ions (510 eV). The compression is now equal to 10 instead of 4 as in the previous case. The ions

are heated first in the shock through ion-ion collisions. This ion temperature decreases and the electron temperature increases as a consequence of the electron-ion collisions. The two temperatures thus become equal. Since the momentum change of the ions require only a few number of kinetic collisions, the thickness of the abrupt transition between the pre-shock and the post-shock is of the order of a mean free path of the ions.

It should be noted that, for shocks propagating with very high speed, the post-shock temperature is so high that the compressed gas is fully ionized. Therefore, the effects of ionisation and excitation become negligible and hence the compression ratio reaches 4 as in the case of the adiabatic shock.

2.1.2 Effect of radiation on shock waves

In the previous section, the effects of radiation heating and cooling have been neglected. However, the radiation emitted in a strong shock will affect its structure. These effects can be determined using mass, momentum, and energy conservation equations, which now have to include the contributions of the radiative flux, energy, and pressure. To this purpose, and with some simplifications, we can use the same approach than in section 2.1, still assuming that the shock is stationary.

Jump relations with radiation

Let us consider a stationary shock propagating in an atomic gas far away from the discontinuity. The medium is then optically thick and we can neglect the contribution of the radiative flux. Let us also assume that the medium is at LTE and that the radiation pressure and energy may be described as follows:

$$P_{\text{rad}} = \frac{1}{3}E_{\text{rad}} = \frac{4}{3c}\sigma T^4 = \frac{1}{3}a_{\text{rad}}T^4 \quad (2.23)$$

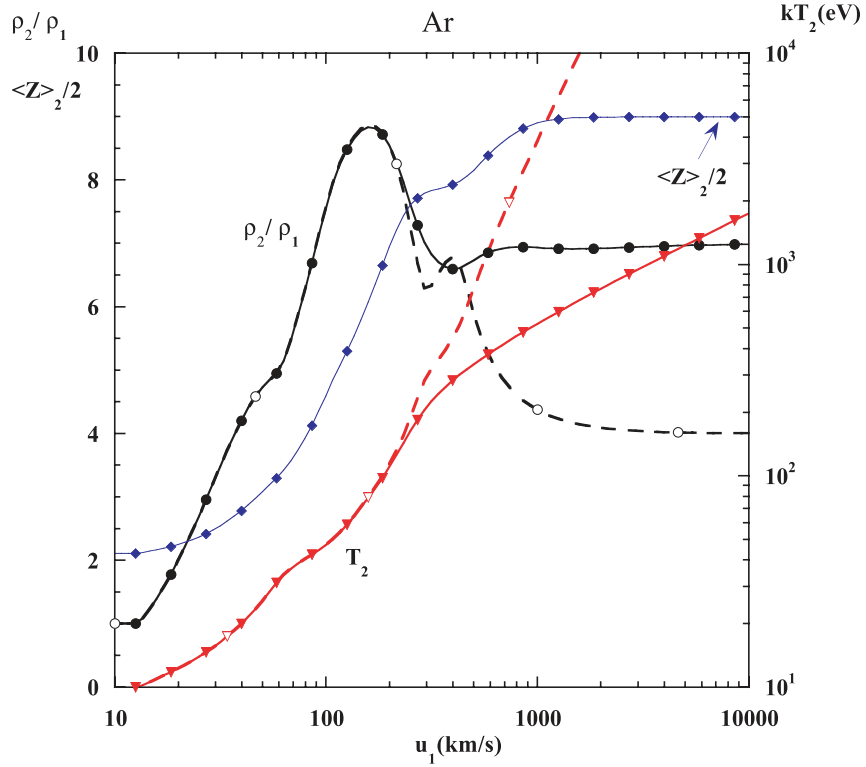
where a_{rad} is the radiation density constant and T is the shock radiation temperature, which we shall suppose to be equal to the electron temperature.

Following Michaut *et al.* (2004), the new jump conditions across the shock discontinuity become:

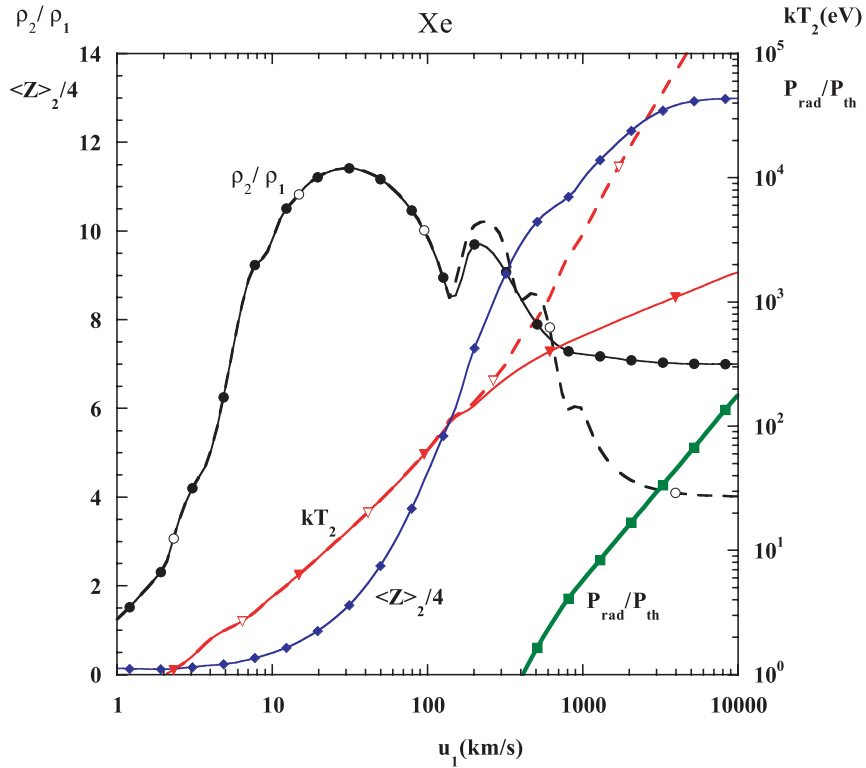
$$\rho_2 u_2 = \rho_1 u_1 \quad (2.24)$$

$$\rho_2 u_2^2 + \rho_2 \frac{k_B T_2}{m} (1 + \bar{z}_2) + \frac{1}{3} a_{\text{rad}} T_2^4 = \rho_1 u_1^2 + \rho_1 \frac{k_B T_1}{m} (1 + \bar{z}_1) + \frac{1}{3} a_{\text{rad}} T_1^4 \quad (2.25)$$

$$\begin{aligned} \rho_2 u_2 \left(\frac{5}{2} \frac{(1 + \bar{z}_2)}{m} k_B T_2 + \epsilon_{\text{exc}_2} + \frac{u_2^2}{2} \right) + \frac{4}{3} a_{\text{rad}} T_2^4 u_2 = \\ \rho_1 u_1 \left(\frac{5}{2} \frac{(1 + \bar{z}_1)}{m} k_B T_1 + \epsilon_{\text{exc}_1} + \frac{u_1^2}{2} \right) + \frac{4}{3} a_{\text{rad}} T_1^4 u_1 \end{aligned} \quad (2.26)$$



(a)



(b)

Figure 2.4: Figure 14 & 17 of Michaut *et al.* (2004) (a): Compression ρ_2/ρ_1 (full circles, thin line), kT_2 in eV (inverted full triangles, thin line) in Argon (a)/ Xenon (b) for initial conditions kT_1 ($= 10$ eV for Ar and $= 0.1$ eV for Xe), $\rho_1 = 5 \times 10^{-4}$ g/cm³, versus shock speed in km/s, with (full markers, full lines) and without (empty markers, dashed lines) radiation. The ionization stage $\langle z \rangle_2$ is plotted with the diamond symbol.

In the radiative regime, the compression ratio ρ_2/ρ_1 approaches to the value of 7 at very high velocities (several hundred of km/s) whereas it is equal to 4 when the effects of radiation energy and pressure have been neglected. This limit is the same for the cases of adiabatic (Bouquet, Teyssier, and Chieze, 2000) as well as the real gas (Michaut *et al.*, 2004). This is due to the fact that, at very high velocities, the medium becomes fully ionized and behaves as a perfect gas. On the contrary, in the comparatively "low" velocity regime, the effect of ionisation and excitation dominates the radiation effects. This is illustrated in Fig. 2.4, taken from Michaut *et al.* (2004) which reports the variations of the Ar and Xe compression ratio versus the shock speed for an initial mass density of 5×10^{-4} g/cm³. At 50 km/s, the compression ratio and the temperature are respectively equal to (5, 32eV) and (11, 30 eV) for Argon and Xenon.

The compression ratio shows bumps for high velocities. These bumps may be attributed to the fact that, as the temperature of the post-shock increases with the velocity, the atom ionises more and more. Thus the external shells in its ionic atomic structure are successively opened, inducing a strong variation in the excitation energy.

The post-shock temperature is very high for the very high-speed shocks. In such cases, the compressed gas is fully ionized and the effects of ionisation and excitation remain negligible like in the adiabatic case. It should be noted that below 100 - 200 km/s, the effects of radiation pressure remain negligible. Thus very energetic lasers like LMJ or NIF are required to reach a domain where this effect can be observed.

Thus, whereas for the range of velocities of 20 - 50 km/s covered by my study, the effects of radiative energy and pressure can be neglected, this is not the case for the radiative flux, which has been neglected in the previous sections, and which may become comparable to the material energy flux. Its effect on the system must be taken into account, as will be shown below.

2.1.3 Radiative hydrodynamics equations

To include the contributions of radiation, it is compulsory to introduce the relevant terms in the fluid equations. The propagation of the radiation in the matter is governed by the processes of absorption and emission of photons, which respectively heats and cools the medium. As the mean free path of photons is always higher than the mean free path of particles, the shock structure is more influenced by the radiative transfer than the viscosity of the fluid.

The propagation of radiation in the matter is described by the radiative transfer equation:

$$\left(\frac{1}{c} \frac{\partial}{\partial t} + \frac{\partial}{\partial s}\right) I(\mathbf{r}, \mathbf{n}, \nu, t) = \eta(\mathbf{r}, \nu) - \chi(\mathbf{r}, \nu) I(\mathbf{r}, \mathbf{n}, \nu, t) \quad (2.27)$$

where $\chi(\rho, \nu, T)$ and $\eta(\rho, \nu, T)$ are respectively the monochromatic opacity and emissivity of the gas.

The specific intensity $I(\mathbf{r}, \mathbf{n}, \nu, t)$ ($\text{erg cm}^{-2} \text{s}^{-1} \text{Hz}^{-1} \text{sr}^{-1}$) is the energy radiated per units of surface area, time, frequency and solid angle, in the direction \mathbf{n} .

The radiative energy density E_{rad} , flux F_{rad} and pressure P_{rad} are respectively defined as the zero, first and second moments of the specific intensity versus the angle, after integration over the photon frequency ν :

$$E_{rad} = \frac{1}{c} \int \oint I(\mathbf{r}, \mathbf{n}, \nu, t) d\Omega d\nu \quad (2.28)$$

$$F_{rad} = \int \oint I(\mathbf{r}, \mathbf{n}, \nu, t) \cos \theta d\Omega d\nu \quad (2.29)$$

$$P_{rad} = \frac{1}{c} \int \oint I(\mathbf{r}, \mathbf{n}, \nu, t) \cos^2 \theta d\Omega d\nu \quad (2.30)$$

$$(2.31)$$

Taking into account radiative effects, the equations of radiative hydrodynamics in the co-moving frame of the shock (Mihalas and Mihalas, 1999; Drake, 2006) can be written as

$$\frac{\partial \rho}{\partial t} = -\nabla \cdot (\rho \mathbf{u}) \quad (2.32)$$

$$\rho \left(\frac{\partial \mathbf{u}}{\partial t} + \mathbf{u} \cdot \nabla \mathbf{u} \right) = -\nabla (P + P_{rad}) \quad (2.33)$$

$$\frac{\partial}{\partial t} \left(\frac{\rho u^2}{2} + \rho \epsilon + E_{rad} \right) + \nabla \cdot \left[\rho \mathbf{u} \left(\epsilon + \frac{u^2}{2} + \frac{P}{\rho} \right) + (E_{rad} + P_{rad}) \mathbf{u} \right] = -\nabla \cdot \mathbf{F}_{rad} \quad (2.34)$$

As mentioned previously, the contributions linked to P_{rad} and E_{rad} are effective only at very high temperature (i.e. velocity). However, for the radiative shocks of interest in this work, the contribution of the radiative flux F_{rad} is non-negligible compared to ρu^3 . These shocks are thus in the *radiation flux dominated regime*.

Most of the experimental shock waves are in this regime. These hydrodynamic equations are strongly non-linear. In the present work, the one-dimensional radiative-hydrodynamic code ‘HELIOS’ (MacFarlane, Golovkin, and Woodruff, 2006) has been employed to derive the physical parameters of the shock in various conditions as presented in the following section. HELIOS will be discussed in detail in the next chapter.

2.2 Radiative shock regimes

Radiative shocks are strong shocks (Mach number, $M \gg 1$), which attain high temperatures and thus are the source of intense radiation (Mihalas and Mihalas, 1984; Zel'dovich, Zel'dovich, and Raizer, 2002; Drake, 2006). Depending on the opacity, the radiation emitted from the shock may be absorbed by the pre-shock region, inducing its pre-heating. Far away from the discontinuity, the structure of the upstream medium is determined by the absorption. On its side, the structure of the transition layer of the downstream medium close to the discontinuity depends on the balance between the emission (cooling) and the absorption (heating). Thus the full structure of the shock mainly depends on the variation of the opacity χ (cm^2/g). The optical depth ($\tau(s)$), measured from the position of the jump, is then the relevant parameter for the absorption. It is given by

$$\tau(s) = \int_{s_{jump}}^s \chi(s') \rho(s') ds' \quad (2.35)$$

where s' characterizes the path of the radiation. As we are interested in the mean frequency averaged radiative flux, the relevant opacity here will be the averaged Rosseland opacity which will be defined in due course.

If $\tau \gg 1$, the regime is referred as optically thick, while in the opposite case ($\tau < 1$) it is optically thin. Flux dominated radiative shocks have been classified depending on the optical depth of upstream and downstream regimes.

An attempt of radiative shock classification has been performed by Drake (Drake (2006)) according to the optical the thickness of the upstream and downstream regimes, resulting in the definition of four different regimes, namely a thin-thick, thin-thin, thick-thick, thick-thin radiative shocks.

Following this author, a *thin-thick* type of radiative shock probably exists only in theory. In the case of a *thin-thin* radiative shocks both upstream and downstream regimes are optically thin, and the shock radiates away its energy in both directions. This regime of radiative shock is present in various astrophysical contexts, for instance, in the internal shocks of stellar jets (Hartigan, 2003). It is possible to generate these type of shocks in the laboratory in very low-density gases. In *thick-thick* radiative shocks, both upstream and downstream zones are optically thick. This regime occurs in the stellar interiors. The radiation coming from the hot downstream region heats the cooler upstream material and forms a precursor. The fourth regime is the *thick-thin* radiative shock, which is characterized by an optically thick downstream and an optically thin upstream region. The radiation from the heated downstream region passes ahead of the shock and creates a cooling layer in the downstream before reaching the final state. There is no absorption of the radiation in the upstream region and therefore, contrary to

the thick-thick case, there is no radiative precursor. Shocks generated in the laser experiments are usually between the thick-thick and thin-thin regimes.

2.2.1 Typical radiative shock waves with a precursor

The radiation from the post-shocked region just behind the shock passes ahead of the shock and generates the precursor. However, it also leads to a radiative cooling layer downstream that extension depends on the opacity. A typical structure of such shocks is presented in McClarren *et al.* (2010). In these cases, the compression in the cooling layer behind the shock is much higher than that in the hydrodynamic case. This kind of shock is most commonly generated in the laboratory experiments (Bozier *et al.*, 1986; Keiter *et al.*, 2002; Reighard *et al.*, 2006; Fleury *et al.*, 2002). In astrophysics, these shocks are present, for instance, in supernovae, when the blast wave emerges from the stellar interior (Ensmann and Burrows, 1992).

A detailed classification of the shocks presenting a radiative precursor is reported in several references (Zel'dovich, Zel'dovich, and Raizer, 2002; Ensmann, 1994; Vaytet *et al.*, 2013):

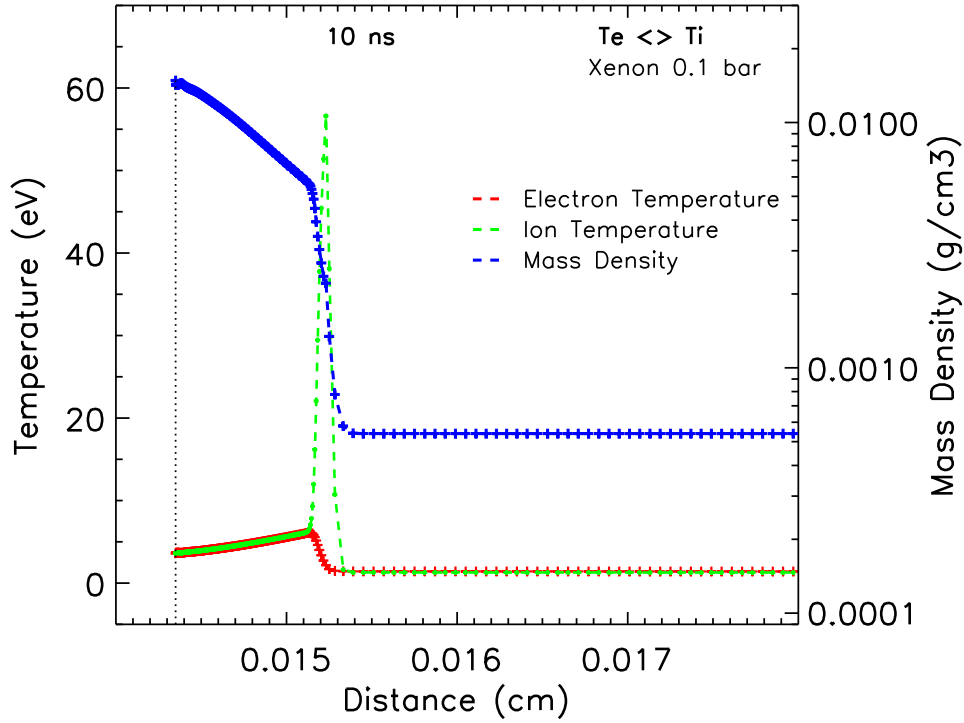
In the case of *sub-critical* shock, the temperature just ahead of the shock front is smaller than the post-shock temperature. Such shocks are relatively weak, and hence the radiative flux transfer from the post-shock to the pre-shock is small. A piston moving with a constant speed of 12 km/s in Xenon gas at 0.1 bar is able to generate such a sub-critical radiative shock. The resulting mass density and electron temperature profiles have been presented at 10 ns in the Fig. 2.5a.

The other regime of radiative shock is known as *supercritical*, in which the pre-shock and the final post-shock temperatures are the same. The mass density and electron temperature profiles of supercritical shock driven by a constant moving piston with speed 45 km/s in Xenon at 0.1 bar are presented in Fig. 2.5b.

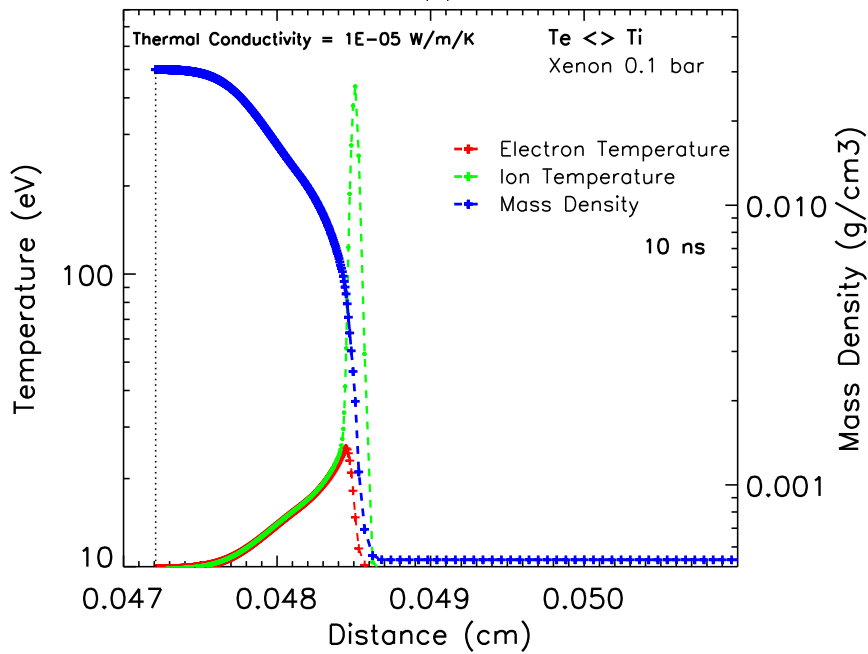
The speeds achieved in the PALS experiment range between $\sim 15 - 55$ km/s for pressure comprised between 0.1- 0.6. Our simulations indicate that, depending on the speeds, the regimes cover either the subcritical or supercritical cases.

2.3 Radiative shock waves experiments

Radiative shock waves have been studied experimentally for more than a decade on high-energy lasers, fast magnetic pinch machines, and pulsed power facilities. Such facilities are able to achieve strong shock conditions (high-temperature, high-pressure) over a very small volume and time. Various diagnostics are able to record the plasma conditions, which are then compared with the results of numerical simulations. The results of these experiments are also employed to validate numerical codes, some of them



(a)



(b)

Figure 2.5: Simulated electron temperature (T_e), ion temperature (T_i) and mass density (ρ) profiles at 10 ns of a radiative shock propagating with a 15 km/s (a: subcritical) and 48 km/s (b: supercritical). The shock is propagating in Xenon at 0.1 bar ($\rho = 5.4 \times 10^{-4} \text{ g/cm}^{-3}$, at 298 K). The initial temperature in Xenon is set to 1eV. The two Mach numbers are respectively equal to 13 and 43. The radiation and ionisation effects are included in the simulation which is performed for two different temperatures ($T_e \neq T_i$) and a negligible thermal conductivity (10^{-05} W/m/K). For this simulation, the shock is launched by a 100 μm thick Aluminium piston moving at the speed of 12 km/s and 45 km/s for case (a) and (b) respectively. The position $x=0$ corresponds to the position of the Xe/Al interface at time $t=0$.

being relevant to the astrophysics, like FLASH (Fryxell *et al.*, 2000) and HERACLES (González, Audit, and Huynh, 2007).

2.3.1 Laser-driven shock experiments

Most of laboratory experiments on radiative shocks have been performed on large-scale laser facilities (Bouquet *et al.*, 2004; Chaulagain *et al.*, 2015; González *et al.*, 2006; Reighard *et al.*, 2006; Stehlé *et al.*, 2010; Doss *et al.*, 2009; Drake *et al.*, 2011; Dizière *et al.*, 2011; Stehlé *et al.*, 2012), in noble gases, at pressures between 0.1 and 1 bar. With laser intensities on the target comprised between 10^{14} and 10^{15} W/cm², these experiments allowed to record shock speeds ranging between 40 and 150 km/s.

Bozier *et al.* (1986), for the first time, experimentally evidenced the generation of a radiative wave propagating ahead of a supercritical shock in xenon (pressure up to 6 bars) at the CEA's Limeil laser facilities (irradiance of 5×10^{14} Wcm⁻²). In this experiment, the laser beam (wavelength of 1.06 μ m, duration 1 ns) of 40 J energy was focused on an aluminum foil acting as a piston. A shock of speed ~ 50 km/s was produced in the gas. A visible streak camera was used to record the precursor emissivity over 10 ns.

Later, Keiter *et al.* (2002) performed a similar experiment at the OMEGA laser facility (2.5 kJ, 1ns, focal spot diameter 600 μ m), still in a planar geometry. The shock propagated here in a low-density SiO₂ aerogel foam ($\rho \sim 9.6$ mg/cm³). In this experiment, X-ray absorption spectroscopic data were recorded to qualitatively predict the temperature of the precursor.

In the year 2000 a new radiative shock experiment was performed, in Xenon at 0.2 bar, at the LULI laser facility (~ 100 J, $\lambda = 0.53$ μ m, $4-6 \times 10^{13}$ W cm⁻²) (Fleury *et al.* (2002); Bouquet *et al.* (2004)). This experiment used a three-layered piston, composed of: a thin polystyrene acting as ablator (2 μ m thick), a titanium foil (3 μ m), acting as x-ray shield, and a layer of a polyethylene foam (25 μ m) as an accelerator. Further, a VISAR (velocity interferometer system for any reflector), and a Mach - Zehnder interferometer were used as a diagnostics to measure the front shock speed and the precursor electron density. Two streak cameras recorded the shock propagation in longitudinal and transverse directions. *This was the first attempt to estimate electron density within the precursor.* Their measurements indicate an electron density ranging between $10^{18} - 10^{20}$ /cm³. The experimental results were in qualitative agreements with 1D numerical MULTI and FCI simulations. However, the speed of the precursor in these 1D simulations was too large. This was then explained later, when multidimensional effects were included in the simulations (Leygnac *et al.*, 2006; González, Audit, and Stehlé, 2009).

Complementary experiments were then performed by González *et al.* (2006) at the PALS laser facility (60 J, 0.35 ns, 438 nm, spot diameter 600 μ m, $\sim 7 \times 10^{13}$ W cm⁻²) in Xe gas. The goal was to study the shocks over longer

times and to inspect the effects of the walls albedo. A doubled layered piston, made of $10\ \mu\text{m}$ polystyrene and $0.5\ \mu\text{m}$ gold, was used. The precursor edge was recorded by shadowgraphy using a visible streak camera. The experimental results were compared with 2D numerical simulations performed with HERACLES (González, Audit, and Huynh, 2007). This comparison allowed quantifying the albedo of the walls. It also showed that the radiative losses at the walls lead to a small curvature of the ionization front and to a reduction of its longitudinal extension (Leygnac *et al.*, 2006; González, Audit, and Stehlé, 2009).

In parallel, another experiment was performed at the OMEGA laser facility ($0.35\ \mu\text{m}$, spot $\sim 700 - 800\ \mu\text{m}$, $\sim 2 \times 10^{15}\ \text{W cm}^{-2}$) by Reighardt *et al.* (Reighardt *et al.* (2006); Reighardt (2007)). *The shock was imaged by an X-ray back-lighter at different times, which enabled to inspect, for the first time, the shape of the shock front.* At higher speeds ($\sim 100\ \text{km/s}$), X-ray radiography pointed out a collapse of the post-shock (Reighardt *et al.*, 2006), which was attributed to the radiation losses through the shock front. For these high-speed conditions, the wall heating leads to the development of secondary wall shocks, interacting with the primary shock (Doss *et al.*, 2009). Such wall shocks have not yet been observed at lower speeds.

Subsequently, an experiment by Stehlé *et al.* (2010) was performed at PALS laser facility with the similar laser parameters as taken in Gonzalez *et al.* (2006). In this experiment, a Mach-Zehnder interferometer and a streak camera were used to record the shock propagation over 50 ns. Time-integrated XUV spectroscopic analysis between 16 and 22 nm of shock was performed. *The experiment showed that of a quasi-stationary regime was reached after 20 ns.*

The first experimental study in Argon gas was reported in 2012 by Visco *et al.* (2012) at OMEGA facility ($0.35\ \mu\text{m}$, spot $\sim 600\ \mu\text{m}$, $\sim 7 \times 10^{14}\ \text{W cm}^{-2}$). The electron temperatures in the radiative precursor and shock-front were measured to be 34 eV and 60 eV, respectively, using X-ray Thomson scattering diagnostic.

In addition, a new experiment at PALS (Jungwirth *et al.*, 2001) was presented by Chaulagain *et al.* (2015), *using, for the first time, a Zn x-ray laser for XUV imaging at 21 nm.* This diagnostic allowed imaging both the precursor and post-shock structure of radiative shocks in Xe gas at 0.3 bar. In this experiment, where the shock wave did not fill the tube, 2D effects became pronounced. The experimental results were successfully compared with the results of 2D ARWEN simulations (Cotelo *et al.*, 2015).

A summary of these different experiments and their principal diagnostics is presented in table 2.1.

Experiment	Laser facility	$I (\times 10^{13})$ W cm^{-2}	λ & τ $\mu\text{m}, \text{ns}$	ρ_0 mg cm^{-3}	u km s^{-1}	Principal diagnostics
Bozier <i>et al.</i> (1986)	CEA's Limeil	20-50	0.351, 1	10 -30	50-80	Visible streak Camera
Fleury <i>et al.</i> (2002)	LULI	5	0.53, 0.5	1	60-65	Visible streak Camera Visible interferometry VISAR
Keiter <i>et al.</i> (2002)	OMEGA	35- 85	0.351, 1	5 -15*	100	x-ray spectroscopy
González <i>et al.</i> (2006)	PALS	10-15	0.438, 0.35	1	65	Visible streak camera Visible interferometry
Reighard (2007)	OMEGA	70-100	0.35, 1	6	100-140	x-ray back-lighting VISAR
Stehlé <i>et al.</i> (2010)	PALS	10-20	1.315, 0.35	1	60	Visible Interferometry XUV spectrometer
Stehlé <i>et al.</i> (2012)	PALS	10-20	1.315, 0.35	1.5	50-55	XUV imaging XUV fast Si diodes
Visco <i>et al.</i> (2012)	OMEGA	70	0.35, 1	1.96**	100-150	x-ray Thomson Scatter- ring
Chaulagain <i>et al.</i> (2015)	PALS	10-20	1.315, 0.35	1.5	50	XUV fast Si diodes

Table 2.1: Summary of the radiative shocks experiments and outcomes in different laser installations. All the experiments are performed in Xe except Keiter *et al.* (2002) and Visco *et al.* (2012). In these two experiments, the first uses SiO_2^* and the second uses Ar^{**} as a shocked medium.

Laser driven radiative shocks: Goal of my thesis

All these experimental studies have been focused on the case of single radiative shocks propagating in a tube. However, in astrophysical conditions, radiative shocks often interact with a denser medium, leading to the development of reflected and transmitted shocks. A few representative examples of such phenomena are the interaction of supernovae remnants with dense molecular clouds (González, Audit, and Stehlé, 2009), the accretion shocks on the photosphere of T-Tauri stars (Orlando *et al.*, 2013) and the bow shocks at the head of stellar jets (Hartigan, 1989; Raga *et al.*, 1999). The collision (or the interaction) of two radiative shock waves is obviously a rare astrophysical event and the template case of supernova remnant DEM L316 (see Fig. 1 of Williams *et al.* (1997)) is still the subject of debates (Williams *et al.*, 2005; Toledo-Roy *et al.*, 2009; Velarde *et al.*, 2006) as the observation of these two different shocks can be also interpreted as the superposition of two blast waves in the field of view of the telescope. In this regard, the development of dedicated laboratory experiments to the study of propagation and interaction of counter-propagating shock waves is important as a tool to characterize such events through their specific signatures.

In this thesis, I will present the results of experiments performed at the Prague Asterix Laser System (PALS) facility (Jungwirth *et al.* (2001)) on the study of the interaction of two radiative shock waves. The experimental objectives were:

- To generate two shocks of different speeds propagating in opposite directions in the tube filled with Xenon gas at low pressure (< 1 bar) with speeds comprised between 12 and 55 km/s.
- To record the electron density by using Mach-Zehnder Interferometer over a duration comprised between 50 and 200 ns. This allowed studying the effect of precursor interaction on to the other one.
- To determine the temperature and the ion charge of gas, using a time and space integrated XUV emission spectroscopy.

The experimental results were interpreted with the help of one-dimensional simulations using the Lagrangian radiation hydrodynamic code HELIOS.

2.3.2 Electromagnetically launched shock by a compact pulsed power device

As discussed in the previous section, most of the plasma laboratory astrophysics studies are mainly performed on large-scale laser facilities, addressing pure hydrodynamic radiative shocks, at very high speed (50 - 150 km/s) and moderate pressure (0.1 - 1 bar). Complementary to laser experiments,

discharge produced plasma has also been a well-established method for generating the strong shocks (Kondo *et al.*, 2008, 2009a,b; Larour *et al.*, 2015). Such device presents a high flexibility and a larger repetition rate, which allows a deeper understanding of shock physics in conditions of astrophysical interest, for instance in the context of stellar jets.

In principle, a coaxial electrode pair filled with gas, followed by an intense electrical surface discharge generates a thin layer of plasma (plasma sheath) at the bottom of the electrode. Due to the high rising current in the plasma layer, a magnetic pressure is produced which accelerates the plasma layer, also termed as plasma focus (Gonzalez, Brollo, and Clausse, 2009). During this motion, the plasma sheath accretes a noticeable part of the background gas. Experiments performed by Serban and Lee (1995), in the light gasses H_2 , D_2 , have shown fast axial shock waves (100 km/s) but the plasma sheath was annular.

Later on, compact pulsed power electric generators were able to launch astrophysically relevant strong shocks in low-pressure noble gases (Kondo *et al.*, 2006). These authors reported shock of speed 45 km/s using conical coaxial electrodes and Xenon gas (0.06 - 11 mbar). The ion - electron energy transfer and ionization relaxation process, as also the radiation effect were investigated by Kondo *et al.* (2008, 2009a,b).

My work on electromagnetically launched shock experiment

My work, focusing on the electromagnetically launched strong shocks relevant for astrophysics, aimed to design and to optimize an electromagnetic generator, to be able to produce strong shocks in noble gasses at low pressures of few mbar. The electromagnetic generator is a powerful accelerating device which ejects a quasi-planar plasma sheath out of a set of coaxial conical electrodes where a pulsed 100-kA current is passing.

Due to the electrical discharge in the gas, a hot and fast moving plasma is generated which travels along the electrodes. The high-intensity currents produce a magnetic field of several Teslas which acts as a piston, accelerating an annular plasma sheath and driving a strong shock towards the top of the cone. I have employed a simple model to optimize the operation parameters. With such optimization, our electromagnetic generator should produce strong shocks over few nanoseconds.

Our preliminary experiments show that the generator is capable of launching supersonic shocks in Argon, in the form of a thin plasma layer with the speed of $\sim 1 - 30$ km/s. Three-dimensional MHD simulation, performed by A. Ciardi, is consistent with the first observations. This is presented in detail in the chapter 6 of the thesis.

1D Simulations

Contents

3.1	HELIOS	23
3.2	LTE approximation	24
	3.2.1 Mean opacity	25
	3.2.2 Equation of State	27
3.3	Single radiative shock waves	27
3.4	Interacting radiative shock waves	40
3.5	Summary	44

Radiative shocks are present in various astrophysical processes implying extreme conditions. Laboratory experiments then allow investigating the underlying physical processes, which take place in these conditions and which are not observable from the Earth due to a lack of spatial resolution of the telescopes/ instruments. However, experiments are not always straightforward to interpret and the help of numerical simulations becomes precious.

In this chapter, I will present, with the help of 1D radiative hydrodynamic simulations, a brief overview of the physics of isolated radiative shocks and of two interacting radiative counter-propagating shock waves.

3.1 HELIOS

Different numerical approaches are used for the simulation of laboratory plasmas. Some of them use fixed grids. Other introduce the possibility of refinement (on the fly) in some meshes (Adaptative Mesh Refinement), to maintain a good resolution in the interesting parts of the plasma. Another approach is based on meshes following the fluid (Lagrangian description), which means that the meshes move with the fluid and no matter may go through a mesh to another. The form of the equations differ in this case (see for instance Orban *et al.* (2013)).

HELIOS is such a one-dimensional Lagrangian radiation hydrodynamic commercial code (MacFarlane, Golovkin, and Woodruff, 2006) and I have used it to simulate our experiment of interacting shock waves. This code is easy to handle and has the presently interesting capability to be able to simulate the case of two shock waves propagating in opposite directions and launched by two different lasers. HELIOS may describe non-LTE plasmas as

it includes an in-line collisional radiative (HELIOS-CR) model for computing non-LTE atomic level populations at each time step of the hydrodynamics simulation. However, I used HELIOS in the LTE approximation, which is appropriate to our experimental conditions (Rodriguez *et al.*, 2011), as will be discussed in the next section.

The code solves the fluid equations of motion using the pressure contributions of electrons, ions, and radiation. It may describe the electrons and ions as two interacting fluids at respective temperatures T_e and T_i . Thermal conduction is described within a flux-limited electron conduction model based on the Spitzer conductivity (Burhop and Spitzer, 1957) and the laser energy deposition is computed with an inverse Bremsstrahlung model (?).

The radiation emission and absorption terms are introduced in the equation of energy for the electrons and in the radiation transport equations. One of the methods, which are proposed, is the flux-limited, multi-group radiation diffusion model (González *et al.*, 2015), where the radiative flux is proportional to the gradient of the radiative energy and is inversely proportional to the Rosseland opacity (Dobbs-Dixon, Cumming, and Lin, 2010). The expression is pondered by a flux-limited diffusion coefficient in order to obtain the good optically thin limit. This coefficient follows the Larsen expression described in Olson, Auer, and Hall (2000). The second method is a (time independent) multi-angle short-characteristics scheme. In our case, where radiation and hydrodynamics are strongly coupled and thus the radiation field varies rapidly, we used the diffusion model together with LTE Planck and Rosseland multi-groups opacities.

In addition, our version of HELIOS uses the PROPACEOS (MacFarlane, Golovkin, and Woodruff, 2006) Equation of State (EOS) and multi-group opacity tables, which are generated by the code¹ and it is not possible to include any other opacity or EOS table.

3.2 Local Thermodynamic Equilibrium

The knowledge of the thermodynamical conditions is required for an adequate simulation of the plasma description.

The Local Thermodynamic Equilibrium (LTE) regime is valid at large electron densities. In that case, the collisions between the electrons and the ions and atoms are so frequent that they maintain, at each time, a steady-state populations of ions. Moreover, within a given ionic stage, the populations of the different energy levels follow the Boltzmann equilibrium and the populations of the different ions the Saha-Boltzmann equation (Fadeyev and Gillet, 2001).

On the contrary, in the case of Non Local Thermodynamic Equilibrium (NLTE) regime, one has to take into account the excitation/deexcitation

¹see <http://www.prism-cs.com/Software/PROPACEOS>

induced by the electron collisions and various radiative processes. This leads to a set of differential time dependent equations (rate equations), which has to be solved through an adequate Collisional Radiative model (CR) (Kunze, 2009)

Therefore, it is crucial to determine if the regime is LTE or NLTE. A criterium is given by Griem (2005).

In our experiment the mass density ranges between $\sim 10^{-4}$ and 10^{-1} g/cm³, while the temperature values are comprised between ~ 0 to 50 eV. The precise calculations performed by Rodriguez et al. (Fig2 of Rodriguez *et al.* (2011)) for Xenon, indicate that the thermodynamical conditions of our radiative shock experiments correspond to the LTE regime.

3.2.1 Mean opacity

The opacity is a fundamental ingredient of the radiative transfer equations, which provide the specific intensity and its moments (radiative flux, energy, and pressure). These last ones enter in the fluid equations (see section 2.1.3 in chapter 2). The coupling of the fluid equations with the radiative transfer equation is demanding in terms of computational resources and most of the codes use simplified radiation transport equations, which require the knowledge of adequate frequency averaged opacity coefficients. The form of the average of the opacity is not obvious, as the average has to be done on the radiative flux or energy, which are unknown before the computation. Then the commonly used opacities are the Planck and Rosseland mean opacities (Mihalas, 1978; Seaton, 1987)

The *Rosseland mean opacity* (κ_R in cm⁻¹ and $\chi_R = \kappa_R/\rho$ in cm²/g) is derived by considering harmonic weighting over the temperature derivative of the Planck function. It gives the correct radiative flux in the optically thick diffusion limit. The average is performed over the total monochromatic opacity $\kappa_\nu^{tot} = \kappa_\nu^{abs} + \kappa_\nu^{scat}$ (in cm⁻¹), where, in the present case, the scattering contribution comes from the electron Thomson scattering,

$$\frac{1}{\kappa_R} = \frac{\int_0^\infty \frac{1}{\kappa_\nu^{tot}} \frac{dB_\nu}{dT} d\nu}{\int_0^\infty \frac{dB_\nu}{dT} d\nu} \quad (3.1)$$

The *Planck mean opacity* (κ_P in cm⁻¹ and $\chi_P = \kappa_P/\rho$ in cm²/g) employs the normalized Planck blackbody energy density distribution as a weighting factor. It will give the correct value for the integrated thermal LTE emission of an optically thin plasma and is expressed as:

$$\kappa_P = \frac{\int_0^\infty \kappa_\nu^{abs} B_\nu d\nu}{\int_0^\infty B_\nu d\nu} \quad (3.2)$$

In the multi-groups description, the radiation transport takes into account the propagation of radiation in N different wavelength bands ($\nu_k - \nu_{k+1}$, $k = 1, N$). Hence, for instance, the medium may be transparent for

some wavelengths and opaque for other ones. The radiation transport equations split into N contributions, each of them being associated to adequate opacity coefficients. The expression of the coefficients is similar to the previous “grey” case ($N = 1$), except that the integrals are performed between the boundary frequencies of the group.

In HELIOS, the monochromatic opacities κ_ν are computed for the different radiation groups using the ATBASE atomic suite of codes. Energy levels and other atomic data relevant for bound-bound and bound-free transitions are computed within a configuration interaction model using Hartree-Fock wave-functions (MacFarlane, Golovkin, and Woodruff, 2006).

Dividing the opacity by the mass density reduces the variation of this quantity with ρ . The literature then often uses the mass absorption coefficient (also termed as *opacity*), which is defined as :

$$\chi_\nu = \kappa_\nu / \rho, \quad (3.3)$$

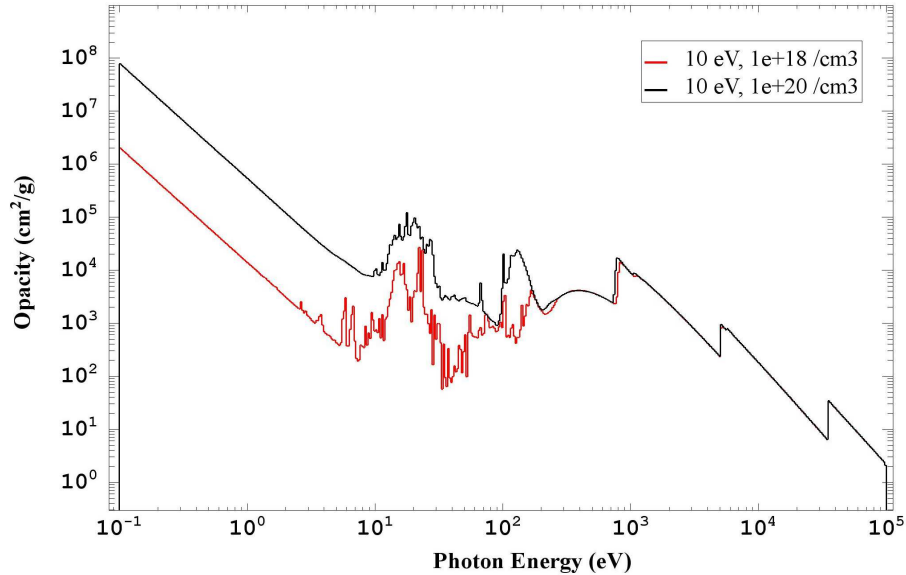


Figure 3.1: PROPACEOS Monochromatic opacity versus the photon energy in eV of Xenon at 10 eV and at two electron densities respectively equal to 10^{18} and 10^{20} cm^{-3} .

An example of the variations of the PROPACEOS opacity χ_ν versus the frequency in eV is given in Fig. 3.10a for Xenon at 10 eV and two electron densities respectively equal to 10^{18} and 10^{20} cm^{-3} , which do correspond to typical conditions of the precursor and post-shock of our laser generated radiative shocks.

3.2.2 Equation of State

The equation of state (EOS) defines the dependence of the pressure, ionisation, internal energy with the mass density and temperature. Several models do exist in the literature.

Our version of HELIOS for LTE plasmas may handle polytropic or PROPACEOS equation of state. Unfortunately, there are not many details about this last method. The authors of the code mention that it uses a QEOS-type model (More *et al.*, 1988) in the strong coupling regime (i.e., at relatively high densities and low temperatures), and an isolated atom model, which uses a detailed atomic structure modeling in the weak coupling region. The properties between the weak and strong coupling regimes are said to be obtained by interpolating in a thermodynamically consistent manner. This EOS includes the contributions from the translation of ions and electrons, electron degeneracy, atom ionization and excitation, and Coulomb interactions (Debye - Huckel correction).

Comparisons on specific cases have been performed by the authors of the code with Los Alamos SESAME data for CH, Al, and Au, showing a good agreement when using these two equations of state.

In this chapter, HELIOS code will then be employed to simulate the detailed characteristics of single and counter-propagating radiative shocks, driven by one or two lasers, in the conditions of our experiments (Chapter 5). The target cell (4-mm length) is filled with Xenon gas at 0.1 bar. This value of pressure is representative and correspond to standard ambient temperature i.e. 298 K and not the initial temperature considered in the simulations. This terminology is maintained throughout the thesis. Two lasers are interacting, at both ends, with two gold-coated ‘CH’ foils (11 μm CH and 0.6 μm Au), each of them resulting in a piston of total thickness 11.6 μm closing the cell.

3.3 Single radiative shock waves

Typical simulations of the radiative shocks, especially multidimensional ones which are time-consuming, use a frequency independent (grey, or one group) opacities. However, then the opacity of the gas under investigation presents strong variations with the frequency, a multi-group approach may be suitable (Vaytet *et al.*, 2011, 2013). When the number N of groups tends to infinity, each group opacity κ_R^k and κ_P^k tends to the local monochromatic opacity κ_ν , which solves the question of the adequate opacity average.

In the following, I will investigate the influence of the opacity and the number of groups on the structure of a shock wave propagating at ~ 50 km/s in Xenon at 0.1 bar. To this purpose, I have performed HELIOS simulations for a laser of fluence 28000 J/cm^2 which is able to drive a shock with the relevant velocity. In addition, I have also analyzed the effects of taking into

account the different ion and electron temperatures.

Reference simulation (1 group, $T_e = T_i = T$)

A result of the simulation is reported at 10 ns in the Fig. 3.2 which reports the variations of electron density (N_e), temperature (T), mean charge (Z) and mass density (ρ). The initial conditions are 4.5×10^{-4} g/cm³ and $T = 1$ eV.

The shock front is located at ~ 0.047 cm (speed of 47 km/s). At this position the temperature peaks at 22 eV. The black vertical dotted line shows the position of the interface between the piston and the backing Xenon gas. This interface is located at ~ 20 μ m from to shock front. The post-shock gas mass density, pressure, electron density and ion charge are respectively equal to 0.02 g/cm³, 1.1×10^4 bars, 5.2×10^{20} /cm³ and 5.6. The high compression is due to ionisation and radiation cooling (chapter 2). Its temperature of 12 eV is the same than in the precursor, where it is constant over the 2 mm of the simulation. The precursor electron density and mean charge are respectively equal to 1.8×10^{19} cm⁻³ and 7. The precursor is not compressed.

The variations of the Rosseland opacities (cm².g⁻¹ and cm⁻¹) with the distance are reported in the Fig. 3.3. The Rosseland opacity is low in the precursor. Hence, 600 cm².g⁻¹ corresponds to 0.5 cm⁻¹, which means that an optical depth of 1 is reached at 2 cm from the shock front. This explains the flat profile of the precursor. With a typical value in the post-shock of 2577 in cm².g⁻¹, this opacity is now 53 cm⁻¹, and an optical depth of 1 is here reached at 200 μ m from the shock front (which is much smaller than the post shock extension).

This simulation was performed using the Spitzer thermal conductivity. To check the conductivity effect, I performed another simulation, with a negligible thermal conductivity (i.e. 10^{-12} W/m/K) for the Xenon layers only. The results are reported in the Fig. 3.4. The interface between the piston and the backing Xenon gas is still close to the shock front. Except for the peak of temperature which is higher (~ 29 eV instead of 22 eV) and thinner, the shock structure is similar to the previous case.

Two fluids with different temperatures T_e and T_i (1 group)

In the previous section, HELIOS simulations have been carried out for the case of equal ion and electron temperatures. I will now investigate the effect of such approximation on the simulated results employing 1) Spitzer, and 2) negligible constant thermal conductivity in the Xenon layers. It is important to note that this two fluids approximation can not be restricted to the Xenon layers only and thus it is valid from the piston (CH/Au) up to the Xenon gas. Thus the dynamics and conditions of the piston are also modified, which may slightly modify the shock velocity.

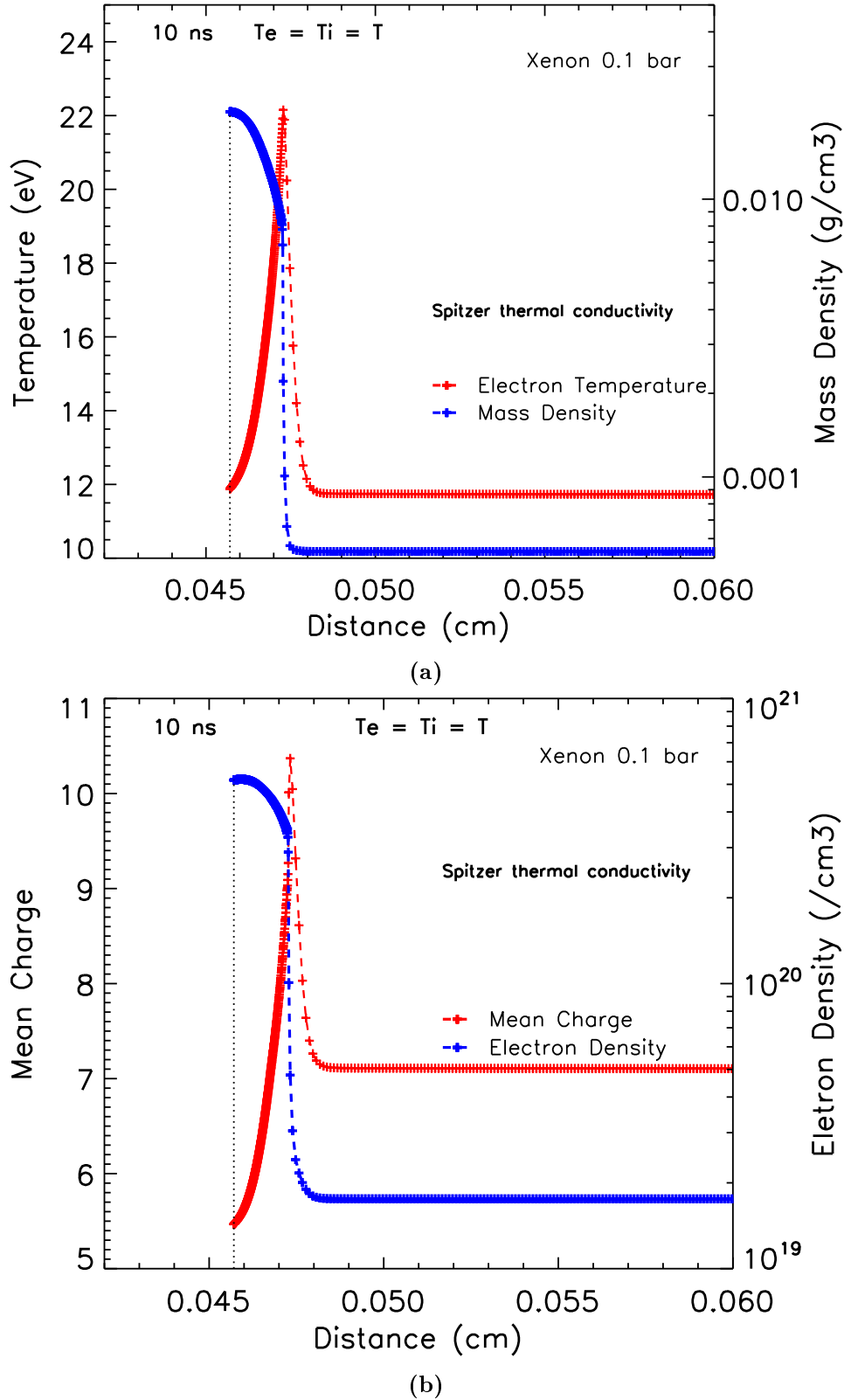


Figure 3.2: Mass density and temperature (a), electron density and mean charge (b) at 10 ns for a radiative shock of speed ~ 47 km/s in Xenon at 0.1 bar. The vertical dotted black lines show the position of the interface between piston and backing Xenon gas. Zero at x-axis is the interface of piston and Xenon at time zero. Spitzer thermal conductivity has been used in the simulation.

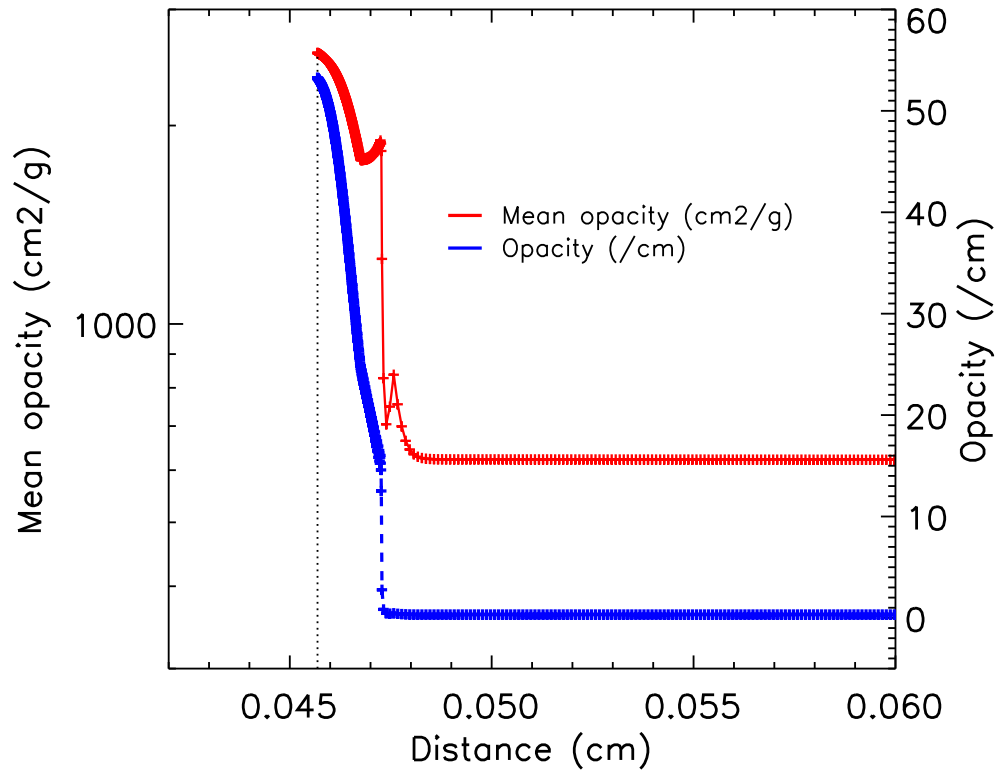
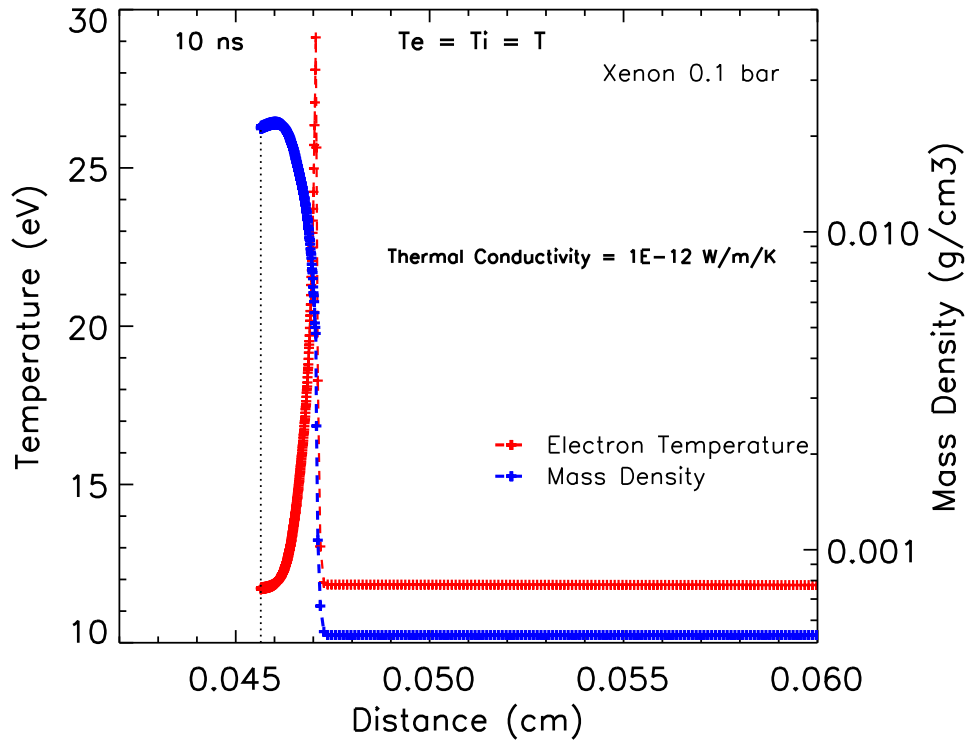
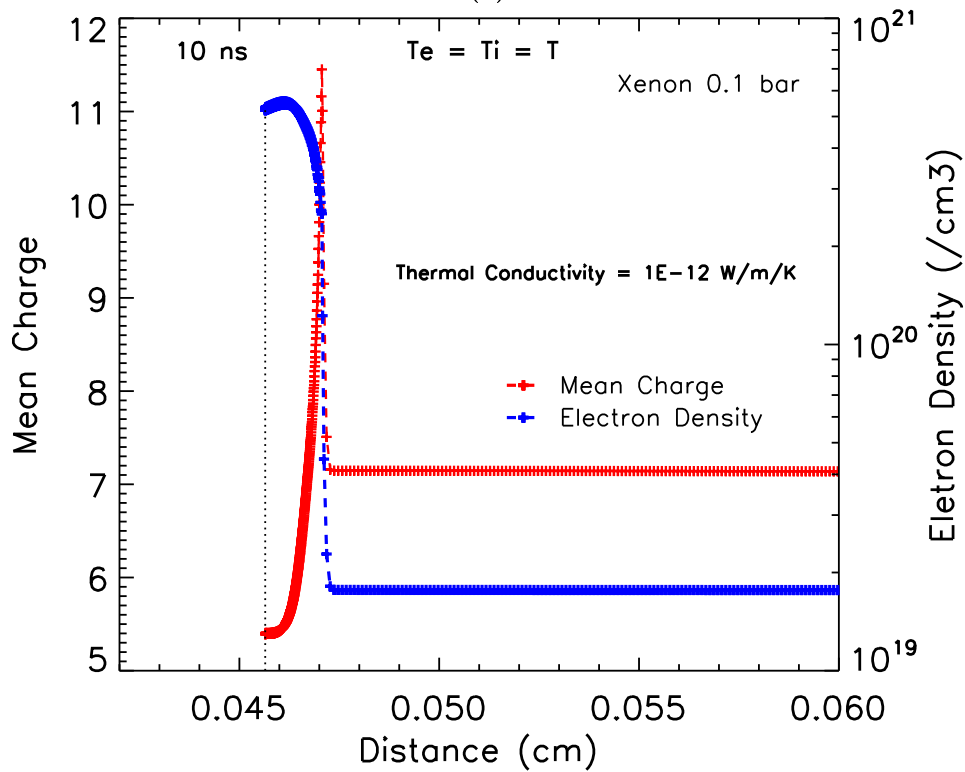


Figure 3.3: Mean Rosseland opacity (in cm^2g^{-1}) and opacity (cm^{-1}) at 10 ns for a radiative shock of speed ~ 47 km/s in Xenon at 0.1 bar. The vertical dotted black lines show the position of the interface between piston and backing Xenon gas. Zero at x-axis is the interface of piston and Xenon at time zero. Spitzer thermal conductivity has been used in the simulation.

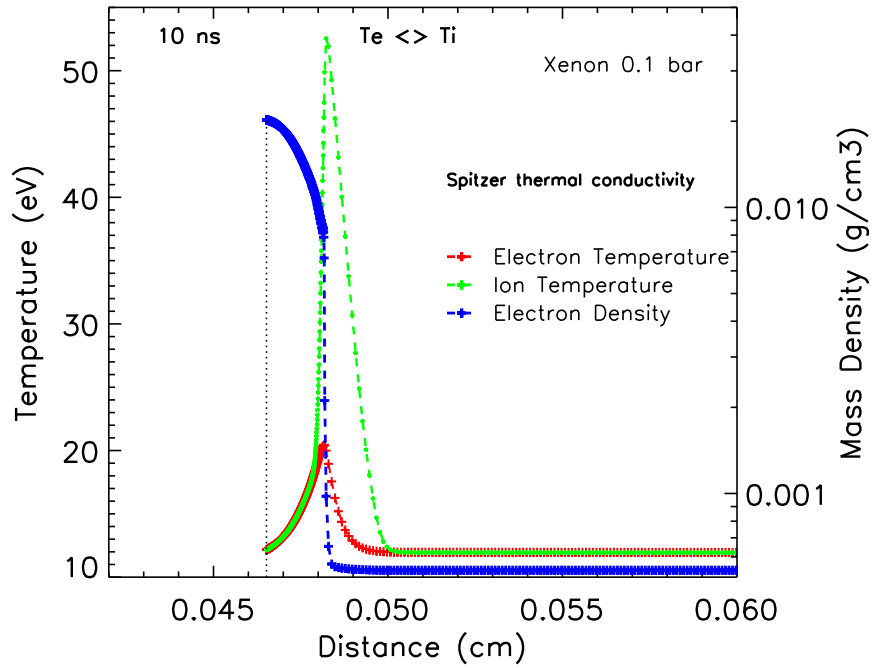


(a)

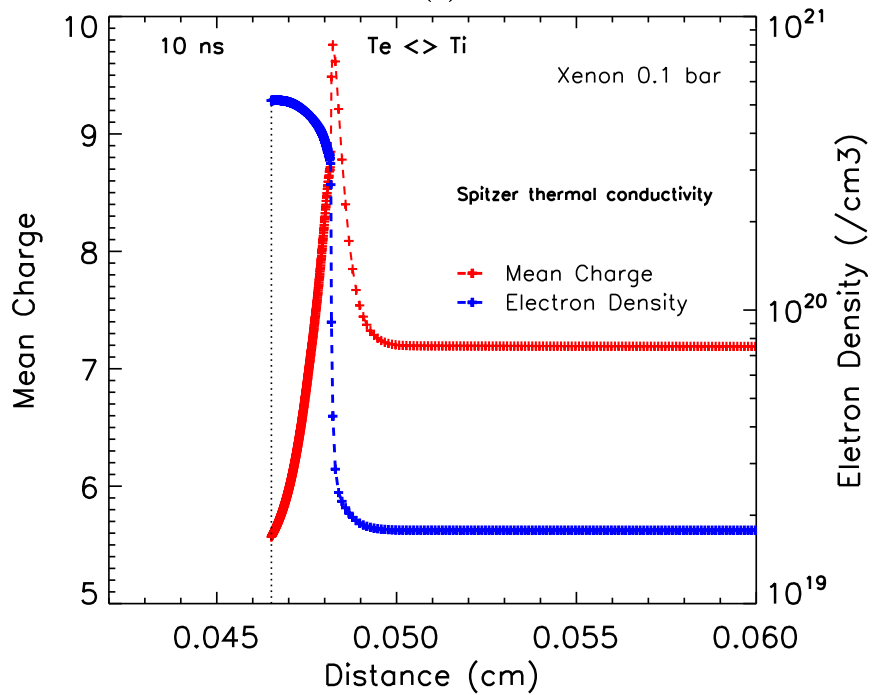


(b)

Figure 3.4: (a): Mass density and temperature (b): electron density and mean charge at 10 ns for a radiative shock of speed ~ 47 km/s in Xenon at 0.1 bar. The vertical dotted black lines show the position of the interface between piston and backing Xenon gas. Zero at x-axis is the interface of piston and Xenon at time zero. A negligible constant thermal conductivity (10^{-12} W/m/K) have been used in the simulation for Xenon.



(a)



(b)

Figure 3.5: (a): Electron density and electron temperature (b): Mass density and mean charge at 10 ns for a radiative shock of speed ~ 48 km/s in Xenon at 0.1 bar, for the case when the electron and ion temperature are different. The vertical dotted black lines show the position of the interface between piston and backing Xenon gas. Zero at x-axis corresponds to the position of the interface between the piston and Xenon at time zero. The Spitzer thermal conductivity has been used in this simulation.

The Fig. 3.5a reports the shock structure at 10 ns for the case of Spitzer thermal conductivity. The shock is located at 0.048 cm. The ion temperature peaks at 53 eV and the electron temperature peaks at the same value of 20 eV than previously. Except for the ion temperature, the shock structure is not significantly changed compared to the case of equal temperatures.

Let us now inspect the role played by the thermal conductivity (see Fig. 3.6). In the case of a negligible thermal conductivity of (10^{-12} W/m/K) for the Xenon layers only, the electron temperature (and as a consequence the mean charge) peaks at higher value 25 eV (instead of 20 eV with the Spitzer conductivity) and the ion temperature reaches to 405 eV (instead of 53 eV). The rest of the shock is not affected by this change in the conductivity. This confirms that the width and height of the ion peak temperature are a direct consequence of the thermal conductivity.

Several groups for the opacity, one temperature.

As mentioned earlier, the number of frequency groups influences the dynamics and morphology of radiative shocks. A set of simulations has been performed considering (only for Xenon) different numbers (N) of frequency group varying between 1 and 100 for $T_e = T_i$. The distribution in energy of the groups is logarithmic and the grid is set up with approximately 85% of the groups having photon energies between 0.1 eV and 3 KeV, while the remaining 15% lie between 3 KeV and 1 MeV.

The Figures 3.7 (a) and (b) show the variations of the electron temperature with the number of groups (from 1 to 100) for the precursor (a) and the front (b). Increasing the number of groups affects mostly the precursor. A similar behavior is found in Vaytet *et al.* (2013).

It should be noted that this multigroup opacity treatment is applied to all the layers (except gold: only one group opacity is provided by the company) in the simulation. This could affect slightly the dynamics of the piston. Concerning the precursor at this time of the simulation, and taking an accountable variation in temperature of 10%, the convergence is achieved after 20 groups.

Variation with the opacity

In order to estimate the effect of the opacity, I have performed several simulations by increasing the Planck and Rosseland opacities in Xenon (Stehlé *et al.*, 2014b) using a common multiplier ranging between 1 to 40. Such procedure is often used to reduce the gap between the available and more sophisticated opacities. To exclude the impacts of the radiation coming from the post-shock to the piston layers, the opacity of the piston (CH and Au) layers have been set to zero.

I present in Fig. 3.8 the results (profiles of temperature, mass density and

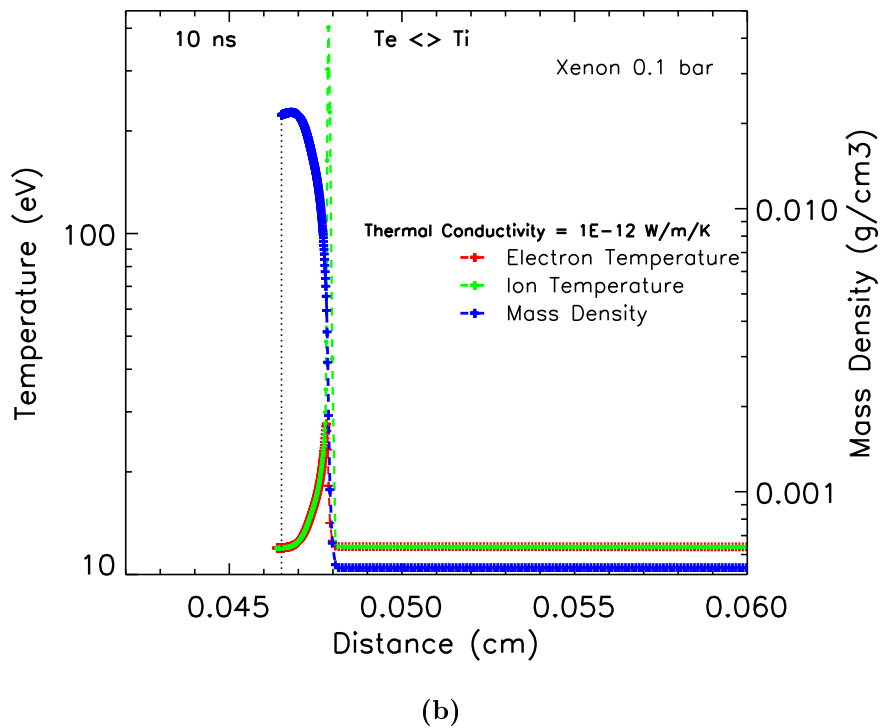
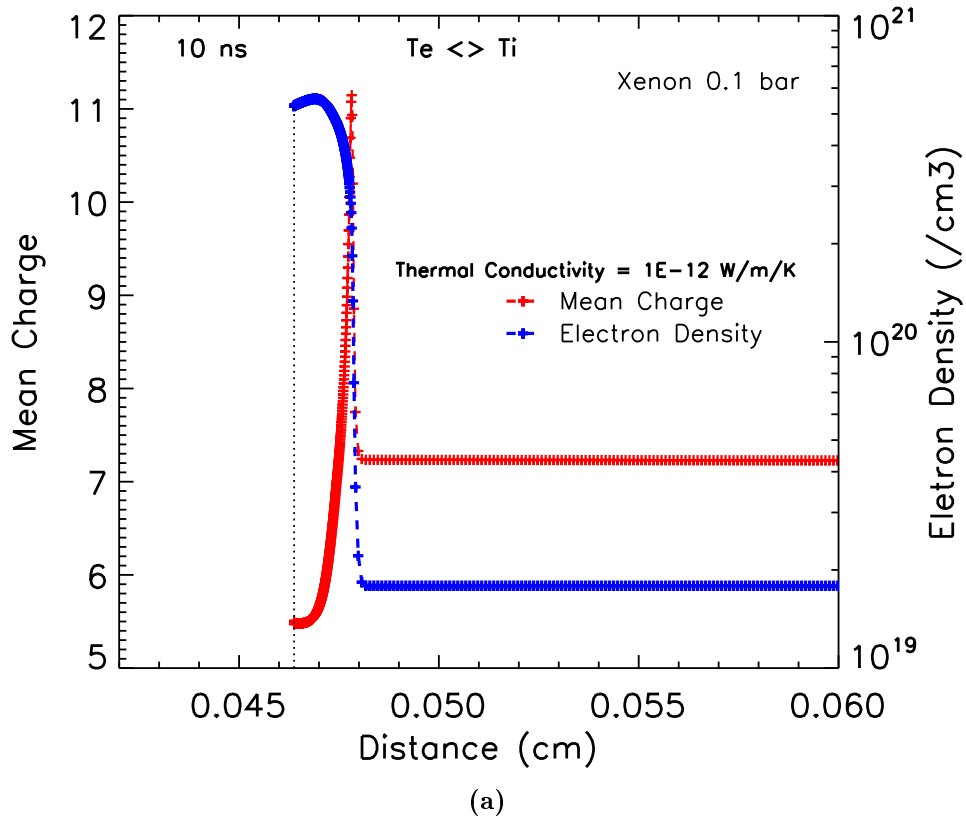


Figure 3.6: (a): Mass density and electron temperature (b): electron density and mean charge at 10 ns for a radiative shock of speed ~ 45 km/s in Xenon at 0.1 bar, for the case when the electron and ion temperature are different. The vertical dotted black lines show the position of the interface between piston and backing Xenon gas. Zero at x-axis corresponds to the position of the interface between the piston and Xenon at time zero. In this simulation value of thermal conductivity (10^{-12} W/m/K) is negligible for Xenon. The peak value of ion temperature is found to be 405 eV whereas theoretically, this value is expected to be ~ 600 eV. It is possible to achieve the expected value by increasing the resolution of the simulation.

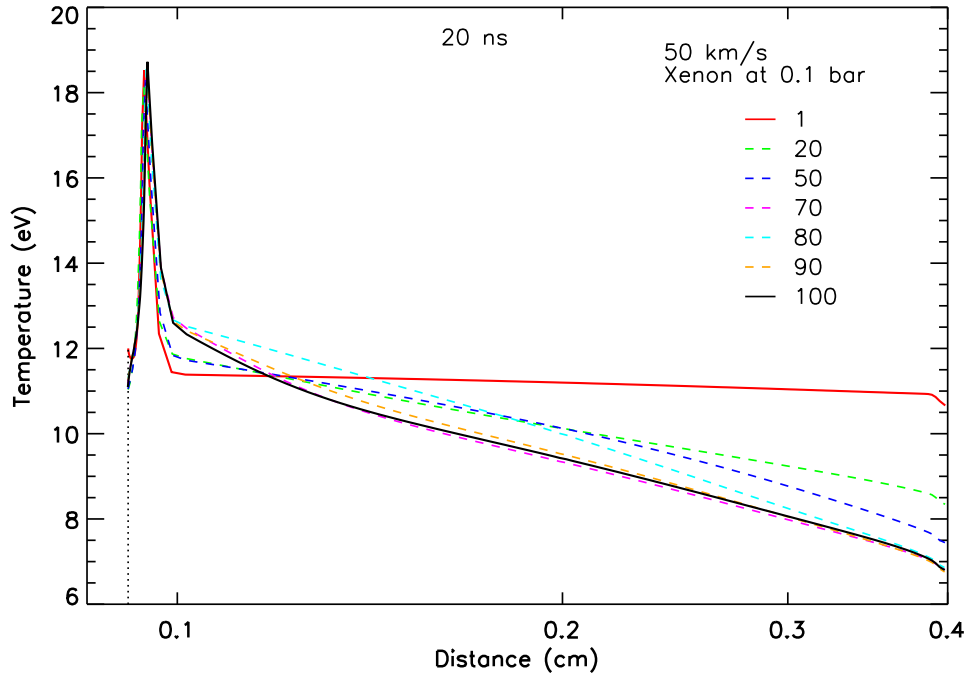


Figure 3.7: Electron temperature profiles for various numbers of frequency groups, $N = 1, 20, 50, 60, 70, 90$ and 100 .

mean charge) of four cases corresponding to an opacity multiplier equal to 1, 10, 30 and 40. The electron and ion temperatures are taken to be equal. Increasing the opacity increases the absorption in the precursor, and thus decreases its length, as the photons emitted by the shock are more rapidly absorbed by the cold pre-shock. Taking as a reference the previous value of the Rosseland opacity of $600 \text{ cm}^2 \cdot \text{g}^{-1}$ and a multiplicative factor of 40, the optical depth of 1 will now be reached at 0.05 cm (instead of 2 cm without any multiplying factor).

The temperature peak value at the shock front also decreases. I do believe that this can be attributed to the increase of the radiative cooling of the peak of temperature with the multiplying factor.

I adopted here an oversimplified method in the selection of the groups boundaries. A more realistic one would be to take into account the variation of the opacity in the different layers with the wavelength. In the case of xenon for instance, it would be then more adapted to refine the description of the opacity between 5 and 100 eV (see Figure 3.10a).

Opacities comparison

The previous study illustrates the role played by the opacity for the radiative shocks waves with a precursor. It seems then logical to compare the

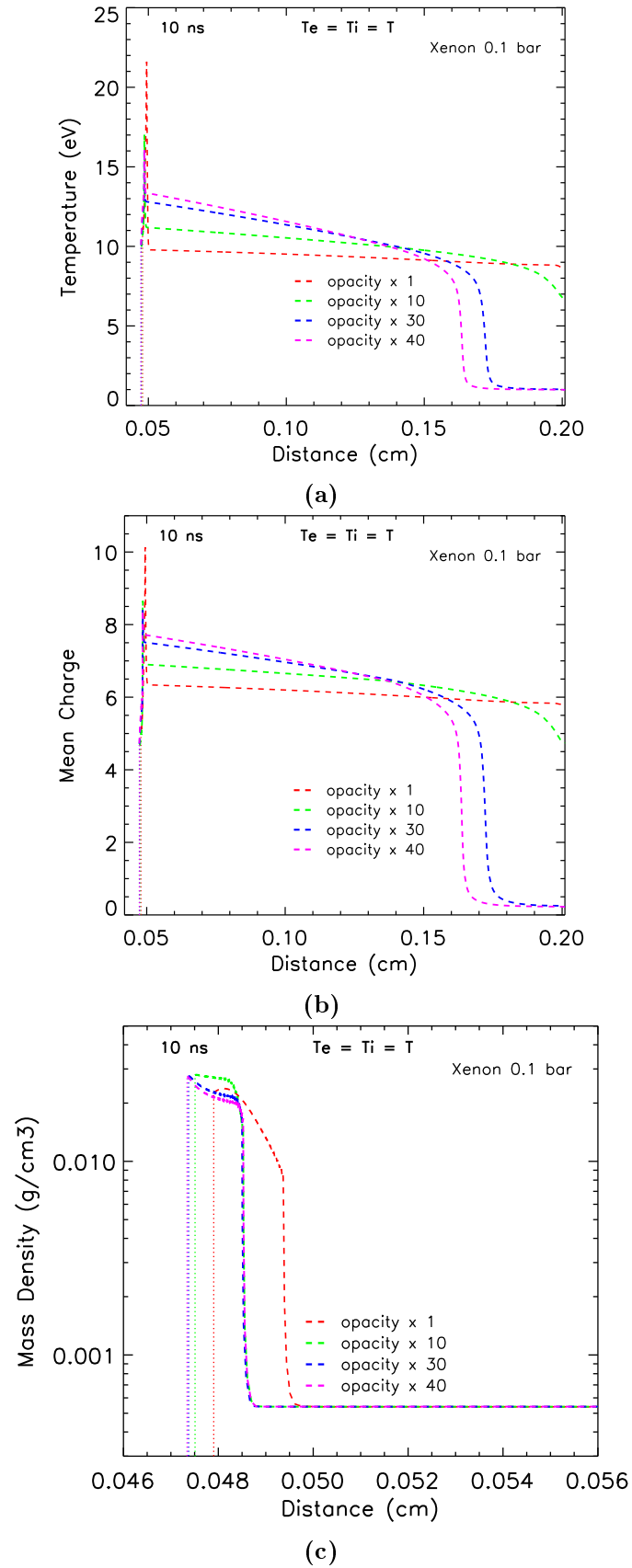


Figure 3.8: (a): Electron temperature (a), mean charge (b) and mass density (c) for four (1, 10, 30 and 40) multipliers of the Xenon opacity at 10 ns.

PROPACEOS opacity, which is used by HELIOS, with more sophisticated calculations.

The Figures 3.9a and 3.9b report the variations of the Planck and Rosseland grey opacities computed for the density of the precursor, $\rho = 1.5 \times 10^{-3} \text{ g/cm}^3$ by two different codes: PROPACEOS (MacFarlane, Golovkin, and Woodruff, 2006) and BiGBART (de la Varga *et al.*, 2011; Ogando and Velarde, 2001). PROPACEOS opacities and EOS, used in HELIOS simulations, computes frequency-dependent opacities, along with specific internal energies and pressures. The atomic code BiGBART able to calculate two type of opacities dependent on atomic structure and frequency dependent. The opacities computed by Rodríguez *et al.* (2015) are also reported for comparison. The two last calculations use the FAC (Flexible Atomic Code) (Gu, 2008) for the calculation of the atomic data.

We see that, for a temperature equal to 10 eV the Rosseland opacity is equal respectively to 800, 15000 and 8000 g/cm^2 , whereas the Planck opacity is equal to 18000, 65000, 370000 g/cm^2 . This means that the PROPACEOS opacity, which is used in HELIOS, is smaller by more than one order of magnitude than the two last opacities. As it is not possible to change the opacity model within HELIOS, we then decided to use the PROPACEOS opacity with a multiplicative factor which we have set equal to 20.

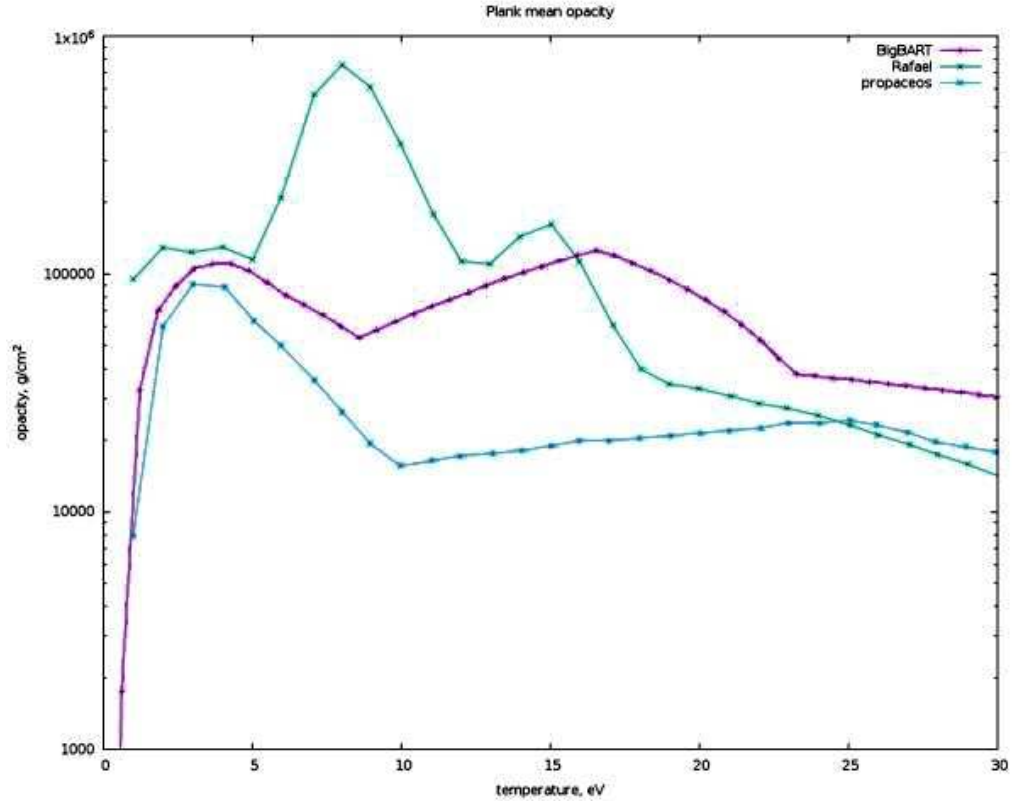
The discrepancies in the average opacity are a consequence of important differences in the monochromatic opacities. This is illustrated in the Fig. 3.10 which compares the monochromatic opacities given by PROPACEOS and Rodríguez *et al.* (2015) (see Fig. 16 of Rodríguez *et al.* (2015)) at 15 eV and $1.5 \times 10^{-3} \text{ g/cm}^{-3}$. This figure indicates a noticeable difference between 5 and 150 eV with more bb transitions for the last method. This explains the differences observed in the corresponding averages.

Synthesis

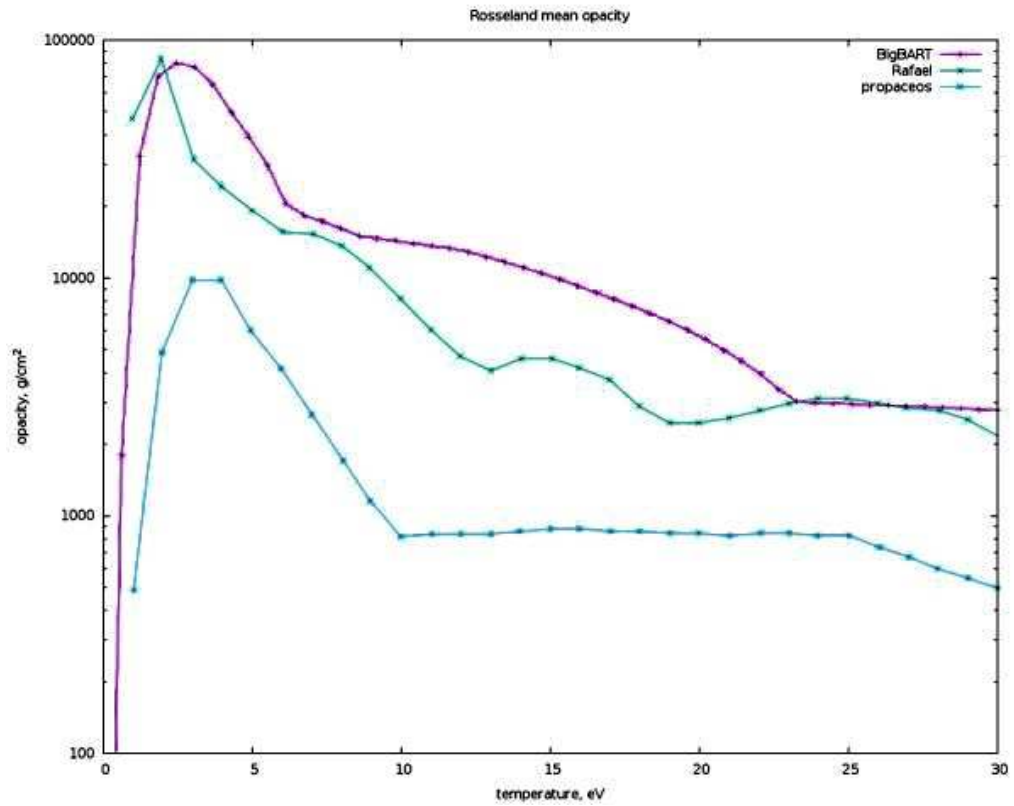
These different simulations, for a shock propagating at $\sim 50 \text{ km/s}$ in Xenon at 0.1 bar, show that the simulations performed with only one temperature are adequate for the description of the shock.

The opacity strongly affects the precursor extension which decreases from more than 4 mm for 1 group to 3 mm then the number of groups is larger than 20. The convergence versus the number of groups is reached after 20 groups.

To fit with more sophisticated opacities, and as it was impossible to include them in HELIOS, I decided to multiply the opacities of Xenon by a factor of 20. This reduces strongly the precursor extension up to $\sim 1 \text{ mm}$ at 10 ns. Taking into account the present huge uncertainty in the opacity, I considered that it was not necessary to use multi-group opacities. *This also means that our 1D simulations will be used - only - for a qualitative interpretation of the experimental results. A quantitative comparison should*

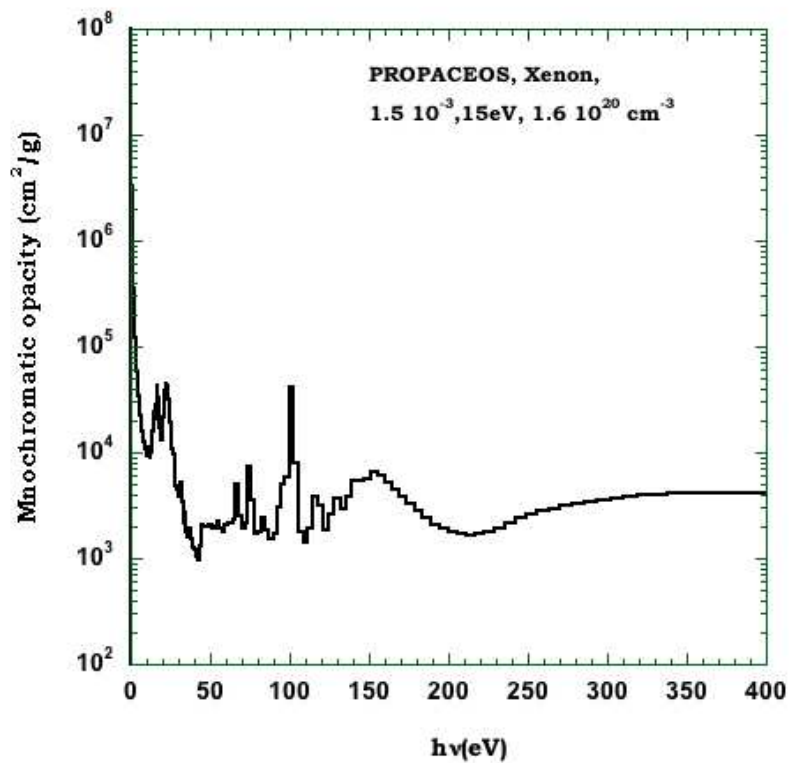


(a)

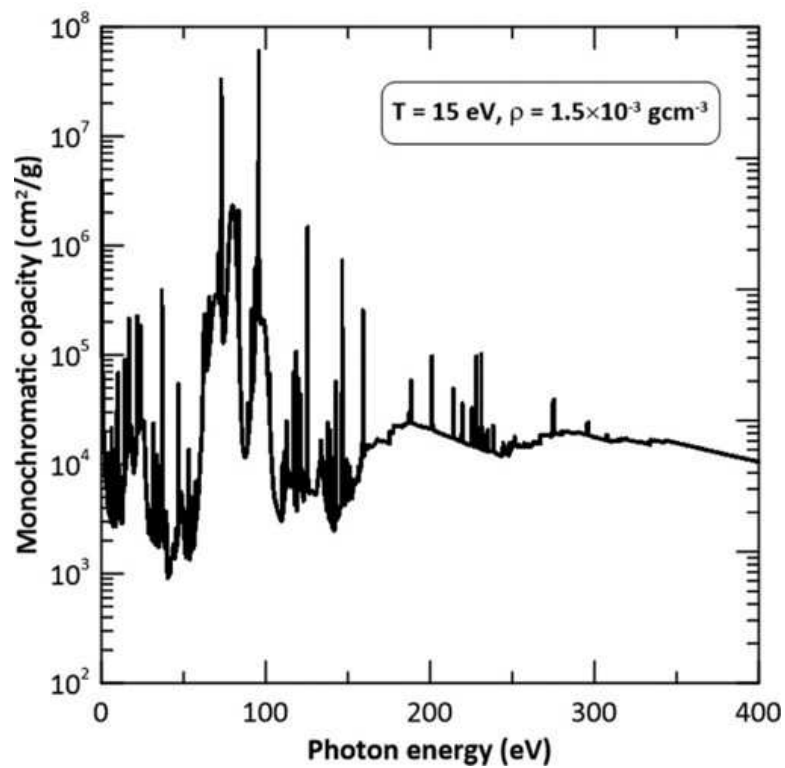


(b)

Figure 3.9: Planck and Rosseland monochromatic opacity profiles T_e for $\rho = 1.5 \times 10^{-3}$ from PROPACEOS (I), BIGBART (II) and Rodriguez et al. (III).



(a)



(b)

Figure 3.10: Monochromatic Xenon opacity versus the photon energy in eV at $T = 15 \text{ eV}$ and for $\rho = 1.5 \times 10^{-3} \text{ g.cm}^{-3}$ for the PROPACEOS (a) and Rodríguez *et al.* (2015) (Fig. 16 of Rodríguez *et al.* (2015)) (b) models.

be, in the future, based on adequate opacities and multi-groups modeling.

3.4 Interacting radiative shock waves

In order to precise what is expected from the experimental study, I will now investigate the characteristic parameters of two counter-streaming shocks propagating in Xenon at 0.1 bar ($\rho = 5.4 \times 10^{-4} \text{ g.cm}^{-3}$) with equal and different velocities. To highlight the effect of the interaction, I will compare the results with those obtained with 1D simulations. All the simulations will be performed with HELIOS. For the Xenon opacity, a multiplier $\times 20$ will be used. The number of groups will be set to be 1 and the electron and ion temperatures will be supposed to be equal.

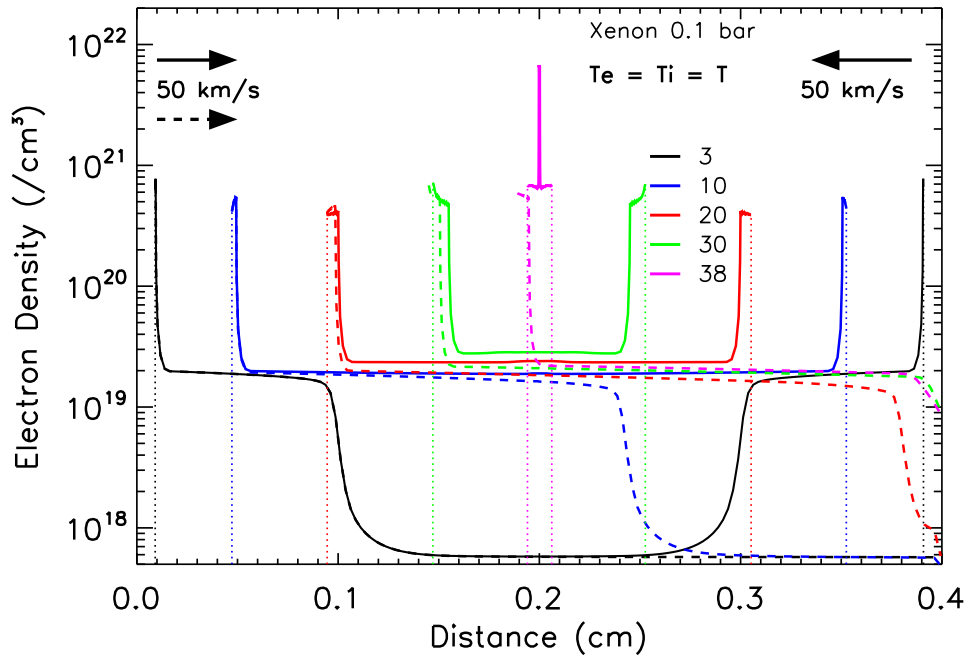
Three representative sets will be considered:

- Case(I): two identical radiative shocks (2RS) at $\sim 50 \text{ km/s}$ propagating in opposite directions (i.e. starting from the left and right end, respectively).
- Case(II): same conditions but without any coupling with radiation.
- Case(III): two counter-propagating radiative shocks propagating with different speeds: $\sim 50 \text{ km/s}$ from the left side of the cell, and $\sim 20 \text{ km/s}$ from the right side.

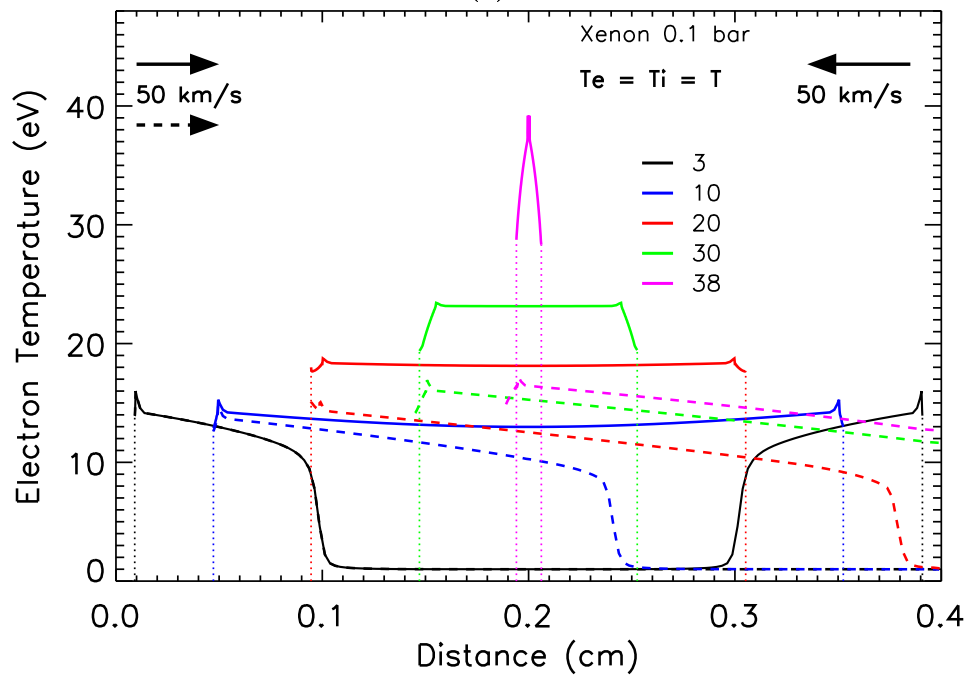
To achieve the aforementioned speeds on the left and right sides, the fluences of the two laser beams have been adjusted. The pulse duration is set to 0.3 ns (peak at 0.15 ns), to reproduce the experimental conditions detailed later in the manuscript.

Case(I): counter propagating shocks with the same speed

This academical case is fully symmetrical and it is equivalent to the case of one RS with a fully reflective boundary (for hydrodynamics and radiation) in the middle of the tube. The Fig. 3.11 shows the variations of the electron density (N_e) and temperature (T_e) in the Xenon layers. The two shocks appear in Xenon at $\sim 2 \text{ ns}$ and the collision occurs at $\sim 38 \text{ ns}$. At 3 ns, the precursor extension is $\sim 0.08 \text{ cm}$, whereas the post-shock electron density and electron temperature are $7.8 \times 10^{20} \text{ cm}^{-3}$ and 16 eV respectively. The length of precursor increases rapidly with time and the two precursors merge suddenly at $\sim 8 \text{ ns}$. After this time, the merging effect increases significantly. It is characterized by a flat common precursor, those electron density and temperature are increasing with time. At the time of the collision ($\sim 38 \text{ ns}$), the post-shock mass and electron density, increase from 0.011 to 0.14 g/cm^{-3} and 6.7×10^{20} to $6.6 \times 10^{21} \text{ cm}^{-3}$, whereas the temperature rises up to 39 eV. The collision leads to the development of two reverse shock



(a)



(b)

Figure 3.11: Electron density N_e (a) and electron temperature T_e (b) versus axial position (along a 0.4 cm long shock tube) at 3, 10, 20, 30 and 38 ns from HELIOS simulations (with opacity $\times 20$) for the cases of single shock of ~ 50 km/s (dotted line) and two identical counter-propagating shocks of ~ 50 km/s (solid lines). The vertical dotted lines show the position of the interface between piston and backing Xenon gas.

waves propagating back with a speed of ~ 15 km/s first in Xenon and, later on, in the different piston layers (not shown in the Figure). These reverse shocks lead to a dense plasma ($N_e > 10^{21}$ cm $^{-3}$) which is not accessible to the experimental diagnostics and will not be detailed here.

To investigate the effects of the interaction, I have reported in Fig. 3.11 the case of 1RS, moving from the left to the right direction in the cell (dotted lines). The wave propagates identically to 2RS until 10 ns. After this time, the profiles of the temperature and electron density differ strongly from the previous case and their values are lower than for the 2RS. The post-shock extension is slightly smaller than for the 2RS, and the shock speed is thus slightly smaller too. This last effect is due to the fact that, for the two interacting waves, the precursor is at a higher temperature than for the isolated shock, and thus the shock propagates in a warmer medium, then modifying the shock conditions (sound speed, opacity, etc). A similar effect in the post-shock extension may be seen for an isolated shock wave propagating in a warmer pre-shock gas.

Case (II): Identical counter-propagating shocks for an ideal gas

In order to highlight the effect of the radiation, another simulation has been performed with the same set of parameters as in the case I, however, putting the Xenon opacity equal to zero. I still use here the PROPACEOS equation of state. The result of the simulation is presented in Fig.3.12. The collision time is now 40 ns instead of 38 ns (thus the shock speed is slightly smaller). The post-shock is no more compressed by radiation cooling. Its compression at 10 ns is 10 instead of 35. This compression is due to the viscous shock (factor 4) followed by the ionisation/excitation of the gas. There is obviously no radiative precursor. Moreover, there are no differences in the N_e , and T profiles of the single shock and that of the two counter-propagating shocks before the collision time.

Case (III): Two shocks at different speeds

The spatial and temporal variations of N_e and T_e , are plotted at times 3, 10, 20, 30, 38 and 49 ns in Fig. 3.13a and 3.13b. The left and the right shocks appear in Xenon at ~ 2 and 3 ns, respectively. Later, at 10 ns, the two precursor extensions are respectively equal to 0.18 and 0.034 cm. The merging of the two precursors starts at ~ 15 ns. As expected from the values of shock speeds, the collision time occurs at 49 ns, which is delayed in comparison to the case (I).

In 2RS, the two radiative precursors merging results in a plateau for the electron density and the temperature. The temperature at collision time is now 28 eV instead of 39 eV in the case I, and the electron density reaches up to 3.1×10^{21} cm $^{-3}$ instead of 6.6×10^{21} cm $^{-3}$.

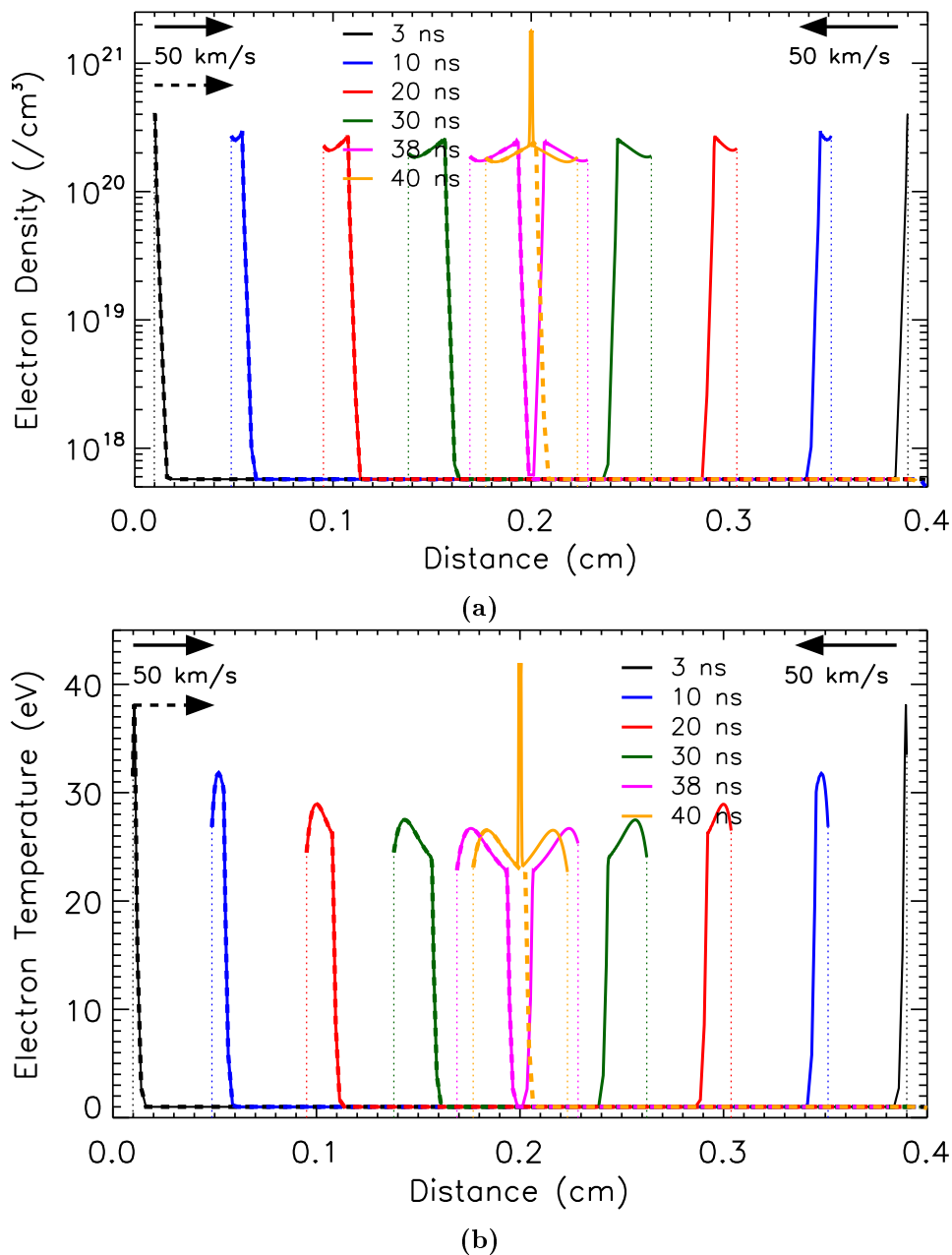


Figure 3.12: Variations of N_e (a) and T_e (b) versus axial position for the case of two identical counter-propagating shocks (of speeds ~ 50 km/s) at 3, 10, 20, 30, 35 and 40 ns as derived from HELIOS simulations. For these simulations, we have neglected the effect of radiation by keeping the Xe opacity equal to zero. The vertical dotted lines show the position of the interface between the piston and backing Xenon gas.

It may be noted that, up to this collision time, the post-shock density conditions and speed are identical for the case of an isolated RS propagating from the left (1RSL) at 50 km/s and this present left shock. This reveals that, in the case of 2RS, there is no noticeable effect of the right shock with speed 20 km/s on the left post-shock of 50 km/s.

On the contrary, we note a difference in extension of the right post shock from the 2RS compared with the case of an isolated shock (1RSR) propagating at 20 km/s from the right, which indicates that the left shock of the 2RS has an influence on the right post-shock (Fig. 3.13a).

3.5 Summary

Radiative shock waves propagating in Xenon at 0.1 bar with a velocity of 50 km/s are characterized by the development of an extended radiative precursor. The huge compression of 38 in the post-shock is a consequence of both the shock and the gas ionisation (factor of 10) as also from the radiative cooling. The post-shock and pre-shock temperature on both side of the peak are identical, indicating that the shock is supercritical.

The spectacular role of the opacity has been highlighted. Due to the uncertainty in the opacity used for Xenon in our simulations, I decided that, at this stage, it was not necessary to refine the simulation in terms of group numbers within the 1D description of the shock wave.

Our numerical study gives the main characteristics of the interaction of two counter-propagating shock waves with speeds equal to 50-50 km/s and 50-20 km/s. The case of identical speeds is simpler due to the symmetry of the problem. However, whatever the speeds, the most important signature of the interaction is the merging of the precursor at 8 ns for 50-50 km/s and at 15 ns for 50-20 km/s. This merging is followed by a regular increase with time of the electron density and the temperature. The collision time is characterized by a sudden increase of the electron density by an order of magnitude, reaching 6.6×10^{21} and 3×10^{21} cm⁻³ respectively, whereas the temperature increases up to 39 and 28 eV.

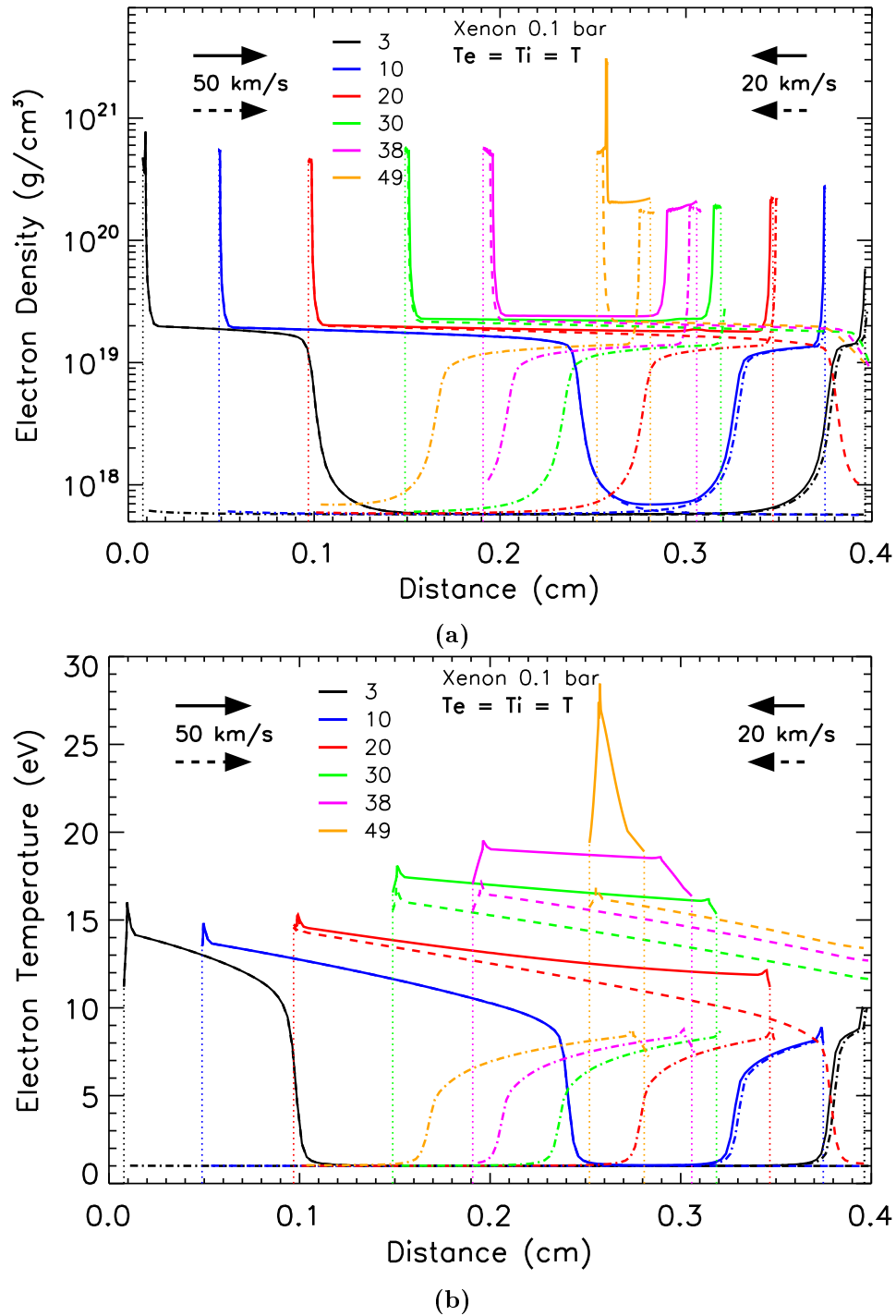


Figure 3.13: Variations of N_e (a) and T_e (b) with axial position for the case of two non-identical counter-propagating shocks (of speeds ~ 50 & 20 km/s) and two single shocks (dotted lines) of speeds ~ 50 & 20 km/s respectively at 3, 10, 30, 35 and 46 ns as derived from HELIOS simulations. The vertical dotted lines show the position of the interface between piston and backing Xenon gas (with opacity $\times 20$).

Laser-driven radiative shock: Experimental Setup

Contents

4.1	Prague Asterix Laser System (PALS) facility	48
4.2	Targets	49
4.2.1	Massive Targets	51
4.2.2	Gaseous Targets	51
4.2.3	Target holder	55
4.2.4	Target filling	56
4.3	Laser Focusing	57
4.3.1	Focal Lenses and Phase Zone Plates	57
4.3.2	Focusing of the MAIN and AUX laser beams	58
4.4	Diagnostics	59
4.4.1	Visible interferometry	61
4.4.2	XUV spectroscopy	65
4.4.3	Visible spectroscopy	67
4.5	Summary	68

When a short pulse of a high-power laser beam is focussed on a thin foil, it transfers a huge amount of energy to the foil material. Almost instantaneously, the laser absorption heats it up to the ablation. A hot and low density corona is generated backwards by this process. Beyond the ablation surface, a shock is formed in the foil as a consequence of the momentum conservation (rocket effect). The shock moves inward in the foil. Our case of the experimental setup, as the foil closes a tube filled with gas, the shock propagates then in the gas, where it is studied through various kinds of diagnostics. The foil then acts as a piston.

We performed the experiments at the Prague Asterix Laser System (PALS) in the Spring 2015 (five weeks: 20th April - 22th May). The objective of the experimental campaign was to study the evolution of two counter streaming radiative shocks, driven by two counter-propagating lasers with an irradiance in the range of 10^{14} W.cm⁻², and therefore to characterize their interaction and collision. In this chapter, I will first present a brief description of the PALS laser facility and of the laser beams used in our experiment. This will

be followed by a presentation of the targets design and an overview of the general setup and of our main diagnostics.

4.1 Prague Asterix Laser System (PALS) facility

The Prague Asterix Laser System (PALS) is a laser facility based on an Infrared high-power iodine laser system (Asterix IV) (Jungwirth *et al.*, 2001). Using different amplifying stages, the laser facility is able to deliver energy up to 1 kJ in 0.3 ns at the fundamental wavelength 1315 nm. The output laser beam can be further subdivided in few auxiliary beams. All auxiliary beams may be frequency doubled ($\lambda = 657$ nm) or tripled (438 nm). The PALS laser facility is capable of firing up to two high energy laser shots per hour. Compared with solid state lasers, this gas laser is known to deliver a quite homogenous beam intensity without hot spots. A spatial profile of the PALS laser beam is shown in the Fig. 4.1a (recorded by PALS team during the experimental campaign) while its pulse characteristics are plotted with time in the Fig. 4.1b.

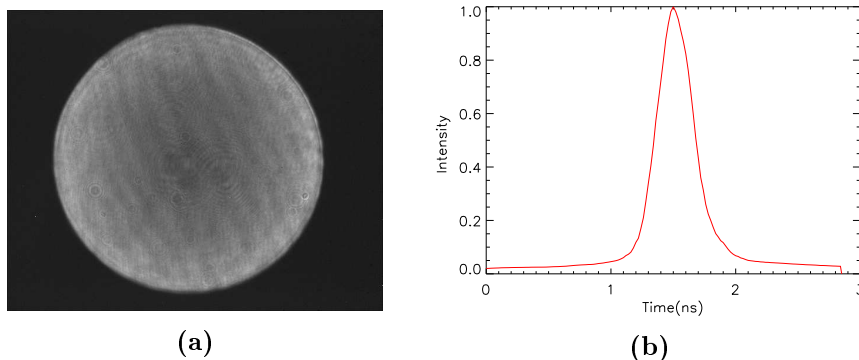


Figure 4.1: a: Spatial profile of the PALS Laser beam. b: Intensity profile of laser pulse $I(t)$ with time.

For our experiments, we used two independent laser beams to drive the two counter streaming shocks in the gaseous target. For this purpose, the fundamental PALS laser beam has been subdivided, after the fourth amplifier (V_4), into two beams with respective energy fractions of 60% and 40% (see Fig. 4.2). The most energetic of these laser beams is then injected through the fifth (V_5) amplifier and its frequency are then tripled. This beam at 438 nm will be hereafter termed as the MAIN laser beam.

The second of the two previous laser beams propagates then without any modification. It will be hereafter called the AUX laser beam (1315 nm). The scheme of the energy distribution is shown in the Fig. 4.2 and the characteristics of MAIN and AUX laser are presented in Table 4.1.

For the experiments, PALS offers two vacuum chambers, with a spherical

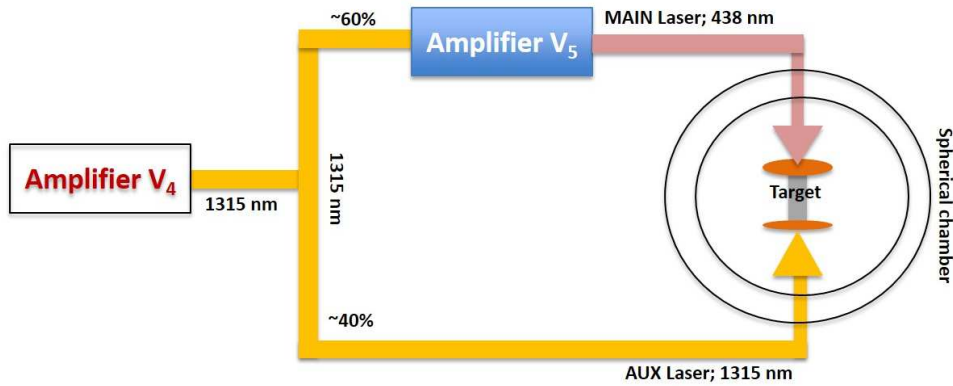


Figure 4.2: Energy distribution scheme for MAIN and AUX laser beams.

LASER	MAIN	AUX
Typical laser energy (J)	120	60
Beam diameter (mm)	290	148
Wavelength (nm)	1315	438
Pulse duration (ps)	350	350

Table 4.1: Nominal characteristics of MAIN and AUX laser beams.

and cylindrical geometry, respectively. The spherical chamber assembly, used in our experiments, is shown in Fig. 4.3. This chamber, having a diameter of 100 cm, is closed by two entrance circular windows of respective diameters 80 cm and 50 cm, to allow the MAIN and AUX beams to penetrate in the chamber and to reach the target. Each of these windows is outfitted with a hinged door. Several circular ports of various diameters also allow for the different diagnostics. The target holder and some diagnostics are mounted on an optical bench which is decoupled from the chamber walls.

4.2 Targets

Our targets schematically consist in small tubes of 4 mm length closed on both sides by two specific foils of thickness $11 \mu\text{m}$, on which the laser beams are focused (one laser per foil) with an irradiance of about 10^{14} cm^{-2} . The tube is filled with gas in which the radiative shock propagates with a velocity of 30 - 60 km/s. The two foils closing the target insure the conversion, through ablation and shock generation, of the laser energy into mechanical energy.

In our experiments, we used specific targets for alignment and characterization of the beam size. These targets were manufactured at the Pole instrumental of Observatoire de Paris.

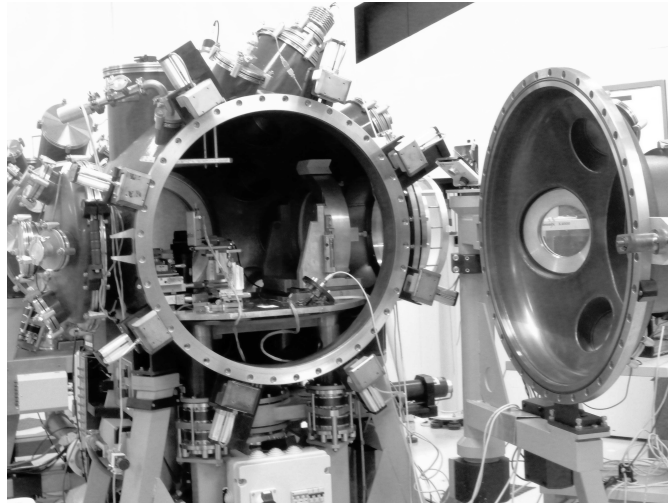


Figure 4.3: Snapshot of the spherical chamber showing the horizontal breadboard, and, on the right, the focusing MAIN lens.

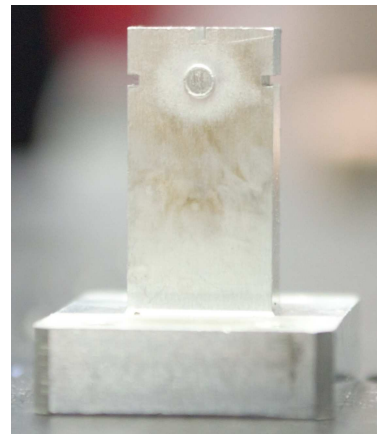
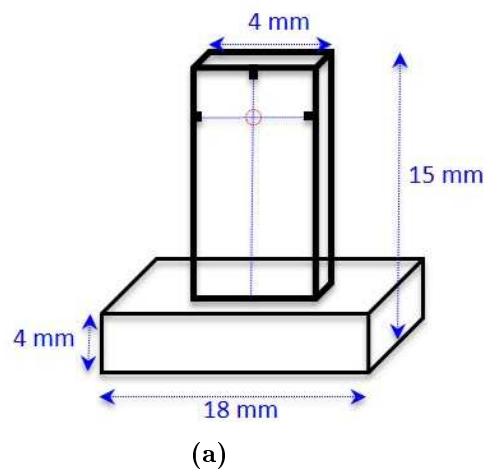


Figure 4.4: Dimension drawing (a) and snapshot (b) of Aluminum massive ("mock") target.

4.2.1 Massive Targets

For the laser alignment on the target we have used special targets, also termed as “mock” targets. A mock target (Fig. 4.4), is an aluminum block with a base. Three cuts made on it help to focus the laser beam at the desired position. The center of each of the two laser spots should be located at the intersection of the vertical and horizontal marks, and the precision of this alignment is less than 20 μm .

Beside alignment purpose, such targets are used to characterize the MAIN and AUX spot diameters in the planes which correspond to the location of the two Parylene foils. Hence, the laser beam, focussed on these targets, generates a crater (Chaulagain, 2015). The detailed analysis of the shape and size of these craters provides a quantitative information about the homogeneity of the incident beam and the size of the focal spot. A detailed discussion about the focalisation of the laser with a massive target will be presented in the section 4.3.2.

4.2.2 Gaseous Targets

The core of the gaseous targets (Stehlé *et al.*, 2014a) consists of a channel of a parallel pipe shape having the dimension of $0.9 \times 0.6 \times 4$ mm, placed at the top of an aluminum structure. The pipe, in which the shocks propagate, is defined by two 500 μm thick vertical lateral sides made with coated fused silica (SiO_2) windows (0.9×4 mm) as shown in the Fig. 4.5. Such windows are suitable for the visible interferometry diagnostic, which uses an auxiliary Q-switched Nd:YLF green Evolution laser (see Section 4.4.1).

The channel is closed at the top with a window made of a 100 nm thick Si_3N_4 membrane which, is itself supported, is by a 200 μm thick silicon frame (2.6×4 mm), made by SILSON company. Such membrane is transparent to XUV radiation, which is necessary for the XUV spectroscopic diagnostic used in the experiment. The transmission of the aforementioned material is obtained from the center for X-ray optics (CXRO) database¹ and is plotted between 0 and 40 nm in Fig. 4.8 .

The pistons, closing the tube from opposite sides, and which will launch the two shocks, are made of Parylene-N (11 μm) coated by Au (0.6 μm) (SCITECH company). They are glued on 0.1 mm thick Nickel disks, with external diameter 5 mm, and internal diameter 1 mm. This disk helps in assembling the targets. It also contributes, together with a larger V-shield (section 4.9), to prevent hard X-ray emitted at the laser impact on the foil to reach the gas in the tube. The Parylene layer is facing the laser and plays the role of an ablator. The gold layer, which is coated on the Parylene, and is located between the Parylene and the gas, aims at blocking the X-rays generated by the laser plasma interaction to reach and preheat the gas in

¹http://henke.lbl.gov/optical_constants/

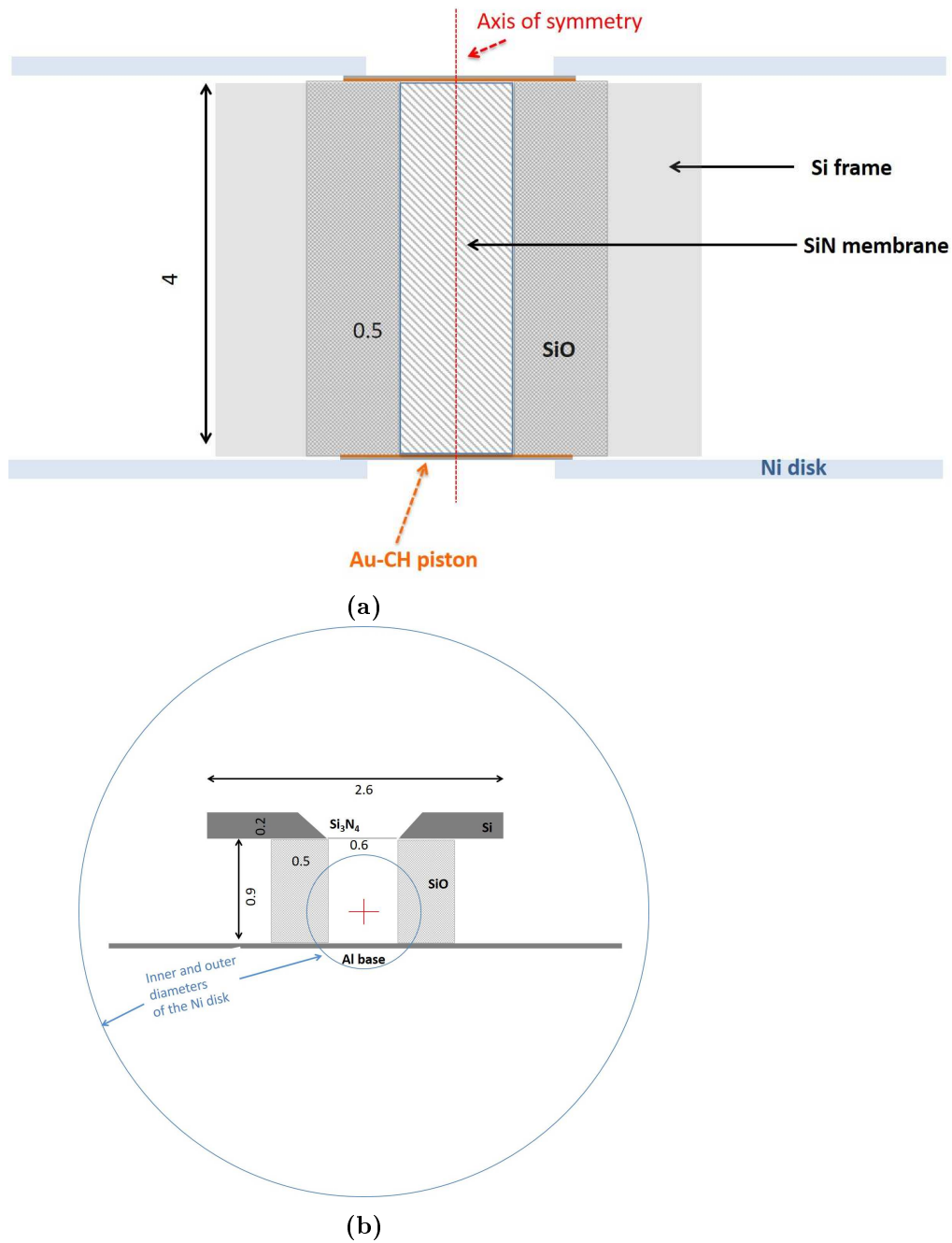


Figure 4.5: Values on the figures are in mm. (a): Vertical cross section view of the gaseous target. (b): Horizontal cross section view.

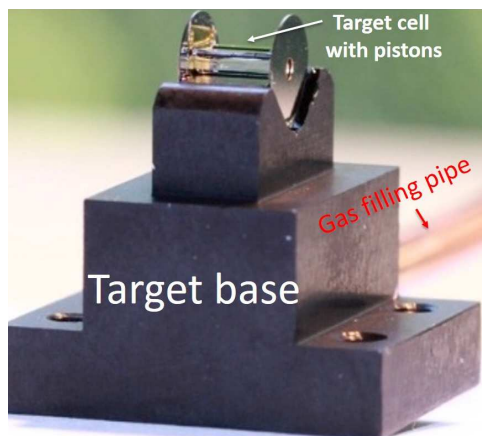


Figure 4.6: Picture of a the gaseous target on its base.

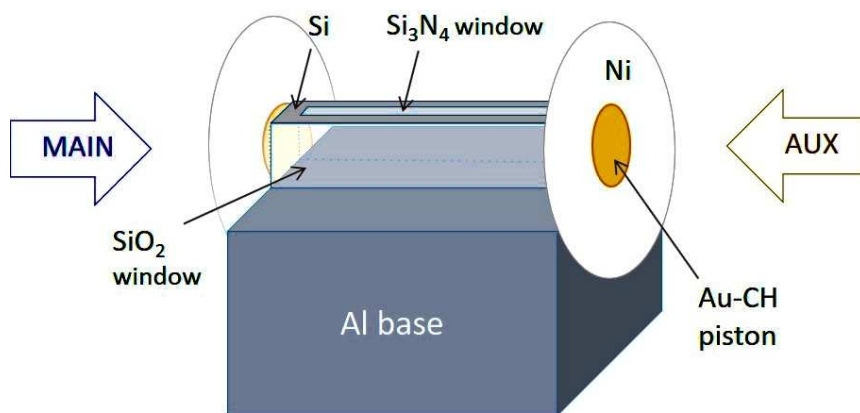


Figure 4.7: Schematic of the gaseous target.

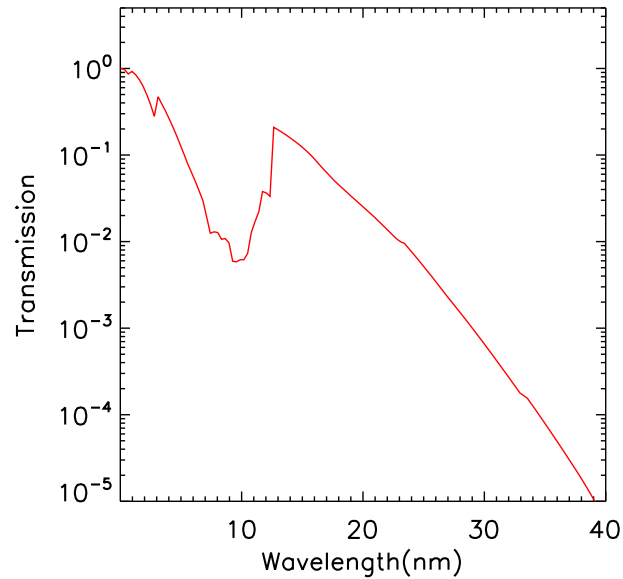


Figure 4.8: Transmission of 100 nm thick Si_3N_4 membrane (CXRO database).

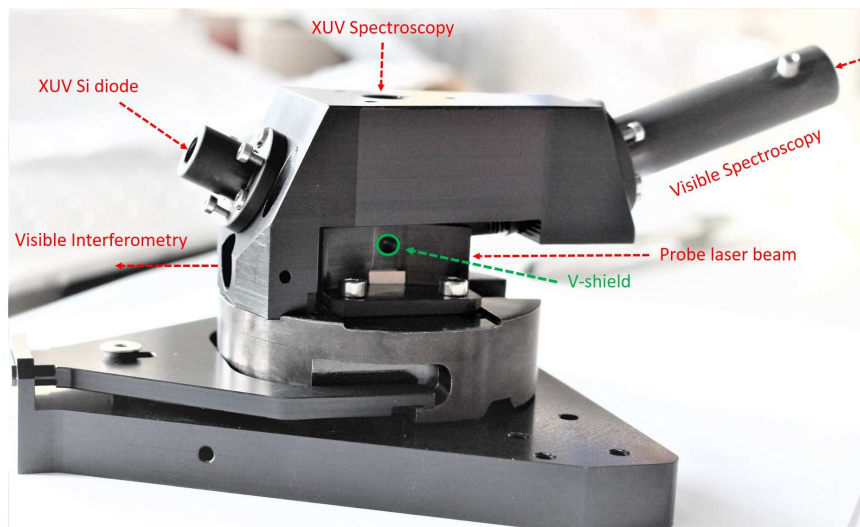


Figure 4.9: Snapshot of a target holder with one V-shield regarding the AUX laser, which will pass through the hole in this shield, marked in green in the Figure. The target, which faces the two diagnostics (tubes), and is located behind the V-shield, is thus not visible.

the cell. These various elements are manually glued on the base of the target to built the shock channel. Each target has been tested against leaks before the experiment and before each shot. The axis of symmetry of the shock waves is required to be located at 0.3 mm from the base and at 0.3 mm from the two vertical SiO₂ windows. Schematics of vertical and horizontal cross section views of the target are presented in Fig. 4.5b. The axis of symmetry is visible in the vertical view, while the position of the laser focus point (‘+’ sign) in the horizontal view. This is achieved during the alignment procedure employing mock targets as discussed in the section 4.3.2. The base of the target consists of a micro-machined aluminum structure. A gas pipe at the bottom of the structure allows for in situ gas filling at a pressure of a fraction of a bar.

A total of 55 targets were manufactured for the experiment. Among them, 31 gave valuable results.

4.2.3 Target holder

We fix the targets on a stainless holder and then place the system into the vacuum chamber. The target holder has been designed and manufactured at Observatoire de Paris. It allows a very reproducible positioning of the target on the vacuum chamber breadboard. The main element of the target holder is a base, where each target is first fixed by screws and removed after each shot to be replaced by a new one. It also includes a diagnostics support (Fig. 4.6) which is attached on it from the top with screws. One of these diagnostics consists in a fast XUV Si diode with a pinhole. The diode is attached to the black tube which is visible on the left part the target holder in Fig. 4.7. This last diagnostic aimed for shock timing, as the pinhole-diode system allows to record the shock passing at the imaged position of the tube (Stehlé *et al.*, 2012; Chaulagain, 2015). Unfortunately, this diagnostic did not work well and will not be mentioned further in the thesis.

The second diagnostic is a visible time-and-space-resolved visible spectrometer. On the target holder, this diagnostic contains a lens which is located inside the black tube on the right part of Fig. 4.9. The lens allows imaging the shock on a linear bundle of 21 fibers connected to the visible spectrometer through a feedthrough (section 4.4.3).

A snapshot of the target holder is shown in the figure 4.9. The red arrows in the Fig. 4.9 shows the distribution of the various diagnostics.

In addition, we used two 3 mm thick stainless steel V-shape shields on both sides of the target which were fixed to the holder. These V-shields have a hole (~ 2.5 mm) shaped entrance to allow laser incidence on the target (in green on the Figure 4.9). The role of the V-shields is to prevent the target from the extra laser or another kind of hard X-ray plasma self-emission linked to the ablation process.

4.2.4 Target filling

The gaseous targets were filled in situ at a fraction of 1 bar with a gas (viz. Xe, Ar, a mixture of Xe and He), which thus provide the medium for the shock propagation. We chose an in-situ filling system (Fig. 4.10) to reduce the difference of pressures inside and outside of the tube. This is critical as a large pressure difference between the target cell and the vacuum chamber can result in the breaking of the ultra-thin Si_3N_4 windows of the target.

To control the pressure, we used a piezo-resistive pressure transducer (Swagelok PTI-S-AC.6-32), which has 10 k Ω bridge resistance and works with 14-30 V biasing voltage. A sensitive Bourdan manometer and a gauge allowed monitoring the pressure inside the target cell. To read the pressure remotely (from the control room) until the last second before the shot, we connected the system with a long cable.

The transducer has been operated with a +17 V DC biasing voltage. The pressure is read using an industrial pressure transducer from Swagelok (0 to 10 Volts, -1.0 bar to 0.6 bar, 0.5% precision) and reading is made with a voltmeter at better than 0.5%. This system generally took approximately one minute to stabilize. A schematic of the aforementioned gas filling system is presented in the Figure 4.10.

The procedure of the target filling is presented as follows:

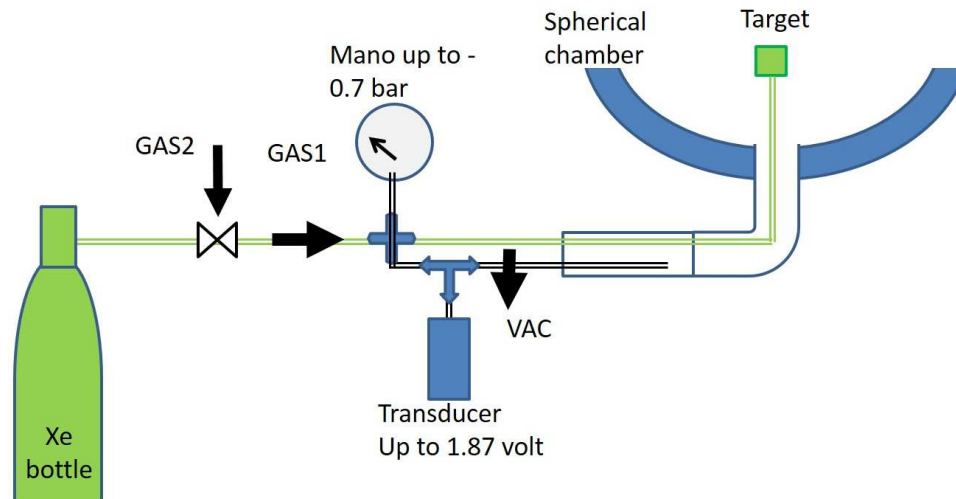


Figure 4.10: In-situ system for target filling and pressure monitoring.

- The target is pumped during the chamber evacuation.
- The target is isolated at the end of the pumping.
- The target is filled to the desired pressure.

- The target is isolated from the gas bottle, to avoid any leakage in chamber.

Then the pressure can be read from the control room till the last second before the shot.

The gases are taken from high grade bottles 99.995% purity. The Xe+He mixture is $10.07\% \pm 0.50\%$ He molar fraction. The filling procedure is preventing the presence of impurities like air. When closing the chamber and during the primary pumping, the filling circuit communicates with the chamber, thus the whole tubing and the target are evacuated down to 0.01 mbar. After the turbo pump is activated, the connection to chamber is closed and the gas is injected. When the target pressure is reached, the cell is isolated from the pressure regulator. In case there is an unacceptable overpressure, it is possible to reconnect to chamber to evacuate and to restart the filling. The pressure reading is possible in the control room, still at precision better than 1% and the value kept for the records is the one just before the shot, which happens normally 1-2 minutes after closing.

4.3 Laser Focusing

4.3.1 Focal Lenses and Phase Zone Plates

Two focal lenses are used to focus the laser beams on the target piston foil for MAIN and AUX, respectively. The MAIN lens is located inside the vacuum chamber whereas the AUX lens is outside this chamber. The specifications of these lenses are given in the Table 4.2.

laser	Diameter (mm)	focal length (mm)	f-number
MAIN	340	564 at 3ω	1.9
AUX	150	1022 at ω	6.9

Table 4.2: Specifications of the MAIN and AUX focal lenses and the f- number (focal length/beam diameter) is given (see table 4.1 for the beam diameters).

Whereas these lenses provide a smooth intensity at the focus, this is not sufficient to launch a planar shock wave. To this purpose, phase zone plates (PZP) have been used between the output laser beam and the lens.

A PZP comprises several phase zone elements, which divide the input beam into several beamlets, which combined with the main focal lens, providing a uniform intensity distribution on the target with a specified diameter (Ross, Pepler, and Danson, 1995; Bett *et al.*, 1995). The PZP are commonly used in EOS laser experiments, which require a uniform intensity distribution on the target (Koenig *et al.*, 1994; Batani *et al.*, 2003).

Two PZP, as discussed below, were used in the experiment:

- The first one, made by COLSICOAT, was already used at PALS for radiative shock experiments (Stehlé *et al.*, 2010). This PZP, used for MAIN (438 nm), is made on a coated BK7 substrate of a diameter of 310 mm and section of 8 mm. It is designed to provide a uniform circular focal spot over a diameter of 0.5 mm.
- The second plate, made by SCITECH, has been used for AUX (1315 nm). The plate is made on a 6.3 mm thick coated Viosil substrate with a square 153 x 153 mm shape. It is designed to provide a uniform circular focal spot over a diameter of 0.250 mm.

Laser	Specified spot diameter (mm)
MAIN	0.5
AUX	0.25

Table 4.3: Specifications of the two Phase Zone Plates.

In terms of energy distribution, $\sim 80\%$ of the laser energy is in the laser spot (C. Spindloe, private comm). The energy of the laser which is given by the PALS installation should be corrected by this factor of 80%. For AUX, another correction of $\sim 10\%$ has to be added, which is linked to the transmission of the entrance window of the vacuum chamber. As a result, for nominal energies of the MAIN and AUX lasers equal to 120 and 60 J (see table 4.1), the fluences on the target are equal to ~ 48800 and 59500 J/cm², respectively. Taking into account the 0.3 ns laser duration of the lasers, this results in an intensity of $\sim 1-2 \times 10^{14}$ W/cm².

4.3.2 Focusing of the MAIN and AUX laser beams

The determinations of the foci of the two lenses were performed with a Hartmann setup using a photographic paper and without any PZP plate. The determination of the size of the beam at the impact is important both to know the initial conditions for the shock waves (laser irradiance, which should be few 10^{14} W/cm⁻² and section of the shock wave). The selection of the best spots size on the piston was done with mock targets and by translating the two laser lenses. The incidence of a laser beam on a solid planar target generates a crater in the foil and an ablated plume propagating backward at high temperature (Mahmood and Ur-Rehman, 2009; Singh and Thakur, 2007). The crater is the result of boiling and ablation of the material. The ablated plasma, which expands towards the incident laser beam, emits in the keV range.

A standard procedure, which works well at low energy (~ 10 J), consists of the estimation of the spot size by measuring the crater on the bulk target, using a standard microscope. At higher energy, the boiling effect makes

this estimation imprecise and we preferred to use a keV imaging diagnostics (Chaulagain *et al.*, 2012), which is based on a pinhole ($25\ \mu\text{m}$ for MAIN keV and $20\ \mu\text{m}$ for AUX) and a keV camera. These two keV cameras have been used during each laser shot to image the impacts of the MAIN and AUX laser beams on the two respective pistons of the target. Each keV camera is a CMOS detector without any glass. It is protected by an Aluminium filter ($200\ \mu\text{m}$ for MAIN and $42\ \mu\text{m}$ for AUX) to block the visible light and to protect the chip from the debris. The specifications of the cameras are presented in the Table 4.4 and the keV camera system is shown in the Fig. 4.11. The two PALS laser lenses were translated up to achieve the suitable diameters on the target, which were finally set to $450 - 500\ \mu\text{m}$ and $250 - 300\ \mu\text{m}$ for the MAIN and AUX beams.

The size of the impact was controlled each day on mock targets before using the laser beams for real shots on gaseous targets. It is worth to precise that the keV diagnostic was still in place for the shots on the gaseous targets. In that case, the beams impact Parylene-N instead of Aluminium. The keV signal is then weaker than for the mock aluminum targets.

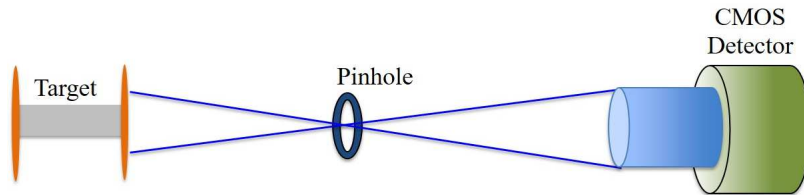


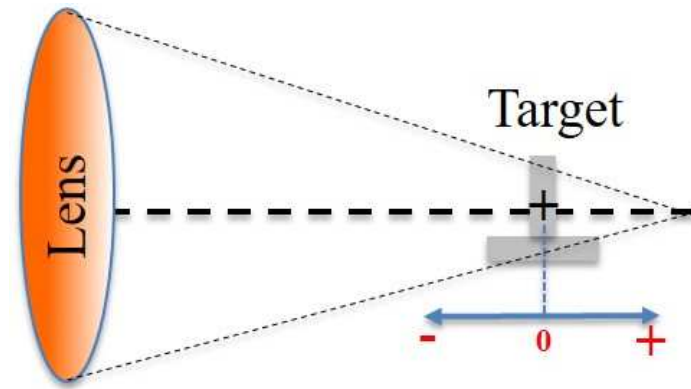
Figure 4.11: Schematic of the keV camera.

	KeV camera MAIN laser	KeV camera AUX laser
Model	UI-122xLE	UI-164xLE
Resolution	752(H) x 480(V)	1280(H) x 1024(V)
Pixel size ($\mu\text{m} \times \mu\text{m}$)	6.0 x 6.0	3.6 x 3.6
Active Area (mm x mm)	4.51 (H) x 2.88 (V)	4.6 (H) x 3.7 (V)
Magnification	1.07	0.68
Pinhole Material	Ta	Pt

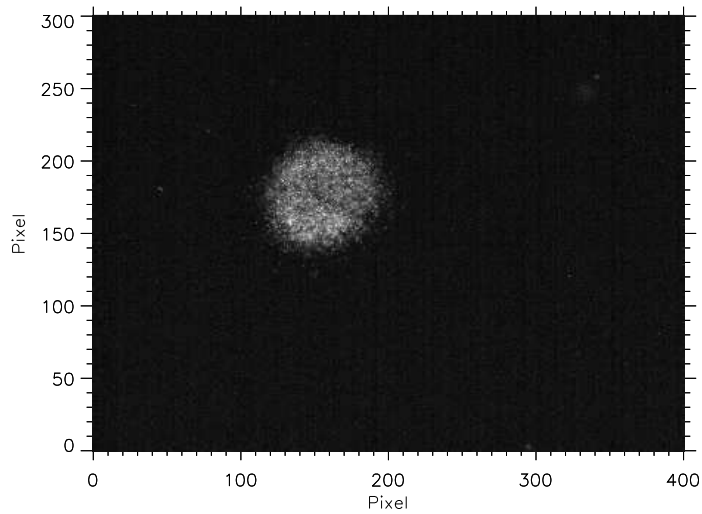
Table 4.4: Specifications of the two uEye keV cameras (1stVision company).

4.4 Diagnostics

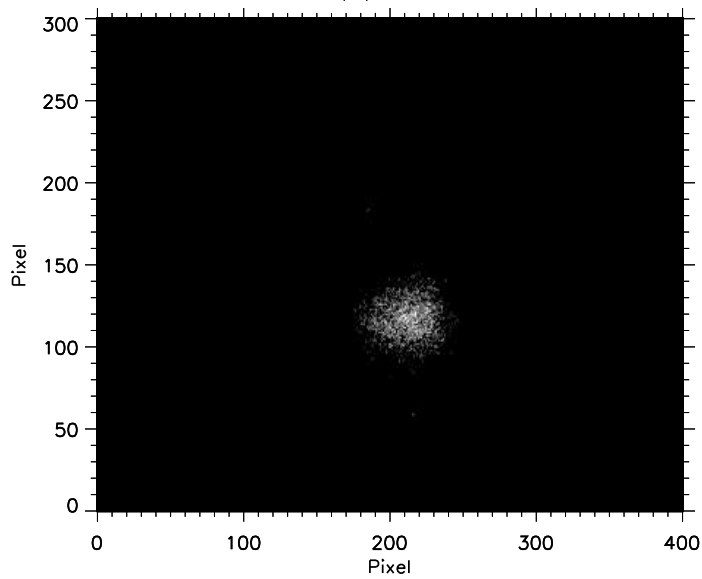
Various kinds of diagnostics were implemented, namely, visible interferometry, XUV and visible spectroscopy. For the same, two keV cameras are inducted to monitor the impact and two visible cameras for target align-



(a)



(b)



(c)

Figure 4.12: (a): Sign convention for the respective positions of the lens and the target. (b): keV image of a MAIN impact on a massive target (lens position: $+1500 \mu\text{m}$). The spot size is $475 \pm 25 \mu\text{m}$. Pixel size for MAIN keV camera is $5.6 \mu\text{m}$. (c): keV image of an AUX impact (lens position: $-1500 \mu\text{m}$). The spot size is $\sim 280 \pm 20 \mu\text{m}$ on target. One pixel = $6.6 \mu\text{m}$ on AUX's keV camera.

ment. In this section, I will describe the setups of the visible interferometry, XUV spectroscopy, and visible spectroscopy. The analysis of the records of visible interferometry and XUV spectroscopy will be discussed in subsequent chapters.

4.4.1 Visible Interferometry

A Mach-Zehnder Interferometer (MZI) has been employed to perform visible interferometry. The recorded interferometric images have been used to study the shock speed and the electron density during the shocks propagation. The experimental setup of this interferometer is presented below.

Mach Zehnder Interferometer

We placed the target, in which shock is produced, in one of the two arms of the interferometer. The probe laser wavelength (527 nm) is supposed to be far away of any atomic absorption resonances in the plasma and thus the contributions to the refractive index come from the plasma free electrons and not from bound electrons (Harilal and Tillack, 2004).

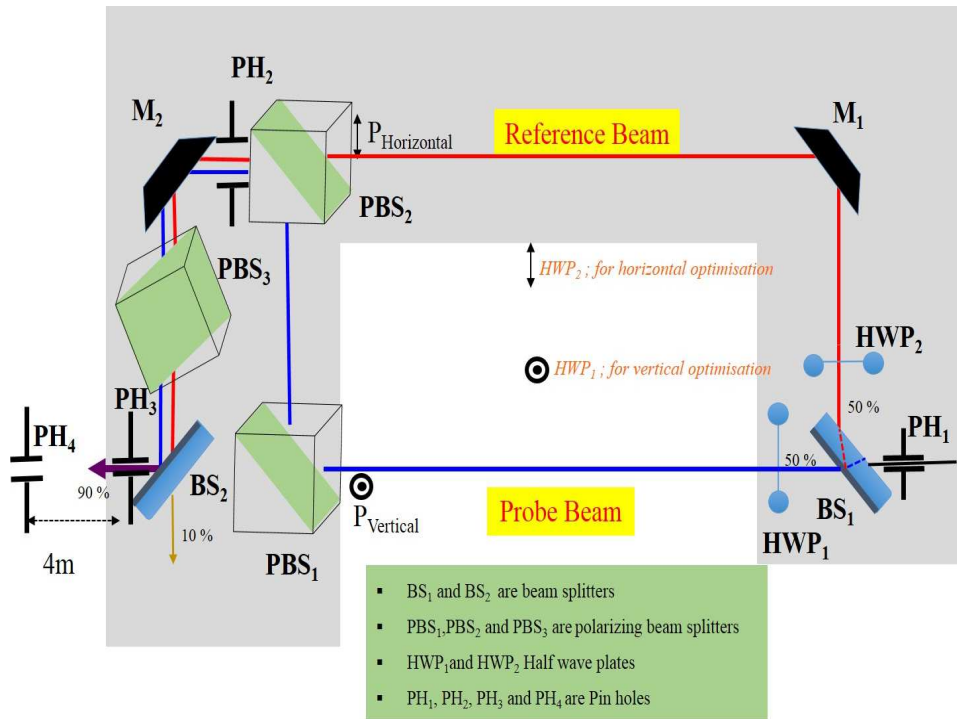


Figure 4.13: First interferometric setup. All the optical elements are 1 inch. For simplicity, the plasma slab is not reported in the probe beam.

The first experimental setup, shown in Fig. 4.13, was used until 04/05/2015.

In this setup,

- the 300 ns long probe laser of wavelength 527nm (beam diameter \approx 1 inch, energy on the target: few tens of microjoules) first passes through an alignment pinhole PH_1 ;
- the non-polarizing beam splitter BS_1 transmits 50 % of the intensity of the incident beam and the remaining 50 % of intensity in the perpendicular direction. At this stage the two arms of the interferometer, namely the reference and probe beams, are produced;
- two half wave plates HWP_1 and HWP_2 are placed respectively in the path of the probe and reference beams. They allow to play with the polarization in order to optimize the fringes contrast, as it will be explained below;
- the vertically polarized probe beam passes through the target (plasma slab). Due to its polarization it is fully reflected by the polarizing cube beam splitter PBS_1 towards the polarizing cube beam splitter PBS_2 ;
- the reference beam is reflected by the mirror M4 on to this cube splitter PBS_2 ;
- At the output of PBS_2 , the two beams overlap but they have orthogonal polarizations, and can't interfere. They then travel through a polarizing beam splitter PBS_3 whose axis makes an angle of 45° with the common direction of incidence of the two beams. This rotates the polarizations of the reference (horizontally polarized) and probe (vertically polarized) beams along the same axis;
- At this stage, the beams share the same polarization and interfere;
- A last non-polarizing beamsplitter plate (90-10 %) BS_2 is placed after PBS_3 to enable the propagation of the two beams on the same axis as the laser beam at the entrance of the interferometer;

The fringes are recorded on a HAMAMATSU C7700 VIS Streak Camera, located after the last alignment pinhole PH_4 . To this purpose, an imaging setup makes the image of the target longitudinal axis (i.e. along the direction of the shock propagation) on the streak slit. This is done with an achromatic spherical doublet of focal length equal to 1000 mm. The magnification is measured using an AGAR grid to 2.26, which means that $10.6 \mu\text{m}$ on target are recorded by one pixel (size of the pixel $24 \mu\text{m}$) on the streak on both directions (Fig. 4.13).

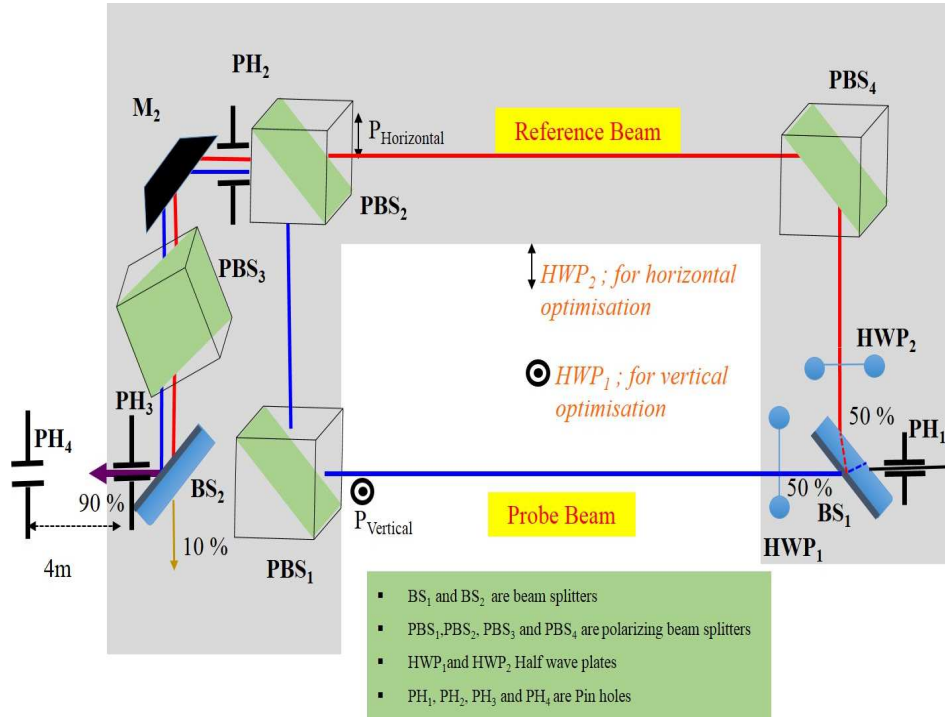


Figure 4.14: Second interferometric setup.

Role of the polarizing devices

Let us suppose that the polarization state of the incoming beam is unknown. The polarization of the probe beam is then fixed to be vertical by the polarizer HWP_1 . Reflected by the polarizing cube PBS_2 , it remains vertical at the entrance of PBS_3 . On this side, the polarization of the reference beam is set to be horizontal after the cube BS_1 using the polariser HWP_2 , and is transmitted as horizontal by PBS_2 . The rotation of PBS_3 allows to project part of the two beams on a common polarization axis and to interfere.

This setup presents the following interest: the intensity of the laser beam in the two arms of the interferometer can be modified (and thus the contrast of the fringes) can be optimized using the two polarizing plates HPW_1 and HPW_2 . However, as the multimode laser is not fully coherent, the dark fringe (zero net intensity) has never been obtained.

Moreover, the setup is designed to also allow alignment and adjustment of the imaging setup with a green HeNe laser, which shares the same path as the probe beam up to PBS_1 .

A more optimized setup was used after 05/05/2015 (i.e. shot number #48033), where the mirror M_1 in the reference beam was replaced by a polarizing beam splitter PBS_4 reflecting the probe beam like the mirror M_1 (Fig. 4.14). This was done in order to reduce the difference between the

two paths l_1 and l_2 and then to optimize the fringe contrast. This was more suitable due to the short coherence length (1- 2 cm) of the probe laser.

Streak camera

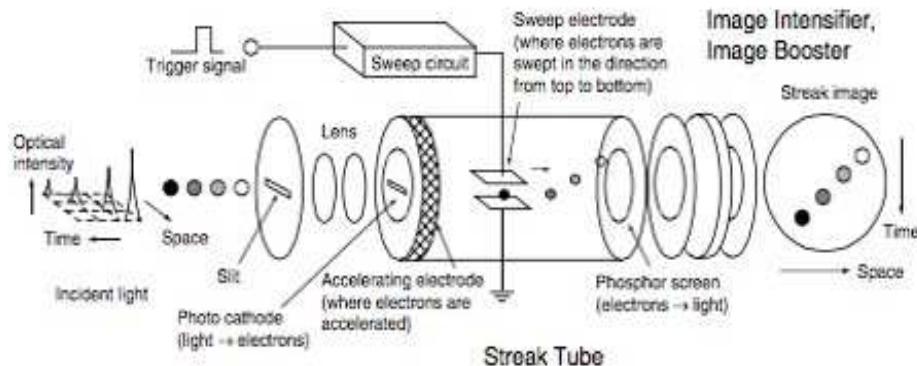


Figure 4.15: Schematic of the Streak camera (from Hamamatsu notice).

A streak camera is a setup, which allows measuring the temporal variation of a fast signal, which is recorded on its slit. As indicated in the notice of the Hamamatsu C770 camera, the light pulse first passes through the slit, then it is focused on the photocathode (size 7×17 mm) of the streak by an input optics. The visible photons are converted into a number of electrons, which is proportional to the intensity of the incident light. These electrons are accelerated and conducted towards the phosphor screen when a high-speed voltage, which is synchronized to the incident light, is applied. As a result, the electrons are swept at high speed from the top to the bottom, after which they are bombarded against the phosphor screen of the streak tube and converted through an output optics to an optical image on a dual mode cooled CCD camera with 512×512 pixels (Fig. 4.15). In the PALS experiment, the sweeping times were kept either 50 or 200 ns. The CCD pixel size is $24 \times 24 \mu\text{m}$.

The streak camera can be operated with time swap mode, with the slit of the camera almost closed. The record consisted then in images (position along the slit versus time), as discussed above, or in a static mode (no time swap) whatever the slit aperture. In that case, the record is a usual 2D spatial image of the object.

During the experiment, we have taken reference images (without any fringe) for every target as shown in the Fig. 4.17a for one target example. In order to record such images, we blocked the reference beam and let the probe beam only to illuminate the target in a static mode, and with the slit open. Then we reduced the slit width to its nominal value ($200 \mu\text{m}$). This enabled us to have the visualization of the portion of the target which was

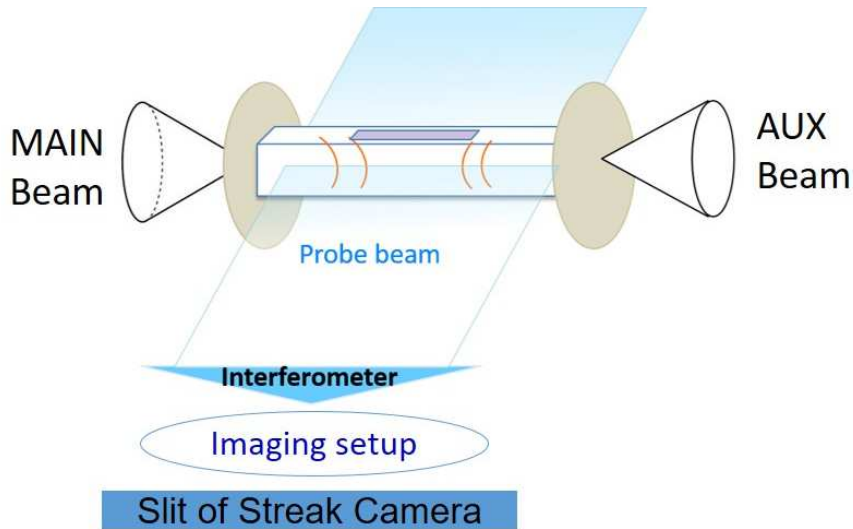


Figure 4.16: Imaging setup of the Mach Zehnder Interferometer setup operating in the longitudinal mode. The channel of the target is fully illuminated by the probe beam. In this mode, the lens images the axis of symmetry of the two shock waves along the slit of the streak camera.

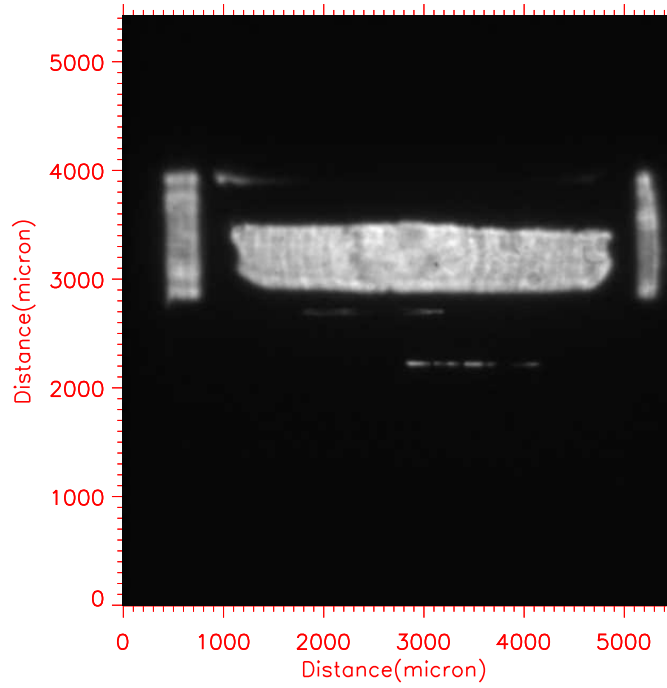
imaged in the slit on the target and also to locate the position of the pistons before the shot. This image is termed as the *reference target image*. Then, the system was placed in the interferometric mode and the fringe pattern was optimized to be perpendicular to the slit and thus, in the *longitudinal mode*, perpendicular to the direction of the shock propagation.

The Fig. 4.17b reports such a typical interferogram recorded during our experiment (cf. Fig. 4.13). The horizontal axis corresponds to the direction of the shock propagation (with a total scale of 5.4 mm on the target) and the vertical axis corresponds to time (scaling 200 ns).

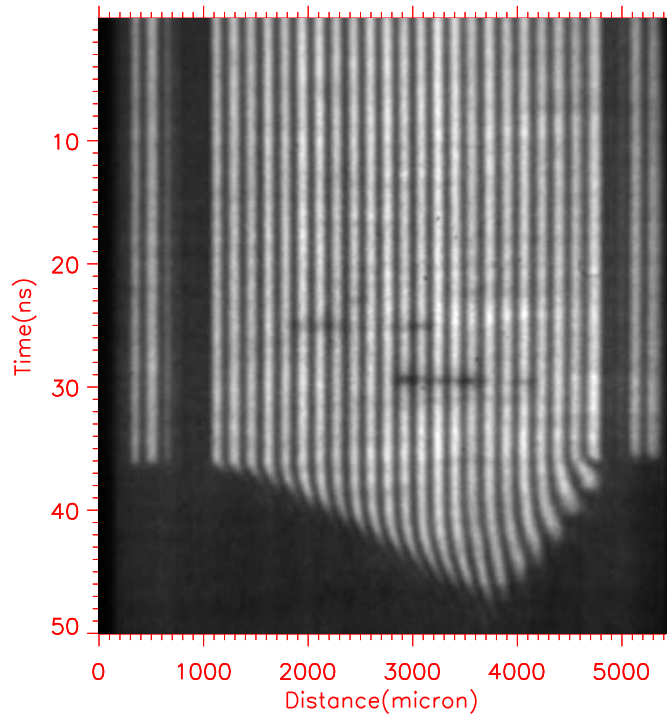
4.4.2 XUV Spectroscopy

The time and space integrated XUV plasma emission are recorded with a Flat Field XUV spectrometer (grazing incidence XUV spectrometer) using a concave grating. Typical ray tracing a grazing incidence XUV spectrometer is shown in Fig. 4.18. In practical, the entrance slit was removed as the plasma extension was small. In the Fig. 4.19, the drawing of the XUV spectrometer setup scheme (red color) is presented together with the spherical chamber and the target. The XUV spectrometer is installed on the top of the spherical chamber, which allows the XUV emission, passing through the Si_3N_4 membrane on the top of the target (see section 4.2.2), to be recorded.

A cooled Andor DX440 CCD (without glass protection) is attached to the spectrometer to record the spectrum of the XUV radiation between 12



(a)



(b)

Figure 4.17: (a): Reference 2D image of a target, before the shot, recorded on the Streak camera. The positions of the two pistons closing the 4 mm long target are located at 800 and 4800 μm . The dark zones along them (between 800 to 1000, and 4600-4800 μm) corresponds to the glue. This glue is then visible through vertical black strips in the interferometric record. (b): Corresponding interferometric time-space record.

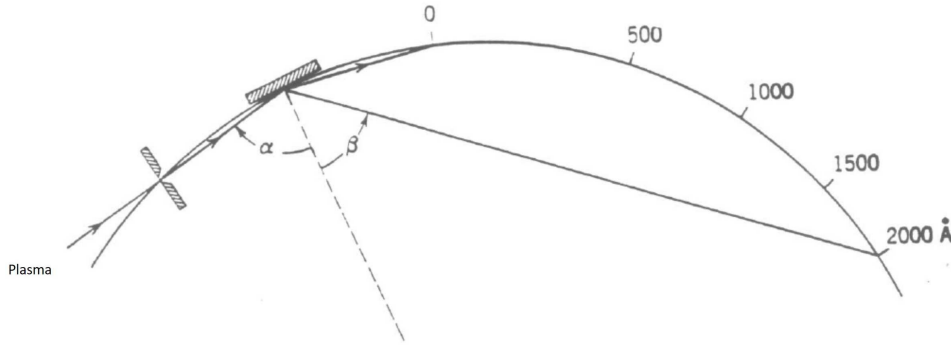


Figure 4.18: Typical ray tracing in a grazing incidence XUV spectrograph. The detector (GMCP or image plate) is installed tangentially to the Rowland circle.

and 40 nm (31- 100 eV). Its characteristics are given in the Table 4.5. Two Al filters of thickness 0.8 and 1.6 μm protect the grating and the CCD camera from debris and visible light. The XUV images recorded on the CCD are time (300 μs) and space (~ 3 mm) integrated.

Andor camera (DX440)	
Pixel Size	13.5 x 13.5 μm
Area	27.6 (H) x 6.9 (V) mm
Active pixels:	2048 x 512

Table 4.5: Specifications of Andor CCD camera.

The curved grating (Table 4.6), used to focus the XUV emission on to the CCD chip, has a variable grooves spacing as shown in the bottom panel of the Fig. 4.19. A typical output record is also presented for illustration.

Grating	
Type	Diffraction
Grooves per mm	1200
Dimensions	30 x 50 x 10 mm
Radius of curvature	5649 mm
Blazing angle	3.7 degree
Blazing wavelength	16 nm

Table 4.6: Specifications of the XUV grating.

4.4.3 Visible spectroscopy

In addition to the interferometry and XUV spectroscopy, we have also implemented a time- and space-resolved visible spectroscopic plasma emission diagnostic.

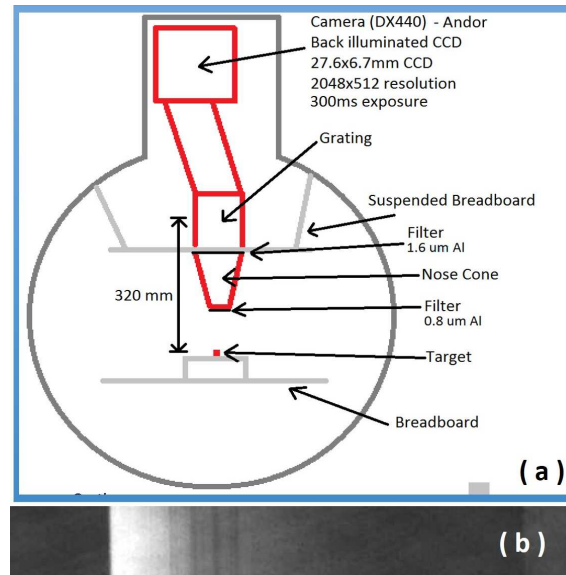


Figure 4.19: (a): Setup of the XUV spectrometer in the spherical chamber; (b) Typical record between ~ 10 and 40 nm is shown in the bottom panel.

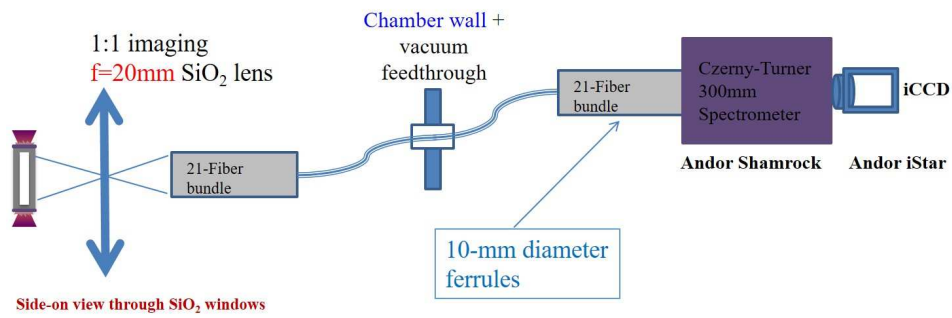
The core of the diagnostics is a Czerny-Turner 300 mm Spectrometer² located outside the vacuum chamber. The light of the plasma is injected on the slit of this spectrometer through a fibers bundle. This bundle consists of three sets of an aligned seven individual fibers looking at different sections of the target channel through an imaging lens located in the black tube of Fig. 4.9. The time resolution is performed through an iCCD camera located at the exit port of the spectrometer (Fig. 4.20a).

A typical record is reported in Fig. 4.20b. The results of this diagnostics show several signatures which differ along the tube. Most of them are in absorption and could be linked to the heating of the target silica window. Their interpretation is not yet achieved and will not be presented in this study.

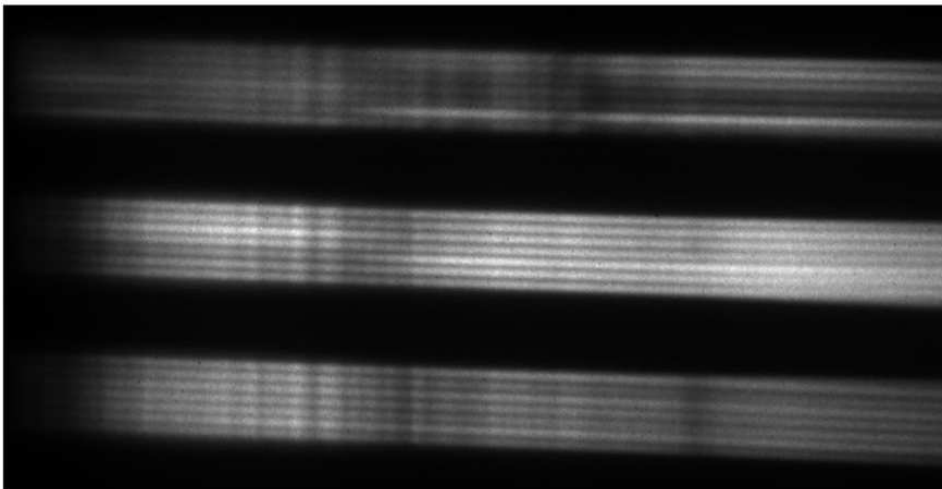
4.5 Summary

In this chapter, I have presented the details of our experimental setup and diagnostics. The next chapter will be dedicated to the presentation of our records, results and their analysis.

²see <http://www.andor.com/spectrograph/shamrock-spectrograph-series>



(a)



(b)

Figure 4.20: (a): Schematic of setup employed to record the time and space visible plasma emission. (b): A typical spectrogram.

Results and interpretation

Contents

5.1	Visible interferometry	71
5.1.1	Longitudinal interferometry: shock speed and electron density	74
5.1.2	Transverse interferometry: lateral extension of the shock	91
5.2	XUV Spectroscopy	92
5.3	Simulations based on experimental results	93
5.4	Summary	97

In the previous chapter, I presented a brief description of our experimental setup. This setup includes two main diagnostics, namely visible interferometry and XUV spectroscopy. The visible interferometry is an adequate tool to probe the electron density of the radiative precursor up to the critical density ($4 \times 10^{21} \text{ cm}^{-3}$ at the wavelength 527 nm of the probing laser), whereas the denser post-shock region is opaque to the visible light. XUV radiation is present in the whole shock structure and thus the time- and space-integrated XUV spectroscopy may allow exploring the self-emission coming from the post-shock and precursor regions.

In this chapter¹, I present the results of the both diagnostics with a particular focus on the interferometric data, which I have extensively studied with the help of a specific data analysis procedure that I have developed. I will then present the main results of the XUV spectroscopic diagnostics. The results will then be interpreted with the help of numerical simulations.

5.1 Visible interferometry

In the visible interferometry, the interferences between the main and reference beams overlapping on the detector produce a pattern of fringes, which follow the relative phase variations between the probe (which passes through the plasma) and the reference beams (see section 4.4.1 of the previous chapter for the experimental setup). The phase variation between two consecutive fringes of the unperturbed beams (i.e. without any plasma) is equal to 2π .

¹Most of results presented in this chapter has been published in Singh *et al.* (2017)

Then, in the presence of the plasma in the probe beam, these fringes become shifted due to the modification of the refractive index. More details about the principle of the interferometry and the Mach-Zehnder interferometric setup may be found in the APPENDIX A, and we recall here only the expression of the phase shift:

$$\Delta\phi \approx -\frac{\pi d}{\lambda N_c} \langle N_e \rangle \quad (5.1)$$

where $\lambda = 527$ nm is the wavelength of the probing laser, $N_c = 4 \times 10^{21}$ cm⁻³ the critical density at this wavelength, and $\langle N_e \rangle$, is the electron density, averaged over the laser path d in the cell, and is defined as:

$$\langle N_e \rangle = \int_0^d \frac{N_e(z, t) dy}{d} \quad (5.2)$$

In order to deduce the electron density, it is necessary to follow the evolution of the positions of the maxima (respectively minima) of the fringes versus time. To this purpose, I have developed a specific data treatment pipeline in the interactive data language (IDL)². To improve the visibility of the fringes obtained in the interferograms, I processed the images with the Fast Fourier Transform (FFT) (Proakis, 2001). This treatment transforms the image from the spatial domain (i.e. our records) into the frequency domain. It then allows to define specific bands of frequency, which represent noise for the image and to clean them. The complete procedure is described below.

First, the FFT of the (512 × 512) interferometric image is derived. In the next step, the low and high-frequency filterings within the FFT of the image are done using low-pass F_- and high-pass F_+ Butterworth frequency filters (Proakis, 2001), as follows:

$$\begin{aligned} F_-(u) &= 1/[1 + C(u/u_0)^{2n}] \quad \text{with } C = 1, n = 1 \\ F_+(u) &= 1/[1 + C(u_0/u)^{2n}] \quad \text{with } C = 1, n = 1 \end{aligned} \quad (5.3)$$

where u represents the position in the FFT image and u_0 is the nominal filter cutoff frequency (represented as the width of the region in pixels). For the low-pass Butterworth frequency filter, u_0 is considered to be 55, whereas for high-pass Butterworth frequency filter it is taken to be 45. The values of u_0 are defined manually by a trial method with the aim to result in better noise reduction.

After this step, the inverse FFT of the filtered FFT image is performed, which results in a clean image in the spatial domain. In Fig. 5.1, the original record for the shot number #48055 (left), the FFT of this image (center) and the final frequency filtered image (right) are presented, showing how the

²http://www.ast.cam.ac.uk/~vasily/idl/idl_introduction.pdf

frequency filtering improves the fringes contrast and thus facilitates their analysis.

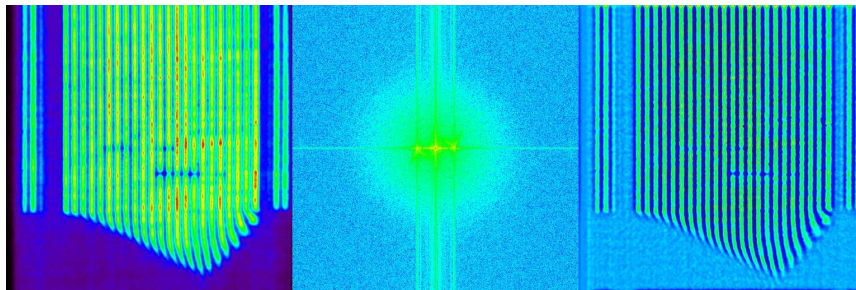


Figure 5.1: Original record of shot #48055 (left), FFT of the original image (center) and the frequency filtered image (right).

Next, the crucial task is to identify and to follow the fringes with the help of a precise determination of the intensity (pixel counts) maxima. In order to locate these maxima, I have adopted the following steps:

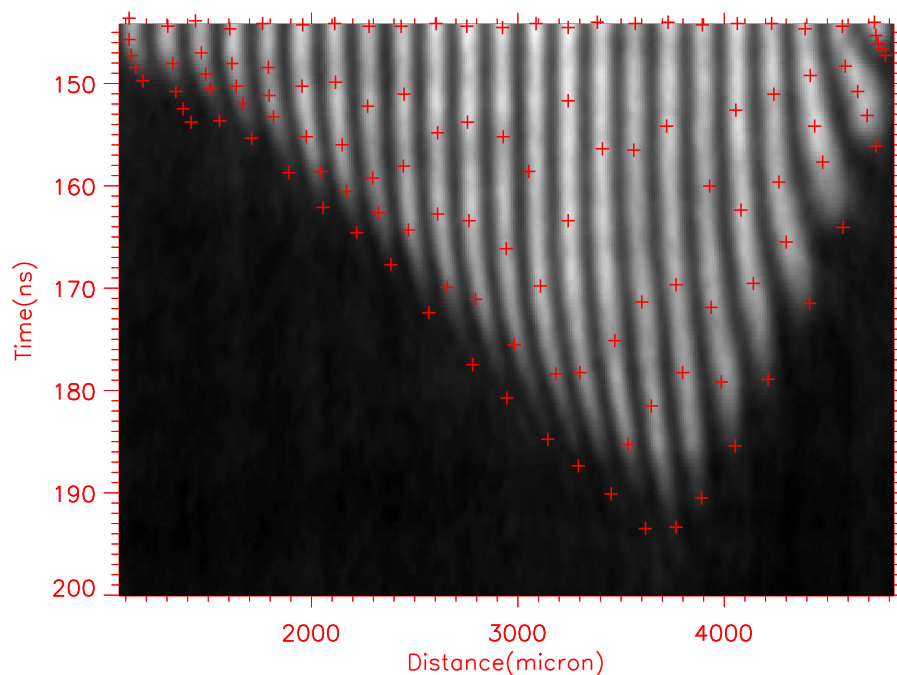


Figure 5.2: A cropped section of the record from shot the #48055. The first five positions have been selected manually '+' signs (in red color) on each fringe. On this record, the distance between two unperturbed fringes is correspond to 15 pixels (i.e. $159 \mu\text{m}$).

- Firstly, I have manually chosen a section of a typical record with the aim to select only the area associated with the shock dynamics.

- Next, five representative points are selected visually (‘+’ marks in red color) on each fringe, covering the important locations on the fringe (c.f. Fig. 5.2). They serve as the input to the spline interpolation for estimating all intermediate pixels locations along the fringe (see Fig. 5.3a).
- In order to obtain the locations representing the fringe maxima, the spline interpolated location points are further refined by selecting the pixel of maximum intensity within ± 5 pixels of the respective spline locations in the X-direction (see Fig. 5.3b).
- The position of fringe maxima for the cropped image, obtained in an aforesaid manner, is shifted so as to represent the same points, however on the full-image (see Fig. 5.4).

The records obtained from the experiments have been processed in this way to estimate the shock section, speed, electron temperature, and density.

5.1.1 Longitudinal interferometry: shock speed and electron density

In the longitudinal interferometry, we perform, on the slit of the streak camera, the image of the axis of symmetry of the shock propagation along the tube to analyse the shock propagation in this direction.

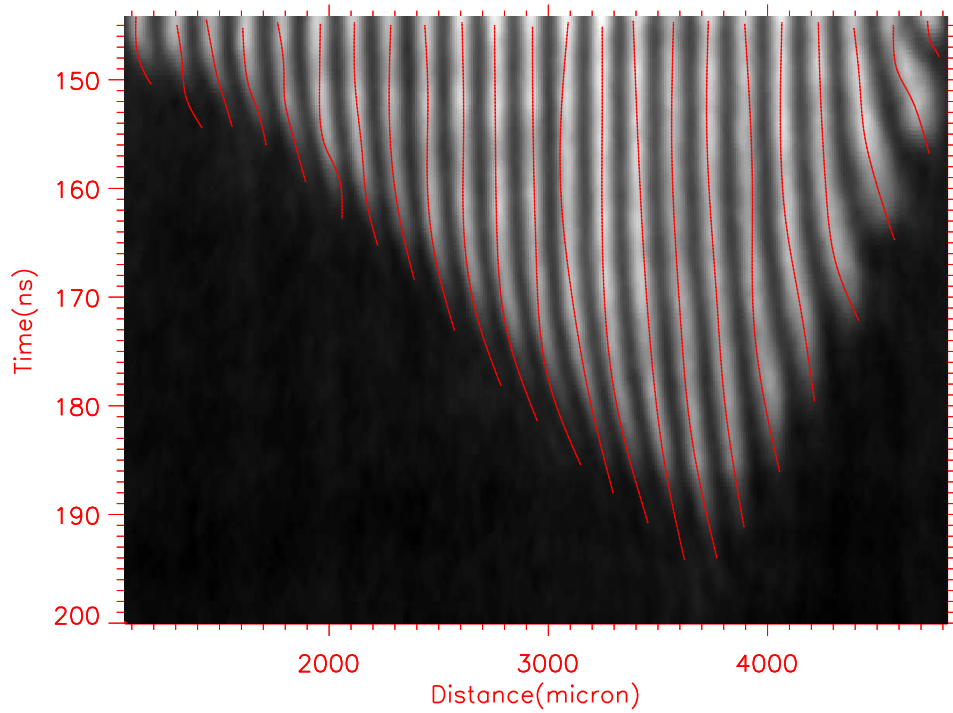
The interferometric images have been processed as explained previously to enhance the fringes contrast. The locations of the maximum intensity in each fringe are then used to derive the shock speed and the average electron density as will be presented below.

Shock speed deduced from the *last fringe* method

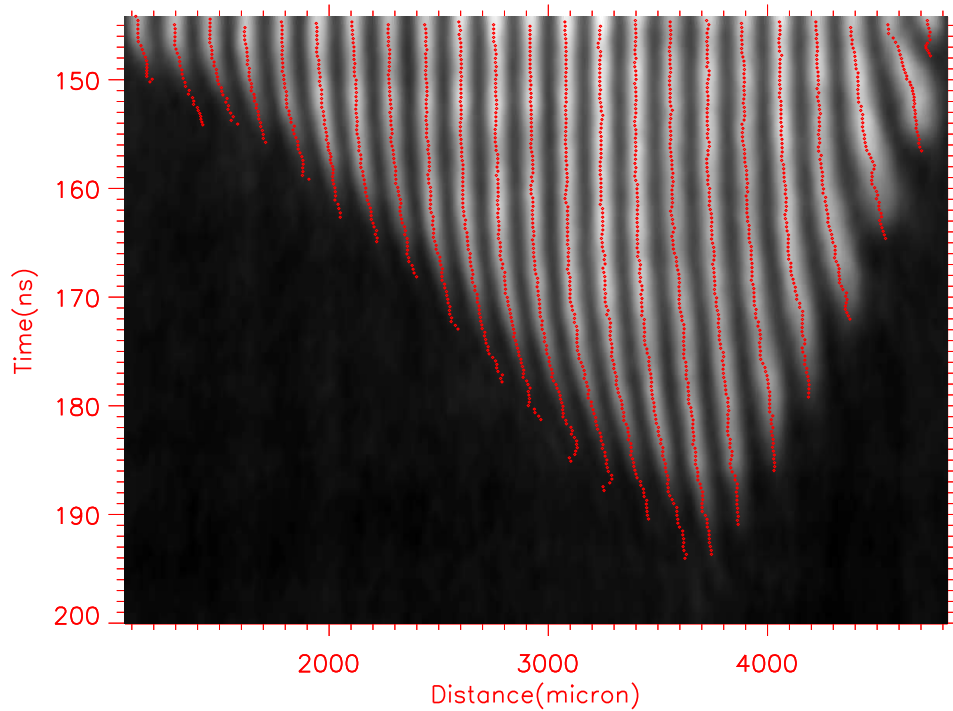
An estimation of the shock speed can be obtained through the interferometric image. In this section, I will present the method to derive shock speed based on the last visible end points of the fringes, also called *last fringe* method. This determination provides rapidly a qualitative estimation of the “shock” speed, which is based on the absorption behavior of the plasma (see Equation A.11 in appendix A) and not on the real position of the front discontinuity. The front discontinuity is not seen in the records due to the strong absorption.

At the positions of the last visible end points of the fringes, the electron density reaches the maximum value accessible to the diagnostic. The fringes are strongly bent and the absorption of the visible light becomes also important. Therefore, it is believed that the shock front is close from this location.

The locations of the fringe maxima have been already deduced following the analysis presented in previous sections. In this regard, the *best visible* end



(a)



(b)

Figure 5.3: (a): Representative points of the fringes as derived from the spline fitting of the 5 manually selected points (Fig. 5.2 (II)) on each fringe. (b): Positions of the fringes maxima along Y-axis for each fringe, derived by locating the points of maximum intensity in X-direction of the previous points obtained by spline fit.

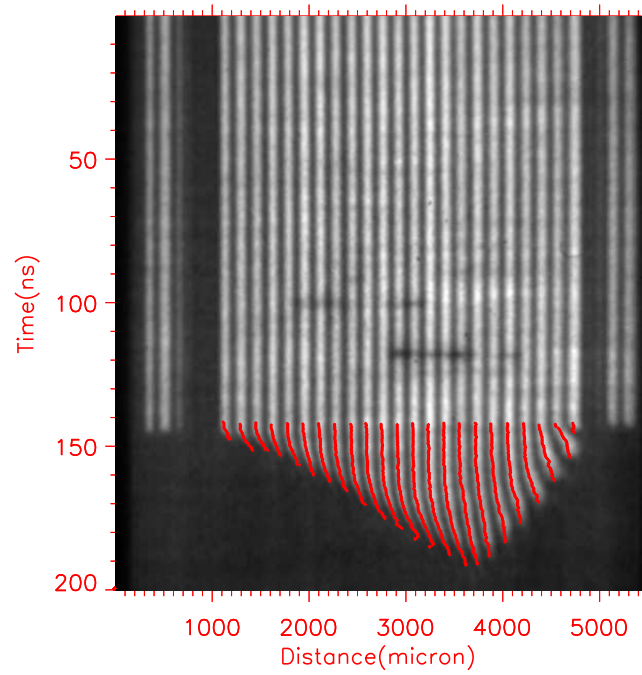


Figure 5.4: Fringe maxima on the full image.

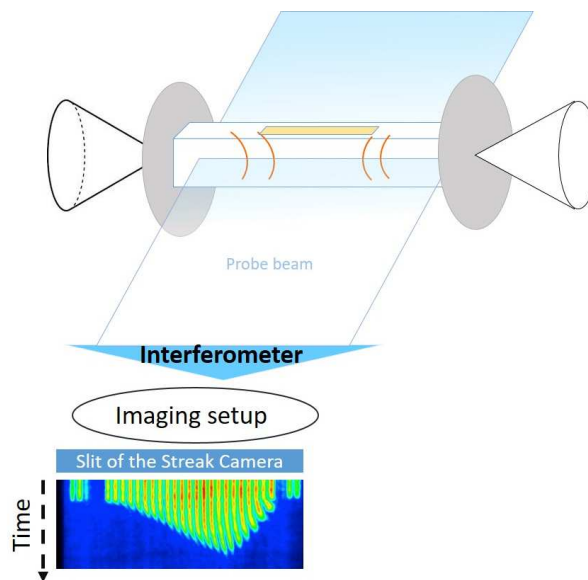


Figure 5.5: Imaging setup of the Mach Zehnder Interferometer operating in the longitudinal mode. The lens images the axis of symmetry of the two shock waves along the slit of the streak camera.

point of each respective fringe is considered for the average speed estimation for the shock.

At very initial time the increase in shock speed is non-linear. This non-linear trend may result in non-physical speed estimations. Therefore, I discarded the end points which appear to be within the five nanoseconds after the shock launching time (e.g. $t = 145$ ns on Fig. 5.6).

However, the above procedure may result in uncertainties as the selected end points may have different intensity (counts) values. In this regard, I have evaluated the uncertainty in the determination of the average speeds. To this purpose, I first selected the best visible end-point of a random fringe. Such an end point gives a reference intensity, which was then used to obtain, on the rest of fringes, the end points having close intensity. This procedure was performed thrice in order to deduce three sets of such end-points (see Fig. 5.6). Each of these three sets of points was then used to estimate the speed through a linear-fit method (lines in white, red and green). It may be noted that these sets of points and fitted lines are very close to each other. Therefore, it is tough to distinguish them on the Fig. 5.6. These three speed determinations enable us to derive an average value with an uncertainty which is equal to the standard deviation of these three values.

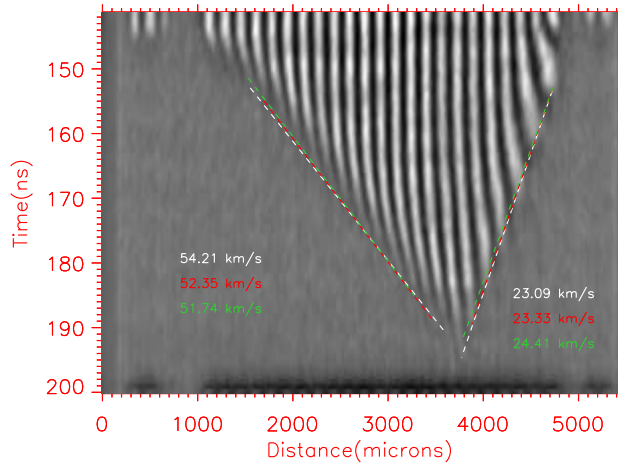


Figure 5.6: Interferometric image recorded for the shot #48055 in Xe at 0.1 bar. The shock speeds for the shocks driven by MAIN (from left side) and AUX (from right side) lasers are respectively equal to ~ 54 and 23 km/s. The time of laser arrival on the piston is at 146 ns. The positions of the Au-Xe interface on the record are respectively 950 ± 50 and 4950 ± 50 microns.

This estimation of the shock average speed is satisfactory for the records, in which the shock speed is almost constant throughout its propagation. However, the variation with the time of the speed may be substantial for some records. In such cases, the uncertainty in the average speed will be in principle higher than the previous estimations. Therefore, I introduced another

method to determine the average velocity: this velocity is then estimated during the initial and in final durations of the shock propagation by deriving the slope of points on the first, middle and last few fringes, respectively. The standard deviation, estimated by this method, is then termed as the uncertainty in the average speed of respective record.

Using these two methods, I have obtained two values of uncertainties for all the MAIN and AUX shocks observed in the experimental records. Finally, the largest uncertainty value of the two is considered as the final uncertainty in the estimation of the respective speed and is shown by error bars in Fig. 5.7a and 5.7b corresponding to the MAIN and AUX shocks, respectively.

The table 5.1 reports, for different noble gases, the values of the velocities recorded in several shots for the counter-propagating shock waves. In addition, one record (#48131) corresponds to the case of an isolated shock wave launched by the MAIN laser. The values of the MAIN and AUX laser energies are also reported. In some cases, the glue on the window prevented the probe laser to pass through the channel. Then it became impossible to derive any value for the velocity. In such cases, I put 'NA' for the corresponding shock velocity.

It may be noted that the shock speeds generated by the MAIN laser vary in the range of 30-55 km/s, while for the shock originated from AUX laser, the speeds vary between 10 and 30 km/s.

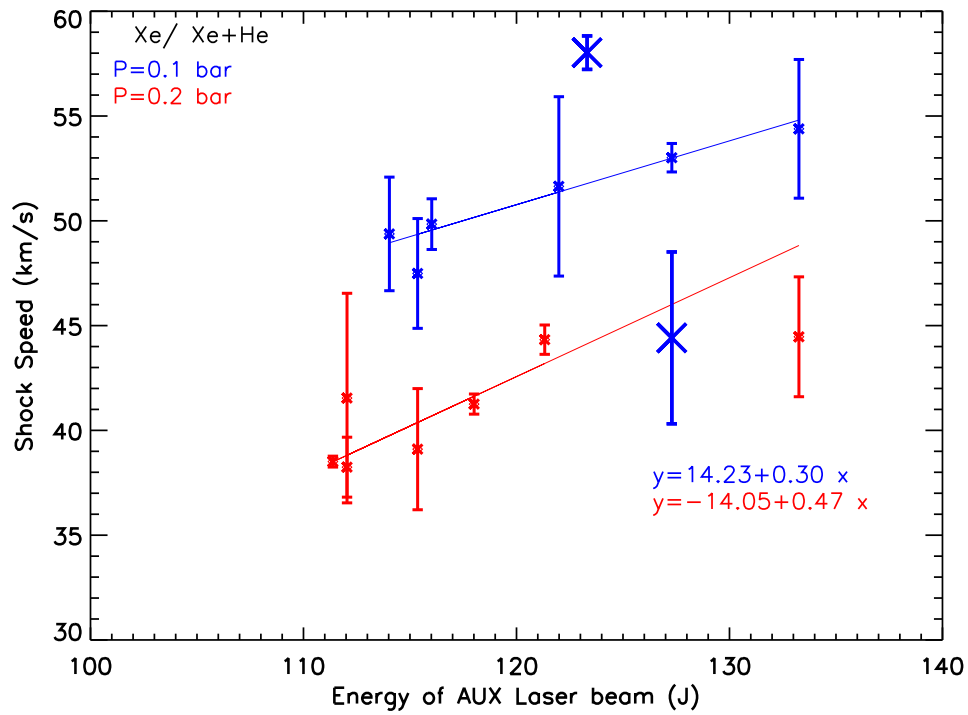
Variations with laser energy and pressure: the case of Xenon

When the number of records is sufficient to make a statistical analysis, we may analyse the variations of the shock speeds with the laser energy of the MAIN and AUX lasers. This is the case for Xe or Xe/He (90%-10%) mixture and for gas pressures ranging between 0.1 and 0.2 bar. At 0.1 bar, all the measurements concern Xenon ($\rho = 5.4 \times 10^{-4} \text{ g.cm}^{-3}$). At 0.2 bar, the records concern a mixture Xe/He (90%-10%, $\rho = 1.0 \times 10^{-3} \text{ g.cm}^{-3}$), except for one point at 121 J which correspond to the case of pure Xe ($\rho = 1.08 \times 10^{-3} \text{ g.cm}^{-3}$). We do believe that, taking into account the precision of our record, the introduction of traces of Helium do not affect much the dynamics of the shock wave, as the corresponding variation of mass density is negligible.

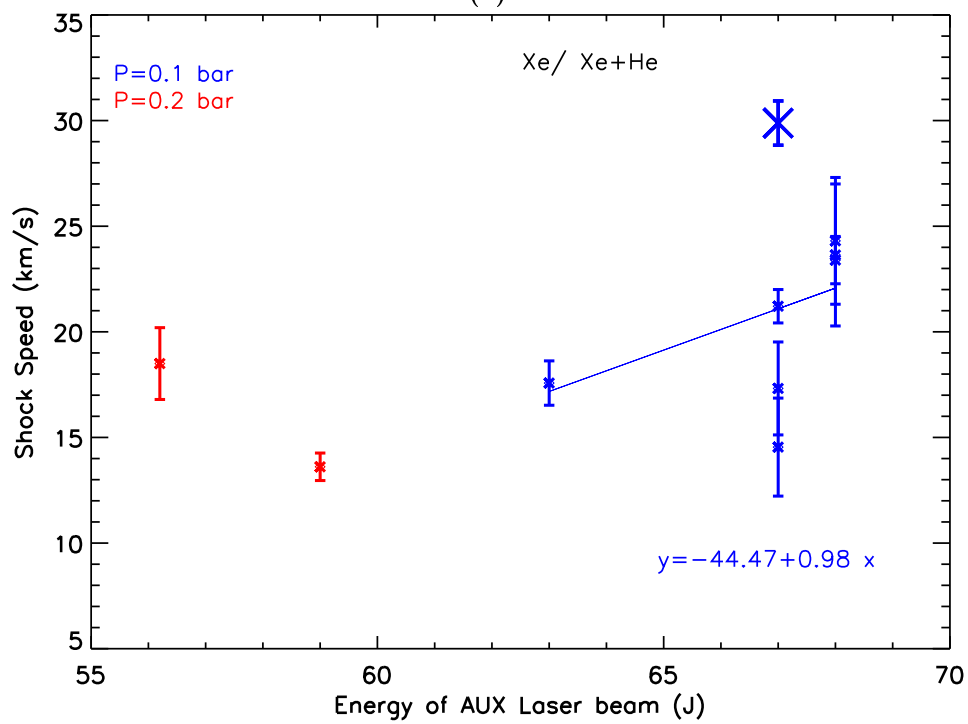
As expected, the shock speed increases with the laser energy and decreases with the pressure (Fig. 5.7a). A linear fit gives the following dependence of the speed in km/s with the MAIN laser energy (in J) at 0.1 and 0.2 bar respectively ³.

$$v_{0.1bar} = 14.23 + 0.30E \quad (5.4)$$

³Two outlier points have been discarded from the set corresponding to 0.1 bar. They are shown for information on the Figure.



(a)



(b)

Figure 5.7: (a) MAIN shock speed (calculated by the *last fringe* method) versus the MAIN energy, for Xenon or Xe/He mixture at different pressures, with the error bars. (b) AUX shock speed versus AUX energy, also for Xenon or Xe/He mixture at different pressures.

$$v_{0.2bar} = -14.05 + 0.47E \quad (5.5)$$

The speeds generated by the AUX laser are lower than the previous ones. Although the records are more sparse, we note that the speeds at 0.1 bar also increase with the laser energy. However, at 0.2 bar, I could not find similar trend due to the lack of records.

Variations with the gas

As can be seen from the Table 5.1, we have also performed several shots in Ar at 0.1, 0.2, 0.3 and 0.8 bar, one shot in He at 0.5 and one in Kr at 0.2 bar.

To compare the velocities obtained for the different gases one can either keep the pressure constant (i.e. the number of atoms) or the mass density. For a given mass density and laser energy, the velocity should be the same in the adiabatic limit. However, due to the radiation cooling and ionisation, this can not be the case. Nonetheless, if we compare the two records of Ar at 0.3 bar ($\rho = 4.93 \times 10^{-4}$ g.cm⁻³, E = 121 J) with Xe at 0.1 bar (5.4×10^{-4} g.cm⁻³, E = 133 J), we measure similar speeds (49 and 54 km/s). These two records are thus interesting to compare. This will be done later on in this chapter.

More generally, we note that the speed of Helium at 0.5 bar is higher by $\sim 40\%$ than for Ar at the same energy (see Fig. 5.8). This is not surprising for this lighter element (Table 5.2). However, it is important to note that the lack of shots prevents us to make any precise conclusion.

Except for this case and for the unique record of Ar at 0.2 bar, which gives also a higher velocity, the velocities of the other records follow more or less the variation with the energy than Xenon.

To compare the radiative effects, it seems justified to perform the comparison at a given shock speed, independent of the laser energy, and for mass densities which are close to each other. In the following, we shall thus compare the results of Xe at 0.1 bar (54 km/s, 5.4×10^{-4} g.cm⁻³), Ar at 0.3 bar (49 km/s, 4.9×10^{-4} g.cm⁻³) and Kr at 0.2 bar (55 km/s, 6.8×10^{-4} g.cm⁻³).

Line averaged electron density $\langle N_e \rangle$

I have estimated the electron density $\langle N_e \rangle$ of the plasma, averaged along the path of the probe laser beam, by analyzing the interferogram records, assuming the same section d of the plasma layer of 600 μm for both MAIN and AUX side shocks.

Shot	Gas	Pressure (bar) at 298 K	$E_{3\omega}$ (J)	MAIN shock speed (km/s)	E_{ω} (J)	AUX shock speed (km/s)
48033	Air	0.3	124	54±1	66	20±2
48034	Air	0.3	131	52±1	74	27±2
48076	Ar	0.5	100	41±1	66	18±1
48077	Ar	0.1	115	42±1	67	18±1
48078	Ar	0.3	112	46±3	65	25±2
48079	Ar	0.3	121	49±5	67	23±3
48080	Ar	0.8	103	38±2	62	21±2
48081	Ar	0.8	113	38±1	68	NA
48082	Ar	0.8	107	36±1	65	NA
48141	Ar	0.2	111	63±1	57	NA
48083	He	0.5	106	57±3	63	NA
48146	Kr	0.2	125	55±2	53	NA
48043	Xe	0.3	138	57±1	72	25±1
48051	Xe	0.1	123	58±1	67	30±1
48055	Xe	0.1	133	54±3	68	22±3
48057	Xe	0.1	127	53±1	68	23±1
48058	Xe	0.1	115	48±3	63	18±1
48059	Xe	0.1	116	50±1	67	21±1
48061	Xe	0.1	127	53±1	67	17±2
48065	Xe	0.1	122	52±4	68	23±3
48066	Xe	0.1	114	50±3	67	15±2
48067	Xe	0.5	115	39±2	65	NA
48068	Xe	0.5	109	36±2	65	12±2
48070	Xe	0.5	109	33±3	65	NA
48138	Xe	0.2	121	45±5	0	0
48131	Xe +He	0.2	112	38±1	0	0
48132	Xe +He	0.2	118	41±4	56	18±2
48133	Xe +He	0.2	112	41±3	56	NA
48134	Xe +He	0.2	111	38±1	60	NA
48136	Xe +He	0.2	115	39±3	59	14±1
48143	Xe +He	0.6	123	39±4	63	18±5
48144	Xe+He	0.2	133	45±3	66	NA

Table 5.1: Shock speeds estimated from the ‘last fringe’ method. ‘NA’ represents the entries which could not be deduced from the record. Further, entries in the bold font are discussed in detail in this chapter.

	Helium	Argon	Krypton	Xenon
Atomic Number	2	18	36	54
Atomic Mass	4	39.95	83.80	131.29
First Ionization Energy (eV)	24.6	15.7	14	12
Density (10^{-4} g.cm $^{-3}$) at 0.1 bar	0.16	1.64	3.44	5.39

Table 5.2: Atomic data and density at 0.1 bar (at room temperature) for He, Ar, Kr and Xe.

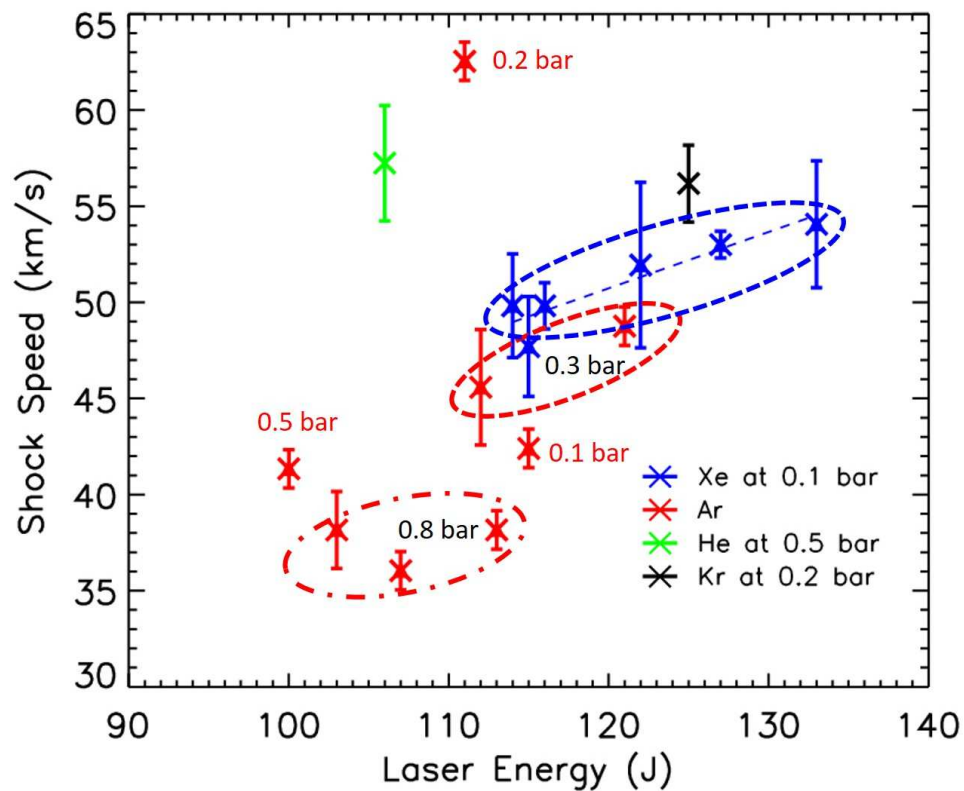


Figure 5.8: MAIN shock speed (calculated by the *last fringe* method) versus the MAIN laser energy, for Xe (at 0.1 bar only), Ar, He and Kr at different pressures, with the error bars.

It should be noted that the beam sections d_{MAIN} and d_{AUX} of MAIN and AUX lasers are approximately 600 and 300 μm respectively on the two pistons and that the transverse horizontal section of the shock tube is equal to $d_{tube} = 600 \mu\text{m}$. Thus the value of $\langle N_e \rangle$ computed for the shock wave launched by MAIN should be close to the physical local value N_e , supposing that the plasma is homogeneous along the transverse section. However, the value obtained for AUX is certainly larger by a factor, which can be estimated, at a first step, as the fraction of d_{tube}/d_{AUX} , giving a factor of about 2.

As explained in the previous section, the pixels representing the positions of the fringe maxima have been already determined with the best possible precision. Therefore, it is possible to calculate the relative phase shift (with respect to zero time) variation along y-axis (time axis) at each fringe maxima. Zero time is time of MAIN and AUX laser rival on the target. With these phase shifts, estimated at each pixel of each fringe, I then derived $\langle N_e \rangle$ using Equation A.22.

Let us take the case of three shots in Xenon for illustrating the method which will be followed (see the left panel of the Figure 5.9). The maximum density is estimated to be $\sim 1.1 \times 10^{19} \text{cm}^{-3}$ (corresponding to phase shift ~ 1.6). The number of subdivisions is taken to 5 bins, with the following phase ($\Delta\phi$) ranges (in the units of 2π) and average electron densities ($\langle N_e \rangle$):

- bin 1: $\Delta\phi \leq 0.6$; $\langle N_e \rangle \leq 3.9 \cdot 10^{18} \text{cm}^{-3}$ (white),
- bin 2: 0.6 - 0.8; $3.9 - 5.7 \cdot 10^{18} \text{cm}^{-3}$ (red),
- bin 3: 0.8 - 1.1; $5.7 - 7.5 \cdot 10^{18} \text{cm}^{-3}$ (blue),
- bin 4: 1.1 - 1.3; $7.5 - 9.3 \cdot 10^{18} \text{cm}^{-3}$ (green),
- bin 5: > 1.3 ; $> 9.3 \cdot 10^{18} \text{cm}^{-3}$ (magenta).

All the records shown in the Table 5.1 have been processed using this method. The limit of detection for the phase shift corresponds to 2 pixels, giving a threshold for the N_e measurement, $\langle N_{emin} \rangle$. This threshold differs from one record to another, due to the variation in the number of fringes (and thus the distance between two unperturbed fringes).

In order to make a comparative investigation of the shocks propagation and interaction in different gases, as already mentioned previously, I selected three cases (shot#48055, shot#48132 and shot#48138) relative to Xe (or Xe-He mixture), one case relative to Ar (shot#48079) and Kr (shot#48146). The corresponding experimental conditions are noted in bold in the Table 5.1.

$\langle N_e \rangle$ in Xenon

The Fig. 5.9 reports the interferometric records for the three Xenon cases. The top and the middle panels correspond to the propagation of two counter-streaming radiative shock waves at 0.1 (shot #48055) and 0.2 bar (#48132). For comparison, one record (#48138 bottom panel) is dedicated to the propagation of single shock (MAIN) at 0.2 bar. The Xe-He mixture (90 - 10 % in numbers of atoms) is used for the investigation in the case of 0.2 bar pressure, while it is only Xe in the case of 0.1 bar. As mentioned previously, at the precision of our records, we consider that this impurity concentration has a negligible effect on the shock speed and the precursor electron density. The limit of detection of $\langle N_e \rangle$ over the section of the tube (0.6 mm) is corresponds respectively to 9×10^{17} , 6×10^{17} and $6 \times 10^{17} \text{ cm}^{-3}$ for the Figures 5.9(a), (b) and (c).

The variations of $\langle N_e \rangle$ with the distance along the shock tube (i.e. parallel to the direction of the shocks) are reported in the right panel of Fig. 5.9 at 10 ns (in red), 20 ns (in blue), 30 ns (in green) and 40 ns (in magenta).

The interaction between the two precursors is clearly visible at 0.1 bar (Fig. 5.9(a)): at 10 ns, the interaction of the counter-propagating shocks has either not yet started or is below the sensitivity of this diagnostic. The interaction occurs at later times, with a typical signature which is as follows: the slope of $\langle N_e \rangle$ is decreasing from the left (MAIN precursor), passes through a minimum and increases at the right (AUX). The minimum itself increases with time up to $7 \times 10^{18} \text{ cm}^{-3}$ at 40 ns.

At 0.2 bar, we have not been able to record the collision in the temporal range (50 ns) of the streak. However, the two records (with MAIN only and with the two shock waves) indicate a precursor for MAIN. The two figures (Fig. 5.9(b)) and (Fig. 5.9(c)) show that the precursor of the MAIN shock wave is not influenced by the presence of AUX shock wave, up to 45 ns. There is no obvious indication about a precursor for AUX in the case of two counter-propagating shock waves (Fig. 5.9(b)). At this pressure and compared with the previous case at 0.1 bar, the absence of precursor for AUX may be attributed to: i) a low shock speed (18 km/s) combined with a larger pressure (hence, for a given gas, the precursor extension increases with the speed and decreases with pressure), ii) a too small longitudinal extension of the eventual precursor (see Fig. 5.9(b)) compared with the resolution of 20 microns (2 pixels). Our 1D numerical simulations with Xenon opacity multiplier $\times 20$ (not presented here), indicate a small precursor for AUX shock. At 15 ns, its extension is $50 \mu\text{m}$ ($900 \mu\text{m}$ for MAIN shock) with a typical electron density $\sim 3.5 \times 10^{19} \text{ cm}^{-3}$ ($2.3 \times 10^{19} \text{ cm}^{-3}$ for MAIN shock), which does not agree with the record. At 42 ns the precursor of MAIN reaches the AUX shock front and the profile is similar to the profile at 20 ns shown in Fig. 3.13a at 0.1 bar, with a plateau of almost constant electron density between the two fronts. This might be compatible with small bending

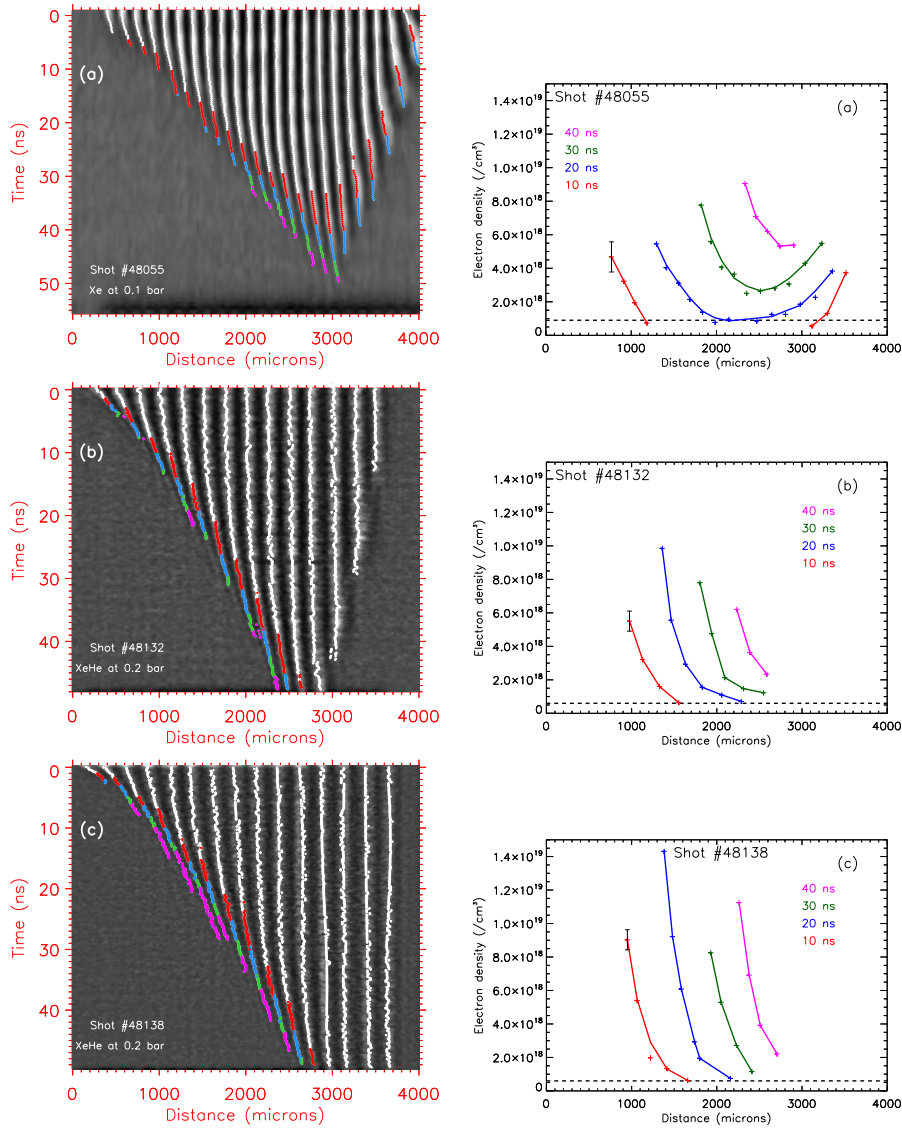


Figure 5.9: Left panel: interferometric records #48055 in Xe at 0.1 bar (a), #48132 in Xe+He at 0.2 bar (b) and #48138 in Xe+He at 0.2 bar (c). Right panel: electron density at 10, 20, 30 and 40 ns versus distance for these records. The positions of maxima have been identified on the records in the left panel. The time $t = 0$, corresponds to the time of laser arrival on the target and the position $x = 0$ corresponds to the interface between the piston (Au layer) and the gas. Its determination is precise within 100 microns. The distances between two unperturbed fringes for records #48055, #48132 and #48138 are 159, 244 and 244 μm respectively. The $\langle N_e \rangle$ uncertainty (± 2 pixels) is indicated by the error bar in the right panels. It corresponds respectively to $\pm 9 \times 10^{17}$, $\pm 6 \times 10^{17}$ and $\pm 6 \times 10^{17} \text{ cm}^{-3}$ for the figures (a), (b) and (c). The limit of detection (2 pixels) is presented by a dotted line on each figure.

of the 4th fringe (from the right) between 45 and 50 ns. As 1D simulations are known to overestimate the precursor electron density, 2D simulations are necessary for a more precise interpretation of the experimental result.

$\langle N_e \rangle$ in Argon and in Krypton

As seen in the Fig. 5.8, the variation with the laser energy of the shock speed in Argon at 0.3 bar (in the red dashed circle) is in good agreement with the corresponding one of Xenon at 0.1 bar (blue linefit). As these two cases have a comparable mass density of $\sim 5 \times 10^{-4}$ g/cm³, this qualitative agreement is expected.

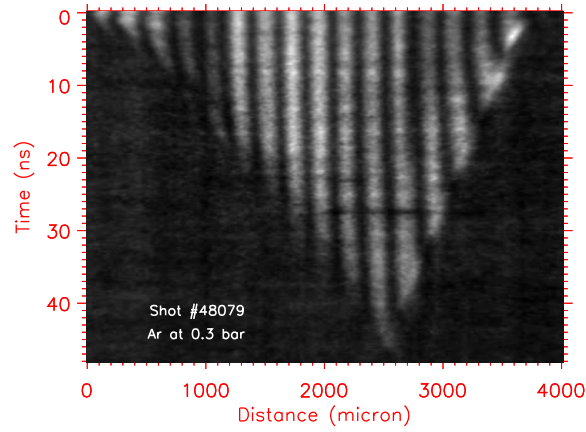
Taking into account the larger pressure (and thus density), the slope of the variation of the slower shock speeds in Ar at 0.8 bar (in a red dash-dot circle) with the laser intensity is compatible with the previous trends. However, any conclusion can not be derived for Argon at 0.2 and 0.5 bar owing to the scarcity of the records.

In Fig. 5.10, the interferometric record for Ar at 0.3 bar (shot #48079, 4.9×10^{-4} g.cm⁻³) is presented. The estimated speeds of MAIN and AUX shocks, deduced from the *last fringe method*, are respectively equal to 49 and 23 km/s, which are close to the speeds of 54 and 23 km/s recorded in Xe at 0.1 bar (shot #48055, 5.39×10^{-4} g.cm⁻³, Fig. 5.9(a)). Contrarily to the Xenon case, we do not see any significant bending in the fringes. The maximum fringe shift is reported in red on the fringe #1. The corresponding electron density is equal to 3.8×10^{18} cm⁻³.

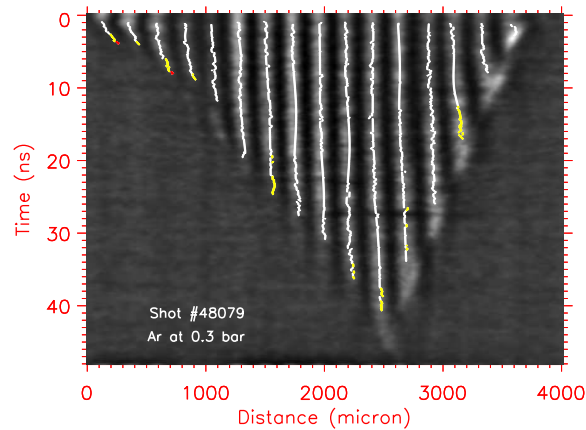
Thus obviously, the radiation effects are less important for Argon than for Xenon at the same density and speed. Part of this difference could be attributed to the huge difference in the atomic numbers (40 and 131) of the two gases, which leads to different peak temperatures for the ions as expected from equation 8.4 of chapter 2. However, the post-shock temperatures deduced from the jump relations for a real gas (Chapter 2) without radiation are very close (~ 25 eV), and thus this could be not the relevant explanation.

To clarify this, I performed HELIOS/PROPACEOS simulations for two counter-propagating shocks at 53 and 23 km/s, respectively in Ar and Xe, at the same initial mass density (5.4×10^{-4} g.cm⁻³) without any opacity multiplier. I have also reported, for information, the case of Xenon with an opacity multiplier equal to 20. The simulated temperature profiles are shown in the Fig. 5.11. One notes immediately that the precursor extension is smaller for Ar than for Xe. The peak temperatures of the MAIN shock are respectively ~ 21 eV (16 eV for opacity multiplier=20) for Xe and 21 eV for Ar. In all the cases, the post-shock temperatures are equal to ~ 11 eV. This indicates that the temperature is not the main explanation of the differences in the precursor length.

More interesting are the differences in the Rosseland opacity (here per unit of length), which is reported in the Fig. 5.11b. We see that, close to the

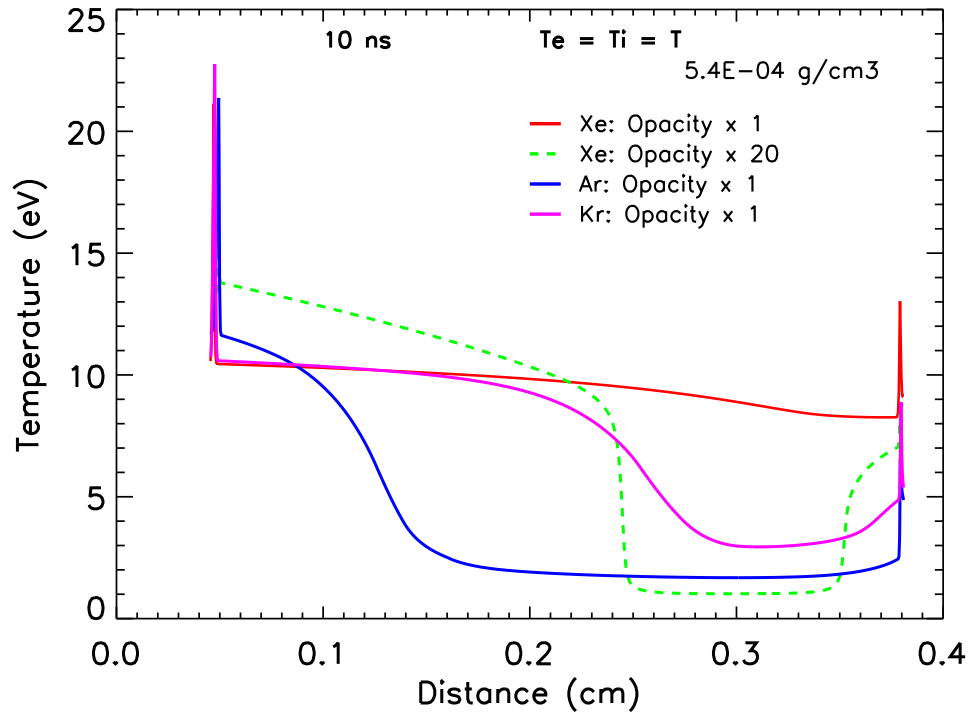


(a)

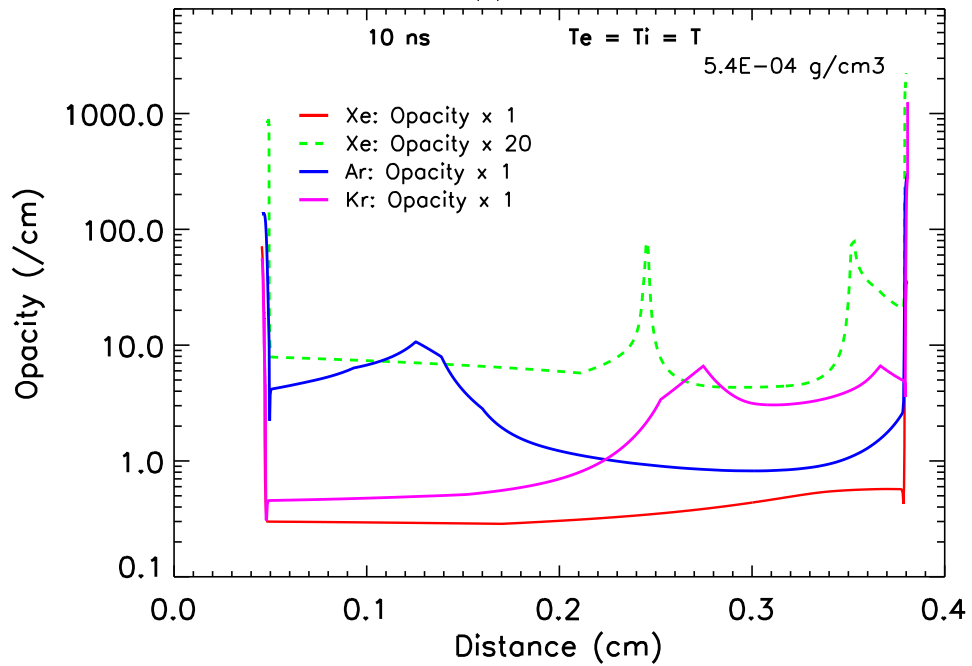


(b)

Figure 5.10: (a): Interferometric record in Ar at 0.3 bar (#48079). The estimated speeds for MAIN and AUX are 49 ± 5 and 23 ± 3 km/s. (b): Same record, where the fringes maxima are marked by points. The bins definition is as follows: bin 0: $N_e \leq 1.1 \times 10^{18} \text{ cm}^{-3}$ (white), bin 1: $1.1 - 1.8 \times 10^{18} \text{ cm}^{-3}$ (yellow) and bin 2: $3.9 - 5.7 \times 10^{18} \text{ cm}^{-3}$ (red). The time $t = 0$, corresponds to the time of laser arrival on the target and the position $x = 0$ corresponds to the interface between the piston (Au layer) and the gas. Its determination is precise within 100 microns.



(a)



(b)

Figure 5.11: Results for temperature (a) and Rosseland opacity (b) obtained from HELIOS simulation at 10 ns for two counter-propagating shocks at ~ 50 and 18 km/s, for Xe (with opacity multiplier 1 and 20), Ar and Kr at $5.4 \times 10^{-4} \text{ g}\cdot\text{cm}^{-3}$ initial mass density. A comparison Ar, Kr and Xe PROPACEOS opacity shown in APPENDIX B.

front, the Argon opacity is close to 4 cm^{-1} , which means that the radiation from the shock is absorbed within 2.5 mm. This has to be compared with the Xenon case (no multiplier), where it is equal to $\sim 0.3 \text{ cm}^{-1}$, which means that the hot precursor is almost transparent over the length of the tube. Thus, the different behaviors of the opacity in the upstream gas explain the quantitative difference in the development of the precursor. The sharp peak of the Xenon opacity, with the multiplier of $\times 20$, is due to the strong rise of the opacity when the temperature decreases below 5 eV, which marks the end of the precursor.

I will present now the case of two counter-propagating shocks in Kr (#48146 in Fig. 5.12) at 0.2 bar ($6.9 \times 10^{-4} \text{ g.cm}^{-3}$). In this case, unfortunately, the AUX shock could not be imaged completely due to the presence of glue at the right edge of the target cell, but the collision was recorded at $\sim 40 \text{ ns}$. The speed of the MAIN shock is estimated to be 55 km/s. Thus, despite a slightly higher initial mass density, this shock wave may be compared with the shot (#48055) in Xe at 0.1 bar ($5.4 \times 10^{-4} \text{ g.cm}^{-3}$, 54 km/s).

Despite the poor quality of the record and the inadequate temporal range (150 ns) selected on the streak camera, we note some bending in all the fringes, indicating the presence of precursor. The maximum fringe deviation (0.63 of the distance between two fringes) is noted at the end of fringe #2 which corresponds to the $\langle N_e \rangle$ value $4.5 \times 10^{18} \text{ cm}^{-3}$. The precursor seems to be more developed here than for the previous Ar case.

The result of the simulation in Xe and Kr with equal initial mass density $5.4 \times 10^{-4} \text{ g.cm}^{-3}$, and for the two respective shock speeds of 50 and 20 km/s, is reported in the Figure 5.11. The peak temperatures of the MAIN shock are respectively $\sim 21 \text{ eV}$ (16 eV for opacity multiplier = 20) for Xe and 22 eV for Kr. The post-shock temperatures ($\sim 10\text{-}11 \text{ eV}$) are close from each other.

The precursor extension in Krypton is smaller than in Xenon, which is logical if we consider the opacity values (Fig. 5.11b). However, if we take into account the multiplying factor for the Xenon opacity, the Krypton precursor is now more extended than for xenon, which is in contradiction with the experiment. This probably means that either the Kr opacity is under estimated by PROPACEOS or that our multiplier for Xenon is overestimated.

Synthesis

The previous experimental investigation confirms that the shock velocity increases with the laser energy and decreases with the mass density. Moreover, for our given shock velocity and mass density, the extension of the radiative precursor, in the experiment, decreases with the atomic number. Among Ar, Kr, and Xe, this last one appears to be the most adapted for the investiga-

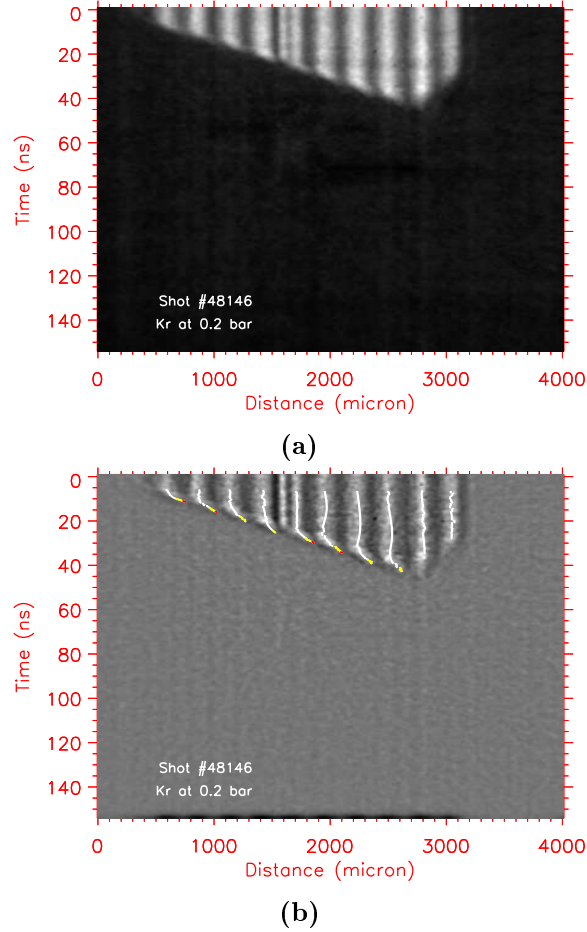


Figure 5.12: (a): Raw interferometric record in Kr at 0.2 bar (shot #48146). The estimated speed for MAIN shock is 53 ± 2 km/s. The time $t = 0$, corresponds to the time of laser arrival on the target. (b): Same record shown in (a) maxima is marked by colored points. The bins definition is as follows: bin 0: $N_e \leq 1.1 \times 10^{18} \text{ cm}^{-3}$ (white), bin 1: $1.1 - 1.8 \times 10^{18} \text{ cm}^{-3}$ (yellow) and bin 2: $3.9 - 5.7 \times 10^{18} \text{ cm}^{-3}$ (red). The time $t = 0$, corresponds to the time of laser arrival on the target and the position $x = 0$ corresponds to the interface between the piston (Au layer) and the gas. Its determination is precise within 100 microns.

tion of the radiative precursor. A similar behaviour is found also at ORION with higher speeds (Clayson *et al.*, 2017).

5.1.2 Transverse interferometry: lateral extension of the shock

The transverse interferometry is a different geometrical imaging setup of the Mach-Zehnder interferometer, which provides qualitative information about the curvature, localisation and transverse extension of the radiative precursor, and thus of the shock.

In the transverse interferometry, we perform the image of a transverse section (on the slit of the streak camera) of the tube which is located at a distance d_{slit} equal to 3 mm from the initial position of the MAIN piston. As the setup is originally adapted for the longitudinal interferometry, we use a Dove prism between the vacuum chamber and the streak camera to rotate the image by 90 degrees.

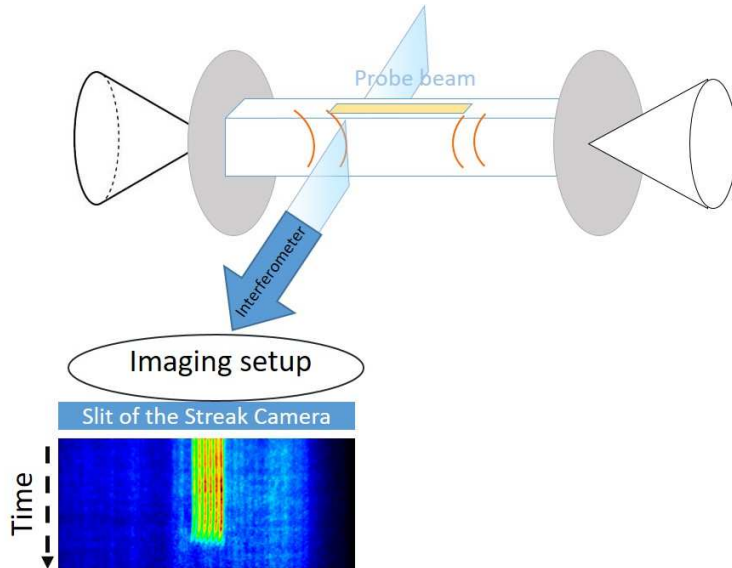


Figure 5.13: Schematics of the Mach Zehnder Interferometer setup to record transverse interferometric images. The lens allows to make, on the slit of the camera, the image of a section perpendicular to direction of shock propagation.

A transverse interferometric record for the MAIN shock alone in Xe at 0.2 bar is reported in Fig.5.14(a). The streak camera first records the unperturbed plasma on the section d_{slit} in the tube. Then it records successively the precursor and the post-shock (which is opaque to visible radiation and appears as a dark zone in the records). Taking into account the offset of 14 ns, the time of shock arrival is recorded at 72 ns after the time t_0 of laser arrival on the target and the shock speed is estimated to be ~ 35 km/s. Due to glue on one lateral window (on the right part of the figure), only 6 fringes

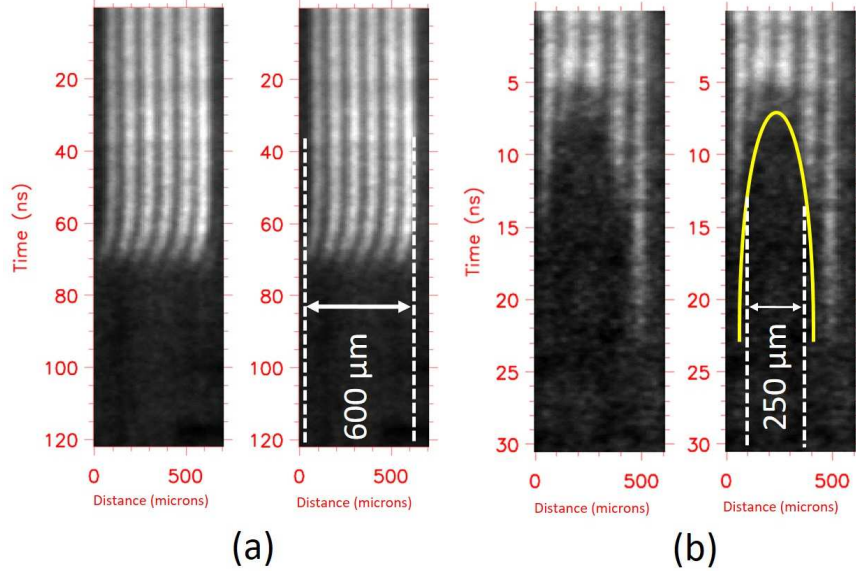


Figure 5.14: Transverse interferometric images for (a): shot #48111 (MAIN shock only). (b): shot #48130 (AUX shock only). The time is measured after an offset equal to 14 and 23 ns respectively after the time of the laser arrival on the target. The position 'zero' on the x-axis of each image corresponds to the base of the target.

are visible. The lateral extension of the shock structure at this time is derived to be $\sim 570 \pm 30 \mu\text{m}$ in qualitative agreement with the specifications of the MAIN phase plate, and the shape of the precursor is relatively flat. The axis of symmetry of the shock is determined to be at ~ 350 microns from the base of the target (i.e. $50 \mu\text{m}$ above the nominal value of $300 \mu\text{m}$).

A record for the AUX shock alone is shown in Fig. 5.14(b), which corresponds to a gate opening of 50 ns. The start time of the image has an offset of +23 ns from t_0 and the distance d_{slit} is set to 700 microns from the initial position of the AUX piston. The AUX shock duration extends from 30 ns to at least 34 ns after t_0 . The shock speed is then estimated to be ranging between 23 and 20 km/s. The shape of the precursor is strongly bent and we note a tiny shift of the second and third fringes (starting from the left) at ~ 8 ns. It may further be noted that the lateral spread of the opaque shock is ranging between $275 \pm 25 \mu\text{m}$ (which is also in agreement with the specifications of the AUX phase plate) and that the axis of symmetry of the shock system is also located at about $350 \mu\text{m}$ from the bottom of the cell.

5.2 XUV Spectroscopy

XUV emission originates from the comparatively hot portions of the plasma. In the present case, it corresponds to the post-shock and the precursor re-

gion which is close to the shock front. The spectrum, recorded by the XUV spectrometer, enables us to analyze the spectroscopic signatures of the radiative shock. One of the aims of this diagnostics was to identify the shocks collision, which leads to higher temperatures, through comparing the spectra obtained for the cases of single and counter-propagating shock waves. However, only a few records were possible to be obtained during the experiment, and unfortunately, the comparison with the case of an isolated shock wave was not performed.

Among the shots recorded, the XUV spectrum of the shot #48143 is presented herewith in detail. This shot was performed for [Xe (90%)+ He (10%)] mixture at 0.6 bar with laser energies of 123 J for MAIN and 63 J for AUX. The interferometric record of this shot is shown in Fig. 5.15. The MAIN shock speed has been estimated to be $\sim 39 \pm 4$ km/s. The estimated AUX shock speed (18 ± 5 km/s) is not precise due to the presence of glue on the right section of the record (note Fig. 5.15). In this interferometric record, we have not been able to retrieve the collision time. However, an extrapolation of the slope corresponding to the speeds ~ 39 km/s (MAIN) and ~ 18 km/s (AUX) enables us to approximately determine the collision time to be between 60 to 65 ns.

The raw spectrum (shown in Fig. 5.16a) recorded for the wavelength range of 15-35 nm (35-82 eV) shows the ‘L edge’ of Aluminum at 17 nm (34 nm in second order) in the first and second (34 nm)orders. These two wavelengths will be used for the wavelength calibration. The net spectrum, correction for the transmission (Henke, Gullikson, and Davis, 1993) of the 100 nm thick Si_3N_4 window ($3 \text{ mm} \times 0.4 \text{ mm}$) is introduced in Fig. 5.16b. A remarkable feature is a strong absorption dip between 19 and 22 nm (56-65 eV). This absorption probably comes from the colder layers (thickness 300 μm) between the shock heated plasma and the Si_3N_4 window. Few lines of Xe VII-VIII are identified through NIST database ⁴ as also Oxygen IV and V lines. Lyman lines of He II (from 1-2 to 1-7) are also present in the spectrum. This information will be useful for the estimation of the electron temperature.

5.3 Simulations based on experimental results

In this section, I will compare the experimental shock characteristics with the results of HELIOS simulations using the PROPACEOS equation of state and opacity (limited to 1 group). As indicated in the chapter 3, this opacity has been multiplied by 20 for the Xenon only. As our interest is to understand the shock structure in Xenon and not the laser matter interaction on the piston, we performed several simulations with Xe gas for various sets of fluences for

⁴http://physics.nist.gov/PhysRefData/ASD/lines_form.html

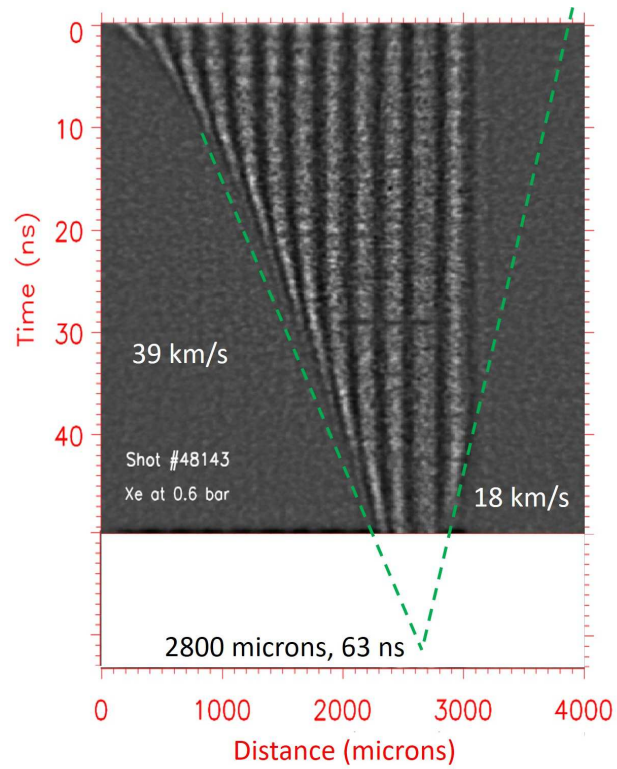
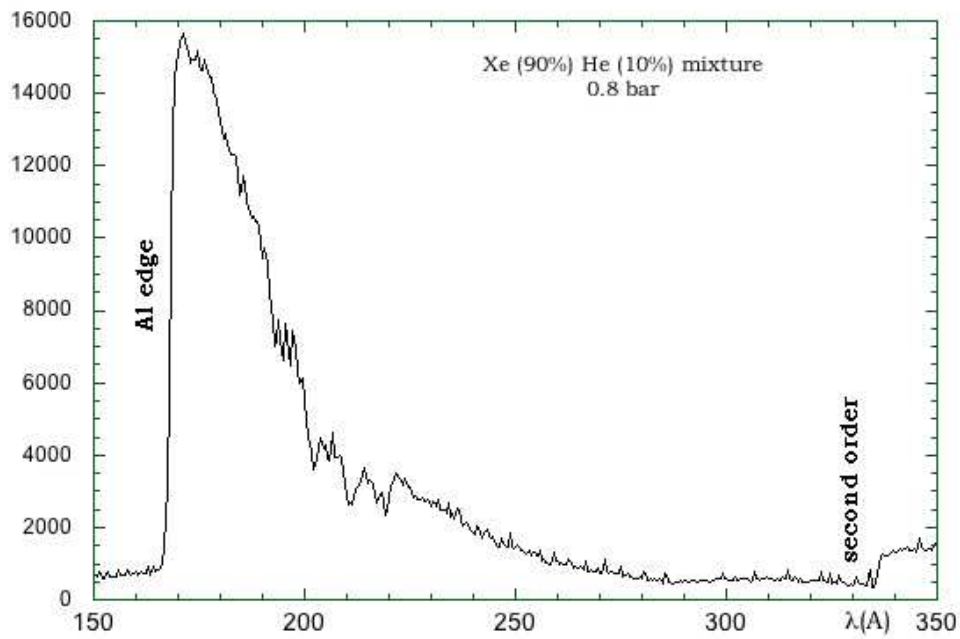
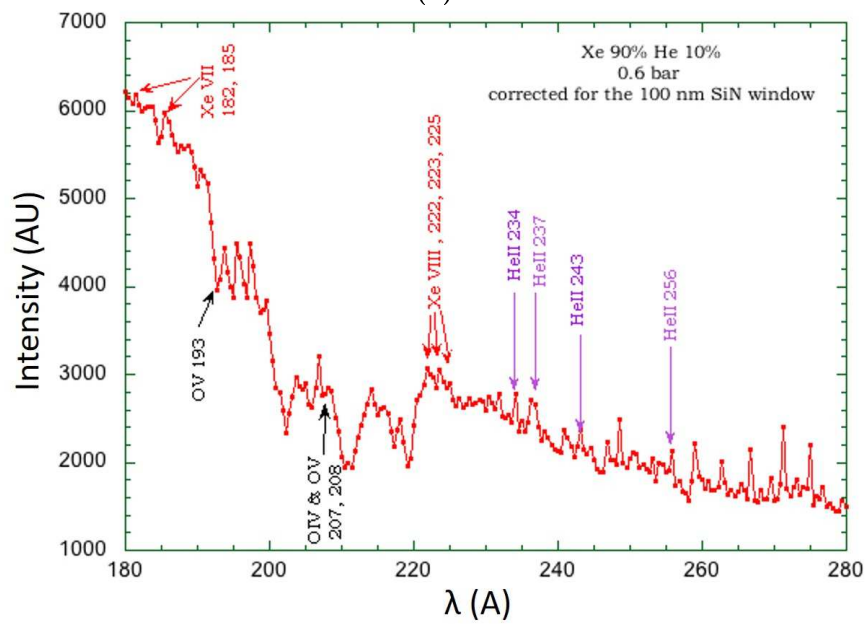


Figure 5.15: Interferometric image for the shot#48143. The time $t = 0$, corresponds to the time of laser arrival on the target and the position $x = 0$ corresponds to the interface between the piston (Au layer) and the gas. Its determination is precise within 100 microns.



(a)



(b)

Figure 5.16: Raw (a) and corrected XUV spectrum (b) for the shot #48143.

the MAIN and AUX beams in order to obtain the best agreement between the simulated and measured shock speeds.

To analyse the results from the shot #48055 (Fig. 5.9(a)), we set the fluences to 32000 & 7500 J/cm². This allows producing the experimental shock speeds 54 and 23 km/s in Xenon at 0.1 bar for the MAIN and AUX beams respectively. The two shocks appear in Xenon at 2 and 3 ns respectively for MAIN and AUX. The merging of the two precursors starts at ~ 15 ns and the shock collision time occurs at 47 ns. In Fig. 5.17, we present the electron density profiles from the simulation (dotted lines) and the experiment (solid lines) at 10, 20, 30 and 40 ns.

At 10 ns, the two simulated precursor extensions are 0.165 and 0.022 cm for MAIN and AUX respectively. The electron density is larger by a factor of 4 than in the experiment. The shapes of the precursors are also very different. However, this 1D picture supposes the plasma to be uniform within the tube. In reality, in the transverse direction, N_e is decreasing from the center to the walls, which results in a lower estimation of the average value ($\langle N_e \rangle$) compared to the value at the target center and in a smoother profile near 0.2 & 0.35 cm at 10 ns. It is also important to note that, for AUX shock, the average $\langle N_e \rangle$ value underestimates the local one by a factor of about 2 (as it is averaged over 0.6 mm instead of 0.3 mm). Moreover, our 1D simulation suffers from an inexact opacity and 2D effects are probably important especially for AUX. Thus we have here only a qualitative interpretation of the experimental results.

The interaction between the two HELIOS radiative precursors starts between 10 and 20 ns, like in the experiment. However, the shape, as well as absolute values of the simulated electron density curves, are not in agreement with the experimental results and the interaction is stronger in the simulation than in the experiment.

In order to interpret the spectroscopic data presented in section 5.2, we performed another 1D simulation in Xenon at 0.6 bar, and adapted the fluences to generate two counter-propagating shocks with the speeds 36 and 18 km/s, close to the experiment. The time evolutions of the electron density, mean charge and electron temperature at 56, 57, 58, 60, 64 and 65 ns are presented in Fig. 5.18. The two shocks appear in Xenon at 2 and 3 ns respectively for MAIN and AUX. Concerning AUX, the combination of a small speed and a relative high pressure does not allow to develop a radiative precursor, in agreement with the experimental results (Fig. 5.15), whereas the MAIN shock has a precursor and its length is increasing with time. The post shock temperature of the MAIN is ~ 21 eV and the ion charge ~ 9 . At 57 ns the precursor of MAIN reaches the AUX shock front. This time is out of our record (see Fig. 5.15) which means that the interaction effect is either absent or occurs at later times. The structure of the AUX post shock is modified by the interaction with the MAIN precursor (Fig. 5.18b). The shock collision occurs at 65 ns (Fig. 5.18a) resulting in the

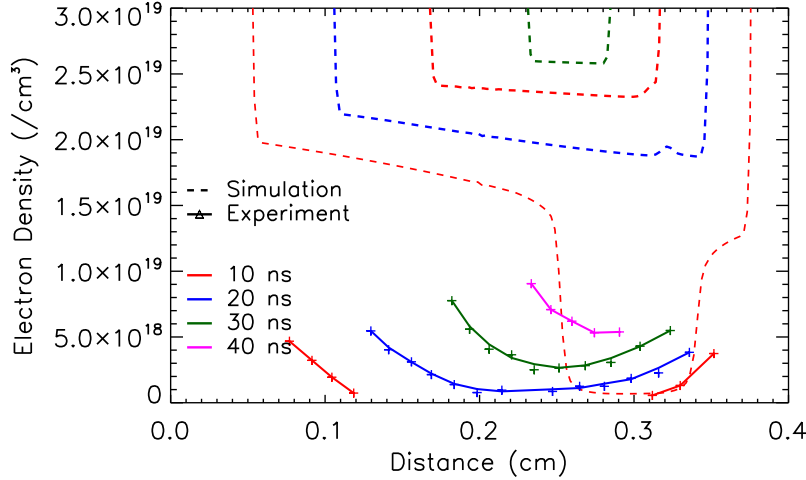


Figure 5.17: Recorded electron density (shot #48055) together with the HELIOS results (with Xenon opacity $\times 20$) at different times in Xenon at 0.1 bar.

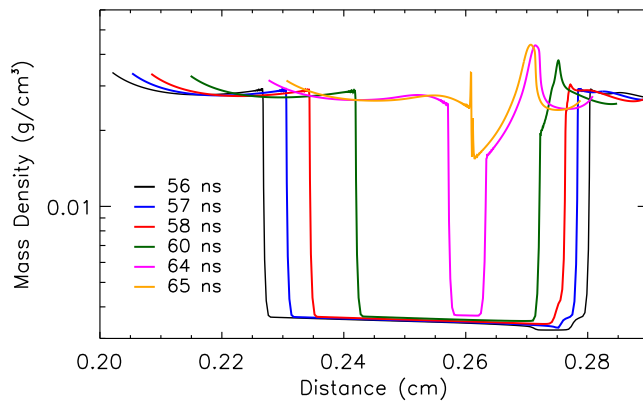
development of two reserve shock waves. At the collision time, the electron density, mass density, electron temperature and ion charge reach respectively $\sim 1.4 \times 10^{21} \text{ cm}^{-3}$, 0.034 g/cm^{-3} , 26 eV and 10. Mean charge is varying between 5-10 which compatible with the presence of lines of Xe VII-VIII in the experimental record shown in Fig. 5.16b.

Moreover, in order to interpret XUV spectroscopic results shown in section 5.2, Rodríguez performed qualitative preliminary computations (as described in Rodríguez *et al.* (2015)) of the XUV spectra emerging from a $600 \mu\text{m}$ thick plasma with two representative values of the mass density, $\rho = 3.2 \times 10^{-2}$ and $3.3 \times 10^{-3} \text{ g/cm}^3$. They show that the lines of HeII can only be observed at a temperature of $\sim 15 \text{ eV}$ and for the lowest density, i.e. in the radiative precursor.

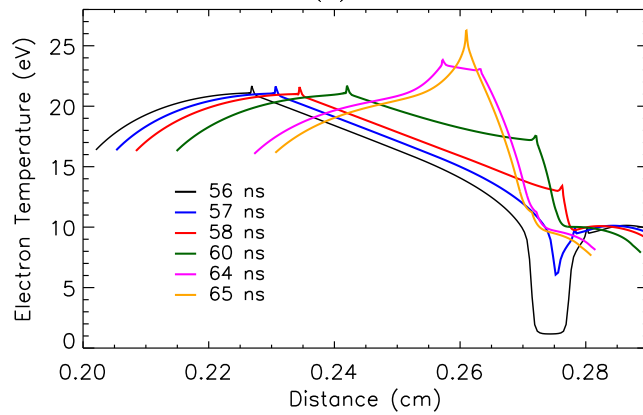
5.4 Summary

In this chapter, I have presented an extensive data analysis of few representative interferometric and spectroscopic records. The average shock speed and electron density have been estimated from the interferograms. The shock speeds of the MAIN and AUX radiative shock waves vary between ~ 30 -55 and 10-30 km/s, respectively and the averaged precursor electron density ranges between 10^{17} and 10^{19} cm^{-3} during the shocks propagation.

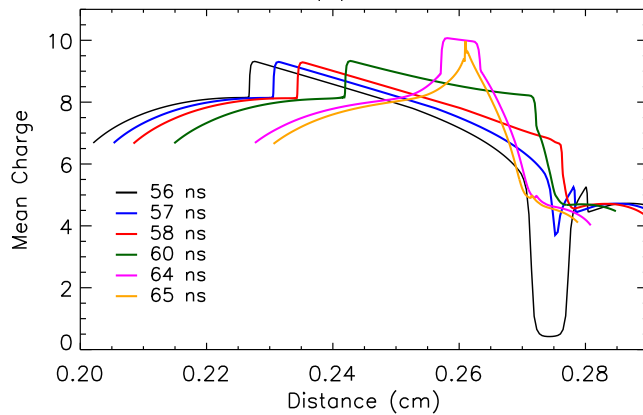
We have demonstrated the interaction effect between the two radiative precursors in the case of Xe at 0.1 bar, at 54 and 23 km/s. The interaction is clearly characterized in the experiment by the enhancement of the ionisation wave followed by the merging of the two radiative precursors at 20 ns. The collision time is recorded at 47 ns. Such behavior is reproduced by the



(a)



(b)



(c)

Figure 5.18: Time evolution of the mass density (a), electron temperature (b) and mean charge (c) at 56, 57, 58, 60, 64 and 65 ns within the shock tube derived from the HELIOS simulations (with Xenon opacity multiplier = 20), for two counter streaming shocks of ~ 39 and 18 km/s in Xenon at 0.6 bar.

simulation.

We have investigated this interaction at a larger pressure, 0.2 bar, with the following speeds ~ 41 km/s for the MAIN and ~ 18 km/s for the AUX shock waves. We do not record any experimental signature of the radiative precursor for AUX. Further, we have not been able to catch experimentally the collision time. The recorded precursor of MAIN is not influenced by AUX wave up to 48 ns (Fig. 5.9(b) and (c) in data analysis chapter), which is the limit of the record. On its side, the 1D simulation predicts a tiny precursor for AUX and that both precursors start to interact at 49 ns. This plausible shocks interaction, occurring at times which are outside of the record, can not be confirmed by our experiment.

The results of the transverse interferometry at 0.2 bar, with speeds of ~ 40 and 20 km/s indicate that the MAIN precursor has a lateral extension of ~ 600 μm whereas it is 300 μm for AUX. The precursor of MAIN is almost flat with a probable small bending at the edges of the tube, whereas the AUX precursor is more curved. This means that the 2D effects are more important for AUX than for MAIN. Still, in the case of Xenon, we have obtained information about the temperature and the mean charge of gas through our time integrated XUV spectra (shot#48143) in Xenon at 0.6 bar. From these results, we may conclude that the mean ion charge is at least equal to 6 and that the temperature has reached 15 eV.

Our simulations give a qualitative description of the shocks interaction when the laser fluence is adjusted to give the correct shock velocities. However, it is now well known that 2D simulations (together with state of the art opacities) fit better with experiments (González, Audit, and Stehlé, 2009; Leygnac *et al.*, 2006; Stehlé *et al.*, 2010). For the same laser energy, the 2D simulations lead to a diminution of the shock speed compared to 1D as also to a diminution of the electron density. For instance, in the case of a shock wave launched by a laser beam at 1315 nm in Xenon at 0.3 bar at PALS and with a laser fluence of 85000 J/cm², ARWEN 2D simulations give a shock speed of 44 km/s in agreement with the experimental one (Cotelo *et al.*, 2015). 1D simulation would require in this case a fluence of 30000 J/cm² to achieve the same velocity.

The space and time integrated XUV records at 0.6 bar, for respective speeds which are equal to ~ 39 and 18 km/s, indicate that the temperature of the shock has reached values up to 15 eV and that the Xenon mean ion charge has also reached values of 6 - 7 whereas 1D simulations predict electron temperature 10-30 eV and ion charge 5-10 (Fig. 5.18c). A more detailed study, based on 2D simulation and radiative transfer post-processing will be necessary to refine the analysis.

We have investigated the case of other noble gases (Ar, Kr) and we have observed that, for a given laser energy, the shock velocity decreases with the mass density. This study has confirmed that, for a given density and shock velocity, the radiative effects increase with the atomic number. For Kr, we

noticed a tiny precursor, without any interaction. To get such effect, it will be necessary to increase the shock velocity and thus the laser energy.

This has been done at the ORION laser facility in UK, where the collision of two counter-propagating shocks at equal speed ~ 80 km/s with laser fluence $\sim 6 \times 10^{14}$ W/cm² has been performed (Clayson *et al.*, 2017; Suzuki-Vidal *et al.*, 2016) for different noble gases and for pressures comprised between 0.1 and 1 bar. A number of diagnostics setup, X-ray backlighting, optical self-emission streak imaging and interferometry (multi-frame and streak imaging), were used to study both the post-shock and the radiative precursor. Although I have not participated in the experiments, I have performed 1D simulations to interpret ORION experimental results. This work is not presented in this thesis.

Optimization of an electromagnetic generator for strong shocks in low pressure gas

Contents

6.1	Principles of operation of a high current generator . . .	102
6.2	Principles of the run-down phase in a PFD	103
6.3	Proposed design for the plasma gun	104
6.4	Dynamic circuit modelling	106
6.5	3-D MHD simulations using GORGON code	111
6.6	Measurements	116
6.7	Summary	118

The previous chapters were dedicated to the study of laser generated radiative shocks. With irradiance more than 10^{14} W/cm², we were able to study shock waves propagating at velocity up to 50 km/s in noble gases with an initial mass density comprised between 5×10^{-4} - 3×10^{-3} g/cm⁻³. Complementary to laser experiments, compact pulsed power generators may drive an electromagnetic coaxial plasma gun to create astrophysical relevant shocks in lower pressure noble gases (Kondo *et al.*, 2006) with a high availability and a rather modest capital cost. The electromagnetically driven shock waves may have larger scales than those by laser; thus they can be observed rather easily (Kondo *et al.*, 2008).

Such electrical pulsed power devices may then : i) create a high-voltage breakdown, through a gas or, more easily, at the surface of a dielectric, ii) produce relatively hot plasma by ohmic heating when the rising current in the device is passing through a portion of gas, iii) accelerate plasma layers under the magnetic pressure associated with the self-generated magnetic field when high electrical current (say 10's of kA) is maintained for a short but sufficient time (say 1 μ s). Such ionization and acceleration are present in Z-pinch plasmas and in plasma focus devices (PFD), providing a clever geometry is employed and the mass under consideration (say 1 mg) is compatible with the stored energy (Martin, Williams, and Kristiansen, 1996).

In this chapter, we will see first how a fast electrical circuit works, then we will discuss the principles of a coaxial plasma gun and of PFD. We will see what is in favor of our objective and what has to be avoided. A geometry capable to reach our objective will be proposed.

The optimization of the coaxial gun (in term of plasma speed) will be performed and some typical figures will be given in the case of a generator with a stored energy around 1 kJ, and a plasma slab of 4-mm diameter, i.e. quite 10 times the transverse dimension of a laser driven RS. The operating conditions are supersonic shocks, up to 10-30 km/s speed, at static pressures of few mbar in heavy rare gases (Ar, Xe). The results of this 0-D model will be then compared to those obtained with 3-D MHD simulations performed with the code GORGON (by Andrea Ciardi at LERMA) which has been used successfully to describe other pulse-power driven plasma experiments (Chittenden *et al.*, 2004) as well as laboratory plasma astrophysics experiments (Ciardi *et al.*, 2007). The diagnostics which have been implemented will be presented to illustrate the model as well as preliminary records of the plasma speed.

6.1 Principles of operation of a high current generator

Our aim being to accelerate a plasma slab using the magnetic pressure, it is obviously needed to drive a high intensity current because the magnetic pressure is expressed by $B^2/2\mu_0$ in the region where exists an induction B. The pressure in bars is simply $4B^2$, with B in Teslas, and, in a cylindrical geometry, 1 Tesla is the field around a 50-kA current at a radius of 1 cm. Thus we should count on roughly 100 kA delivered by the generator, but such a high current is delivered only in a pulsed mode by a laboratory scale device.

There are numbers of technical solutions to achieve such electrical parameters; one may use rather slow generators at moderate high voltage like capacitors bank with the advantage of well know techniques but with limited adjustments. According to an abundant literature ¹ a convenient device is a medium-energy capacitor bank feeding a low-inductance circuit. An R-L-C circuit is a well-known combination delivering a high peak current in the pseudo-periodic mode. For a capacitor C initially charged under U_0 , key performances are as follows :

- Current intensity $I(t)$ is a damped sinusoid
- Pseudo pulsation $\omega = \sqrt{[1/(LC) - R^2/(4L^2)]}$

¹Institute for Plasma Focus Studies, resource website, <http://plasmafocus.net/> last connection in 2016

- First current peak $I_{peak} = U_0/[\sqrt{(L/C)} + 0.8R]$
- Time of current peaking $T/4 = \pi/(2\omega)$
- Equivalent impedance $Z = \sqrt{(L/C)}$

For a safe handling in air, a voltage not higher than 30 kV is recommended. Taking a total capacitance of 6 μF , 2700 J are stored under 30 kV. For an inductance of 240 nH, the expected peak current might be 150 kA at 1.9 μs . This set of values will be a guideline for the development presented in further sections.

6.2 Principles of the run-down phase in a PFD

Our aim is thus to create a fast moving plasma sheath with quite a one-dimension geometry. The issues are to initiate this plasma at the best, then to maintain – even improve – its structure during the acceleration, finally to launch it.

Instead of creating a gas breakdown in volume, which would lead rapidly to concentrate the current in an arc, the idea for PFD operation is to start from a surface discharge (Lee, 1969; Bernard, 2002). In the classical coaxial geometry of the Mather-type PFD, the central electrode (usually the anode) is a cut metal cylinder and the outer one is a second metal cylinder of the same length or, better, a squirrel cage allowing many viewpoints to the plasma. Both electrodes are attached to a dielectric bottom plate, made of polymer or ceramic. When the capacitor bank is switched on, the high voltage is applied to this cm-size gap and a radial surface discharge is initiated at the interface with the gas, forming a quite uniform ring-shaped layer of thickness around 1 mm. An insulating sleeve is adjusted around the central electrode to force the plasma to flow rapidly upwards, under the magnetic pressure in this region. The result is an elongation the discharge path, preventing an arcing in the plasma layer.

At later times, as the current is growing, the plasma layer is strongly influenced : it is pushed upwards by the magnetic pressure $\mathbf{j} \times \mathbf{B}$, it is heated by the ohmic effect, then its ionization degree increases, it becomes denser as a percentage (10-40%) of the heavy particles from the swept volume are accreted (Potter, 1971). This electromagnetically driven motion is called the rundown phase. Due to the accretion, it is described by a so-called snowplow model, which will be discussed later in detail. In quite all the designs, even if very high speeds are reported (Lee, 1969; Serban, 1995), the plasma is bell shaped, which does not fulfill our requirements.

At the end of the rundown phase, which matches roughly with the current peak, the plasma stays connecting the upper ends of the electrodes, and the radial component of the magnetic forces grows rapidly. Then the plasma is

strongly pushed to the axis, giving the so-called Z-pinch. This stage made the PFD popular because the pinched plasma is a source of fast electrons, fast ions, hard radiation, and possibly neutron beams; it must be avoided in our case. It was also quoted (Lee and Serban, 1996) that optimal PFD are matching a universal factor comprising anode radius, peak current and gas density, meaning a robustness of the design when a geometry has been chosen.

6.3 Proposed design for the plasma gun

The previous description has shown the positive influence of a surface discharge, the modification of the shape by the sleeve and the issue of the pinching effect. Accordingly, the following design is proposed, following a work by Kondo et al. (Kondo *et al.*, 2006, 2008).

To ensure a rapid discharge, with the values given in the section 6.1, a highly coaxial circuit is chosen for all the large parts: the energy bank, the closing switch and all the connections. The initial phase is kept with two coaxial electrodes pressed on a flat insulator. Homogeneity of the plasma sheath is expected by choosing a rather small radial gap of 2.5 mm. The effect of magnetic forces during the rundown phase must be enhanced, especially due to the increase of the mass of the plasma, as described above. As the current curve is the rising part of a sinusoid, a trick is used to increase the local magnetic field. B around a conductor varies as the inverse of the distance to axis, so the proposed shape for the anode is a cone. However, a final divergence must be avoided and that is obtained by a rounded tip. In order to keep constant the plasma length along the current path, the radial gap is kept constant, so the outer electrode is a hollow cone with the same angle. Above the cone the accelerator is connected to a conducting tube where the plasma can propagate freely in the background gas. The distance of the plasma sheath to the cone tip is increasing rapidly and the main current, which is still high, will pass preferably through the diffuse plasma remaining between the electrodes. Thus there will be no magnetic pressure anymore acting on the sheath, which can propagate freely. The resulting device is described in Fig. 6.1a and the acting magnetic forces shown in Fig. 6.1b.

Technically, such a configuration is convenient even at 15 kV because the sharp edge of the anode touching the insulator forms a so-called triple point where the electric field is enhanced at the surface of the insulator, which triggers efficiently a discharge in presence of gas at low pressure (0.1 – 10 mbar) as proposed by Kondo et al. (Kondo *et al.*, 2006). Polyacetal is a convenient material for dielectric and mechanical performances.

The direction and the orientation of the magnetic force are other points to be discussed. The high-intensity current (up to ~ 150 kA) generates a strong

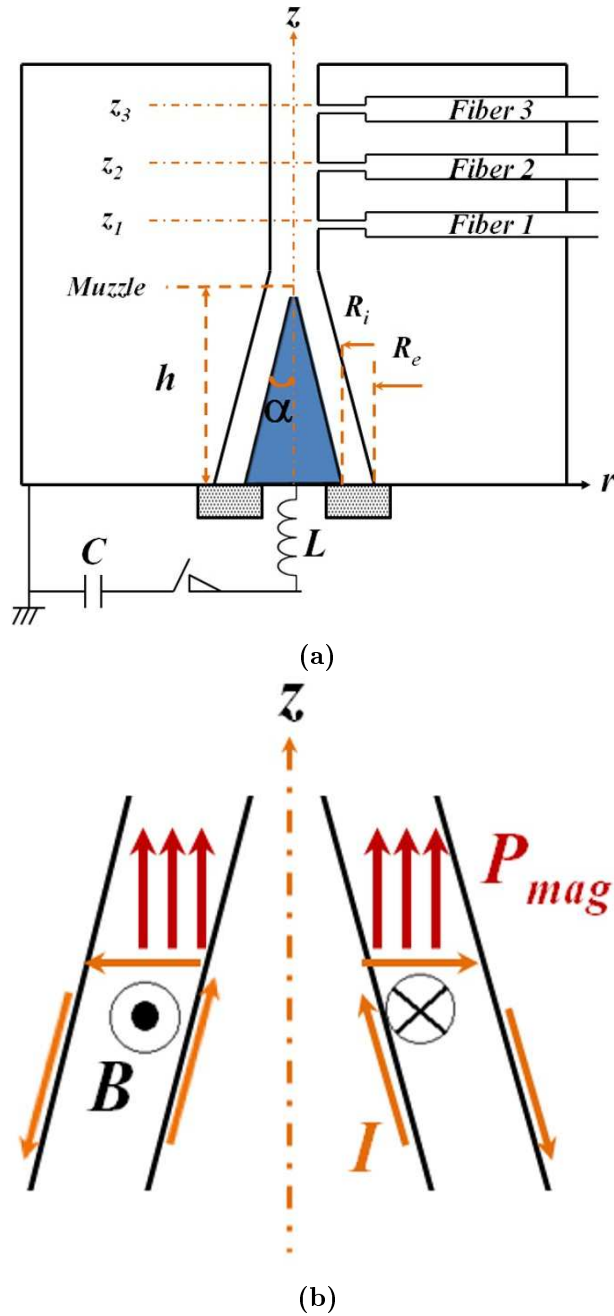


Figure 6.1: (a): Sketch of the shock generator showing the pulsed electrical circuit, the set of coaxial conical electrodes with a constant radial gap and the plastic insulator, featured in grey, on which a planar surface discharge is initiated. The installation of three optical fibers allows looking radially at the plasma moving in the shock tube. (b): Schematics of the plasma dynamics inside the coaxial gun: in fast-pulse mode, the electrical current flows in the superficial layers of the two coaxial conical electrodes and through an annular plasma layer. The magnetic pressure P_{mag} pushes the discharge axially.

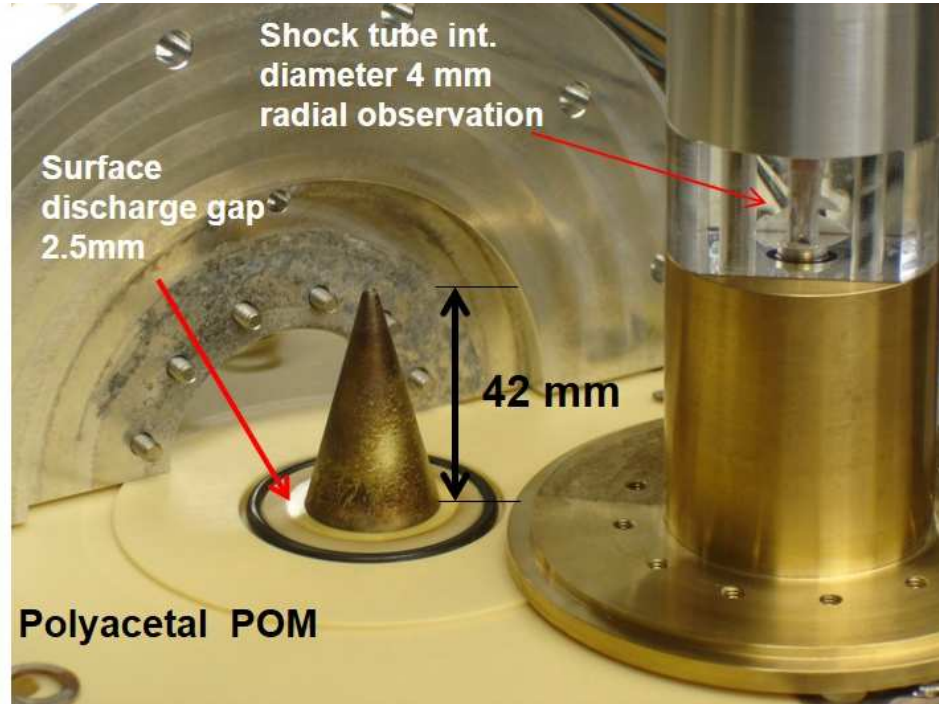


Figure 6.2: Exploded view of the plasma gun.

azimuthal magnetic field between the electrodes, thus the magnetic pressure $\mathbf{j} \times \mathbf{B}$ which accelerates the annular plasma sheath stays perpendicular to the sheath locally (Fig. 6.1b). The more planar is the initial sheath, the more axial will be the magnetic pressure. Finally, if the roles of the electrodes are exchanged, the direction of the current will be inverted, and the same for \mathbf{B} , so the pressure will stay oriented in order to expel the plasma. Compared with the Mather-type plasma focus (Potter, 1971; Zambra *et al.*, 2009), the plasma sheath considered here is quite planar close to the insulating surface and, later, is expected to stay planar and perpendicular to the axis. As in a PFD, the thickness of the plasma sheath increases gradually (Zambra *et al.*, 2009), but it is assumed to stay in the mm-range. We employ coaxial conical brass electrodes, each 42-mm high, with a constant gap of 2.5 mm. At the bottom level, internal and external radii of electrodes are 12.5 mm and 15 mm respectively. This small-size discharge cell, on top of the generator, will be modelled in the following

6.4 Dynamic circuit modelling

We optimize the electric generator for various gases, namely Ar and Xe, with the motivation to produce plasma shocks with speeds $\sim 1 - 30$ km/s, i.e. Mach numbers up to 200. For that, we design the electrodes and set

the electrical circuit parameters to produce 1- μ s pulses in the gas chamber. The geometry of the electrodes is as mentioned above. The half angle of the conical electrode is chosen to be $\alpha = 15^\circ$ and thus the height of the cone is $h \sim 42$ mm.

Eleven ($N = 11$) capacitors, each with capacitance C_0 of 0.6 μ F, are connected in parallel, giving an equivalent capacitance of the bank $C = 6.6$ μ F; charging voltage U_0 of the bank is set to 15 kV. Thus, the available electrical energy is 750 J. The circuit resistance is used to be 1 m Ω and damping resistance is set to zero, which yields a total resistance ($R = R_{cir} + R_{damp}/N$) of 1 m Ω and a pseudo-periodic regime is expected.

Based on the above geometrical and electrical parameters, we have estimated the time evolution of various parameters of the radial discharge layer, namely speed, mass, acceleration etc. at a different position along the axis, from $z = 0$ to h . For this calculation, we need to solve a set of three equations which give the main current ($-dq/dt$) supposed to flow only through the plasma layer, the mass accretion rate (dM/dt) and the velocity v of the plasma. These equations together with initial conditions are explained below. The electrical equation is written classically:

$$Ld^2q/dt^2 + Rdq/dt + q/C = 0 \quad (6.1)$$

When the R , L and C parameters are not time-dependent, the circuit equation 6.1 has an analytical solution, a damped sinusoid for the current $I = -dq/dt$, and that was used as a test of the iterative solving process and to confirm the parameters of the external circuit with a short circuit load. The inductance of the external circuit L_0 is computed from the ringing frequency in short circuit (66 nH), which results in a circuit impedance $Z_0 = \sqrt{L_0/C}$ to be 0.1 Ω . In the plasma gun mode, the sheath carrying the current (see Fig. 6.1b) is accelerated by the magnetic pressure, and it behaves as the deformable part of the circuit; then L is time-dependent and a numerical solver is necessary for equation 6.1. We used a lumped-parameter model which has proven to describe similar circuits successfully (Potter, 1971; Zambra *et al.*, 2009). Gonzalez (Gonzalez *et al.*, 2004) showed that the mass and momentum equations for a current sheath, in the shape of an annular piston moving forward in the axial direction, can be given by

$$dM/dt = \varepsilon\rho_0\pi(R_e^2 - R_i^2)v \quad (6.2)$$

where, ε is accretion factor, and that the transformation of magnetic to kinetic energy is expressed by

$$d(Mv)/dt = lI^2/2 \quad (6.3)$$

where l is the linear inductance of the gun and can be expressed as $l = (\mu_0/4\pi) \ln (R_e/R_i)$, the radii being estimated where the plasma sheath is currently located. The equations 6.2 and 6.3 have been introduced in the

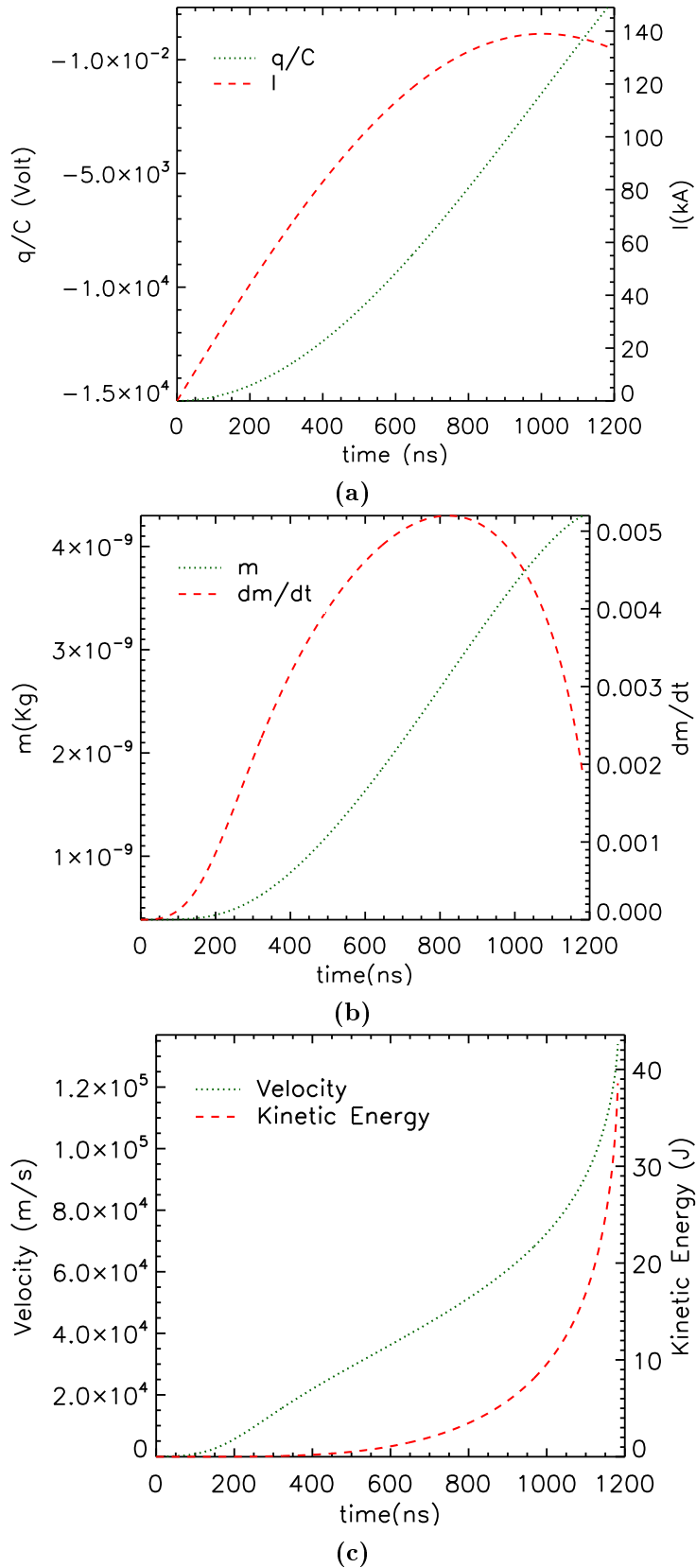


Figure 6.3: Time dependence of the main parameters for Ar gas at 1 mbar according to the circuit model. (a): current (kA) and voltage (V), (b): accreted mass (kg) and rate of accretion (kg/s), (c): speed (m/s) and kinetic energy (J).

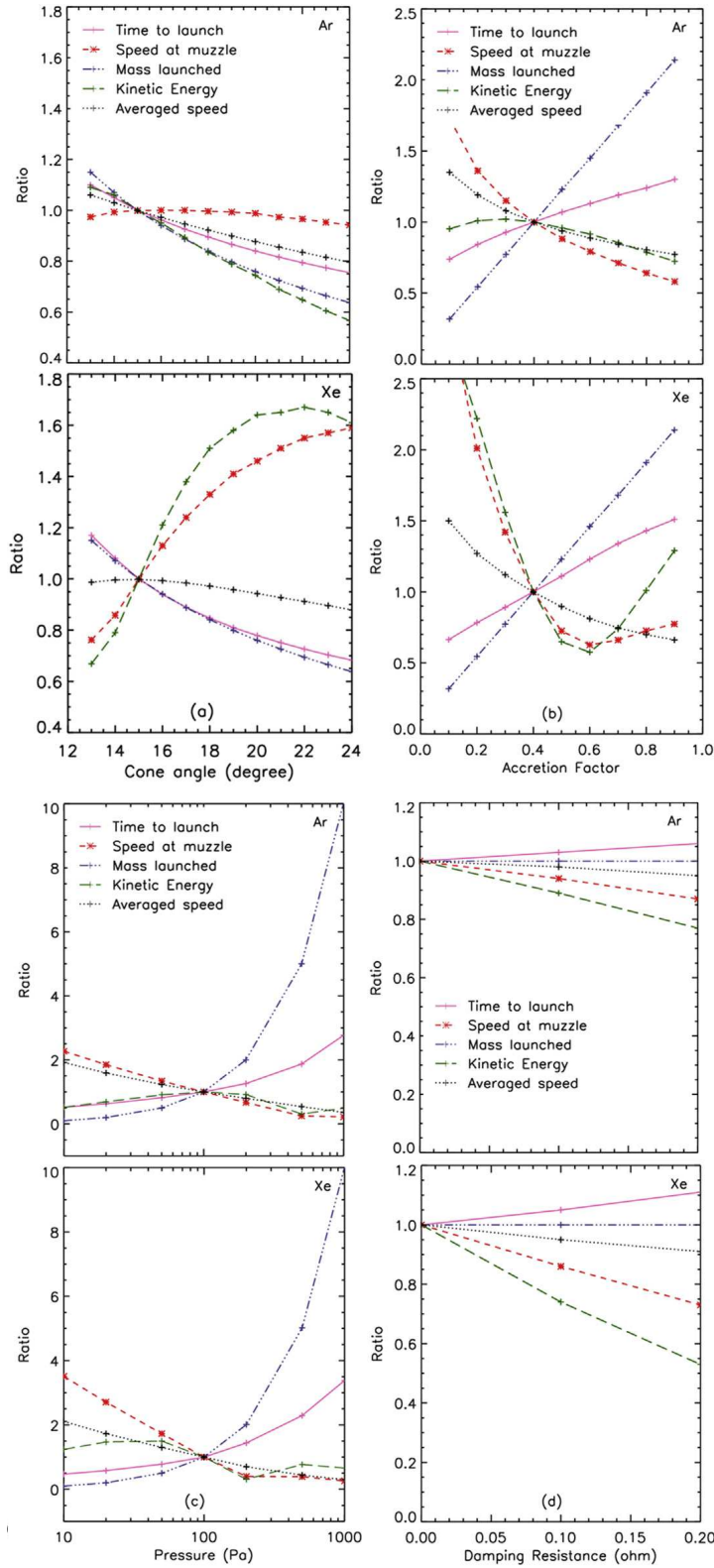


Figure 6.4: Plot of the different output parameters (normalized with respect to the peak values) obtained at the top of the inner electrode. For each group, upper panel represents the variation for Ar gas whereas lower panel is for Xe gas. Profiles of output parameters are given: (a) with cone angle (b) with accretion factor, (c) with gas pressure and (d) with damping resistance.

time-dependent iterative solving of equation 6.1. Therefore, from equations 6.2 and 6.3, we get

$$dv/dt = \frac{[\frac{U^2}{2} - \epsilon\rho_0\pi(R_e^2 - R_i^2)v^2]}{M} \quad (6.4)$$

From equation 6.4, we may note that initial value of mass, $M(t_0)$, cannot be set to zero as it would lead to a nonphysical divergence of the acceleration. In this regard, we have considered an initial thickness of the current sheath of 1 mm and integrated the gas density at rest, leading to $M(t_0)$ equal to 3.5×10^{-10} kg for Ar and 1.3×10^{-9} kg for Xe. A higher limit has to be put too: $M(t_0)$ must be small compared with the mass at the end of the launching phase, that is the mass contained in the gap times the accretion factor. The above value for $M(t_0)$ follows that criterion and, within these limits, the choice of initial mass is not influencing the results.

Parameter	Reference Value	Variation
Half angle of the cone	15°	13°, 14°, 15°, 16°, ... 24°
Accretion factor, ϵ	0.4	0.1, 0.2, 0.3, ... 0.9
Pressure, P	100 Pa	10, 20, 50, 100, 200, 500, 1000
Damping resistance, R_{damp}	0 ohm	0, 0.1, 0.2

Table 6.1: Input parameters, their standard values and range of variation.

As the motion is mainly along the z -axis, the speed v is the derivative of the plasma position $v = dz/dt$. We solved these equations by a time-dependent method, where the initial condition is that at the onset time, t_0 , the charge q is set to CU_0 . Further, the current $i = -dq/dt$ is taken to be zero at t_0 . Thus, using equation 6.1, the initial rate of change of the current is $d^2q/dt^2 = -q/L_0C$. Then all the first time-derivatives are updated at the first time step $t_0 + \Delta t$, with $\Delta t = 0.43$ ns, using equations 6.1-6.4. The quantities like q , M , v , z are updated at the next step, then the iteration is pursued. Initially, position, acceleration, and velocity of the sheath are set to be zero, as well as the rate of change of the mass.

As we initiate the electrical current into the gas inside the chamber, the plasma sheath is accelerated with respect to its initial mass, as seen above. At later times, the mass accretion is masking the influence of this arbitrary value. We have calculated the plasma evolution in the discharge for different sets of initial conditions which are reported in Table 6.1.

Fig. 6.3 shows the behavior for the standard values reported in Table 6.1 in the case of Argon at 1 mbar. The corresponding values of charge, mass and velocity will be hereafter called the reference values. In Fig. 6.3a the variation of current and voltage in the first half-period is classical, showing that the pulse generator departs slightly from a pure RLC circuit. Fig. 6.3b represents the accreted mass which increases in time as well, whereas

the rate of mass accretion culminates with a competition of speed growth and decrease of the swept volume per time step, because it depends on the squared radii. In Fig. 6.3c, plotted are the speed and kinetic energy of the plasma sheath. First, the speed of the plasma is increasing slowly with time, quite linearly as the mass, and the kinetic energy is roughly a third power of the time.

That leads to choose a design where the acceleration is imposed for a sufficiently long time. However, the estimated speed of plasma is ~ 140 km/s which is a very optimistic value. The reason may come from two reasons: (i) a part of the current flows through the large shocked volume, reducing the magnetic pressure acting on the plasma sheath, (ii) energy transfer from magnetic to thermal energy and ionization is reducing the kinetic one. The observation of a very bright emission from the plasma will be a clear evidence of this redistribution of the energy.

Further, we made a comparative study of the parameters indicated in Table 6.1 and applied to two gases, namely Ar and Xe. In order to check the effects of the initial conditions (cone angle, accretion factor, pressure and damping resistance), we have performed a systematic study by varying only one parameter and keeping the others constant and equal to the reference values given by the second column of Table 6.1. The tested range is listed in the third column of Table 6.1. Similarly, for each set, the variation of the plasma conditions at the top of the muzzle is normalized to the reference value. Fig. 6.4 summarizes the variation of the selected different output parameters : the time t_m to reach the muzzle ($z = h$), the electrical current and the axial speed at muzzle, the launched mass M , the kinetic energy and the average speed at the top of the electrode, calculated from the initial point, $v=h/(t_m - t_0)$.

Table 6.2 summarizes the respective ratios for Ar and Xe at the top of the coaxial electrodes. As the values of interest are obtained at constant stored energy in the capacitors, there is a benefit to work with a lighter gas like Argon. However, the results obtained using this circuit model show that the reference values are ensuring a satisfactory behavior for both gases.

Speed	Kinetic energy	Time to launch	Mass
222%	151%	66%	31%

Table 6.2: Launching performance Ar/Xe.

6.5 3-D MHD simulations using GORGON code

Our simplified model (cf section 6.4) is convenient to perform quickly some parametric tests in the acceleration phase and to help designing the device, but it is not capable to treat the shock dynamics in detail nor to give valuable

information on the plasma parameters in the shock region. So, refined numerical simulations of the experiments were performed in collaboration with A. Ciardi (Ciardi, 2014) using the GORGON code (Chittenden *et al.*, 2004; Ciardi *et al.*, 2007; Suzuki-Vidal *et al.*, 2014). GORGON is an explicit, parallel code designed to solve the resistive MHD equations on a three-dimensional (3-D) Cartesian grid employing a Van Leer type algorithm. The code treats the plasma as a single fluid but solves separately the energy equations for ions and electrons, allowing different temperatures for the two species. Both thermal conduction and resistive diffusion are treated using Braginskii-like transport coefficients.

Variables	At rest	Shock	Post-shock
Ar density ρ (g/cm ³)	1.8E-6	2.5E-5	1.0E-5
Electron density N_e (/cm ³)	1.0 E+15	2.0E+18	1.5E+18
Electron Temperature T_e (eV)	0.03 (1*)	10	15-18
Ion density n_i (/cm ³)	3.0E+16	3.5E+17	2-3E+7
Ion Temperature T_i	0	50	15-20
Average Speed $\langle V \rangle$ km/s	0	50	20-40
$\langle z \rangle$	0.2	6	7-9

Table 6.3: Values of variables in various conditions: at rest (with seed electrons), inside the shock and inside post-shock region. A star * denotes the insulator surface.

This code describes the creation of the surface discharge, then its acceleration by the magnetic pressure. It provides the mapping of all the plasma parameters and local B-field in the launching cone as well as in the free flight region. The 3-D simulation was performed for Argon gas at 1 mbar only, the discharge current law being taken from experiment. The Table 6.3 presents the ranges of all the variables in the regions of interest.

As an example, Fig. 6.5 shows an enlarged mapping of $\log(n_e)$ at two times: in the launching phase, then when the shock has deeply penetrated in the shock tube. Taking the zero time as a reference, the averaged speed z/t is 40 km/s in this simulation. When the two snapshots are considered, the estimate of the instantaneous speed $\Delta z/\Delta t$ is higher at 56 km/s. The time history of plasma merging and early free flight into the shock tube is presented in Fig 6.6. During the acceleration (inside the double cone) the plasma is well localized on a planar, annular sheath which is carrying the current, as assumed in the lumped parameter model. We see that the merging is well achieved at the muzzle shortly before 1250 ns. When the shock has penetrated inside the tube (1500 ns), the computed B-field is negligible at this location and the propagation is quite free, as expected for the chosen design of the device. However, a high current is still passing through the gas at that time, a sufficient electron density remaining in the conical gap for that.

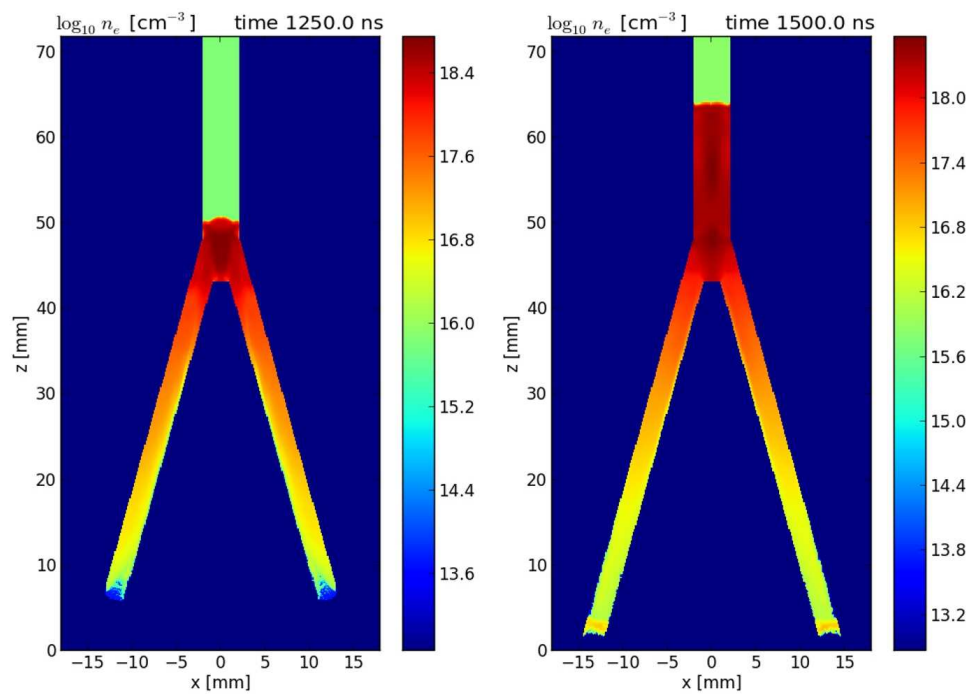


Figure 6.5: Example of mapping of the electron density from a 3-D MHD simulation (background gas Argon at 1 mbar) when the plasma sheath is : (left) at the exit of the plasma gun, (right) in free flight conditions (log scales for the false colors).

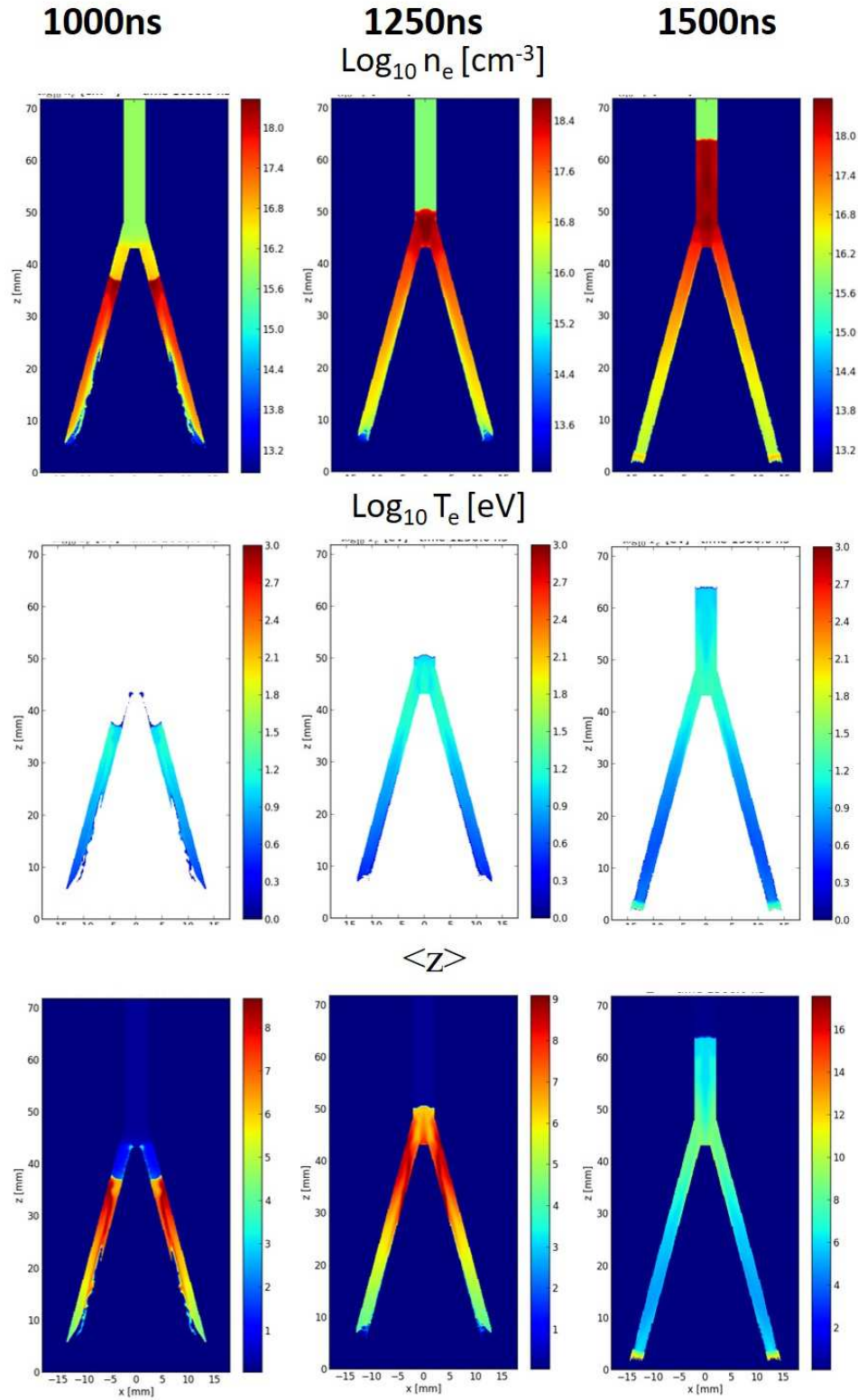


Figure 6.6: Time history of plasma merging and early free flight through the mapping of the electron density, electron temperature and average ionic charge, as given by a 3-D MHD simulation (background gas Argon at 1 mbar) (scales for the false colors).

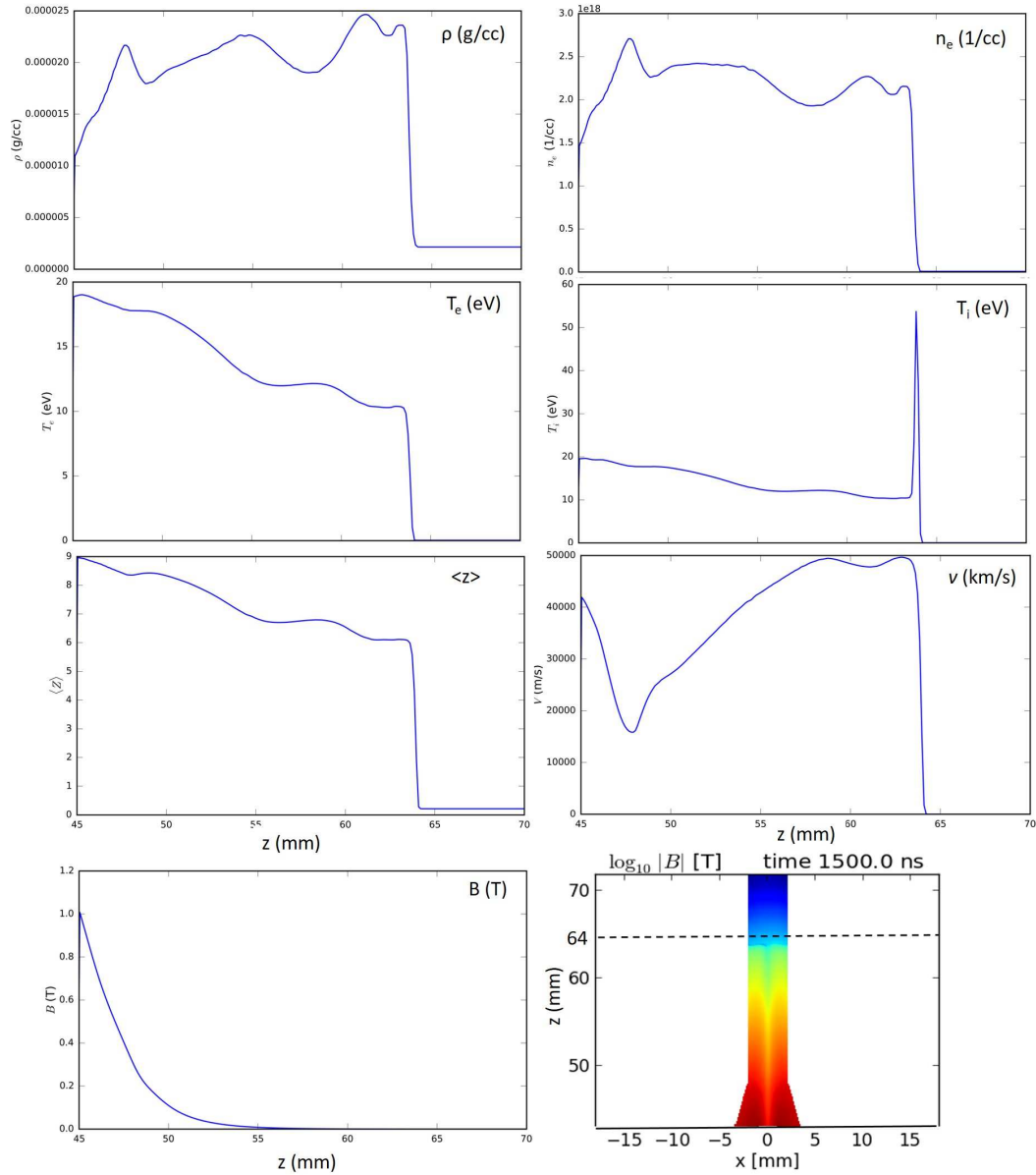
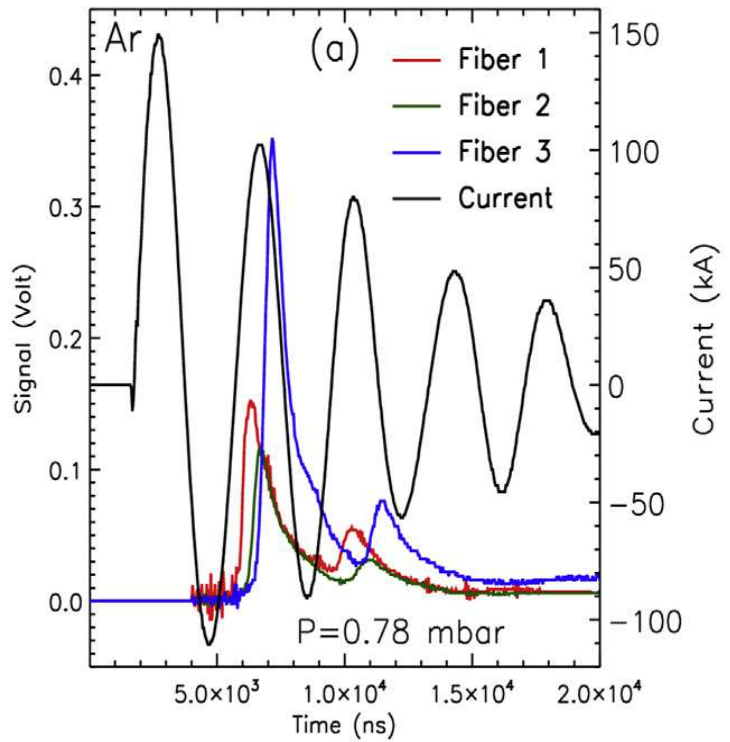


Figure 6.7: Axial profiles, values taken in the shock tube along a line slightly off-axis at a distance of 1 mm, for mass density, ion temperature, ion density, average ion charge, magnetic field, electron temperature, electron density and average speed at 1500 ns (background gas Argon at 1 mbar). A mapping of $|B|$ is given, with a dashed line indicating shock front position as well.

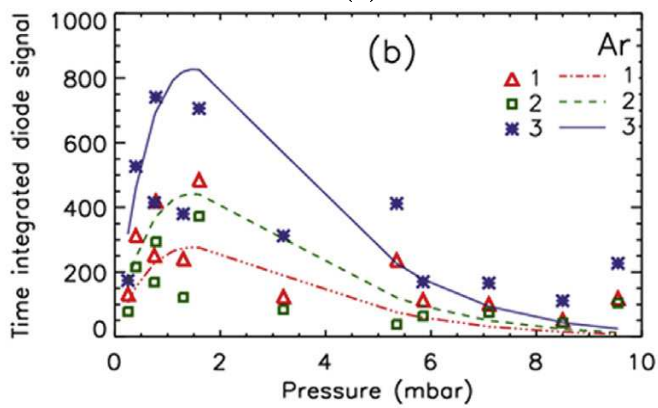
To confirm the steep structure of the shock, Fig. 6.7 presents the axial profiles of electron temperature T_e , number density N_e , mass density ρ and average ion charge $\langle Z \rangle$, at 1500 ns, inside the tube with an enlarged axial position scale. Steep fronts are observed for mass density, electron density and temperature, as in the earliest simulations (Potter, 1971; Kondo *et al.*, 2008). The shock region is at 10 eV and $\sim 2 \times 10^{18}$ electrons.cm⁻³; the post-shock region is hotter. Argon ionization stages of 5 (shock) to 9 (post-shock) are obtained, forecasting an emission spectrum in the UV or harder. A wider view of the plasma is given by other quantities at the shock front and behind: ion temperature, average speed and local magnetic field in Fig. 6.7. We get the confirmation of the extinction of B after the first 5 mm inside the shock tube as well as the shock speed at 50 km/s, coherent with the constant speed of 56 km/s mentioned just above. At present, these parameters are guiding the choice of diagnostics, like ultra-fast interferometry or UV-spectroscopy.

6.6 Measurements

The aim of these tests was to show the consistence of the above model by measuring the plasma speed close to the plasma gun muzzle. The parameters of the device are the reference ones as defined in Table 6.1. A rather simple and noise-free method for diagnosing a plasma gun, during the rundown phase, is to record the light emitted by the plasma sheath with a spatial resolution compatible with the plasma structure. If we consider a line of sight which is radial or tangential, i.e. perpendicular to the direction of propagation, one expects to see a sudden rise when the plasma enters the detection volume, possibly a plateau when the plasma travels inside the volume, then a slow decrease when the hotter plasma leaves the volume but when the shock remnants are still present. So the expected signal is a triangular asymmetric pulse (Serban and Lee, 1995), or some kind of double exponential pulse (Stehlé *et al.*, 2012). A peak indicates the time of flight for the given position, allowing to compute a mean speed providing the launching time ($t=0$) and all positions are known. An instant speed is accessible providing two close detectors are considered. That has been proposed and tested successfully in the case of radiative shocks driven by one PALS laser beam (Stehlé *et al.*, 2012), the detectors being collimated and filtered silicon diodes. For cooler plasmas, the visible emission is more relevant. Inside a squirrel cage plasma focus, Serban has installed a set of optical fiber looking tangentially at the drift zone (Serban and Lee, 1995). Despite a conical field of view, the results were conclusive at speeds as high as 100 km/s in D₂. An improved version with collimated optical fibers (acceptance angle 2°) was developed too (Serban and Lee, 1995). A non intrusive method was developed (Velošo *et al.*, 2012b,a) by imaging the plasma on a set of optical fibers, allowing to play with the magnification.



(a)



(b)

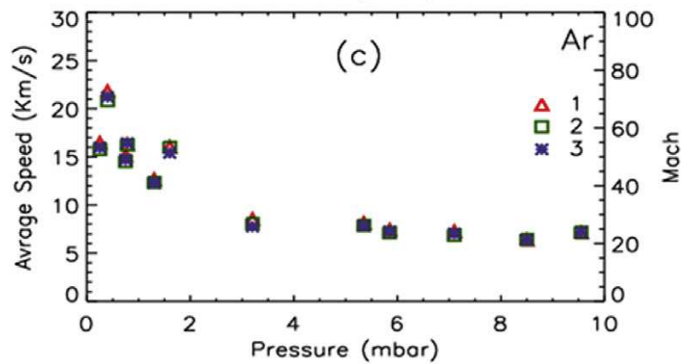


Figure 6.8: Experimental results : (a) time history of the passive optical records compared to the main current for Argon gas close to the reference pressure (b) time-integrated signal vs Ar pressure for the different fibers. (c) averaged speed vs Ar backing pressure.

In our case (see Fig. 6.1a), three 1-mm PMMA (Poly(methyl methacrylate)) optical fibers are installed radially, along a transparent section of the shock tube at $z \sim 62.5$ mm, 70 mm and 77.5 mm, and fast DET10A detectors record the transient presence of the plasma sheath in the respective lines of sight. The recorded spectral range is limited to the whole visible in a preliminary stage; a band-pass filtering might give information on the presence of specific ionic species, characteristic of a plasma temperature level, however the amount of light was not sufficient to do so. Fig. 6.8a presents the time evolution of the electrical current, with a period of 4 μ s, and the delayed, side-on observational data of the moving plasma inside the shock tube. The behavior of the electrical circuit is following well the expected ringing of a weakly damped RLC circuit, the zero-time being fixed at the onset of the current. On optical channels, a steep rise and a peak are the signature of a mm-thick fast-shock structure (Serban and Lee, 1995) consistent with early numerical simulations (Potter, 1971; Tou, Lee, and Kwek, 1989; Kwek, Tou, and Lee, 1990; Veloso *et al.*, 2012b). On each fiber signal, secondary peaks, namely the one delayed by 4-5 μ s, are attributed to current restrikes at the pseudoperiod. To avoid the mixing of shocks, further experiments should be conducted in an aperiodic regime, with a heavy-duty damping resistor added in series to each capacitor, $R_{damp} \sim NZ$.

On Fig. 6.8b and c are presented the exploitation of optical records with the Ar background pressure, this parameter varying in the widest range: (b) the integrated emission which presents a maximum between low pressure side when the temperature is high but the number of emitters is low and the high pressure side when the temperature is much lower, (c) the averaged speed z_i/t_i for the first peak on each fiber. The relative intensities recorded in the three locations are not significant, because of a strong copper deposition closer to the muzzle, which affected the detection. The long-life noise on the optical signals was making the local speed, calculated as $(z_i - z_j)/(t_i - t_j)$, a non-reliable output. One can note Mach numbers in the range 20 – 60 with a pressure dependence similar to previous work (Kondo *et al.*, 2006). The reported observations are consistent with a high-speed, millimetric, planar plasma travelling in the shock tube. The speed is lower than deduced from the simplified model, possibly due to the lack of dissipation terms which is overestimating the transfer to kinetic energy. At the contrary a realistic simulation as the one performed using GORGON is in better agreement.

6.7 Summary

For this part of the work, the objective was to show that, in complement of laser experiments, a compact pulsed power generator might drive astrophysically relevant shocks, in low pressure noble gases, with a higher availability and at a rather modest capital cost. The longitudinal acceleration of a

plasma sheath in a low backing gas pressure has been demonstrated in coaxial plasma guns as early as in the 70's, even leading to speeds of 100 km/s in light gas as H_2 , which were measured and modeled. A choice was made to revisit this type of device. At present, the electromagnetic coaxial plasma guns are quite only considered as the initiators of a strong, radial, plasma implosion plasma focus devices (PFD), due to a good ability to produce a pinch plasma and emission of energetic particles and hard X-ray. For that reason it was necessary to adapt the principle of a PFD with two major constraints: increase the conversion of stored energy into the kinetic energy of a plasma sheath, prevent totally any pinching.

That objective was reached by defining the electrical and geometrical parameters of a low-inductance and compact pulsed power generator. An optimization process has been established to match achievable electrical parameters of the circuit (capacitance, inductance, peaking current intensity) with a plasma motion in the accelerating tube over few cm, leading to a final speed of 10-30 km/s. A model was built up to describe the dynamics of an RLC circuit with a varying element composed of the moving plasma sheath, accelerated by the self generated magnetic pressure. The change in plasma position along the axis is increasing the inductance and the mass accretion is increasing the plasma mass. It was shown that a change in the electrode geometry, namely a 30° conical shape, was increasing the energy conversion and preventing any focusing. The further step, in contrast with PFD, is the merging of the plasma ring into a rather planar one which is injected in a drift tube.

Considering Ar or Xe at gas pressure in the range 0.1 – 10 mbar, and a highly coaxial, 1-kJ device, the simple model was sufficient to predict performances agreeing with the only work quoted in the literature. Basic observations of the moving plasma, using side-on detection of the visible emission, give features coherent with the model. Mach numbers from 20 to 60 are obtained, fitting with the objective of strong shock formation. A refined 3-D MHD numerical simulation indicates very promising features of the shock, in view of exploring mm-size shocks in a regime complementary to laser driven ones, and on a table-top device allowing a higher repetition rate.

Conclusions and perspectives

7.1 Conclusions

Although ubiquitous in the astrophysical environments, radiative shocks are complex phenomena, which still require an important effort to understand them. Beside observations, which suffer from a lack of angular resolution, laboratory experiments provide today an interesting approach to improve our present knowledge. In this context, my thesis work is dedicated to the experimental and numerical study of the characteristics of two counter propagating radiative shocks propagating at different velocities (20-50 km/s). Most of the work presented here is the outcome of the *first-of-its-kind* experimental campaign held in year 2015 at Prague and Laser Asterix system (PALS) laser facility.

In this manuscript, I presented the setup for the aforesaid shock experiment. Following this, the data analysis, results, interpretation as well as relevant numerical simulations concerning various diagnostics *viz.* visible interferometry and XUV spectroscopy have been presented. Although a large fraction of the experimental records were performed for Xenon at various pressures, I have also studied the shock characteristics of different gases like Ar, Kr and He. Our results are complementary to those obtained at ORION laser facility, also in 2015, relative to the collision of identical radiative shock waves at higher velocities (80 km/s). In parallel, in this thesis, I have also worked on the optimization of a setup dedicated to electromagnetically generated strong shocks at lower velocities. In the following, I briefly present a brief summary of the main results of my thesis work.

In the third chapter, I have presented a series of 1D hydrodynamic simulations (realized with the commercial code HELIOS) on isolated and counter-propagating shock waves at equal and different velocities. The simulations confirm that a single radiative shock propagating in Xenon gas at 0.1 bar is characterized by an extended precursor and a large compression of 30 in the post shock. At 50 km/s the temperature evolution with the distance shows identical post-shock and pre-shock values. This indicates that the numerical shock is of supercritical nature. However, I find that there is an important uncertainty in the Xenon opacity, which makes the refinement of the simulation unnecessary, especially in terms of group numbers. Next, I have investigated the interaction two counter propagating shocks for identical (50-50 km/s) and non identical (50-20 km/s) shock speeds. For the

case of identical speeds, the precursors merge together at around 10 ns. The interaction is then characterized by a regular increase of the electron density and the temperature with the time. The shocks collision, at 38 ns, leads to a jump in the electron density ($6 \times 10^{21} \text{ cm}^{-3}$) and temperature (39 eV). On the other hand, for the case of non-identical shock speeds (case representing our experiments), the precursors interaction starts later than in the former case. The shocks collision occurs at 49 ns and it is characterized by a sudden increase of the electron density, also by an order of magnitude ($4 \times 10^{21} \text{ cm}^{-3}$), whereas the temperature increases up to 29 eV.

Although the data analysis of all the experimental records obtained during the PALS experimental campaign has been carried out, only a few representative interferometric and spectroscopic records for Xe gas are discussed in details in this thesis. The interferometric records allowed me to estimate the average shock speed and time variation of the electron density during the shock propagation. The shock speeds of the MAIN and AUX radiative shock waves are found to be ranging between ~ 30 -55 and 12-25 km/s, respectively, whereas the averaged precursor electron density is varying between 10^{17} and 10^{19} cm^{-3} during the shocks propagation.

From the interferometric records, I have investigated the effect of the interaction between the two radiative precursors for the shocks propagating in Xenon at 0.1 bar with respective speeds of 50 ± 3 and 23 ± 3 km/s. The interaction starts at 20 ns, and is followed by the merging of the two radiative precursors. This precursor interaction is characterized through the enhancement of the ionisation wave. The shocks collision is recorded at 50 ns. On the contrary, the same interaction behavior is not seen at 0.2 bar (shock speeds $\sim 38 \pm 4$ and 18 ± 2 km/s for the MAIN and AUX shock waves, respectively). Moreover in this case, there is no signature of a radiative precursor for the AUX shock. The precursors interaction, if any, should then could occur at times which are outside of the record, and can not be confirmed by the experiment. This indicates that, for a given gas and shock speed, the radiative effects decreases with the initial mass density.

The investigation of the lateral extension of the shock has been made through the analysis of transverse interferograms. At 0.2 bar, the MAIN shock, with a speed ~ 40 km/s, has a lateral precursor extension of $\sim 570 \pm 30 \mu\text{m}$ whereas it is $275 \pm 25 \mu\text{m}$ for AUX shock which is propagating with a speed of 20 km/s. The MAIN shock precursor is almost of a flat spatial profile whereas the AUX precursor is more curved, suggesting that the 2D effects are much more important for AUX than for MAIN. One of the explanations is that the spot size of AUX laser on the target is smaller than the target width whereas the MAIN laser has a spot size which is equal to the target width.

In order to interpret the experimental results with appropriate 1D simulations, I have optimized the lasers fluences to numerically obtain a shock speed equal to that recorded in the experiment. In the corresponding simu-

lations for Xenon at 0.1 bar, I note the interaction of the two precursors. However, I do not find a good quantitative agreement for the electron density. Beside the question of the imprecise opacities, this disagreement might also be attributed to 2D effects (González, Audit, and Stehlé, 2009; Leygnac *et al.*, 2006; Stehlé *et al.*, 2010),(Cotelo *et al.*, 2015).

The analysis of space- and time-integrated XUV record at 0.6 bar is presented for two counter propagating shocks of speeds $\sim 36\pm 4$ and 18 ± 5 km/s for MAIN and AUX, respectively. The presence of HeII Balmer lines and Xenon lines tends to indicate a temperature of the shock of about 15 eV and a Xenon mean ion charge around 6 - 7. The 1D simulations predict electron temperature in the range of 10-30 eV while ion charge to be ranging between 5 and 10.

In addition to this study, which was focused on the Xe case, I have investigated the shock characteristics for Ar, Kr at close mass density ($\sim 6 \times 10^{-4}$ g/cm³), which correspond to 0.3 bar and Kr gas 0.2 bar. Almost no precursor is found to be present in case of Ar, whereas a tiny precursor have been observed for Kr. This indicates that, for a given density and shock speed, the radiative effects increase with the atomic number.

In parallel, I have worked on the optimization of the design of an experimental setup, where the shock is generated electromagnetically. This setup allows studying shock ~ 30 km/s in noble gas at ~ 1 mbar. The parameters of a low-inductance and compact pulsed power device have been optimized with a simple model, in view of building-up and accelerating a plasma sheath in Ar and Xe at gas pressure in the range 0.1-10 mbar. Simple observations of the moving plasma, using side-on detection of the visible emission, give features coherent with the model. Shocks corresponding to mach numbers ranging from 20 to 60 are obtained.

7.2 Perspectives

The experimental results presented in this thesis correspond to the case of two counter-propagating radiative shocks. We have been able to study the time variations of the precursor interaction and the effect of gas pressure, with 1D time dependent interferometric records obtained with a streak camera. Together with the help of XUV spectroscopy, we could estimate the shock speed, electron density, and shock temperature. However no information is provided about the lateral extension of the precursor, and we were not able to record XUV data for all the shots. Therefore, in order to make these results more comprehensive, we have designed, and participated in, a follow-up experimental campaign in September 2016 at PALS. This time we focussed on single shocks in close experimental conditions, but with a wider range in terms of speeds (45-100 km/s). We replaced the time dependent streak camera interferometric study by an instantaneous 2D interferometric

image (GOI) obtained with a short pulse sub picosecond laser and cameras. XUV spectra were also recorded. The records were performed at three different times of the shock propagation, allowing to deduce the shock speed and the time evolution of the precursor morphology. This follow up experiment will allow to complete the analysis of the laser generated shock waves presented in this thesis.

The preliminary analysis I have performed on these new records is very promising. An example of these interferometric records is given in the Figure 7.1a for the shot #30364 in Xe+He at 0.6 bar. The high speed of the shock is related to the energy of the laser which is here 170 J, whereas it was less than 120 J in the previous experiment. The comparison with the interferometric record (not shown) before the shot allows to deduce the electron density which reaches $1.8 \times 10^{19} /\text{cm}^3$. The high quality record shows clearly 2D effects for this shock wave.

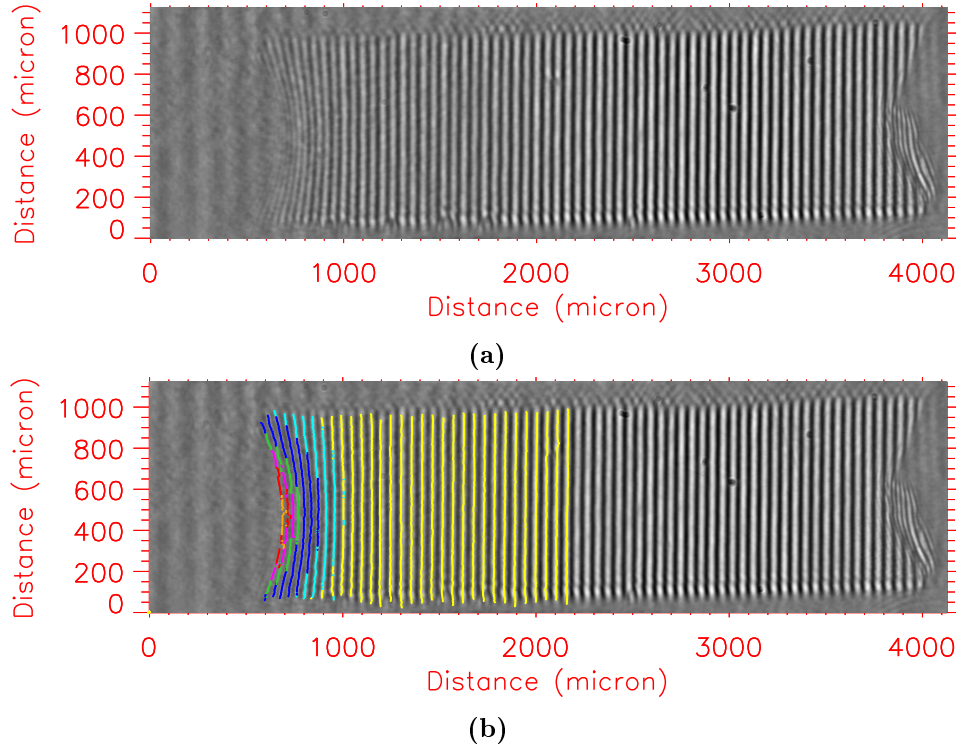


Figure 7.1: Interferometric record obtained at 5.46 ns for a single radiative shock of speed ~ 100 km/s propagating in Xe+He gas at 0.6 bar driven by laser at 348 nm with energy 170 J. The different colors in (b) correspond to: yellow: $\leq N_e \leq 3.5 \times 10^{17} \text{ cm}^{-3}$; cyan: $3.7 - 7.4 \times 10^{17} \text{ cm}^{-3}$; blue: $7.4 - 1.5 \times 10^{18} \text{ cm}^{-3}$; green: $1.5 - 1.8 \times 10^{18} \text{ cm}^{-3}$; magenta: $1.8 - 2.2 \times 10^{18} \text{ cm}^{-3}$; red: $2.2 - 2.6 \times 10^{18} \text{ cm}^{-3}$; orange: $2.6 \times 10^{18} \text{ cm}^{-3} - 1.8 \times 10^{19} \text{ cm}^{-3}$.

This analysis is now ongoing and the results of this experimental cam-

paign will be compared with that obtained from the analysis of records from 2015 presented in this manuscript. This instantaneous imaging interferometric diagnostic does not follow the shock continuously with the time but it gives a precise map of the electron density which can be inverted through Abel inversion to obtain the local estimation of the electron density.

In parallel, in the electromagnetically launched shocks, we have upgraded our table top setup to achieve higher speeds. For this, we have used 12 capacitors each of $1 \mu\text{F}$ at the place of the previous 11 capacitors each of $0.6 \mu\text{F}$. We have implemented new diagnostics, namely a visible interferometer working in the Gated Optical Imaging mode and time and space visible spectroscopy similar to the one described in the chapter 4. For the visible interferometry, we have Mach Zehnder Interferometer setup and we will image the shock at different times with the help of a SL300 picosecond high energy Nd:YAG laser ($\lambda = 532 \text{ nm}$ and energy = 0.24 J). The experiment will soon be performed on this new setup and the analysis of such records will also be undertaken in future allowing a comparison of electromagnetically launched shocks with the laser-driven shock, which should make the bridge between thin and optically thicker shocks.

Thesis summary

Radiative shocks (RS) are present in various astrophysical environments, especially in stars. They are then present in all the supersonic accretion/ejection processes during the stellar evolution, from the early phase of the protostellar collapse, up to the magnetosphere accretion on to the already formed T- Tauri stars, up to the late stage of the supernovae shocks.

Radiative shocks are strong shocks (i.e. Mach number, $M \gg 1$), which reach high temperatures and thus are the source of intense radiation. Although the observation of (i.e. spatially resolved) signatures of such shocks in the astrophysical environments is very difficult, an alternate approach, named laboratory plasma astrophysics provides a powerful tool to study them on the Earth.

These waves have been experimentally studied since more than a decade, mostly on large-scale laser facilities, in noble gases and with different targets geometries. The ablation process, generated by the interaction between the laser and a foil, induces a shock wave in the foil, which then propagates in the gas at a speed of several tens of km/s. Numerical simulations can describe these shocks with an improving precision. With laser intensities on target comprised between 10^{14} and 10^{15} W/cm², these experiments allowed to record shock speeds ranging between 40 and 150 km/s.

All previous experimental studies have been focused on the case of single radiative shocks. However, in astrophysical conditions, the radiative shock in general interacts with a denser medium, leading to the development of reflected and transmitted shocks. A few representative examples of such phenomena are the interaction of supernovae remnants with dense molecular clouds, the accretion shocks on the photosphere of T-Tauri stars and the bow shocks at the head of fast stellar jets. The collision (or the interaction) of two radiative shock waves is obviously a rare astrophysical event and the template case of the supernova remnants DEM L316 (see Fig. 1 of Williams *et al.* (1997)) is still the subject of debates Williams *et al.* (2005); Toledo-Roy *et al.* (2009); Velarde *et al.* (2006). In this regard, the development of dedicated laboratory experiments to the study of propagation and interaction of counter-propagating shock waves is important as a tool to characterize such events through their specific signatures.

Complementary to laser experiments, compact pulsed power generators may drive an electromagnetic coaxial plasma gun to create astrophysical relevant shocks in lower pressure noble gases, with a high availability and a

rather modest capital cost. The electromagnetically driven shock waves may have larger scales than those by laser. Thus they can be analyzed rather easily with the adequate diagnostics (Kondo *et al.*, 2008).

In this thesis, I am presenting radiative shocks in the context of laboratory astrophysics, using two experimental approaches: laser-driven shocks and electromagnetically driven shocks.

First chapter of my thesis is Radiative shock waves, in which the physics of radiative shocks have been studied. Radiative shock waves are hypersonic shock waves, which are heated to high temperature and, as a consequence, become the source of intense radiation. This radiation, in turn, modifies the dynamics and structure of the shock itself, which makes its structure more complicated. Radiative shock waves occur in several astrophysical circumstances such as in the accretion shock of protostellar formation (Stahler, Palla, and Salpeter, 1986), the supernova explosion and the interaction of their remnants with the dense interstellar medium (Chevalier, 1977), the bow shocks at the head of stellar jets (Hartigan *et al.*, 2001).

Radiative shock waves can now be studied in the laboratory, which allows to compare the data with models existing in the literature and to check the ability of the numerical codes to reproduce them (see for instance Bouquet *et al.* (2004); Leygnac *et al.* (2006)). The experimental study of radiative shock characteristics is crucial in understanding these various energetic processes occurring in the astrophysical plasmas.

The jump conditions (Rankine-Hugoniot relations) for the simple case of an ideal gas, which rely on the values of the thermodynamical quantities on both sides of the discontinuity. Let us consider a one-dimensional shock propagating in a gas at rest with the speed u_s . In the frame associated with the shock front, the pre-shock (upstream) fluid velocity is then $u_1 = -u_s$, while, behind the shock (post-shock or downstream region), this velocity is u_2 , as shown in the Fig. 2.1. Considering the case of strong shocks, where M may be considered to be $\gg 1$, jump conditions for ideal gas are:

$$\frac{\rho_2}{\rho_1} = \frac{(\gamma + 1)}{(\gamma - 1)} \quad (8.1)$$

$$\frac{T_2}{T_1} = \frac{2M^2\gamma(\gamma - 1)}{(\gamma + 1)^2} \quad (8.2)$$

$$k_B T_2 = \frac{2(\gamma - 1)}{(\gamma + 1)^2} m u_s^2 \quad (8.3)$$

For mono-atomic gases, $\gamma = 5/3$, the compression ratio is estimated to be 4, and the post-shock temperature is

$$k_B T_2 = \frac{3}{16} m u_1^2 = \frac{3}{16} m_P A u_1^2 \quad (8.4)$$

This temperature is thus proportional to the square of the shock velocity and to the atomic mass. In contrast to the discussion on ideal gas, in the case of a real gas is a little more complicate. It is to note that in this case, a part of the kinetic energy is used to excite and ionize the post-shock gas. As a result, its temperature is lower than that for the case of ideal gas. In addition, the pressure is also modified due to ionisation (Michaut *et al.*, 2004). Including the effect of ionization with the average charge \bar{z} in the medium for the case real gas, jump relations for real gas are:

$$\rho_2 u_2 = \rho_1 u_1 \quad (8.5)$$

$$\rho_2 u_2^2 + \rho_2 \frac{k_B T_2}{m} (1 + \bar{z}_2) = \rho_1 u_1^2 + \rho_1 \frac{k_B T_1}{m} (1 + \bar{z}_1) \quad (8.6)$$

$$\rho_2 u_2 \left[\frac{5}{2} \frac{(1 + \bar{z}_2)}{m} k_B T_2 + \epsilon_{\text{exc}_2} + \frac{u_2^2}{2} \right] = \rho_1 u_1 \left[\frac{5}{2} \frac{(1 + \bar{z}_1)}{m} k_B T_1 + \epsilon_{\text{exc}_1} + \frac{u_1^2}{2} \right] \quad (8.7)$$

In the previous both cases, the effects of radiation heating and cooling have been neglected. However, the radiation emitted in a strong shock will affect its structure. These effects can be determined using mass, momentum, and energy conservation equations, which now have to include the contributions of the radiative flux, energy, and pressure. This case is more complex now. Taking into account radiative effects, the equations of radiative hydrodynamics in the co-moving frame of the shock (Mihalas and Mihalas, 1999; Drake, 2006) can be written as

$$\frac{\partial \rho}{\partial t} = -\nabla \cdot (\rho \mathbf{u}) \quad (8.8)$$

$$\rho \left(\frac{\partial \mathbf{u}}{\partial t} + \mathbf{u} \cdot \nabla \mathbf{u} \right) = -\nabla (P + P_{\text{rad}}) \quad (8.9)$$

$$\frac{\partial}{\partial t} \left(\frac{\rho u^2}{2} + \rho \epsilon + E_{\text{rad}} \right) + \nabla \cdot \left[\rho \mathbf{u} \left(\epsilon + \frac{u^2}{2} + \frac{P}{\rho} \right) + (E_{\text{rad}} + P_{\text{rad}}) \mathbf{u} \right] = -\nabla \cdot \mathbf{F}_{\text{rad}} \quad (8.10)$$

The contributions linked to P_{rad} and E_{rad} are effective only at very high temperature (i.e. velocity). However, for the radiative shocks of interest in our experiments, the contribution of the radiative flux F_{rad} is non-negligible compared to ρu^3 . These shocks are thus in the *radiation flux dominated regime*. Most of the experimental shock waves are in this regime. These hydrodynamic equations are strongly non-linear.

Depending on the opacity, the radiation emitted from the shock may be absorbed by the pre-shock region, inducing its pre-heating. Far away from the discontinuity, the structure of the upstream medium is determined by the absorption. On its side, the structure of the transition layer of the downstream medium close to the discontinuity depends on the balance between

the emission (cooling) and the absorption (heating). Thus the full structure of the shock mainly depends on the variation of the opacity χ (cm^2/g). The optical depth ($\tau(s)$), measured from the position of the jump, is then the relevant parameter for the absorption. It is given by

$$\tau(s) = \int_{s_{\text{jump}}}^s \chi(s')\rho(s') ds' \quad (8.11)$$

where s' characterizes the path of the radiation. As we are interested in the mean frequency averaged radiative flux, the relevant opacity here will be the averaged Rosseland opacity which will be defined in due course.

If $\tau \gg 1$, the regime is referred as optically thick, while in the opposite case ($\tau < 1$) it is optically thin. Flux dominated radiative shocks have been classified depending on the optical depth of upstream and downstream regimes.

We are more interested in the kind of shock have a radiative precursor. It is possible to produce a radiative shock at the high energy laser facilities with laser intensity of $\sim 10^{14}$ W/cm². A short summary of number of experiment performed at high power laser facilities have been listed in table 2.1. Other than laser driven radiative shock it is possible to launch comparatively slower radiative shocks (~ 10 -30 km/s) using electromagnetic generators.

The chapter two is dedicated to the numerical analysis of radiative shock waves and of the main physical processes, which play a role in these complex processes. Radiative shocks are present in various astrophysical processes implying extreme conditions. Laboratory experiments then allow investigating the underlying physical processes, which take place in these conditions and which are not observable from the Earth due to a lack of spatial resolution. However, experiments are not always straightforward to interpret and the help of numerical simulations becomes precious.

Different numerical approaches are used for the simulation of laboratory plasmas. Some of them use fixed grids. Other introduce the possibility of refinement (on the fly) in some meshes (Adaptative Mesh Refinement), to maintain a good resolution in the interesting parts of the plasma. Another approach is based on meshes following the fluid (Lagrangian description), which means that the meshes move with the fluid and no matter may go through a mesh to another. The form of the equations differ in this case (see for instance Orban *et al.* (2013)).

HELIOS is such a one-dimensional Lagrangian radiation hydrodynamic commercial code (MacFarlane, Golovkin, and Woodruff, 2006) and I have used it to simulate our experiment of interacting shock waves. This code is easy to handle and has the presently interesting capability to be able to simulate the case of two shock waves propagating in opposite directions and launched by two different lasers. HELIOS may describe non-LTE plasmas as it includes an in-line collisional radiative (HELIOS-CR) model for computing

non-LTE atomic level populations at each time step of the hydrodynamics simulation. However, I used HELIOS in the LTE approximation, which is appropriate to our experimental conditions (Rodriguez *et al.*, 2011), as will be discussed in the next section.

The code solves the fluid equations of motion using the pressure contributions of electrons, ions, and radiation. It may describe the electrons and ions as two interacting fluids at respective temperatures T_e and T_i . Thermal conduction is described within a flux-limited electron conduction model based on the Spitzer conductivity and the laser energy deposition is computed with an inverse Bremsstrahlung model.

The radiation emission and absorption terms are introduced in the equation of energy for the electrons and in the radiation transport equations. One of the methods, which are proposed, is the flux-limited, multi-group radiation diffusion model, where the radiative flux is proportional to the gradient of the radiative energy and is inversely proportional to the Rosseland opacity. The expression is pondered by a flux-limited diffusion coefficient in order to obtain the good optically thin limit. This coefficient follows the Larsen expression described in Olson, Auer, and Hall (2000). The second method is a (time independent) multi-angle short-characteristics scheme. In our case, where radiation and hydrodynamics are strongly coupled and thus the radiation field varies rapidly, we used the diffusion model together with LTE Planck and Rosseland multi-groups opacities.

In addition, our version of HELIOS uses the PROPACEOS (MacFarlane, Golovkin, and Woodruff, 2006) Equation of State (EOS) and multi-group opacity tables, which are generated by the code ¹ and it is not possible to include any other opacity or EOS table. The knowledge of the thermodynamical conditions is required for an adequate simulation of the plasma description. In our experiment the mass density ranges between $\sim 10^{-4}$ and 10^{-1} g/cm³, while the temperature values are comprised between and ~ 0 to 50 eV. The precise calculations performed by Rodriguez et al. (Fig2 of Rodriguez *et al.* (2011)) for Xenon, indicate that the thermodynamical conditions of our radiative shock experiments correspond to the LTE regime.

The equation of state (EOS) defines the dependence of the pressure, ionisation, internal energy with the mass density and temperature. Several models do exist in the literature.

Our version of HELIOS for LTE plasmas may handle polytropic or PROPACEOS equation of state. Unfortunately, there are not many details about this last method. The authors of the code mention that it uses a QEOS-type model (More *et al.*, 1988) in the strong coupling regime (i.e., at relatively high densities and low temperatures), and an isolated atom model, which uses a detailed atomic structure modeling in the weak coupling region. The properties between the weak and strong coupling regimes are said to be obtai-

¹see <http://www.prism-cs.com/Software/PROPACEOS>

ned by interpolating in a thermodynamically consistent manner. This EOS includes the contributions from the translation of ions and electrons, electron degeneracy, atom ionization and excitation, and Coulomb interactions (Debye - Huckel correction).

I have performed HELIOS 1D simulations for different cases for single and counter propagating shocks in chapter 2 of my thesis. Radiative shock waves propagating in Xenon at 0.1 bar with a velocity of 50 km/s are characterized by the development of an extended radiative precursor. The huge compression of 38 in the post-shock is a consequence of both the shock and the gas ionisation (factor of 10) as also from the radiative cooling. The post-shock and pre-shock temperature on both side of the peak are identical, indicating that the shock is supercritical.

The spectacular role of the opacity has been highlighted. Due to the uncertainty in the opacity used for Xenon in our simulations, I decided that, at this stage, it was not necessary to refine the simulation in terms of group numbers within the 1D description of the shock wave.

Our numerical study gives the main characteristics of the interaction of two counter-propagating shock waves with speeds equal to 50-50 km/s and 50-20 km/s. The case of identical speeds is simpler due to the symmetry of the problem. However, whatever the speeds, the most important signature of the interaction is the merging of the precursor at 8 ns for 50-50 km/s and at 15 ns for 50-20 km/s. This merging is followed by a regular increase with time of the electron density and the temperature. The collision time is characterized by a sudden increase of the electron density by an order of magnitude, reaching 6.6×10^{21} and $3 \times 10^{21} \text{ cm}^{-3}$ respectively, whereas the temperature increases up to 39 and 28 eV.

When a short pulse of a high-power laser beam is focussed on a thin foil, it transfers a huge amount of energy to the foil material. Almost instantaneously, the laser absorption heats it up to the ablation. A hot and low density corona is generated backwards by this process. Beyond the ablation surface, a shock is formed in the foil as a consequence of the momentum conservation (rocket effect). The shock moves inward in the foil. Our case of the experimental setup, as the foil closes a tube filled with gas, the shock propagates then in the gas, where it is studied through various kinds of diagnostics. The foil then acts as a piston.

We performed the experiments at Prague Asterix Laser System (PALS) in the Spring 2015 (five weeks: 20th April - 22th May). The objective of the experimental campaign was to study the evolution of two counter streaming radiative shocks, driven by two counter-propagating lasers with an irradiance in the range of $10^{14} \text{ W.cm}^{-2}$, and therefore to characterize their interaction and collision. In the chapter third chapter, I have first presented a brief description of the PALS laser facility and of the laser beams used in our experiment. This followed by a presentation of the targets design and an overview of the general setup and of our main diagnostics.

The Prague Asterix Laser System (PALS) is a laser facility based on an Infrared high-power iodine laser system (Asterix IV) (Jungwirth *et al.*, 2001). Using different amplifying stages, the laser facility is able to deliver energy up to 1 kJ in 0.3 ns at the fundamental wavelength 1315 nm. The output laser beam can be further subdivided in few auxiliary beams. All auxiliary beams may be frequency doubled ($\lambda = 657$ nm) or tripled (438 nm). The PALS laser facility is capable of firing up to two high energy laser shots per hour. Compared with solid states lasers, this gas laser is known to deliver a quite homogenous beam intensity without hot spots.

For our experiments, we used two independent laser beams to drive the two counter streaming shocks in the gaseous target. For this purpose, the fundamental PALS laser beam has been subdivided, after the fourth amplifier (V_4), into two beams with respective energy fractions of 60% and 40% (see Fig. 4.2). The most energetic of these laser beams is then injected through the fifth (V_5) amplifier and its frequency are then tripled. This beam at 438 nm will be hereafter termed as the MAIN laser beam.

The second of the two previous laser beams propagates then without any modification. It will be hereafter called the AUX laser beam (1315 nm). The scheme of the energy distribution is shown in the Fig. 4.2 and the characteristics of MAIN and AUX laser are presented in Table 4.1.

For the experiments, PALS offers two vacuum chambers, with a spherical and cylindrical geometry, respectively. The spherical chamber assembly, used in our experiments, is shown in Fig. 4.3. This chamber, having a diameter of 100 cm, is closed by two entrance circular windows of respective diameters 80 cm and 50 cm, to allow the MAIN and AUX beams to penetrate in the chamber and to reach the target. Each of these windows is outfitted with a hinged door. Several circular ports of various diameters also allow for the different diagnostics. The target holder and some diagnostics are mounted on an optical bench which is decoupled from the chamber walls.

Our targets (see Fig. 4.5) schematically consist in small tubes of 4 mm length closed on both sides by two specific foils of thickness 11 μm , on which the laser beams are focused (one laser per foil) with an irradiance of about 10^{14} cm^{-3} . The tube is filled with gas in which the radiative shock propagates with a velocity of 30 - 60 km/s. The two foils closing the target insure the conversion, through ablation and shock generation, of the laser energy into mechanical energy.

In our experiments, we used specific targets for alignment and characterization of the beam size. These targets were manufactured at the Pole instrumental of Observatoire de Paris.

The gaseous targets were filled in situ at a fraction of 1 bar with a gas (*viz.* Xe, Ar, a mixture of Xe and He), which thus provide the medium for the shock propagation. We chose an in-situ filling system (Fig. 4.10) to reduce the difference of pressures inside and outside of the tube. This is critical as a large pressure difference between the target cell and the vacuum chamber

can result in the breaking of the ultra-thin SiN windows of the target.

First of all we performed focalization of MAIN and AUX laser beam on target by using Al-massive targets. The two PALS laser lenses were translated up to achieve the suitable diameters on the target, which were finally set to 450 - 500 μm and 250 - 300 μm for the MAIN and AUX beams. The size of the impact was controlled each day on mock targets before using the laser beams for real shots on gaseous targets. It is worth to precise that the keV diagnostic was still in place for the shots on the gaseous targets. In that case, the beams impact Parylene-N instead of Aluminium. The keV signal is then weaker than for the mock aluminum targets.

Various kinds of diagnostics were implemented, namely, visible interferometry, XUV, and visible spectroscopy. For the same, two keV cameras are inducted to monitor the impact and two visible cameras for target alignment.

For visible interferometry, we have taken reference images (without any fringe) for every target as shown in the Fig. 4.17a for one target example. In order to record such images, we blocked the reference beam and let the probe beam only to illuminate the target in a static mode, and with the slit open. Then we reduced the slit width to its nominal value (200 μm). This enabled us to have the visualization of the portion of the target which was imaged in the slit on the target and also to locate the position of the pistons before the shot. This image is termed as the *reference target image*. Then, the system was placed in the interferometric mode and the fringe pattern was optimized to be perpendicular to the slit and thus, in the *longitudinal mode*, perpendicular to the direction of the shock propagation. The Fig. 4.17b reports such a typical interferogram recorded during our experiment (cf. Fig. 4.13). The horizontal axis corresponds to the direction of the shock propagation (with a total scale of 5.4 mm on the target) and the vertical axis corresponds to time (scaling 200 ns).

The time and space integrated XUV plasma emission are recorded with a Flat Field XUV spectrometer using a concave grating. In the Fig. 4.19, the drawing of the XUV spectrometer setup scheme (red color) is presented together with the spherical chamber and the target. The XUV spectrometer is installed on the top of the spherical chamber, which allows the XUV emission, passing through the Si_3N_4 membrane on the top of the target (see section 4.2.2), to be recorded.

In addition to the interferometry and XUV spectroscopy, we have also implemented a time- and space-resolved visible spectroscopic (see Fig. 4.20a) plasma emission diagnostic.

In chapter 5, I present the results of the two diagnostics with a particular focus on the interferometric data, which I have extensively studied with the help of a specific data analysis procedure that I have developed. The visible interferometry is an adequate tool to probe the electron density of the radiative precursor up to the critical density ($4 \times 10^{21} \text{ cm}^{-3}$ at the wavelength 527 nm of the probing laser), whereas the denser post-shock region

is opaque to the visible light. XUV radiation is present in the whole shock structure and thus the time- and space-integrated XUV spectroscopy may allow exploring the self-emission coming from the post-shock and precursor regions.

In the visible interferometry, the interferences between the main and reference beams overlapping on the detector produce a pattern of fringes, which follow the relative phase variations between the probe (which passes through the plasma) and the reference beams (see section 4.4.1 of the previous chapter for the experimental setup). The phase variation between two consecutive fringes of the unperturbed beams (i.e. without any plasma) is equal to 2π . Then, in the presence of the plasma in the probe beam, these fringes become shifted due to the modification of the refractive index. More details about the principle of the interferometry and the Mach-Zehnder interferometric setup may be found in the APPENDIX A, and we recall here only the expression of the phase shift:

$$\Delta\phi \approx -\frac{\pi d}{\lambda N_c} \langle N_e \rangle \quad (8.12)$$

where $\lambda = 527$ nm is the wavelength of the probing laser, $N_c = 4 \times 10^{21}$ cm⁻³ the critical density at this wavelength, and $\langle N_e \rangle$, is the electron density, averaged over the laser path d in the cell, and is defined as:

$$\langle N_e \rangle = \int_0^d \frac{N_e(z, t) dy}{d} \quad (8.13)$$

In this chapter, I have presented an extensive data analysis of few representative interferometric and spectroscopic records. I am presenting here summary of results obtained bellow.

The average shock speed and electron density have been estimated from the interferograms. The shock speeds of the MAIN and AUX radiative shock waves vary between ~ 30 -55 and 10-30 km/s, respectively and the averaged precursor electron density ranges between 10^{17} and 10^{19} cm⁻³ during the shocks propagation.

We have demonstrated the interaction effect between the two radiative precursors in the case of Xe at 0.1 bar, at 54 and 23 km/s. The interaction is clearly characterized in the experiment by the enhancement of the ionisation wave followed by the merging of the two radiative precursors at 20 ns. The collision time is recorded at 47 ns. Such behavior is reproduced by the simulation.

We have investigated this interaction at a larger pressure, 0.2 bar, with the following speeds ~ 41 km/s for the MAIN and ~ 18 km/s for the AUX shock waves. We do not record any experimental signature of the radiative precursor for AUX. Further, we have not been able to catch experimentally the collision time. The recorded precursor of MAIN is not influenced by AUX wave up to 48 ns (Fig. 5.9(b) and (c) in data analysis chapter), which is the

limit of the record. On its side, the 1D simulation predicts a tiny precursor for AUX and that both precursors start to interact at 49 ns. This plausible shocks interaction, occurring at times which are outside of the record, can not be confirmed by our experiment.

The results of the transverse interferometry at 0.2 bar, with speeds of ~ 40 and 20 km/s indicate that the MAIN precursor has a lateral extension of ~ 600 μm whereas it is 300 μm for AUX. The precursor of MAIN is almost flat with a probable small bending at the edges of the tube, whereas the AUX precursor is more curved. This means that the 2D effects are more important for AUX than for MAIN. Still, in the case of Xenon, we have obtained information about the temperature and the mean charge of gas through our time integrated XUV spectra (shot#48143) in Xenon at 0.6 bar. From these results, we may conclude that the mean ion charge is at least equal to 6 and that the temperature has reached 15 eV.

Our simulations give a qualitative description of the shocks interaction when the laser fluence is adjusted to give the correct shock velocities. However, it is now well known that 2D simulations (together with state of the art opacities) fit better with experiments (González, Audit, and Stehlé, 2009; Leygnac *et al.*, 2006; Stehlé *et al.*, 2010). For the same laser energy, the 2D simulations lead to a diminution of the shock speed compared to 1D as also to a diminution of the electron density. For instance, in the case of a shock wave launched by a laser beam at 1315 nm in Xenon at 0.3 bar at PALS and with a laser fluence of 85000 J/cm^2 , ARWEN 2D simulations give a shock speed of 44 km/s in agreement with the experimental one (Cotelo *et al.*, 2015). 1D simulation would require in this case a fluence of 30000 J/cm^2 to achieve the same velocity.

The space and time integrated XUV records at 0.6 bar, for respective speeds which are equal to ~ 39 and 18 km/s, indicate that the temperature of the shock has reached values up to 15 eV and that the Xenon mean ion charge has also reached values of 6 - 7 whereas 1D simulations predict electron temperature 10-30 eV and ion charge 5-10 (Fig. 5.18c). A more detailed study, based on 2D simulation and radiative transfer post-processing will be necessary to refine the analysis.

We have investigated the case of other noble gases (Ar, Kr) and we have observed that, for a given laser energy, the shock velocity decreases with the mass density. This study has confirmed that, for a given density and shock velocity, the radiative effects increase with the atomic number. For Kr, we noticed a tiny precursor, without any interaction. To get such effect, it will be necessary to increase the shock velocity and thus the laser energy.

This has been done at the ORION laser facility in UK, where the collision of two counter-propagating shocks at equal speed ~ 80 km/s with laser fluence $\sim 6 \times 10^{14}$ W/cm^2 has been performed (Clayson *et al.*, 2016; Suzuki-Vidal *et al.*, 2016) for different noble gases and for pressures comprised between 0.1 and 1 bar. A number of diagnostics setup, X-ray backlig-

hting, optical self-emission streak imaging and interferometry (multi-frame and streak imaging), were used to study both the post-shock and the radiative precursor. Although I have not participated in the experiments, I have performed 1D simulations to interpret ORION experimental results. This work is not presented in this thesis.

The previous chapters were dedicated to the study of laser generated radiative shocks. With irradiance more than 10^{14} W/cm², we were able to study shock waves propagating at velocity up to 50 km/s in noble gases with an initial mass density comprised between 5×10^{-4} - 3×10^{-3} g/cm⁻³. Complementary to laser experiments, compact pulsed power generators may drive an electromagnetic coaxial plasma gun to create astrophysical relevant shocks in lower pressure noble gases (Kondo *et al.*, 2006) with a high availability and a rather modest capital cost. The electromagnetically driven shock waves may have larger scales than those by laser; thus they can be observed rather easily (Kondo *et al.*, 2008).

Such electrical pulsed power devices may then : i) create a high-voltage breakdown, through a gas or, more easily, at the surface of a dielectric, ii) produce relatively hot plasma by ohmic heating when the rising current in the device is passing through a portion of gas, iii) accelerate plasma layers under the magnetic pressure associated with the self-generated magnetic field when high electrical current (say 10's of kA) is maintained for a short but sufficient time (say 1 μ s). Such ionization and acceleration are present in Z-pinch plasmas and in plasma focus devices (PFD), providing a clever geometry is employed and the mass under consideration (say 1 mg) is compatible with the stored energy (Martin, Williams, and Kristiansen, 1996).

In this chapter, we will see first how a fast electrical circuit works, then we will discuss the principles of a coaxial plasma gun and of PFD. We will see what is in favor of our objective and what has to be avoided. A geometry capable to reach our objective will be proposed.

The optimization of the coaxial gun (in term of plasma speed) will be performed and some typical figures will be given in the case of a generator with a stored energy around 1 kJ, and a plasma slab of 4-mm diameter, i.e. quite 10 times the transverse dimension of a laser driven RS. The operating conditions are supersonic shocks, up to 10-30 km/s speed, at static pressures of few mbar in heavy rare gases (Ar, Xe). The results of this 0-D model will be then compared to those obtained with 3-D MHD simulations performed with the code GORGON (by Andrea Ciardi at LERMA) which has been used successfully to describe other pulse-power driven plasma experiments (Chittenden *et al.*, 2004) as well as laboratory plasma astrophysics experiments (Ciardi *et al.*, 2007). The diagnostics which have been implemented will be presented to illustrate the model as well as preliminary records of the plasma speed.

Our aim being to accelerate a plasma slab using the magnetic pressure, it is obviously needed to drive a high intensity current because the magnetic

pressure is expressed by $B^2/2\mu_0$ in the region where exists an induction B . The pressure in bars is simply $4B^2$, with B in Teslas, and, in a cylindrical geometry, 1 Tesla is the field around a 50-kA current at a radius of 1 cm. Thus we should count on roughly 100 kA delivered by the generator, but such a high current is delivered only in a pulsed mode by a laboratory scale device.

There are numbers of technical solutions to achieve such electrical parameters; one may use rather slow generators at moderate high voltage like capacitors bank with the advantage of well know techniques but with limited adjustments. According to an abundant literature ¹ a convenient device is a medium-energy capacitor bank feeding a low-inductance circuit. An R-L-C circuit is a well-known combination delivering a high peak current in the pseudo-periodic mode. For a capacitor C initially charged under U_0 , key performances are as follows :

- Current intensity $I(t)$ is a damped sinusoid
- Pseudo pulsation $\omega = \sqrt{1/(LC) - R^2/(4L^2)}$
- First current peak $I_{peak} = U_0/[\sqrt{(L/C) + 0.8R}]$
- Time of current peaking $T/4 = \pi/(2\omega)$
- Equivalent impedance $Z = \sqrt{(L/C)}$

For a safe handling in air, a voltage not higher than 30 kV is recommended. Taking a total capacitance of 6 μF , 2700 J are stored under 30 kV. For an inductance of 240 nH, the expected peak current might be 150 kA at 1.9 μs . This set of values will be a guideline for the development presented in further sections.

For this part of the work, the objective was to show that, in complement of laser experiments, a compact pulsed power generator might drive astrophysically relevant shocks, in low pressure noble gases, with a higher availability and at a rather modest capital cost. The longitudinal acceleration of a plasma sheath in a low backing gas pressure has been demonstrated in coaxial plasma guns as early as in the 70's, even leading to speeds of 100 km/s in light gas as H_2 , which were measured and modeled. A choice was made to revisit this type of device. At present, the electromagnetic coaxial plasma guns are quite only considered as the initiators of a strong, radial, plasma implosion plasma focus devices (PFD), due to a good ability to produce a pinch plasma and emission of energetic particles and hard X-ray. For that reason it was necessary to adapt the principle of a PFD with two major constraints: increase the conversion of stored energy into the kinetic energy of a plasma sheath, prevent totally any pinching.

¹Institute for Plasma Focus Studies, resource website, <http://plasmafocus.net/> last connection in 2016

That objective was reached by defining the electrical and geometrical parameters of a low-inductance and compact pulsed power generator. An optimization process has been established to match achievable electrical parameters of the circuit (capacitance, inductance, peaking current intensity) with a plasma motion in the accelerating tube over few cm, leading to a final speed of 10-30 km/s. A model was built up to describe the dynamics of an RLC circuit with a varying element composed of the moving plasma sheath, accelerated by the self generated magnetic pressure. The change in plasma position along the axis is increasing the inductance and the mass accretion is increasing the plasma mass. It was shown that a change in the electrode geometry, namely a 30° conical shape, was increasing the energy conversion and preventing any focusing. The further step, in contrast with PFD, is the merging of the plasma ring into a rather planar one which is injected in a drift tube.

Considering Ar or Xe at gas pressure in the range 0.1 – 10 mbar, and a highly coaxial, 1-kJ device, the simple model was sufficient to predict performances agreeing with the only work quoted in the literature. Basic observations of the moving plasma, using side-on detection of the visible emission, give features coherent with the model. Mach numbers from 20 to 60 are obtained, fitting with the objective of strong shock formation. A refined 3-D MHD numerical simulation indicates very promising features of the shock, in view of exploring mm-size shocks in a regime complementary to laser driven ones, and on a table-top device allowing a higher repetition rate.

Appendices

Visible Interferometry

Laser interferometry is used in plasmas to deduce the electron density through the variation of the refractive index caused by the ionisation of the matter. In this appendix, firstly, the experimental setup of Mach Zehnder interferometry as well as the underlying physical principles are presented.

A.0.1 Refractive index of a plasma

In order to derive the refractive index of a gas, one starts with the set of Maxwell's equations for a monochromatic plane wave propagating in the plasma (see for instance equation 4.1.1 of reference (Hutchinson, 2002)). Free electrons and ions are supposed to be distributed uniformly and the net total charge density is equal to zero.

For harmonic waves propagating in the direction of $+x$ and with the pulsation ω , one obvious solution is given by:

$$E(x, t) = E_0 e^{i(kx - \omega t)} \quad (\text{A.1})$$

where E_0 and k are complex quantities.

The relation between k and ω is given by the dispersion relation,

$$k^2 = \frac{\varepsilon \mu \omega^2}{c^2} \left(1 + i \frac{4\pi\sigma}{\omega\varepsilon} \right), \quad (\text{A.2})$$

where, μ is the electric permittivity and ε is permeability.

The free electrons are accelerated by the electric field and therefore, equation their motion is given as:

$$m_e \frac{dv}{dt} = -e E_0 e^{-i\omega t} \quad (\text{A.3})$$

The obvious solution for the electron velocity v is:

$$v = -i \frac{e}{m_e \omega} E \quad (\text{A.4})$$

and thus the electrons carry a current with a density J ,

$$J = N_e e v = i \frac{N_e e^2}{m_e \omega} E \quad (\text{A.5})$$

where N_e is the electron density. Due to the larger mass of the ions, the corresponding current is negligible.

The previous equation allows to derive the plasma conductivity σ , which is equal to $iN_e e^2 \omega / m_e$. Putting this value in the equation (A.2), and assuming a thin medium, where $\varepsilon \approx 1$ and $\mu = 1$ one obtains finally:

$$k^2 = \frac{\omega^2}{c^2} \left(1 - \frac{\omega_p^2}{\omega^2}\right) \quad (\text{A.6})$$

where ω_p is the plasma frequency defined as:

$$\omega_p^2 = \frac{4\pi N_e e^2}{m_e} \quad (\text{A.7})$$

Equation A.6 shows that a electromagnetic wave with a pulsation larger than ω_p can't propagate in the plasma. This allows to derive a critical electron density N_c in cm^{-3} as:

$$N_c = \frac{m_e \omega^2}{4\pi e^2} = \frac{4\pi m_e c^2}{e^2 \lambda^2} \quad (\text{A.8})$$

For instance, for a radiation of $1 \mu\text{m}$ wavelength, this upper limit is equal to $N_c = 4.46 \times 10^{21} \text{cm}^{-3}$.

Therefore the index of refraction is given by the expression,

$$n = \sqrt{1 - \frac{\omega_p^2}{\omega^2}} = \sqrt{1 - \frac{N_e}{N_c}} \quad (\text{A.9})$$

Finally, one obtains:

$$E(x, t) = E_0 e^{i(kx - \omega t)}, \quad \text{with } k = n \frac{\omega}{c} \quad (\text{A.10})$$

As a consequence of the variation of the refractive index in the different plasma layers, the light is refracted. Indeed the Snell laws stipulate that if a beam is incident on a plane interface between layers, (of refractive index n_1 and n_2), it undergoes a bending from the angle of incidence. The incident beam, the refracted beam and the normal to the interface lie in the same plane, and one has $n_1 \sin\theta_1 = n_2 \sin\theta_2$, where θ_1 is the angle of incidence and θ_2 is the angle of refraction. Thus, a monochromatic beam propagating in a plasma with increasing density becomes more and more deflected.

A.0.2 Absorption of the laser beam

Beside refraction the light is absorbed by the plasma, and the absorption also increases rapidly near the critical density. In the absence of any atomic bound-bound or bound-free transition, this absorption is due to the inverse Bremsstrahlung process (ion-electron collision (Pfalzner, 2006)) by

the plasma free electrons. The absorption coefficient κ (in cm^{-1}) is then given by (NRL formulary):

$$\kappa(N_e, T_{ev}) = 3.17 \cdot 10^{-7} Ln\Lambda \langle Z \rangle \left(\frac{N_e}{\omega} \right)^2 \frac{1}{T_{ev}^{3/2} (1 - N_e/N_c)^{1/2}} \quad (\text{A.11})$$

where T_{ev} is the temperature in eV, N_e is the electron density in cm^{-3} and $Ln\Lambda$ is the Coulomb Logarithm, defined as $\Lambda = \text{Max}(2., \text{Min}(X, Y))$, with (NRL formulary):

$$X = 23. - \log \left(\langle Z \rangle \frac{N_e^{1/2}}{T_{ev}^{3/2}} \right) \quad \text{and} \quad Y = 24. - \log \left(\frac{N_e^{1/2}}{T_{ev}} \right) \quad (\text{A.12})$$

The transmission $T(d)$ through a layer of thickness d is given by:

$$T(d) = \exp\left(-\int_0^d \kappa(l) dl\right) \quad (\text{A.13})$$

For instance, for $\lambda = 527$ nm, taking $N_e = 10^{19} \text{cm}^{-3}$, $\langle Z \rangle = 10$, $T = 10$ eV, which are typical values for the post-shock in our experiments in Xenon, and supposing a homogenous plasma thickness $d = 600 \mu\text{m}$, the transmission is about 0.9, whereas at $5 \times 10^{19} \text{cm}^{-3}$, it falls to 0.1.

A.0.3 Principle of interferometry

In the optical interferometry technique (Ovsyannikov and Zhukov, 2000), the interference of two plane waves is performed by addition of the two corresponding coherent electric fields. The analyzed medium (here the plasma), in which one of the beam is propagating induces a deshaping between the beams which affects the resulting intensity depending if the fields interfere in phase or out of phase i.e. constructively or destructively.

Two techniques are used: the wave front and the amplitude division.

The wave front division is obtained by using two portions (Fresnel mirrors, Young's double slit, Lloyd's mirror, prisms etc.) of the original wave front, which are then superimposed to produce interference.

In the amplitude division, the two beams are separated by division of the amplitude over the same section of the wave front. Michelson and Mach Zehnder interferometers etc., are the typical examples of this technique of amplitude division.

The principle of interference of two coherent monochromatic traveling waves 1 and 2, with electric fields E_1 and E_2 , propagating in the same direction and polarized in the same plane can be understood as follows: for a given time t , at the point r where these waves superpose, the amplitude of the electric field is the vector addition of the two corresponding elementary amplitudes, i.e.,

$$\begin{aligned}
E(r, t) &= E_1(r, t) + E_2(r, t) \\
&= a_1 \exp(ikr + \omega t + i\phi_1) + a_2 \exp(ikr + \omega t + i\phi_2)
\end{aligned}$$

where ϕ_1 and ϕ_2 are the phases of the two waves at r . The total intensity,

$$I(r, t) = |E_1 + E_2|^2 \quad (\text{A.14})$$

One gets:

$$I = I_1 + I_2 + 2\sqrt{(I_1 I_2)} \cos \Delta\phi \quad (\text{A.15})$$

where $I_1 = a_1^2$ and $I_2 = a_2^2$ are the intensities at the point of interference due to the two waves acting independently and $\Delta\phi = \phi_1 - \phi_2$ represents the phase difference between the two waves. In the case of equal intensities I_1 , one gets

$$I = 4I_1 \cos^2(\Delta\phi/2) \quad (\text{A.16})$$

and the interferometric pattern consists of dark ($\Delta\phi = \pi + 2n\pi$) and bright patterns ($\Delta\phi = 2n\pi$).

In general the two beams are only partially coherent and the minimum of the fringe intensity is not equal to zero. The fringe contrast

$$FC = \frac{I_{max} - I_{min}}{I_{max} + I_{min}} \quad (\text{A.17})$$

is then a measure of the interference quality. FC is maximum and equal to 1 in the case of fully coherent beams of the same intensity $I_1 = I_2$.

A.0.4 Mach Zehnder Interferometer

The Mach Zehnder Interferometer is a device commonly and efficiently used to estimate the change in refractive index by the plasma. Such change is, in most the cases, related to variations in the electron density. We employed this interferometric setup in our experiment.

The principle of this interferometer is based on the division of the incident light beam into two beams with the help of a beam-splitter, which can be a coated glass plate or a cube. After this division, one of the beams (*probe* beam), is allowed to pass through the medium of interest (a plasma in our case) and then made to interfere with the other unaffected part of the beam (*reference* beam), with the help of second beam-splitter as may be noted from Fig. A.1.

In order to understand the principle of interference and its use in estimating plasma properties, let us consider l_1 and l_2 , which are the total path lengths (including the path in the optical elements) for the light travelling from the source to the detector for the upper and lower paths (cf. Figure A.1) respectively. Suppose for the moment that the sample is removed from beam

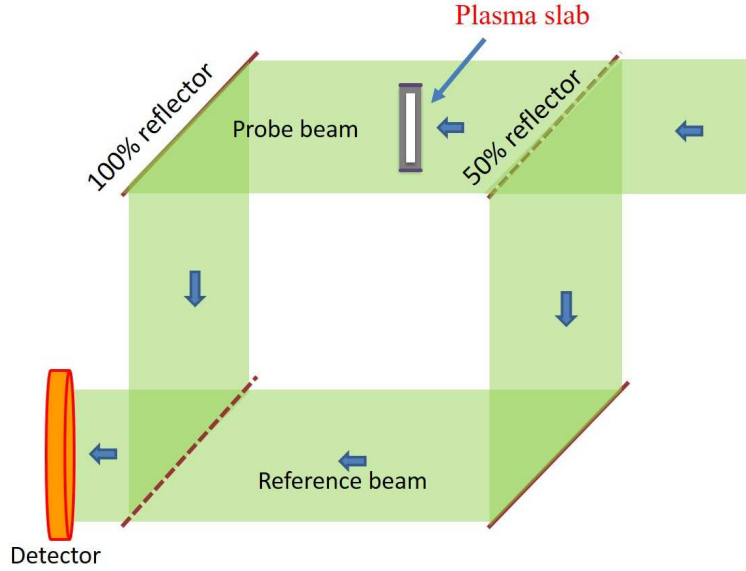


Figure A.1: Schematics of Mach Zehnder interferometer, with two mirrors, two 50% beam splitters and the detector. A plasma slab is placed in one of the two arms of the interferometer.

1 (see Figure A.1), the two optical paths of the probe and reference beams differ in terms of phases. Simplify, to supposing, that the beams propagate in air ($n=1$), these phases are then equal to the $2\pi l_1/\lambda$ and $2\pi l_2/\lambda$.

Thus, accounting for the phase difference δ between the two beams travelled up to detector A can be given as,

$$2\pi \frac{l_1 - l_2}{\lambda} = \delta \quad (\text{A.18})$$

If the two beams are perfectly parallel at the position of the detector, the interferometric figure presents a flat intensity, which passes through minima and maxima when one length of the 2 arms is slightly changed. Usually one introduces a small tilt between the two directions of propagations, which leads to the apparition of parallel linear dark and bright fringes.

In order to obtain interference patterns, it is important to make the paths l_1 and l_2 as close as possible, compared to the coherence length of the laser. For the multimode Evolution 15 laser used in the PALS experiment, this length is approximately 1 cm (value communicated by the constructor).

If we introduce the sample in the probe beam 1 this sample will introduce an additional phase denoted by δ_{sample} and the net phase shift is then $\delta + \delta_{sample}$.

The principle of the deduction of the electron density with the Mach Zehnder interferometer is to measure the refractive index of the test plasma slab, which is placed in the probe beam. We assume for the moment that

this plasma slab is a phase object for the incoming beam, which means that it does not significantly affect the intensity of the probe beam, while it only changes the phase of the wave [5].

The additive phase difference in the probe arm, introduced by the plasma, can be defined as,

$$\phi = \int_0^d k_{plasma} dl = \int_0^d n \frac{\omega}{c} dl \quad (\text{A.19})$$

where n is the local refractive index at position l of the plasma slab and the integral is performed over the slab thickness d . Therefore, the phase difference introduced by the plasma, relative to the propagation into vacuum of the reference beam, is equal to

$$\Delta\phi = \int_0^d (k_{plasma} - k_0) dl \quad (\text{A.20})$$

where $k_0 = \omega/c = 2\pi/\lambda$ is the wave vector of the beam propagating in vacuum.

As long as $N_e < N_c$, the beam propagates in the plasma, the plasma refractive index is given by equation A.9 and one has:

$$\Delta\phi = \frac{\omega}{c} \int_0^d \left[\left(1 - \frac{N_e}{N_c}\right)^{1/2} - 1 \right] dl, \quad (\text{A.21})$$

At very small electron density ($N_e \ll N_c$), the phase shift can be written as

$$\Delta\phi \approx -\frac{\omega}{2cN_c} \int_0^d N_e dl = -\frac{\pi d}{\lambda N_c} \langle N_e \rangle \quad (\text{A.22})$$

where

$$\langle N_e \rangle = \int_0^d \frac{N_e(z, t) dy}{d} \quad (\text{A.23})$$

is the electron density averaged over the path d .

In practice, a reference record is first taken without plasma. To deduce the density, one has to analyze how the fringes depart from their reference positions.

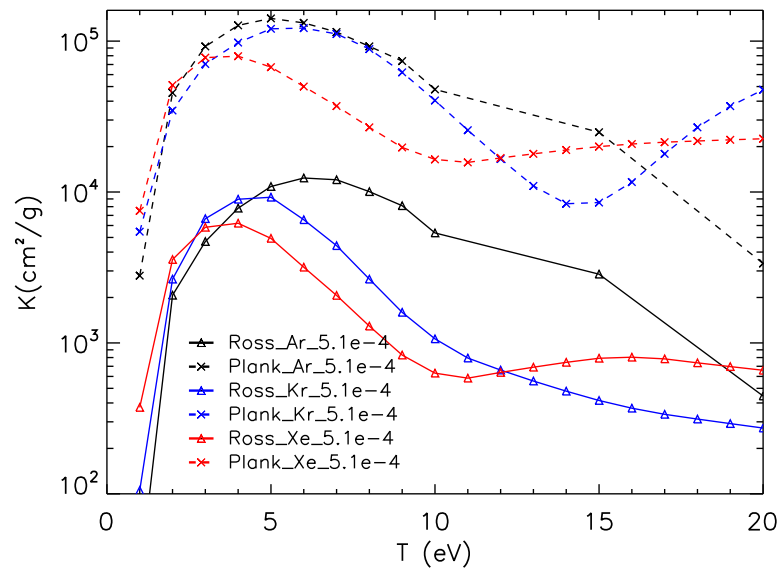
The space between two fringes (inter-fringe) corresponds to a phase variation of 2π . A shift of the fringe by 2π from its reference position (where $N_e = 0$) corresponds to an electron density variation equal to $\langle N_e \rangle = 2\lambda N_c/d$. For $\lambda = 527$ nm, and supposing an homogeneous plasma of thickness $600 \mu\text{m}$, this gives $\langle N_e \rangle = 7 \times 10^{18} \text{ cm}^{-3}$.

Opacities and mean charge

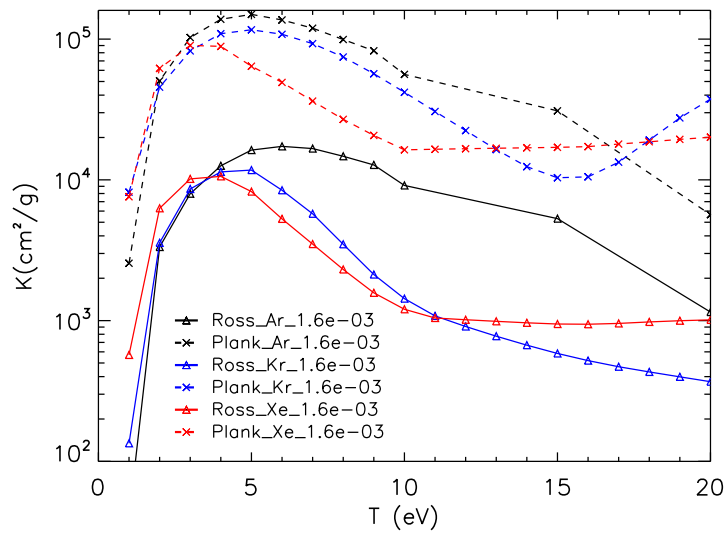
The variations, in logarithmic scale, with the temperature of the PROPA-CEOS Rosseland and Planck opacities (section of chapter 5; see for intense Fig. 5.11) as also of the mean charge of the plasma are reported for two densities $1.6 \times 10^{-3} \text{ g/cm}^3$ and $5.1 \times 10^{-4} \text{ g/cm}^3$ for three noble gases Ar, Kr and Xe in Fig. B.1 and B.2.

$\rho = 5.1 \times 10^{-4} \text{ g/cm}^3$ correspond to typical density of the precursor. For this density, Xenon and Krypton have quite similar variations for the Rosseland opacity with a bump of $7000 \text{ cm}^2/\text{g}$ at 3 eV for Xe and $12000 \text{ cm}^2/\text{g}$ at 4 eV for Krypton. At 10 eV, the two opacities decrease respectively to 600 and $900 \text{ cm}^2/\text{g}$. In comparison with these two cases the opacity of Argon is broader and more regular. Its opacity peaks at 6 eV to $13000 \text{ cm}^2/\text{g}$. At 10 eV, it has decreased to $7000 \text{ cm}^2/\text{g}$, which is higher than for the two previous gases.

The mean charge variations increase regularly with the temperature. At 10 eV, these mean charges are respectively equal to 6.5, 5.5 and 5 for Xe, Kr and Ar.

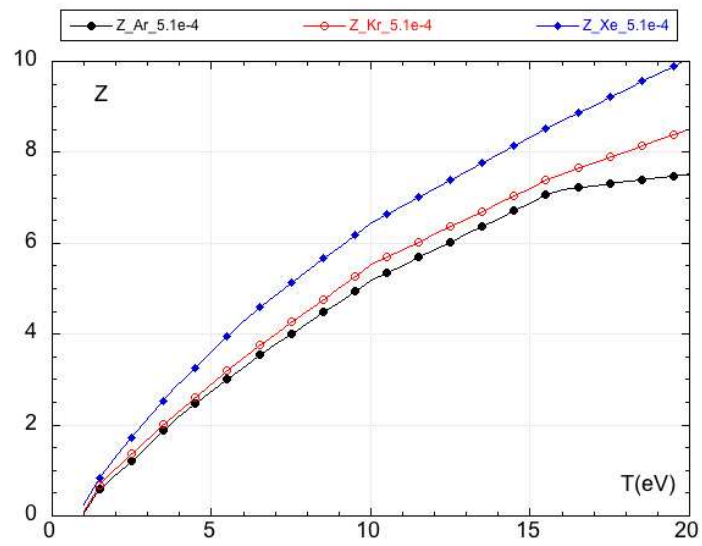


(a)

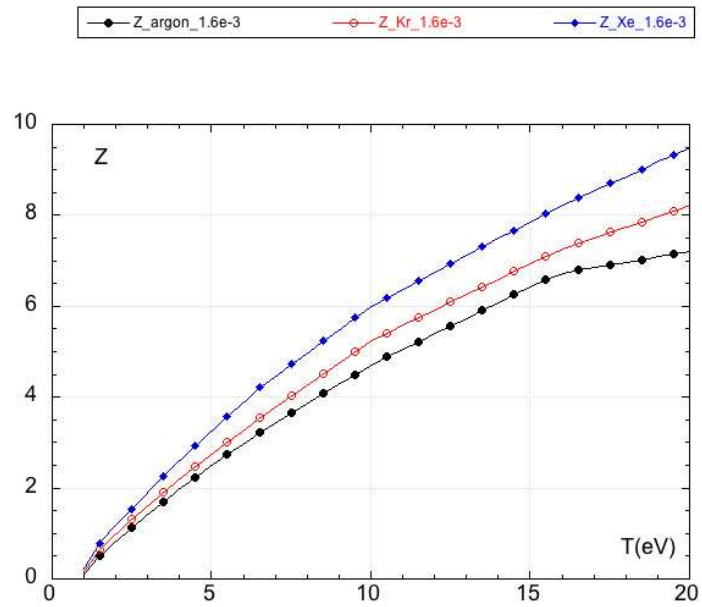


(b)

Figure B.1: Rosseland and Planck opacity for three gases Xe, Kr and Ar at mass densities $5.1 \times 10^{-4} \text{ g/cm}^3$ (a) and $1.6 \times 10^{-3} \text{ g/cm}^3$ (b).



(a)



(b)

Figure B.2: Mean charge for three gases Xe, Kr and Ar at mass densities $1.6 \times 10^{-3} \text{ g/cm}^3$ (a) and $5.1 \times 10^{-4} \text{ g/cm}^3$ (b).

References

- Batani, D., Strati, F., Telaro, B., Löwer, T., Hall, T., Benuzzi-Mounaix, A., Koenig, M.: 2003, Production of high quality shocks for equation of state experiments. *European Physical Journal D* **23**, 99. DOI. ADS.
- Bernard, A.: 2002, Plasma focus et applications. *Le Vide* **57**(306).
- Bett, T.H., Jinks, P., Stevenson, R.M., Danson, C.N., Pepler, D.A., Ross, I.N.: 1995, Binary phase zone-plate arrays for laser-beam spatial-intensity distribution conversion. *Applied Optics* **34**, 4025. DOI. ADS.
- Bouquet, S., Teyssier, R., Chieze, J.P.: 2000, Analytical study and structure of a stationary radiative shock. *The Astrophysical Journal Supplement Series* **127**(2), 245.
- Bouquet, S., Stehlé, C., Koenig, M., Chièze, J., Benuzzi-Mounaix, A., Batani, D., Leygnac, S., Fleury, X., Merdji, H., Michaut, C., *et al.*: 2004, Observation of laser driven supercritical radiative shock precursors. *Physical review letters* **92**, 225001.
- Bozier, J., Thiell, G., Le Breton, J., Azra, S., Decroisette, M., Schirmann, D.: 1986, Experimental observation of a radiative wave generated in xenon by a laser-driven supercritical shock. *Physical review letters* **57**(11), 1304.
- Burhop, E., Spitzer, L.: 1957, *Physics of fully ionized gases. interscience tracts on physics and astronomy no. 3*, JSTOR.
- Chaulagain, U.: 2015, Radiative shocks: experiments, modelling and links to Astrophysics. PhD thesis, Pierre and Marie Curie University.
- Chaulagain, U., Stehlé, C., de Sá, L., Larour, J., Auvray, P., Kozlova, M., Krus, M., Dostal, J., Propupek, J., Suzuki-Vidal, F., *et al.*: 2012, Laboratory experiments of radiative shocks in the context of stellar accretion. In: *SF2A-2012: Proceedings of the Annual meeting of the French Society of Astronomy and Astrophysics* **1**, 305.
- Chaulagain, U., Stehlé, C., Larour, J., Kozlová, M., Suzuki-Vidal, F., Barroso, P., Coteló, M., Velarde, P., Rodríguez, R., Gil, J.M., Ciardi, A., Acef, O., Nejdil, J., de Sá, L., Singh, R.L., Ibgui, L., Champion, N.: 2015, Structure of a laser-driven radiative shock. *High Energy Density Physics* **17**, 106. DOI. ADS.
- Chevalier, R.A.: 1977, The interaction of supernovae with the interstellar medium. *Annual review of astronomy and astrophysics* **15**, 175. DOI. ADS.

- Chittenden, J.P., Lebedev, S.V., Jennings, C.A., Bland, S.N., Ciardi, A.: 2004, X-ray generation mechanisms in three-dimensional simulations of wire array Z-pinch—the evolution of magnetic tower jets in the laboratory. *Plasma Physics and Controlled Fusion* **46**, B457. DOI. ADS.
- Ciardi, A.: 2014,. *private communication*.
- Ciardi, A., Lebedev, S.V., Frank, A., Blackman, E.G., Chittenden, J.P., Jennings, C.J., Ampleford, D.J., Bland, S.N., Bott, S.C., Rapley, J., Hall, G.N., Suzuki-Vidal, F.A., Marocchino, A., Lery, T., Stehle, C.: 2007, The evolution of magnetic tower jets in the laboratory. *Physics of Plasmas* **14**(5), 056501. DOI. ADS.
- Clayson, T., Suzuki-Vidal, F., Lebedev, S.V., Swadling, G.F., Burdiak, G.C., Patankar, S., Smith, R.A., Foster, J., Skidmore, J., Gumbrell, E., Graham, P., Danson, C., Stehlé, C., Singh, R.L., Chaulagain, U., Larour, J., Kozlova, M., Spindloe, C.: 2016, Counter-propagating radiative shock experiments on the Orion laser facility. In: *APS Meeting Abstracts*. DOI. ADS.
- Clayson, T., Suzuki-Vidal, F., Lebedev, S., Swadling, G., Stehlé, C., Burdiak, G., Foster, J., Skidmore, J., Graham, P., Gumbrell, E., *et al.*: 2017, Counter-propagating radiative shock experiments on the orion laser and the formation of radiative precursors. *High Energy Density Physics* **23**, 60.
- Cotelo, M., Velarde, P., de la Varga, A.G., Portillo, D., Stehlé, C., Chaulagain, U., Kozlova, M., Larour, J., Suzuki-Vidal, F.: 2015, Simulation of radiative shock waves in Xe of last PALS experiments. *High Energy Density Physics* **17**, 68. DOI. ADS.
- de la Varga, A.G., Velarde, P., Cotelo, M., de Gaufridy, F., Zeitoun, P.: 2011, Radiative properties for warm and hot dense matter. *High Energy Density Physics* **7**(3), 163 . DOI. <http://www.sciencedirect.com/science/article/pii/S1574181811000498>.
- Dizière, A., Michaut, C., Koenig, M., Gregory, C., Ravasio, A., Sakawa, Y., Kuramitsu, Y., Morita, T., Ide, T., Tanji, H., *et al.*: 2011, Highly radiative shock experiments driven by gekko xii. *Astrophysics and Space Science* **336**(1), 213.
- Dobbs-Dixon, I., Cumming, A., Lin, D.N.C.: 2010, Radiative Hydrodynamic Simulations of HD209458b: Temporal Variability. *The Astrophysical Journal* **710**, 1395. DOI. ADS.
- Doss, F.W., Robey, H.F., Drake, R.P., Kuranz, C.C.: 2009, Wall shocks in high-energy-density shock tube experiments. *Physics of Plasmas* **16**(11), 112705.

- Drake, R.P.: 2006, *High-energy-density physics : Fundamentals, inertial fusion, and experimental astrophysics, Shock wave and high pressure phenomena*, Springer, Berlin, Heidelberg, New York. ISBN 3-540-29314-0. <http://opac.inria.fr/record=b1128433>.
- Drake, R., Doss, F., McClarren, R., Adams, M., Amato, N., Bingham, D., Chou, C., DiStefano, C., Fidkowski, K., Fryxell, B., *et al.*: 2011, Radiative effects in radiative shocks in shock tubes. *High Energy Density Physics* **7**(3), 130.
- Ensmann, L.: 1994, Test problems for radiation and radiation-hydrodynamics codes. *The Astrophysical Journal* **424**, 275. DOI. ADS.
- Ensmann, L., Burrows, A.: 1992, Shock breakout in sn 1987a. *The Astrophysical Journal* **393**, 742.
- Fadeyev, Y.A., Gillet, D.: 2001, The structure of radiative shock waves. III. The model grid for partially ionized hydrogen gas. *Astronomy and Astrophysics* **368**, 901. DOI. ADS.
- Fleury, X., Bouquet, S., Stehlé, C., Koenig, M., Batani, D., Benuzzi-Mounaix, A., Chieze, J.-P., Grandjouan, N., Grenier, J., Hall, T., *et al.*: 2002, A laser experiment for studying radiative shocks in astrophysics. *Laser and Particle Beams* **20**(02), 263.
- Fryxell, B., Olson, K., Ricker, P., Timmes, F.X., Zingale, M., Lamb, D.Q., MacNeice, P., Rosner, R., Truran, J.W., Tufo, H.: 2000, FLASH: An Adaptive Mesh Hydrodynamics Code for Modeling Astrophysical Thermonuclear Flashsheracles: a three-dimensional radiation hydrodynamics code. *Astrophysical Journal, Supplement* **131**, 273. DOI. ADS.
- Gonzalez, J.H., Brollo, F.R., Clause, A.: 2009, Modeling of the Dynamic Plasma Pinch in Plasma Focus Discharges Based in Von Karman Approximations. *IEEE Transactions on Plasma Science* **37**, 2178. DOI. ADS.
- Gonzalez, J.H., Clause, A., Bruzzone, H., Florido, P.C.M.Z.: 2004, A Lumped Parameter Model of Plasma Focus. *IEEE Transactions on Plasma Science* **32**, 1383. DOI. ADS.
- González, M., Audit, E., Huynh, P.: 2007, HERACLES: a three-dimensional radiation hydrodynamics code. *Astronomy and Astrophysics* **464**, 429. DOI. ADS.
- González, M., Audit, E., Huynh, P.: 2007, Heracles: a three-dimensional radiation hydrodynamics code. *Astronomy and Astrophysics* **464**(2), 429.
- González, M., Audit, E., Stehlé, C.: 2009, 2D numerical study of the radiation influence on shock structure relevant to laboratory astrophysics. *Astronomy and Astrophysics* **497**, 27. DOI. ADS.

- González, M., Stehlé, C., Rus, B., Busquet, M., Thais, F., Acef, O., Barroso, P., Bar-Shalom, A., Bauduin, D., Kozlova, M., Lery, T., Madouri, A., Thomas, M., Polan, J.: 2006, Astrophysical radiative shocks: From modeling to laboratory experiments. *Laser and Particle Beams* **24**, 535–540. DOI. ADS.
- Gonzalez, M., StehlE, C., Audit, E., Busquet, M., Rus, B., Thais, F., Acef, O., Barroso, P., Bar-Shalom, A., Bauduin, D., *et al.*: 2006, Astrophysical radiative shocks: From modeling to laboratory experiments. *Laser and Particle Beams-Pulse Power and High Energy Densities* **24**(4), 535.
- González, M., Vaytet, N., Commerçon, B., Masson, J.: 2015, Multigroup radiation hydrodynamics with flux-limited diffusion and adaptive mesh refinement. *Astronomy and Astrophysics* **578**, A12. DOI. ADS.
- Griem, H.R.: 2005, *Principles of Plasma Spectroscopy*, 386. ADS.
- Gu, M.F.: 2008, The flexible atomic code. *Canadian Journal of Physics* **86**(5), 675.
- Harilal, S.S., Tillack, M.S.: 2004, Laser plasma density measurements using interferometry. <http://link.aps.org/doi/10.1103/PhysRevE.64.066412>.
- Hartigan, P.: 1989, The visibility of the Mach disk and the bow shock of a stellar jet. *Astrophysical Journal* **339**, 987. DOI. ADS.
- Hartigan, P.: 2003, Shock Waves in Outflows from Young Stars. *Astrophysics and Space Science* **287**, 111. DOI. ADS.
- Hartigan, P., Morse, J.A., Reipurth, B., Heathcote, S., Bally, J.: 2001, Proper Motions of the HH 111 Jet Observed with the Hubble Space Telescope. *Astrophysical Journal Letters* **559**, L157. DOI. ADS.
- Henke, B.L., Gullikson, E., Davis, J.C.: 1993, X-ray interactions: Photoabsorption, scattering, transmission, and reflection at $0 < i > e < / i > = 50$ -30,000 eV, $0 < i > z < / i > = 1$ -92. *Atomic data and nuclear data tables* **54**(2), 181.
- Hugoniot, P.H.: 1887, Mémoire sur la propagation du mouvement dans les corps et ples spécialement dans les gaz parfaits. *Journal de mathématiques pures et appliquées* **3**, 477.
- Hugoniot, P.H.: 1889, Mémoire sur la propagation des mouvements dans les corps et spécialement dans les gaz parfaits (deuxième partie). *Journal de l'École Polytechnique* **58**, 1.
- Hutchinson, I.H.: 2002, *Principles of Plasma Diagnostics*, 458. ADS.

- Jungwirth, K., Cejnarova, A., Juha, L., Kralikova, B., Krasa, J., Krousky, E., Krupickova, P., Laska, L., Masek, K., Mocek, T., *et al.*: 2001, The prague asterix laser system. *Physics of Plasmas* **8**, 2495.
- Keiter, P., Drake, R., Perry, T., Robey, H., Remington, B., Iglesias, C., Wallace, R., Knauer, J.: 2002, Observation of a hydrodynamically driven, radiative-precursor shock. *Physical review letters* **89**(16), 165003.
- Koenig, M., Faral, B., Boudenne, J.M., Batani, D., Benuzzi, A., Bossi, S.: 1994, Optical smoothing techniques for shock wave generation in laser-produced plasmas. *Physical Review E* **50**, R3314. DOI. ADS.
- Kondo, K., Nakajima, M., Kawamura, T., Horioka, K.: 2006, Compact pulse power device for generation of one-dimensional strong shock waves. *Review of Scientific Instruments* **77**(3), 036104. DOI. ADS.
- Kondo, K., Nakajima, M., Kawamura, T., Horioka, K.: 2008, Relaxation layer in electro-magnetically driven strong shocks. *Journal of Physics Conference Series* **112**(4), 042028. DOI. ADS.
- Kondo, K., Nakajima, M., Kawamura, T., Horioka, K.: 2009a, Atomic process in electro-magnetically driven strong shock wave. *Nuclear Instruments and Methods in Physics Research A* **606**, 223. DOI. ADS.
- Kondo, K., Nakajima, M., Kawamura, T., Horioka, K.: 2009b, Radiation effect and relaxation layer in electro-magnetically driven strong shock waves. In: *APS Meeting Abstracts*. ADS.
- Kunze, H.-J.: 2009, *Springer series on atomic, optical, and plasma physics* **125**, Springer, Berlin, Heidelberg, New York. <http://www.springer.com/series/411>.
- Kwek, K., Tou, T., Lee, S.: 1990, Current sheath structure of the plasma focus in the run-down phase. *IEEE Transactions on Plasma Science* **18**(5), 826.
- Larour, J., Singh, R.L., Stehlé, C., Ciardi, A., Chaulagain, U., Suzuki-Vidal, F.: 2015, Optimization of an electromagnetic generator for strong shocks in low pressure gas. *High Energy Density Physics* **17**, 129. DOI. ADS.
- Lee, S.: 1969, Transverse ionizing shock waves in a planar electromagnetic shock tube. PhD thesis, Australian National University.
- Lee, S., Serban, A.: 1996, Dimensions and lifetime of the plasma focus pinch. *IEEE Transactions on plasma science* **24**(3), 1101.
- Leygnac, S., Boireau, L., Michaut, C., Lanz, T., Stehlé, C., Clique, C., Bouquet, S.: 2006, Modeling multidimensional effects in the propagation of radiative shocks. *Physics of Plasmas (1994-present)* **13**(11), 113301.

- MacFarlane, J.J., Golovkin, I.E., Woodruff, P.R.: 2006, HELIOS-CR A 1-D radiation-magnetohydrodynamics code with inline atomic kinetics modeling. *Journal of Quantitative Spectroscopy and Radiative Transfer* **99**, 381. DOI. ADS.
- Macquorn Rankine, W.J.: 1870, On the Thermodynamic Theory of Waves of Finite Longitudinal Disturbance. *Philosophical Transactions of the Royal Society of London Series I* **160**, 277. ADS.
- Mahmood, S., Ur-Rehman, H.: 2009, Electrostatic solitons in unmagnetized hot electron-positron-ion plasmas. *Physics Letters A* **373**, 2255. DOI. ADS.
- Martin, T.H., Williams, M., Kristiansen, M.: 1996, *Jc martin on pulsed power* **3**, Springer Science & Business Media, ???.
- McClarren, R.G., Drake, R.P., Morel, J.E., Holloway, J.P.: 2010, Theory of radiative shocks in the mixed, optically thick-thin case. *Physics of Plasmas* **17**(9), 093301.
- Michaut, C., Stehlé, C., Leygnac, S., Lanz, T., Boireau, L.: 2004, Jump conditions in hypersonic shocks. Quantitative effects of ionic excitation and radiation. *European Physical Journal D* **28**, 381. DOI. ADS.
- Mihalas, D.: 1978, *Stellar atmospheres /2nd edition/*. ADS.
- Mihalas, D., Mihalas, B.W.: 1984, *Foundations of radiation hydrodynamics*. ADS.
- Mihalas, D., Mihalas, B.W.: 1999, *Foundations of radiation hydrodynamics*.
- More, R., Warren, K., Young, D., Zimmerman, G.: 1988, A new quotidian equation of state (qeos) for hot dense matter. *Physics of Fluids (1958-1988)* **31**(10), 3059.
- Ogando, F., Velarde, P.: 2001, Development of a radiation transport fluid dynamic code under amr scheme. *Journal of Quantitative Spectroscopy and Radiative Transfer* **71**(2), 541.
- Olson, G.L., Auer, L.H., Hall, M.L.: 2000, Diffusion, P_1 , and other approximate forms of radiation transport. *Journal of Quantitative Spectroscopy & Radiative Transfer* **64**, 619. DOI. ADS.
- Orban, C., Fatenejad, M., Chawla, S., Wilks, S.C., Lamb, D.Q.: 2013, A Radiation-Hydrodynamics Code Comparison for Laser-Produced Plasmas: FLASH versus HYDRA and the Results of Validation Experiments. *ArXiv e-prints*. ADS.

- Orlando, S., Bonito, R., Argiroffi, C., Reale, F., Peres, G., Miceli, M., Matakos, T., Stehlé, C., Ibgui, L., de Sá, L., Chièze, J.-P., Lanz, T.: 2013, Radiative accretion shocks along nonuniform stellar magnetic fields in classical T Tauri stars. *Astronomy & Astrophysics*.
- Ovsyannikov, A.A., Zhukov, M.F.: 2000, *Plasma diagnostics*, Cambridge International Science Publishing, Cambridge. <http://public.ebib.com/choice/publicfullrecord.aspx?p=258189>.
- Pfalzner, S.: 2006, *An introduction to inertial confinement fusion*, 1st edn., *Series in Plasma Physics*, Taylor & Francis, Taylor & Francis. <http://gen.lib.rus.ec/book/index.php?md5=EACF38292FD79113F78BB532AB5301B8>.
- Potter, D.E.: 1971, Numerical Studies of the Plasma Focus. *Physics of Fluids* **14**, 1911. DOI. ADS.
- Proakis, J.G.: 2001, *Digital signal processins*, Wiley Online Library, ???.
- Raga, A., Mellema, G., Arthur, S., Binette, L., Ferruit, P., Steffen, W.: 1999, 3d transfer of the diffuse ionizing radiation in ism flows and the preionization of a herbig-haro working surface. *Revista Mexicana de Astronomia y Astrofisica* **35**, 123.
- Reighard, A.B.: 2007, Collapsing radiative shock experiments on the omega laser. PhD thesis, The University of Michigan.
- Reighard, A., Drake, R., Dannenberg, K., Kremer, D., Grosskopf, M., Harding, E., Leibrandt, D., Glendinning, S., Perry, T., Remington, B., *et al.*: 2006, Observation of collapsing radiative shocks in laboratory experiments. *Physics of Plasmas (1994-present)* **13**(8), 082901.
- Rodriguez, R., Gil, J.M., Florido, R., Rubiano, J.G., Mendoza, M.A., Martel, P., Minguez, E., Symes, D.R., Hohenberger, M., Smith, R.A.: 2011, Determination of the average ionization and thermodynamic regimes of xenon plasmas with an application to the characterization of blast waves launched in xenon clusters. *High Energy Density Physics* **7**(2), 71 . DOI. <http://www.sciencedirect.com/science/article/pii/S157418181100022X>.
- Rodríguez, R., Espinosa, G., Gil, J.M., Stehlé, C., Suzuki-Vidal, F., Rubiano, J.G., Martel, P., Minguez, E.: 2015, Microscopic properties of xenon plasmas for density and temperature regimes of laboratory astrophysics experiments on radiative shocks. *Physical Review E* **91**(5), 053106. DOI. ADS.
- Ross, I.N., Pepler, D.A., Danson, C.N.: 1995, Binary phase zone plate designs using calculations of far-field distributions. *Optics Communications* **116**, 55. DOI. ADS.

- Seaton, M.J.: 1987, Atomic data for opacity calculations. I. General description. *Journal of Physics B: Atomic and Molecular Physics* **20**(23), 6363.
- Serban, A.: 1995, Anode geometry and focus characteristics. PhD thesis, Nanyang Technology University. <http://hdl.handle.net/10497/1568>.
- Serban, A., Lee, S.: 1995, A simple optical fiber axial speed detector. *Review of Scientific Instruments* **66**, 4958. DOI. ADS.
- Serban, A., Lee, S.: 1995, A simple optical fiber axial speed detector. *Review of scientific instruments* **66**(10), 4958.
- Singh, J.P., Thakur, S.N. (eds.): 2007, *Laser-induced breakdown spectroscopy*, Elsevier, sciencedirect.
- Singh, R., Stehlé, C., Suzuki-Vidal, F., Kozlova, M., Larour, J., Chaulagain, U., Clayson, T., Rodriguez, R., Gil, J., Nejd, J., *et al.*: 2017, Experimental study of the interaction of two laser-driven radiative shocks at the pals laser. *High Energy Density Physics* **23**, 20.
- Stahler, S.W., Palla, F., Salpeter, E.E.: 1986, Primordial stellar evolution - The protostar phase. *The Astrophysical Journal* **302**, 590. DOI. ADS.
- Stehlé, C., González, M., Kozlova, M., Rus, B., Mocek, T., Acef, O., Colombier, J.P., Lanz, T., Champion, N., Jakubczak, K., *et al.*: 2010, Experimental study of radiative shocks at pals facility. *Laser and particle beams* **28**(02), 253.
- Stehlé, C., Kozlová, M., Larour, J., Nejd, J., Champion, N., Barroso, P., Suzuki-Vidal, F., Acef, O., Delattre, P.-A., Dostál, J., *et al.*: 2012, New probing techniques of radiative shocks. *Optics Communications* **285**(1), 64.
- Stehlé, C., Lefèvre, R., Chaulagain, U., Champion, N., Barroso, P., Reix, F., Jagourel, P., Larour, J., Meltchakov, E., Mercier, R., *et al.*: 2014a, Critical components for xuv probing of laser driven shocks. In: *X-Ray Lasers 2012*, Springer, ???, 239.
- Stehlé, C., Kozlová, M., Larour, J., Nejd, J., Suzuki-Vidal, F., Cohen, M., Chaulagain, U.P., Champion, N., Barroso, P., Acef, O., *et al.*: 2014b, Reply on the comment of the paper “new probing techniques of radiative shocks”. *Optics Communications* **318**, 226.
- Suzuki-Vidal, F., Lebedev, S., Pickworth, L., Swadling, G., Burdiak, G., Skidmore, J., Hall, G., Bennett, M., Bland, S., Chittenden, J., *et al.*: 2014, Shock formation in counter-streaming jets on the magpie pulsed-power generator. In: *APS Meeting Abstracts* **1**, 5005.

- Suzuki-Vidal, F., Clayson, T., Swadling, G.F., Patankar, S., Burdiak, G.C., Lebedev, S.V., Smith, R.A., Stehle, C., Chaulagain, U., Singh, R.L., Larrour, J., Kozlova, M., Spindloe, C., Foster, J., Skidmore, J., Gumbrell, E., Graham, P., Danson, C.: 2016, Counter-streaming radiative shock experiments on the Orion laser. In: *APS Meeting Abstracts*. ADS.
- Toledo-Roy, J.C., Velázquez, P.F., de Colle, F., González, R.F., Reynoso, E.M., Kurtz, S.E., Reyes-Iturbide, J.: 2009, Numerical model for the SNR DEM L316: simulated X-ray emission. *Monthly Notices of the RAS* **395**, 351. DOI. ADS.
- Tou, T., Lee, S., Kwek, K.: 1989, Nonperturbing plasma-focus measurements in the run-down phase. *IEEE Transactions on Plasma Science* **17**(2), 311.
- Vaytet, N.M.H., Audit, E., Dubroca, B., Delahaye, F.: 2011, A numerical model for multigroup radiation hydrodynamics. *Journal of Quantitative Spectroscopy and Radiative Transfer* **112**, 1323. DOI. ADS.
- Vaytet, N., Chabrier, G., Audit, E., Commerçon, B., Masson, J., Ferguson, J., Delahaye, F.: 2013, Simulations of protostellar collapse using multigroup radiation hydrodynamics. ii. the second collapse. *arXiv preprint arXiv:1307.1010*.
- Vaytet, N., González, M., Audit, E., Chabrier, G.: 2013, The influence of frequency-dependent radiative transfer on the structures of radiative shocks. *Journal of Quantitative Spectroscopy and Radiative Transfer* **125**, 105. DOI. ADS.
- Velarde, P., García-Senz, D., Bravo, E., Ogando, F., Relaño, A., García, C., Oliva, E.: 2006, Interaction of supernova remnants: From the circumstellar medium to the terrestrial laboratory. *Physics of Plasmas* **13**(9), 092901. DOI. ADS.
- Veloso, F., Moreno, J., Tarifeño-Saldivia, A., Pavez, C., Zambra, M., Soto, L.: 2012a, Non-intrusive plasma diagnostics for measuring sheath kinematics in plasma focus discharges. *Measurement Science and Technology* **23**(8), 087002.
- Veloso, F., Tarifeño-Saldivia, A., Pavez, C., Moreno, J., Zambra, M., Soto, L.: 2012b, Plasma sheath kinematics and some implications on the modeling of very low energy plasma focus devices. *Plasma Physics and Controlled Fusion* **54**(9), 095007.
- Visco, A., Drake, R., Glenzer, S., Döppner, T., Gregori, G., Froula, D., Grosskopf, M.: 2012, Measurement of radiative shock properties by x-ray thomson scattering. *Physical review letters* **108**(14), 145001.

- Williams, R.M., Chu, Y.-H., Dickel, J.R., Beyer, R., Petre, R., Smith, R.C., Milne, D.K.: 1997, Supernova Remnants in the Magellanic Clouds. I. The Colliding Remnants DEM L316. *Astrophysical Journal* **480**, 618. ADS.
- Williams, R.M., Chu, Y.-H., Dickel, J.R., Gruendl, R.A., Seward, F.D., Guerrero, M.A., Hobbs, G.: 2005, Supernova Remnants in the Magellanic Clouds. V. The Complex Interior Structure of the N206 Supernova Remnant. *Astrophysical Journal* **628**, 704. DOI. ADS.
- Zambra, M., Kalise, D., Fernandez, J., Hernandez, E., Pasten, D., Munoz, V.: 2009, Current sheet thickness in the plasma focus snowplow model. *J. Plasma Fusion* **8**(879-882). <https://people.ricam.oeaw.ac.at/d.kalise/files/plasma.pdf>.
- Zel'dovich, I.B., Zel'dovich, Y.B., Raizer, Y.P.: 2002, *Physics of shock waves and high-temperature hydrodynamic phenomena*, Courier Dover Publications, London, New York, Sydney.

